Research and development in axial field motors

by

M.T. Mohammad
B.Sc., Diploma Tech., M.Sc. Eng.

A thesis submitted to the
University of Warwick
for the degree of Doctor of Philosophy
September, 1978.

To my wife

and my children

Lamise and Bayrum

To my wife

and my children

Lamise and Bayrum

Acknowledgements

I would like to express my thanks to the following:

To my wife for her continual understanding of the nature of the work and my children for their non-understanding of any work.

To Mr. A.E. Corbett for his valuable supervision and encouragement during the course of this project.

To Mr. M. Legg in the Engineering workshop for his skill, unlimited kindness and patience which left no room for the impossible, Mr. T. Whitehead, the University photographer for his excellent work and understanding, and Mr. M. Davies for his continual help in the Library.

Thanks are also due to members of staff and students of the machine group for their help and advice.

The author is also thankful to:

the Ministry of Higher Education, Baghdad, Iraq, for granting him a research award.

Mr. G, Latimer (Alcan aluminium) for supplying the aluminium and for his valuable advice in aluminium casting and Mr. J. Cawley (British Steel) for supplying the steel strip and advice.

Finally thanks are due to Mr. C. Patel for typing the thesis at the hospital.

List of symbols

S_1, S_2, R_1, R_2	Stator and rotors
B	Air gap flux density (B_p - peak value)
D_1	Inner principal diameter
D_2	Outer principal diameter
E	Induced emf
e	Air gap eccentricity
g	Physical air gap length
$\bar{g}$	Magnetic air gap length
k,n	Order of harmonic
x_m	Magnetizing reactance
V	Line voltage
I	Peak fundamental current
i	Current in phase A
i_b	Bar current
T	Turns per coil
T_b	Bar torque
N	Coils per phase
$\bar{N} = T.N$	Turns per pole per phase, total both sides.
α	Angular distance around air gap
α_o	Slot opening angle
α_d	Slot pitch angle
K_1	Fundamental winding factor
$K_{6k \pm 1}$	Winding factor for $6k \pm 1$ harmonic
p	Pole pairs
q	Number of slots per pole per phase
μ_o	Permeability of free space
μ_r	Relative permeability

z	Machine's total number of slots
z_b	Bar load impedance
θ_b	Bar load impedance phase angle
s	Slot width
t	Tooth width
$\bar{s}$	Slip
w	Mains frequency
R_e	Effective resistance of a bar
r_1	Phase resistance of stator winding
r	Resistance of bar load impedance
r_2	r - referred to primary of the equivalent circuit
X_e	Effective reactance of a bar
x_1	Stator leakage reactance per phase
x	Reactance of bar load impedance
x_2	x - referred to the primary of the equivalent circuit
m	Number of phases in the machine
Φ_T	Total gap flux per pole
Φ_K	Air gap flux
η	Efficiency
P_o	Output power
P.f.	Power factor
SCT	Schwarz-Christofel transformation
MSW	Magnetic slot wedge
UMP	Unbalanced magnetic pull
Air gap length	(means always physical gap length)

Additional symbols used in the test are defined where necessary.

CHAPTER 1

Aspects of axial field machine

1.1 General

The history of axial field induction machines started with the birth of radial machines as far as the main principles are concerned. The first suggestion to produce a rotating field without mechanical means put forward by Professor W. Bailey in 1879 (ref.1.1), represents the first real start in the field of electric machines. He constructed a four pole electromagnet system on a common yoke supplied by polyphase alternating currents. He proved the existence of a rotating field by suspending over the poles a copper disc which started to rotate under the influence of the field. The idea of employing alternating current as a main element in machines was then developed by G. Ferraris and Tesla and demonstrated in the construction of small motors.

This concept of the rotating magnetic field remains the basis of any induction machine regardless of the shape and construction. Years later came an explosion of activity in improvements in the field of machine design. These included the better understanding of the machines, physical improvements in shape, construction and improved materials used for manufacturing the different parts. Generally the position of the active conductors and the direction of the magnetic field decides the nature and shape of the machine. For optimum energy conversion, these two elements in any machine have to be mutually perpendicular. In radial air-gap machines the active conductors run parallel to the machine's shaft, and the magnetic field is radial to produce the required torque. For a long time, interest has been mainly concentrated on radial induction machines since they are very robust, easy to produce and give desirable performance. Therefore any new design to replace the radial machine is required to offer some new features which do not exist in the radial machines or are difficult to obtain without changing some of the desirable features.

In the axial field disc machines the active conductors run radially and the magnetic field is therefore directed axially. The history of electrical machines shows that many of the early machines were of disc type, starting with Faraday's disc generator. But because of the technical design requirements for axial field machines, the relative simplicity of design and cheapness of materials required in radial machines and the unimportance of weight in most applications, few attempts have been made to develop disc type machines. They soon became a topic of only historical interest and attention has been concentrated on radial machines.

A review of the patents and articles appearing since the fifties ref. (1.2, 1.3, 1.4) shows that the interest seemed to be steering back towards the axial field design and a number of universities and industries are now involved in the production of different types of these machines. This is due to the need of the market for special feature motors. By using these motors a drive system can become more economic, effective and lower in weight which are some of the market requirements. The less demanding construction requirements of the d.c. axial field disc motor initiated the work on this type of machine at Warwick University. However the work soon extended to a.c. axial field disc motors.

The first prototype three-phase a.c. axial field disc motor at Warwick University was built by B. Caraldi, ref.1.5. The stators have a flat shape and fitted with a three-phase, four pole, double-layer winding. one of the important limitations of this prototype is that the rotor had to be a double cage because of the particular method of fixing the rotor on the shaft.

This rotor is shown in Fig.(1.1) and it consists of a laminated magnetic core with two copper cages made of copper rings joined to copper radial bars by small screws. Two thick steel rings are fitted at the

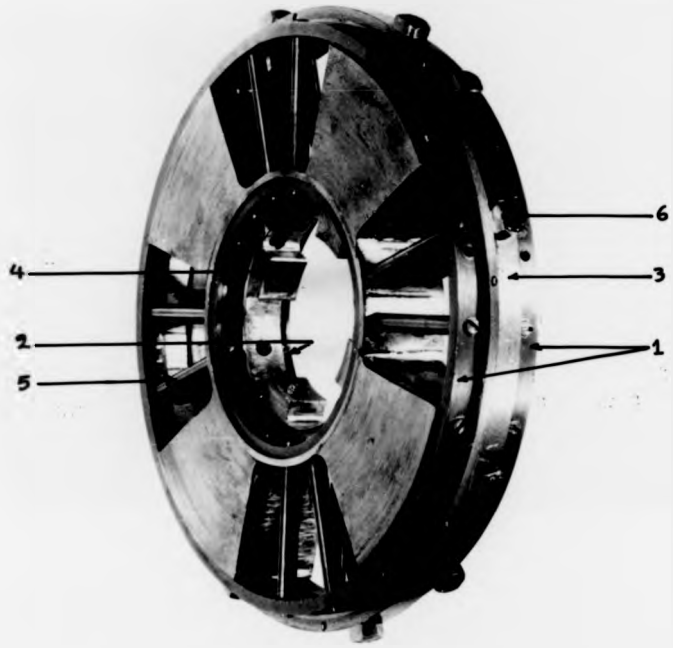

Fig 1.1 - The rotor of the first prototype a.c. axial field disc motor after some of the iron has been machined for experimental studies in ref. (1.5).

1,2 - Outer and inner copper cage and rings

3,4 - Outer and inner steel retaining rings

5 - Fo rty copper bars

6 - Thirteen radial steel bolts joining rings 3 & 4 radially.

Ring 4 is used for fixing the rotor on the shaft

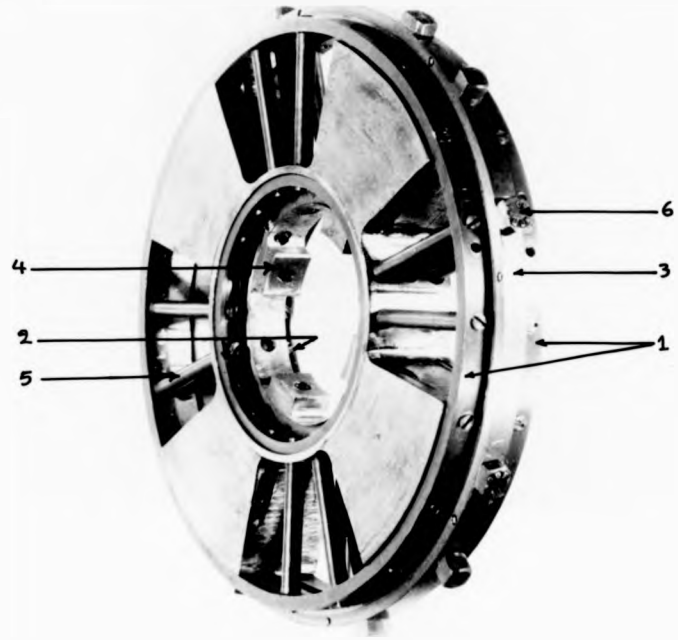

Fig 1.1 - The rotor of the first prototype a.c. axial field disc motor after some of the iron has been machined for experimental studies in ref. (1.5).

1,2 - Outer and inner copper cage and rings

3,4 - Outer and inner steel retaining rings

5 - Fo rty copper bars

6 - Thirteen radial steel bolts joining rings 3 & 4 radially.

Ring 4 is used for fixing the rotor on the shaft

inner and outer diameters between the copper cages and are joined radially by thirteen steel bolts with hexagonal heads. Therefore this rotor is expected to behave as if it is made of three cages, (ref. 1.5), two of copper separated by a steel cage the inner ring of which is used to fix the rotor on to the shaft. Such a design gives rise to considerable iron loss, high rotor weight, large inertia and low power/weight ratio, and reduces the flatness feature of the machine. Therefore any new rotor design must provide a comprehensive answer to all these problems and at the same time provide some other advantages. The work is therefore concentrated on the need to develop a comprehensive design which can yield an efficient a.c. axial field, three phase, four pole disc induction motor. The design introduced in this thesis by the author differs in many respects from the first prototype. A completely new production method is used in the manufacture of the rotor, giving single or double cage rotors with very desirable properties. This new design reduces the machine's weight considerably causing an increase in power/weight ratio of about 25% above that in the first prototype and comparing very well in this respect with radial machines of the same rating. The new rotor design satisfies most of the requirements. It offers the following advantages:-

1. Easy fabrication and very rigid construction using aluminium casting technique.
2. It is arranged for the rotor to carry a number of ventilation elements in the shape of fan blades produced together with the cage in one casting process.
3. The rotor is fixed on to the shaft through its aluminium inner end ring by using the fixing technique explained fully in page 93 which is applicable in single and double cage rotors. This novel fixing method is found to be successful. It improves the machine's performance, as it reduces the mass and inertia compared to that in the first prototype and consequently increases the power/weight ratio.

4. The cage production technique can be used to produce both single and multiple cage rotors on a common core.
5. The single cage rotors can be produced as thin as less than half the thickness of the first prototype and even the double cage is thinner.
6. The considerable reduction in the rotor thickness and the elimination of any extra fixing elements, gives rise to lower inertia and more balanced rotors compared with the previous prototype design.

   Improvements made to the stator achieved reduction in copper loss by employing larger wire gauge and higher utilization of space and introduced a new ventilation technique.

The axial field disc machine (Fig. 1.2) shows three principal configurations which are desirable in totally different applications. These machines can be produced from a double stator design with the rotor rotating in between, or a single stator with the rotor rotating between the stator and a magnetic return path which can be an integral part of the rotor. The use of double stator does not mean necessarily an increase in the weight of the motor compared to a radial machine of the same rating, due to shorter wires used in the windings and less metal needed in manufacturing the end plates and casing. An alternative double stator design can be achieved by producing the two stators in one core back to back fed with two series connected windings. Each stator will face a single or double cage rotor carried on the same shaft. In the single stator version, the fact that there is no stator on one side of the air gap facilitates coupling to an external load in a short axial space by making the load an integral part of the rotor.

The technique of winding the steel strip (page 91) introduced by the author to produce the disc shaped rotor and stator cores followed by

Aluminium –

Steel
Lamination –

L_g - Air-gap length on one side

L_s - Thickness of the stator core

$2L_r$ - Thickness of the rotor core

$2L_i$ - Thickness of the liminated bridge between the two cages

D_1 - Internal diameter

D_2 - External diameter

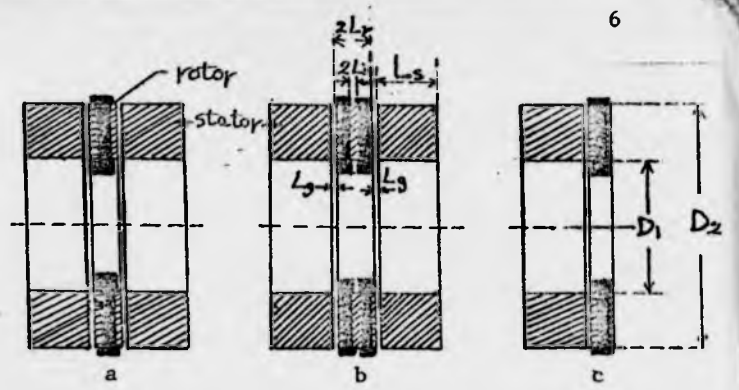

Fig 1.2A - Schematic representation of the a.c. axial field disc motor.

a - with double stator single cage rotor
b - with double stator double cage rotor
c - with single stator single cage rotor

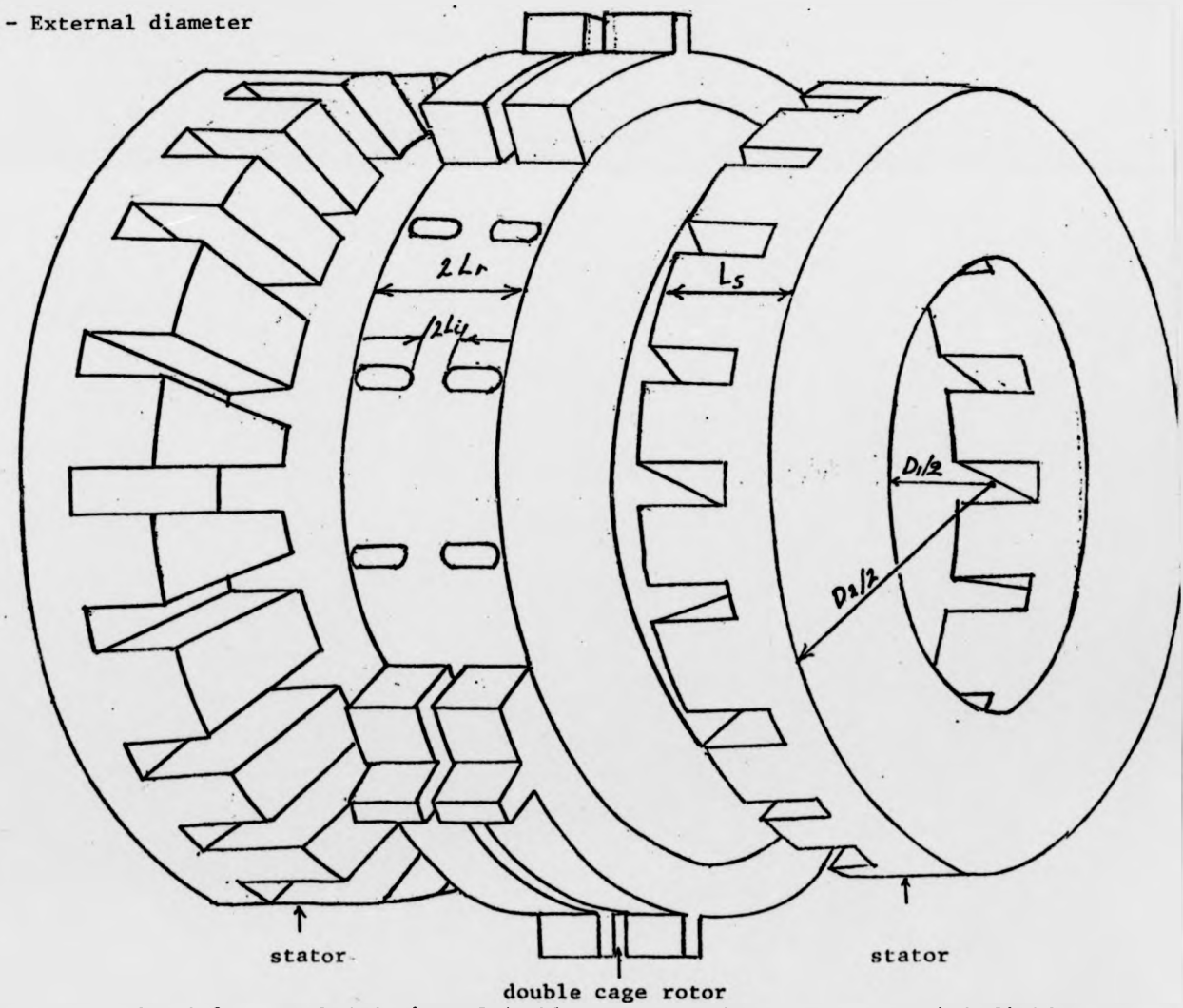

Fig. 1.2B - Exploded view of double stator double cage a.c. axial field disc motor

The two stators and the rotor are laminated in the form of a coiled spring

machining is believed by the author to be a suitable method of production. It may be compared with the production methods used in the radial machines of preparing the steel laminations, punching the slots in each, and pressing them together. The shorting effects due to machining can be reduced by annealing and giving the spring coil a few gentle shakes before it cools down to make the layers move and separate. Any idea of designing the core by stacking it from two or more pieces can increase the reluctance of the flux path in the circumferential direction in the lamination giving rise to high magnetizing current which can weaken the design. The only acceptable change could be when the idea of using strips is dropped in favour of some new design which can accelerate and improve the production without reducing the performance. Using the above experience and design method a three-phase, axial field prototype disc motor has been built and tested.

The present chapter continues to expound the general background of the axial field machines and discusses some of their new features and behaviour. Chapter 2 is concerned with developing a production method for planar aluminium cages and the practical conditions required to achieve satisfactory casting results. In Chapter 4 a formula for air-gap flux density is developed taking into account the effect of open slots in the stator using conformal transformation. Chapters 3, 5, and 6 describe experimental studies on the machine. In Chapter 3 the harmonic content of the machine is studied and measured. Means of reducing these harmonics are discussed and investigated experimentally. The first part of Chapter 5 is concerned with the manufacture of the machine and the measuring techniques employed in the practical work. The second part of the chapter involves study on unbalanced magnetic pull caused by rotor axial eccentricity. Suggestions are made for reducing the pull in single sided motor applications. Chapter 6 involves studies on the iron loss

at different parts of the machine, investigation on the effects of magnetic slot wedges and skewing on the machine performance and the noise level, and finally it introduces performance results of the machine operated with different rotors for the same pair of stators. Four different rotors have been made, namely unskewed single-cage laminated, skewed single cage laminated, unskewed cage solid and unskewed double cage laminated rotors. Chapter 7 describes some of the work done on the low inertia d.c. axial field motor. Results are obtained for perfor mance characteristics and the energy balance is studied with particular attention to commutation. Study on the dynamic performance of the motor under different inertias showed fast response to step inputs with a very short mechanical time constant compared to a printed circuit motor tested using a similar method. The new design technique for the face type commutator furnished very good results and reduced the cost by increasing the manufacturing reliability. Chapter 8 starts with general discussion and conclusions on most of the results. It contains some suggestions for future work, theories and derivation of equations and some photographs showing the motor complete with single and double cage rotors introduced by the author.

at different parts of the machine, investigation on the effects of magnetic slot wedges and skewing on the machine performance and the noise level, and finally it introduces performance results of the machine operated with different rotors for the same pair of stators. Four different rotors have been made, namely unskewed single-cage laminated, skewed single cage laminated, unskewed cage solid and unskewed double cage laminated rotors. Chapter 7 describes some of the work done on the low inertia d.c. axial field motor. Results are obtained for perfor mance characteristics and the energy balance is studied with particular attention to commutation. Study on the dynamic performance of the motor under different inertias showed fast response to step inputs with a very short mechanical time constant compared to a printed circuit motor tested using a similar method. The new design technique for the face type commutator furnished very good results and reduced the cost by increasing the manufacturing reliability. Chapter 8 starts with general discussion and conclusions on most of the results. It contains some suggestions for future work, theories and derivation of equations and some photographs showing the motor complete with single and double cage rotors introduced by the author.

1.2 Active Dimensions

The KVA rating of an m-phase radial induction machine with T_{ph} turns per phase and I_{ph} ampere per phase is given in ref. 1.6 as ;

$$S = 4.44\ m\ k_1 f \Phi\ T_{ph}\ I_{ph} * 10^{-3}\ KVA \quad \ldots\ldots\ldots\ 1.1$$

where k_1 is the fundamental winding factor.

Φ is the no load flux per pole and f is mains frequency.

It is given also that $\bar{B}$ the specific magnetic loading (mean flux density over the gap surface) is :-

$$\bar{B} = \frac{2p\Phi}{\pi DL}\ wb/m^2 \quad (D \text{ is stator bore}) \quad \ldots\ldots\ldots\ 1.2$$

and that ac the specific electric loading or the number of ampere-conductors per meter of armature periphery is:-

$$ac = \frac{2m\ T_{ph}\ I_{ph}}{\pi D}\ \text{amp. - cond. per m.} \quad \ldots\ldots\ldots\ 1.3$$

Substituting equations 1.3 and 1.2 in equation 1.1 gives :-

$$S = 0.0111 k_1 \bar{B}\ ac(D^2Ln)\ \ KVA \quad (n \text{ in rev/sec})$$

The mechanical output power (Pm) found from this equation is :-

$$Pm = 0.0111 k_1 \bar{B}\ ac\ (D^2Ln)\eta\ \cos\phi\ \ KW \quad \ldots\ldots\ldots\ 1.4$$

Where η, $\cos\phi$ are the efficiency and power factor respectively.

Similar equations to 1.1 - 1.4 can be derived for axial-field disc machines. The only modifications are those necessary to take account of the different geometry. If as before, $\bar{B}$ is the mean flux density over the gap surface,

$$\bar{B} = \frac{2P\Phi}{\frac{\pi}{4}(D_2^2 - D_1^2)}\ wb/m^2 \quad \ldots\ldots\ldots\ 1.5$$

where D1 and D2 are the main diameters shown in Fig.(1.2).

In the axial air-gap disc machines the specific electric loading is not constant within the machine, it is maximum at the inner circumference and a minimum at the outer circumference.

If ac is defined as the maximum specific electric loading, then

$$ac = \frac{2m\, T_{ph}\, I_{ph}}{\pi D_1} \quad \text{amp. - cond. per m} \quad \ldots\ldots 1.6$$

Substituting equations 1.6 and 1.5 in equation 1.1 gives

$$S = 4.44\, m K_1 f\, \frac{\bar{B}(D_2^2 - D_1^2)}{8p}\, \frac{D_1\, ac}{2m} * 10^{-3} \text{ KVA}$$

and the mechanical output power is :-

$$Pm = \frac{4.44 K_1 \frac{2}{\pi} nB\, ac.\, (D_2^2 - D_1^2)\, D_1 \gamma \cos\phi * 10^{-3}}{16} \text{ KW}$$

$$= G(D_2^2 - D_1^2)\, D_1 \qquad G = 0.0027 K_1 n \bar{B}\, ac\, \gamma \cos\phi \quad \ldots\ldots\ldots 1.7$$

To find the value of D_1 which gives maximum output power, equation 1.7 has to be differentiated with respect to D_1, with D_2 fixed and equating to zero, giving that;

$$D_1 = \frac{D_2}{\sqrt{3}} \quad \ldots\ldots\ldots\ldots\ldots\ldots 1.8$$

In the experimental machine a value $D_1 = \frac{D_2}{2}$ was chosen. This value is of the same order as that given by equation 1.8, and it also provides a suitable means for comparing the results of the experimental machine with those of the first prototype of ref. 1.5.

Equation 1.7 shows that the output power of the experimental machine can be increased either by extending the machine radially to increase the active conductor length or by employing more than one cage in the same rotor core to increase the rotor electric loading. This can increase the weight of the machine but at the same time the increase in the output power may justify such an increase in the weight thereby maintaining a power-to-weight ratio of the same order.

The choice of the method for increasing the output power of the machine depends on the nature of application in which the motor is required.

Therefore when the axial length is not a critical requirement, the power can be increased by employing a double cage rotor. But where the application requires short axial length with no limitation on the diameter the power can be increased by enlarging the machine radially. In most of the applications a compromise of the two cases is useful.

The total axial length of the double stator, double cage motor operating in the aligned mode is 2(Ls + Lg + Lr) plus the thickness of the end plates of the frame, wehre L's are the dimensions shown in Fig. (1.2).

The overall diameter of the machine is D_2 plus a radial length of approximately $D_2/7$ accounting for the overhang. The conductor's active length in the rotor and the stators is $\left(\frac{D_2 - D_1}{2}\right)$ and it remains unchanged no matter how many cages are in use.

1.3 Machine's mmf

The field at the air-gap is the resultant combination of mmfs due to currents in the three phase windings of a machine. It is general practice to superimpose the mmfs of the windings instead of fluxes to allow for magnetic saturation. In the air-gap of the practical machine there are two types of mmf combinations, the first combination occurs at each stator separately as a result of combined mmfs in the three phases of each stator. This type of mmf combination is the same in each stator for any condition. The second combination occurs between the mmfs of the two stators. There are two possible combinations; the first is that the two mmfs can be arranged to assist each other in a "push-pull" manner and this position is known as the aligned position, the second possibility is where the two mmfs are partially or totally opposing each other.

It is shown in Chapter 3, that the aligned position is a position where the harmonic amplitude in the gap flux is a minimum, and it increases rapidly as the stators are misaligned due to the departure of the flux from being normal. There is a certain position of the stator slotting at which the three phases have minimum balanced currents. Unfortunately this position does not coincide exactly with the position of minimum harmonic amplitude. Therefore a position not far away from the "minimum balanced currents" position and having small harmonic amplitude has been chosen as the optimum relative position of the stators.

1.3.1 Misalignment in double cage motor

A double cage, double stator motor is shown in fig. 1.3a with the

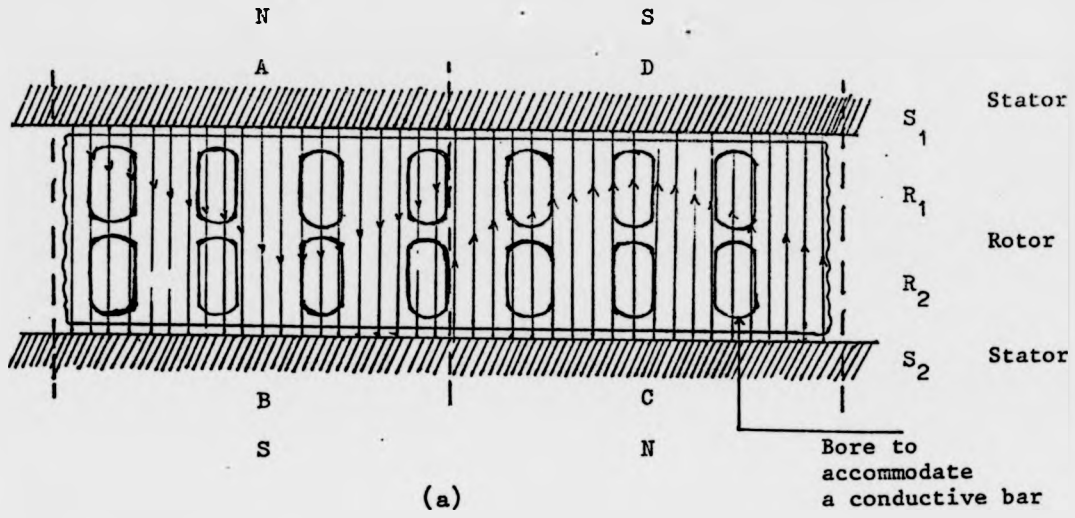

(a)

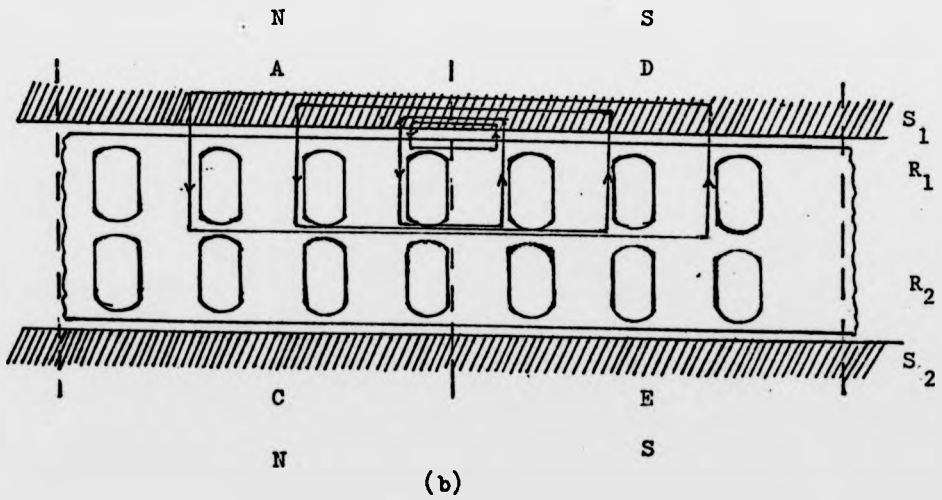

(b)

Fig.(1.3) - Developed diagram of magnetic circuit in a double cage, double stator motor.

two stators in the aligned position assuming the flux from either stator crosses both air-gaps in straight lines since opposite poles face each other. The rotor is at zero magnetic potential relative to the stators as long as the magnetic balance is preserved. Therefore the flux lines at A cross the air-gap, and continue axially into the rotor crossing the air gap at B, proceeding circumferentially through the stator to C and continue in the same manner as before but in reverse direction until they arrive back at A. But if one of the stators is rotated such that pole C is aligned with pole A (complete misalignment) as shown in fig. 1.3b, the flux lines at A after crossing the air-gap pass circumferentially through the rotor, cross the air-gap at D and then travel back to A through the stator core. Therefore the rotor no longer has zero potential and it has to be thicker to prevent magnetic saturation and non-linearities in the magnetic return path between the two cages. Therefore the machine behaves as if it has two rotors joined back to back rotating in one magnetic field.

1.3.2 Misalignment in single cage motor

In a single cage, double stator motor, the different rotor construction produces a totally different situation in respect of flux distribution. When the two stators are in alignment the situation is similar to that in the double cage motor as shown in fig. 1.4a. But when the stators are in misalignment, the flux lines from A cannot cross the gap axially through the rotor and the only possible path is circumferentially through 1,2,3, shown in fig. 1.4b,c depending on the degree of misalignment and thickness of the magnetic bridges over the slots.. Therefore it is possible to conclude that the motor can only be operated successfully under completely aligned conditions. Since misalignemnt causes the air-gap flux to deviate from normal position, the speed will decrease as misalignment increases,ref. 1.7. Therefore this behaviour of the single cage machine can be considered as a method of speed control by adjusting the slip mechanically but inevitably it is

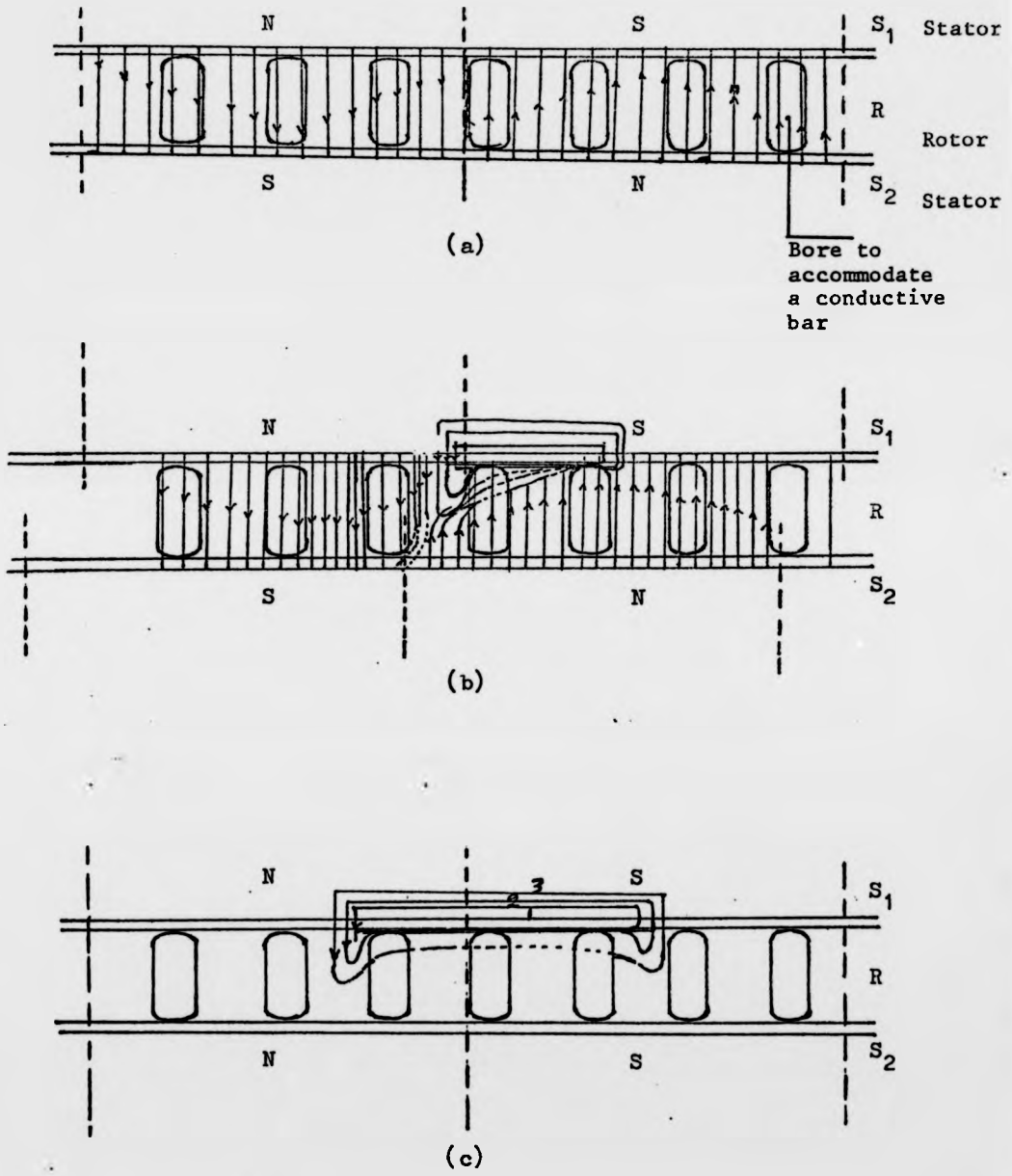

Fig.(1.4) - Developed diagram of magnetic circuit of a single cage double stator motor.

accompanied by heavy losses.

1.4 General applications

The machine due to its special features together with the new production method described in the present work can offer the following advantages:-

a. Short axial length and flat shape having high power/weight ratio.

b. Possible axial separation between rotor and stator.

c. It is possible to run the motor with two stators or one.

d. The air-gap can be varied by displacing the stators.

e. The stators can be rocked relative to each other, and in a single cage motor such an angular displacement can change the speed of rotation of the shaft.

f. The rotor can now be produced with lower inertia than the first prototype built at this University.

Due to some of these features, these machines have found a number of applications. In the earlier application Pensabene (1.2) used property "d" to design a small electric motor-pump unit for water circulating. The motor was designed to work at two different air-gap lengths, the short gap length at the start where a high starting torque is required to enable the motor to start against adverse conditions. This short gap length is achieved by using the UMP between the rotor and stator. The pump is provided with hydraulic discharge and suction chambers which are so arranged that as the pump gathers speed a hydraulic thrust arising from a pressure difference between the chambers is applied in opposite direction to the magnetic pull so as to cause the air-gap to extend to its maximum lengths to make the motor more quiet by reducing the high frequency noise.

At the present time electric motor driven pumps for the same purpose have been designed and manufactured by SMC-(U.K) Fig. 1.5 employing fixed gap-length. The stator has a single phase permanent capacitor type winding separated completely from the rotor assembly by a diaphragm.

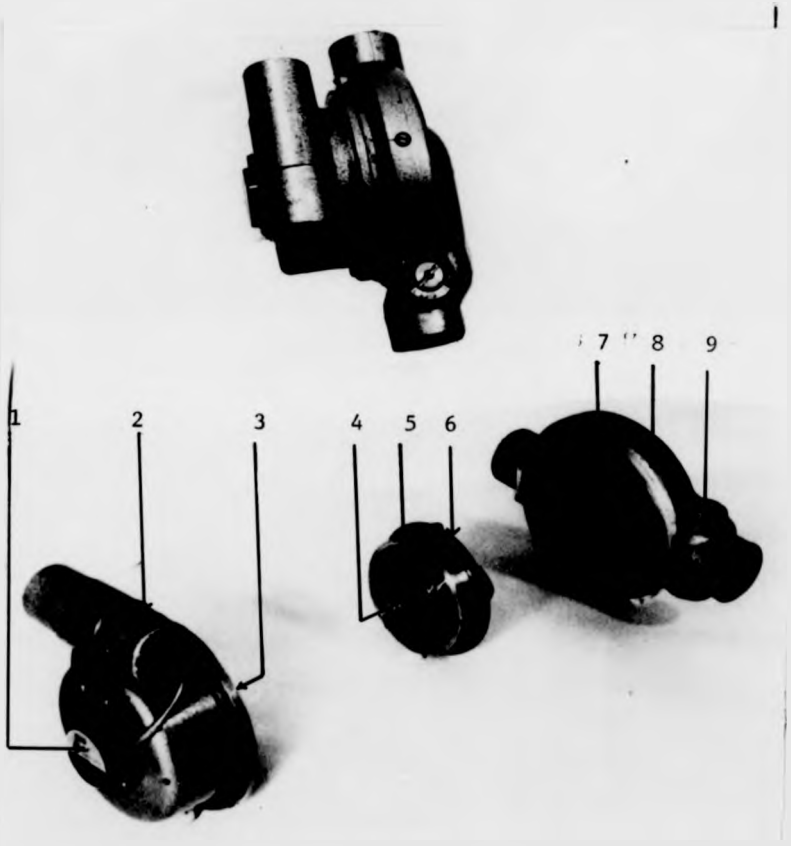

Fig. 1.5 - Single phase, permanent capacitor motor-drive pump, (cadet), courtesy of SMC Ltd (UK)

1. - Terminal box
2. - Condenser
3. - Steel diaphram
4. - Bolt and washer
5. - Planar cage rotor
6. - Impeller (magnetic return path)
7. - O-ring
8. - Pump casing
9. - Mechanical regulator

Fig. 1.5 - Single phase, permanent capacitor motor-drive pump, (cadet), courtesy of SMC Ltd (UK)

1. - Terminal box
2. - Condenser
3. - Steel diaphram
4. - Bolt and washer
5. - Planar cage rotor
6. - Impeller (magnetic return path)
7. - O-ring
8. - Pump casing
9. - Mechanical regulator

[illegible]. This diaphragm is set against the stator and acts as one side of the air-gap. On the other side of the gap is located the disc rotor as an integral component with the pump impeller blades. The existence of the impeller helps in balancing the [illegible] UMP between rotor core and the stator. Axial field machines can also be employed in the same applications as radial machines with important advantages of short axial length and high power/weight ratio.

1.5 Types of machine

The motor can be designed with different types of rotor which can be used with single or double stators. The rotor can be designed in a number of different configurations depending on the material, construction and shape of the rotor, such that by nominating the type of the rotor indication can be given to the type of the machine as follows: -

a. - Ironless rotor(eddy-current):

Due to the shape of these machines they lend themselves very well to [illegible] conducting type rotor designs. The rotor is made of a copper or aluminium disc with inner and outer hubs. The motor performance can be changed over a wide range by changing the cross-sectional area of the hubs. The removal of the magnetic core from the rotor eliminates the UMP, which is the attraction between the rotor and stator. But the use of a conductive disc in an alternating field causes repulsive forces to be set up in the conductor owing to the induced eddy currents. The main drawback of the conducting disc machine is its inherently large air gap which leads to high magnetizing current and rather low efficiency. Some of the advantages of this design are low rotor inertia and ease of manufacture, ref. (1.7,1.8).

b. - Iron rotor:

In this configuration the rotor is made of magnetic materials (solid or laminated) in the form of a flat-disc with a number of holes drilled radially to be filled with planar single or multiple cages of conducting material. This type of rotor gives higher inertia but at the same time provides a much smaller air-gap and considerably higher efficiency. These rotors can be manufactured by either drilling radial holes in the core after winding of the steel strip or by simultaneously punching of the holes during winding using a special indexing machine. The complete conducting cage is produced later by one aluminium casting process.
The first design technique is used in the present work, and the first envisaged features of a single cage rotor are shown in fig.1.6. An alternative design technique is to cut slots in the core and then inserting a ready-punched cage by pressing it into the slots. The complete cage is punched out of high conductivity copper or aluminium sheet in the shape of thin discs to fit the core.

c. - Reluctance rotors:

This type of rotor can be produced by modifying the iron type rotors by removing the iron at certain places to produce the saliency, reference 1.9. The conductive cage produces the induction torque which is required to take the speed to near synchronous value where the reluctance torque becomes effective and can lock the rotor's poles into synchronism with the stator's rotating field. Since the motor is operating at synchronous speed there is no iron loss in the rotor. Therefore it is expected that

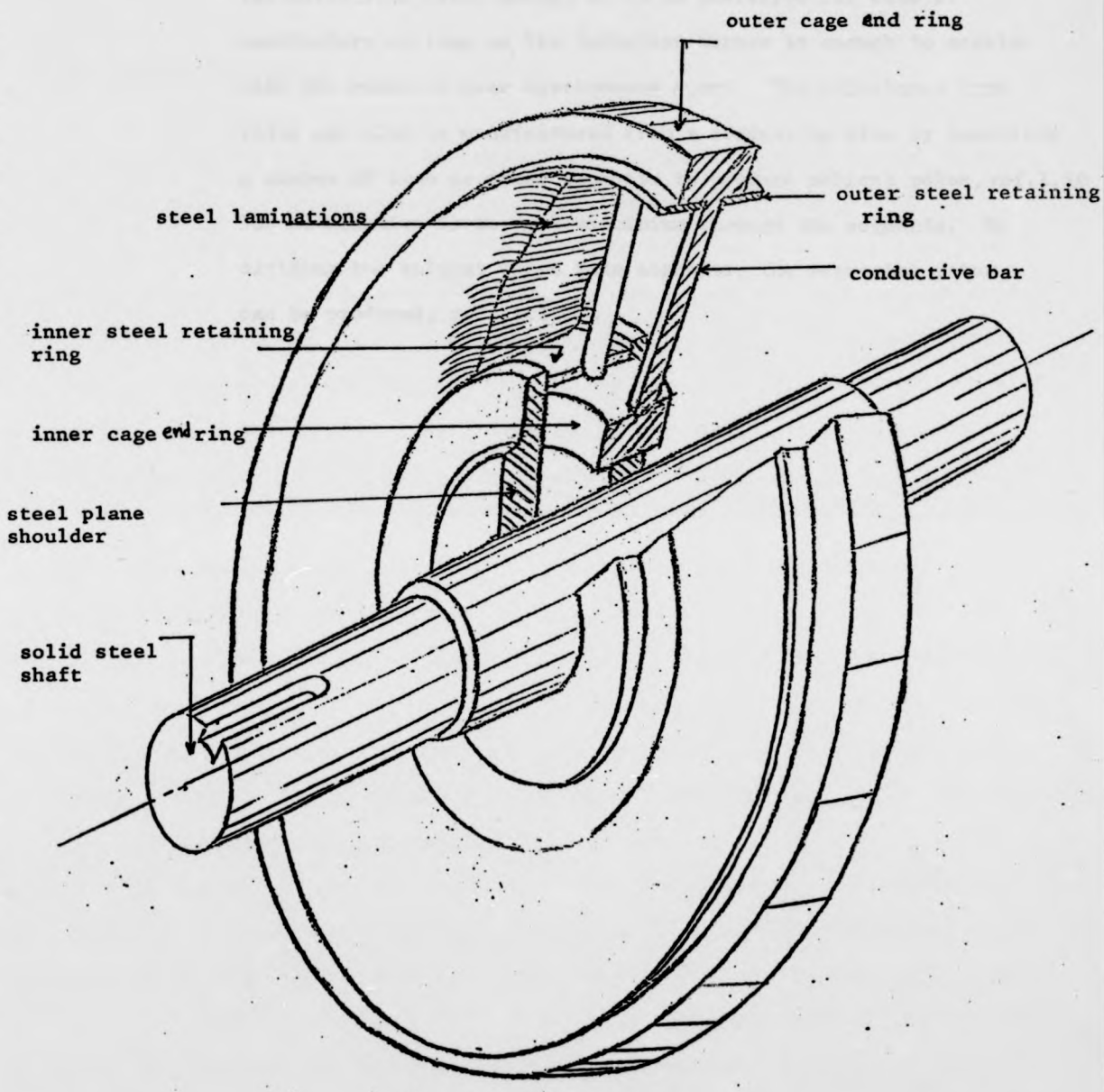

Fig. (1.6) - The first envisaged construction of a complete steel core single cage rotor for the experimental motor.

the solid iron rotor design is to be preferred for ease of manufacture as long as the induction torque is enough to accelerate the rotor to near synchronous speed. The reluctance type rotor can also be manufactured from a conducting disc by inserting a number of iron or steel segments to produce salient poles, ref.1.10 The alternative is to cast aluminium through the segments. By dividing the salient poles into segments, the segmental rotor can be produced, ref. 1.11.

CHAPTER 2

PLANAR ALUMINIUM CAGES

2.1 Aluminium Casting

2.1.1 Introduction

Casting has been the established method of producing conventional aluminium squirrel cage rotors of very desirable properties for many years. This type of casting process started about 1925 and progressed so rapidly that the rotors of nearly all squirrel cage induction motors are now cast in aluminium.

Rotors of below 11 KW are normally pressure die cast, while the larger ones are either centrifugally cast or gravity die cast. The old technique of manufacturing the squirrel cage by welding or brazing end ring and conductor bars together is still used for making very large rotors. There are a number of defects that occur in aluminium squirrel cage casting. These depend on the type of aluminium chosen, type of casting process, mould structure and the conditions provided for casting.

One of these defects is the tendency of the metal to "hot-shortness". This occurs when any tensile stress applied to an alloy while it is in the "two phase" solid/liquid condition will naturally cause the metal crystal to separate where there is no solid/solid contact. The reason for these stresses is the contraction or shrinkage of a hollow casting about a strong core.

The second of these defects is the 'cold shuts' which are discontinuities in the metal arising from streams of metal coming from different directions that make physical contact without completely fusing, because of heavy oxide film or lack of fluidity and feeding. The temperature of the molten metal and the mould just prior to the casting process are very important factors which would control the casting characteristics. The temperatures and some other requirements have to be decided by a number of experimental trials and to be fixed as the best casting conditions as is shown later.

It is required to establish a casting method which can give a satisfactory

planar cage rotor casting employing conventional casting methods. Therefore to start with gravity sand casting is advantageous since it is an easy and cheap casting process. The results obtained from this method are however random and unsatisfactory. After a continuous search and trials it was concluded that the centrifugal casting technique is suitable. It is found also that the grain refining technique can improve the metal castability and rigidity by producing finer grain sizes in the molten metal. The high speed running tests showed that the cages produced can stand very high speed.

2.1.2 Cage construction

The rotor of the experimental machine has a planar shape and consists of a steel core wound of steel strip in the shape of a flat spiral with a number of holes extending radially to accommodate the bars. It is required to introduce a design technique by which it is possible to produce an electrically conductive cage in which the bars are running radially through the holes to join the inner and outer end rings which short-circuit the bars and enclose the laminations and are at the same level as the laminations. A set of ten blades are designed to sit perpendicularly on the outer ring surface as an integral part of the cage. The bars, end rings and the blades are to produce in one operation as a solid piece.

2.1.3 Choices in Aluminium Casting

As explained earlier, the rotor is wound in the shape of a concentric spring using thin continuous steel strip. The only means which holds the laminated layers together are two steel rings fitted at the two rotor diameters. When the rotor rotates under the effect of the magnetic field, there are mainly two forces acting directly on the laminations. These are the centrifugal force acting radially and the UMP. The axial movement is very critical due to the sudden increase in the unbalanced magnetic pull under small changes

in the air-gap which cause the gap length to increase in one side and decrease in the other. It is therefore an essential requirement that the bars should fit tightly enough in the holes to prevent any such disastrous movement, since these bars are the skeleton of the rotor. A suitable way to meet such requirements fully is by using an aluminium casting technique in cage production.

The fact that aluminium can flow in the slots and fill them completely gives a large amount of metal in a bar compared with brazing or welding processes, gives lower electrical resistance for a certain slot size and produces a quiet rotor. The shrinkage property of aluminium can provide enough enclosing at the outer diameter and produce balanced rotors. The selection of the casting process depends on a number of factors, such as cost, amount of production, rotor characteristics required and the shape of the rotor. Experience showed that the selection of the casting process depends heavily on the shape and nature of the rotor. As an example, poor casting results have been obtained when sand casting process was used for cage production. The main difficulty is that due to the rotor's structure, the bars and end rings are at the same level, a feature which makes the metal flow slow and be less dependent on gravity. The shape of the rotor lends itself very well to the centrifugal casting technique. This type of casting furnished much sounder products which due to the higher metal density also have lower electrical resistance.

The choice of aluminium metal (ref.2.1) is another important factor which depends on the conductivity and castability required. Conductivity and castability are two interrelated factors, since the purer is the aluminium, the higher is its conductivity, but the poorer is its castability. But it is possible always to improve the castability of a pure aluminium by treating it with certain types of grain refiners with only slight reduction in its conductivity. The types and properties of aluminium suitable for rotor casting in U.K. are given in table (2.1).

Alcan aluminium 17070 is therefore chosen for casting the rotors since it

in the air-gap which cause the gap length to increase in one side and decrease in the other. It is therefore an essential requirement that the bars should fit tightly enough in the holes to prevent any such disastrous movement, since these bars are the skeleton of the rotor. A suitable way to meet such requirements fully is by using an aluminium casting technique in cage production.

The fact that aluminium can flow in the slots and fill them completely gives a large amount of metal in a bar compared with brazing or welding processes, gives lower electrical resistance for a certain slot size and produces a quiet rotor. The shrinkage property of aluminium can provide enough enclosing at the outer diameter and produce balanced rotors. The selection of the casting process depends on a number of factors, such as cost, amount of production, rotor characteristics required and the shape of the rotor. Experience showed that the selection of the casting process depends heavily on the shape and nature of the rotor. As an example, poor casting results have been obtained when sand casting process was used for cage production. The main difficulty is that due to the rotor's structure, the bars and end rings are at the same level, a feature which makes the metal flow slow and be less dependent on gravity. The shape of the rotor lends itself very well to the centrifugal casting technique. This type of casting furnished much sounder products which due to the higher metal density also have lower electrical resistance.

The choice of aluminium metal (ref.2.1) is another important factor which depends on the conductivity and castability required. Conductivity and castability are two interrelated factors, since the purer is the aluminium, the higher is its conductivity, but the poorer is its castability. But it is possible always to improve the castability of a pure aluminium by treating it with certain types of grain refiners with only slight reduction in its conductivity. The types and properties of aluminium suitable for rotor casting in U.K. are given in table (2.1).

Alcan aluminium 17070 is therefore chosen for casting the rotors since it

Fig (2.1)- Solid Experimental Core

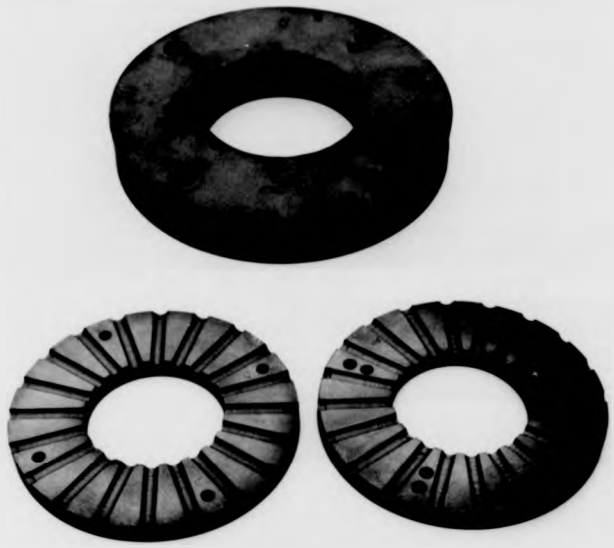

Table (2.1)- Alcan Aluminium for Rotor Casting

Al-designation	Al(%)	Min. rated Conductivity relative to Cu
10080	99 Min.	54%
13070	99.3 "	55%
15070	99.5 "	57%
17070	99.7 "	59%

Properties	Cu	Al	Al as percent of Cu
Specific Gravity	8.9	2.7	30%
Relative Conductivity	100%	62%	62%
Specific Heat (Cal./Kg./C°)	90	220	230%
Heat Conductivity(Cal/m.SecC°	90	50	56%

Table (2.2)- Relative Properties of Copper and Aluminium

Fig (2.1)- Solid Experimental Core

Table (2.1)- Alcan Aluminium for Rotor Casting

Al-designation	Al(%)	Min. rated Conductivity relative to Cu
10080	99 Min.	54%
13070	99.3 "	55%
15070	99.5 "	57%
17070	99.7 "	59%

Properties	Cu	Al	Al as percent of Cu
Specific Gravity	8.9	2.7	30%
Relative Conductivity	100%	62%	62%
Specific Heat (Cal./Kg./C°)	90	220	230%
Heat Conductivity(Cal/m.SecC°)	90	50	56%

Table (2.2)- Relative Properties of Copper and Aluminium

offers the largest conductivity and good fluidity, but is also the most prone to hot shortness. The difficulties arising in the casting process were solved by the author step by step after continuous trials and using different improving elements.

2.1.4 Evaluation of Aluminium as Casting Element

Copper and aluminium are the only two conductors used widely in machines and they cover almost all machine requirements. The general properties of the two metals in connection with the machine requirements are given in table (2.2). It is possible to show that properties of aluminium given in the table are not inferior to those of the copper for rotor production since some increase in the dimensions of the aluminium cage axially can compensate for any copper superiority without altering the core dimensions. Therefore to produce an equivalent cage of aluminium having the same electrical resistance as that of a copper cage, the volume of the cage has to be relatively larger, but the total mass of the aluminium cage is less than that of the copper cage due to the lower specific gravity of aluminium. This reduction in the mass means that an aluminium cage rotor is subject to less stress from centrifugal forces, less starting inertia and less vibrations while running. The reduction in the mass can also partly compensate for high heat capacity of aluminium in the cage. The heat conductivity of aluminium is less than that of the copper, but the increase in the volume of the equivalent aluminium cage can improve the heat transmission from the cage. Considering the above discussion it is clear that aluminium can be a satisfactory casting element in planar cage production if consideration is given to the change in the size and the relative cost.

2.2 Casting methods

2.2.1 Sand Casting

Cheapness, simplicity and easy fabrication are among the reasons which decide the type of casting methods which have been investigated in this work. Gravity sand casting is therefore firstly chosen since it is a straightforward process compared to the other casting methods. The bars, end rings and fan blades are produced in one casting process as follows: a wooden pattern has been designed to the exact shape and dimensions of the rotor with the outer diameter 24mm larger than the rotor diameter and carrying ten blades. By inserting the pattern in the sand the required shape of the cage is produced. The pattern is then replaced by the steel core with its centre coincident with the pattern centre. The difference at the outer diameters of the pattern and the core provide the space for outer ring formation of 12mm thick. The molten metal is poured at the centre of the warm core, so that it runs into the slots to form the conductor bars and into the cavities to form the end rings and the fan blades. The sand die is then let to cool down and the rotor has to pass a number of tests starting with a visual check.

2.2.2 Experimental Core

It is required to carry on a number of casting trials to produce the required planar cage and to fix the best casting conditions with respect to the temperature of the molten metal relative to the core and the quality of the cages produced. It is essential in every trial to be able to test the different parts of the cage visually and detect any defects and to find the solution. To achieve such a requirement, an experimental core has been designed to use in the casting trials as the core of the rotor.

This core is shown in fig (2.1) and is a replica of the original core of the rotor made of solid steel with the same dimensions. It consists of two similar halves, each half containing twenty half slot sections, such that, when they are put together and fixed by four screws they form a complete flat shape

2.2 Casting methods

2.2.1 Sand Casting

Cheapness, simplicity and easy fabrication are among the reasons which decide the type of casting methods which have been investigated in this work. Gravity sand casting is therefore firstly chosen since it is a straightforward process compared to the other casting methods. The bars, end rings and fan blades are produced in one casting process as follows: a wooden pattern has been designed to the exact shape and dimensions of the rotor with the outer diameter 24mm larger than the rotor diameter and carrying ten blades. By inserting the pattern in the sand the required shape of the cage is produced. The pattern is then replaced by the steel core with its centre coincident with the pattern centre. The difference at the outer diameters of the pattern and the core provide the space for outer ring formation of 12mm thick. The molten metal is poured at the centre of the warm core, so that it runs into the slots to form the conductor bars and into the cavities to form the end rings and the fan blades. The sand die is then let to cool down and the rotor has to pass a number of tests starting with a visual check.

2.2.2 Experimental Core

It is required to carry on a number of casting trials to produce the required planar cage and to fix the best casting conditions with respect to the temperature of the molten metal relative to the core and the quality of the cages produced. It is essential in every trial to be able to test the different parts of the cage visually and detect any defects and to find the solution. To achieve such a requirement, an experimental core has been designed to use in the casting trials as the core of the rotor.

This core is shown in fig (2.1) and is a replica of the original core of the rotor made of solid steel with the same dimensions. It consists of two similar halves, each half containing twenty half slot sections, such that, when they are put together and fixed by four screws they form a complete flat shape

core with twenty slots runing radially. Each half is tapered at its outer diameter from outside towards the centre of the slots to ease the extraction of the cage from the core. The same four screws are used as extracting tools when it is required to remove the cage from the core.

2.2.3 Casting Results using standard casting techniques

A number of attempts have been made to produce the cages by gravity sand casting. The main variables were the temperature of aluminium and the temperature of the core. The results obtained are shown in fig (2.2). In "a" the core is warmed up to 300°C and the aluminium poured at its centre at a temperature of 730°C. In "b" the temperature of the core is increased to 400°C and that of aluminium to 760°C. The results shows that some of the bars have suffered cold shut and some cracks and shrinkage cavities have appeared in the outer ring. It is believed that the cold shut of the bars and the shrinkage cavities at the ring may be caused by the normal shrinkage during solidification in the absence of adequate feeding, or by entrapped gases in the cavities. The main reasons for the cracks in the ring is believed to be that the solid steel core prevents the aluminium ring from shrinking freely as it solidifies, giving rise to enough restraint to break it in some places.

To test the validity of this, in "c" both the core and aluminium were heated up to a high temperature (800°C), and the result obtained shows that all the cracks disappeared completely. By heating the steel to such a temperature the shrinkage of the steel when it is cooling down counterbalances the shrinkage of the aluminium and prevents the cracking. A large number of trials and continuous study of the problem led to the somehow improved result at "d" by introducing three new factors in the casting process as follows:

(a) A number of laminated layers* have been wound at the outer surface of the experimental core and the slots are extended radially through the laminated layers. These layers can provide the space for aluminium shrinkage during cooling.

* This condition already exist in the machine core since it is made of laminations.

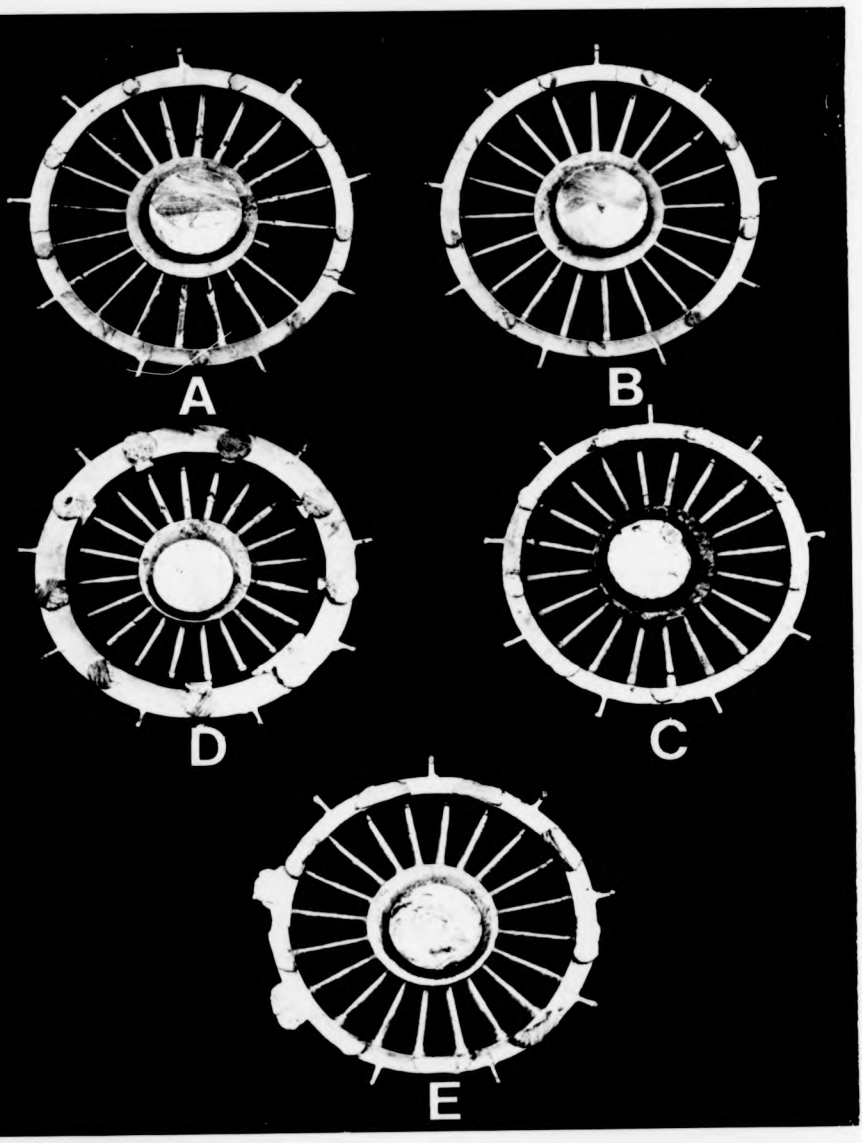

Fig (2.2)- Planar aluminium cages without steel core.

(b) The core after being warmed up, has been dipped in a mixture of 54% water, 28% Foseco Dycotte, 18% Sodium Silicate and heated again to 400°C. This mixture can provide two functions; firstly it makes the metal flow more easily and improve the feeding rate, and secondly it acts as an insulation between aluminium and the core.

(c) Much larger risers have been used to improve the feeding rate.

Providing all the three factors in one casting operation the result at Fig.2.2d is achieved. But even this result has not reached the required standard since in some other trials under similar conditions, cold shut effects and some cracks showed up. Therefore, results a to d do not satisfy the visual test* but it is possible to conclude that the conditions for good casting could be as follows:

(1) Steel core heated to 400°C and aluminium to 750°C. Overheating the aluminium is not recommended since high temperature aluminium produces coarse grain size which in turn will give rise to hot-shortness and increase the tendency to form shrinkage cavities. Aluminium at high temperatures reacts with water vapour to produce aluminium oxide and hydrogen gas.

(2) Spray the warmed core with the mixture mentioned above and heat it up.

(3) Use as many large risers as possible choosing the round shape risers since they are more effective.

To reduce the cracks and cavities in any casting, it is necessary to be able to control the grain size in the molten metal. To produce fine grain size and consequently good casting production, grain refiner technique muse be used.

2.2.4 Solidification and Refining of Molten Aluminium

When the molten aluminium cools down very slowly with all the metal maintained at a uniform temperature, solidification will start just below the freezing point. A few nuclei distributed throughout the liquid will form and grow in all the preferred directions to form a coarse grain structure. If the entire liquid cools uniform ly and rapidly, many nuclei will originate to produce a fine-grained structure. But if the cooling is not uniform, that is

* (i.e. searching for any missing bars or cracks and cavities)

if one part of the liquid cools rapidly and the other slowly, nuclei will form only where cooling is first attained and it will grow in the direction of thermal gradient, giving elongated or what is known as columnar crystals. This is usually the type of the behaviour found in casting processes.

It is possible to control the columnar size by controlling the temperature, the thermal conductivity of the mould and the mass of the molten metal. Fig.(2.3) shows specimens taken from molten aluminium after etching in dilute Tuckers* reagent to expose the grain structure. Fig.(2.3a) shows the effect of casting temperature on the grain size of pure aluminium. Fine grain structure can be obtained more effectively by inserting artificial nuclei known as grain refiners. There are a large number of grain refiners available on the market mainly in the form of tablets to produce grain refining effect on aluminium. The efficient grain refiner recommended for use with the 99.7% aluminium is 0.2% of aluminium weight of Titanium and Boron. The resistance of the aluminium is slightly increased, but such an increase is outweighted by the sounder casting production. Fig.(2.3b) shows the grain structure in pure aluminium dealt with (Ti + B) grain refiner, showing that the grain size stays satisfactory even after holding the metal for a long time before casting. The grain refining used in this work helped very much in stopping the cracks and cavities, but it did not show any effect on the cold shut and hot shortness effects. The amount of grain refiner used is enough to raise the ultimate tensile strength of the metal to more than twice the value without refiner as shown in fig.(2.6).

The casting results achieved till now are mostly random and some are unexpected, making the casting process non-controllable. It is thought therefore the only factor which can alter the situation, is by changing the casting method. Therefore the sand casting method has been abandoned in favour of the centrifugal casting technique.

* 45cc HCl + 15cc HNO_3 + 15cc HF + 25cc Water

Fig (2.3a)- Effect of Casting temperature on 99.7% pure Al.

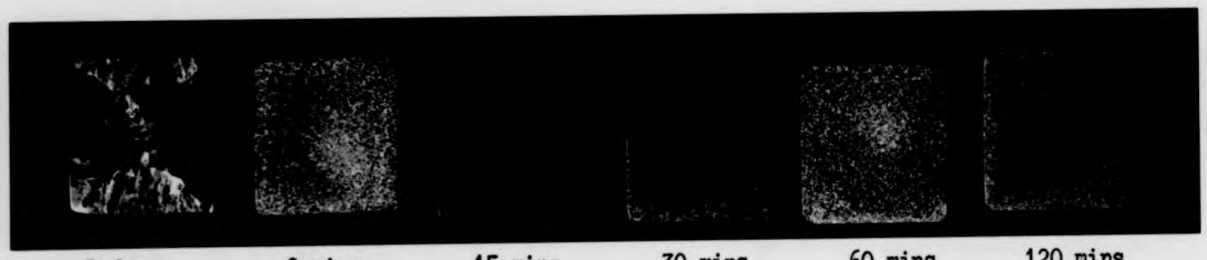

Fig (2.3b)- Effect of 0.2%-wt of (Ti + B) grain refiner on 99.7% Al, at 2, 15, 30, 60 and 120 minutes after the refiner has been added.

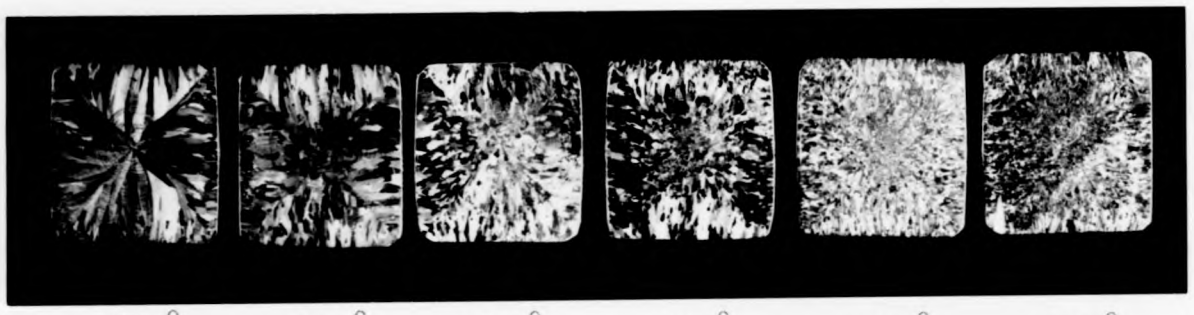

725 C^0 720 C^0 715 C^0 710 C^0 700 C^0 690 C^0

Fig (2.3a)- Effect of Casting temperature on 99.7% pure Al

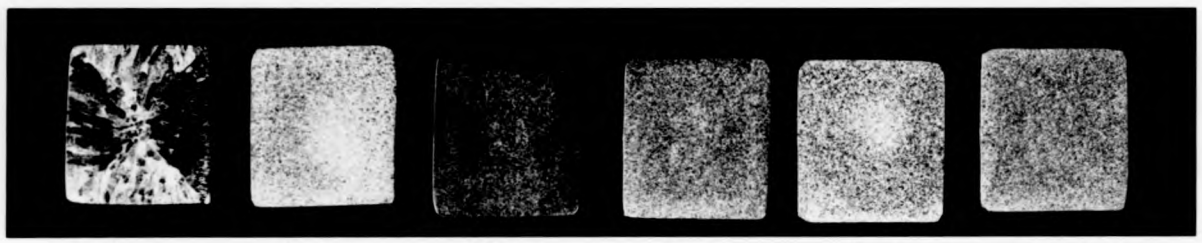

Before 2 mins 15 mins 30 mins 60 mins 120 mins

Fig (2.3b)- Effect of 0.2 -wt of (Ti + B) grain refiner on 99.7 Al,

2.2.5 Centrifugal Casting

It is shown in the previous section that it is difficult to nominate any specific conditions which can guarantee good quality castings using the gravity sand casting technique. One of the main causes for such a limitation is the shape of the rotors since it is flat with the bars runningat the same level as the end rings making casting under gravity difficult owing to the molten metal having insufficient head to flow fast and fill the spaces in the slots and end rings. To make the metal fill the mould, pressure or external force must be exerted on the molten metal. The special shape of the rotor lends itself very well to centrifugal casting. It is therefore necessary to use centrifugal casting to produce rotors of good characteristics. This method of casting gives much sounder products and due to its high filling density gives lower resistance.

A mould has been designed using cast iron as shown in fig (2.4a,b). It consists of two end plates joined together through a ring which separates them by a distance equal to the rotor thickness. The ring is cut into two equal halves, the inner wall of each half containing five slots. These slots are cavities which produce the ten fan blades on the outer end ring of the cage. The inner diameter of this ring is larger than the rotor diameter by an amount equal to twice the thickness of the cage end ring. The lower end plate has a hollow short shaft which can be locked to the shaft of a d.c motor for rotating it. Experiments showed that the best casting results can be obtained with the mould heated up to 400°C, aluminium heated upto 750°C and speed of rotation of the mould 450 rpm. The results obtained by this method under these conditions and with the help of the previous experience were found to be very satisfactory. Fig. (2.2E) shows a sample of cage cast by this method. It is a cage with continuous bars and clear rings having a good, sound nature. The same procedure was applied to the rotor cores and four different rotors have been fabricated using centrifugal casting. Three of these rotors are shown in fig (2.5) having characteristics shown in Table(2,3).

2.2.5 Centrifugal Casting

It is shown in the previous section that it is difficult to nominate any specific conditions which can guarantee good quality castings using the gravity sand casting technique. One of the main causes for such a limitation is the shape of the rotors since it is flat with the bars running at the same level as the end rings making casting under gravity difficult owing to the molten metal having insufficient head to flow fast and fill the spaces in the slots and end rings. To make the metal fill the mould, pressure or external force must be exerted on the molten metal. The special shape of the rotor lends itself very well to centrifugal casting. It is therefore necessary to use centrifugal casting to produce rotors of good characteristics. This method of casting gives much sounder products and due to its high filling density gives lower resistance.

A mould has been designed using cast iron as shown in fig (2.4a,b). It consists of two end plates joined together through a ring which separates them by a distance equal to the rotor thickness. The ring is cut into two equal halves, the inner wall of each half containing five slots. These slots are cavities which produce the ten fan blades on the outer end ring of the cage. The inner diameter of this ring is larger than the rotor diameter by an amount equal to twice the thickness of the cage end ring. The lower end plate has a hollow short shaft which can be locked to the shaft of a d.c motor for rotating it. Experiments showed that the best casting results can be obtained with the mould heated up to 400°C, aluminium heated upto 750°C and speed of rotation of the mould 450 rpm. The results obtained by this method under these conditions and with the help of the previous experience were found to be very satisfactory. Fig. (2.2E) shows a sample of cage cast by this method. It is a cage with continuous bars and clear rings having a good, sound nature. The same procedure was applied to the rotor cores and four different rotors have been fabricated using centrifugal casting. Three of these rotors are shown in fig (2.5) having characteristics shown in Table(2.3).

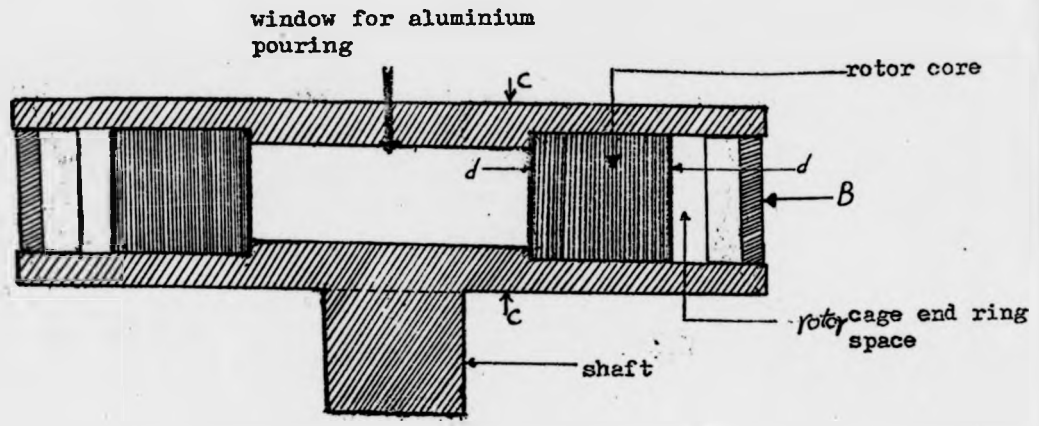

Fig (2.4a)- Cross Section through the AA-axis of the Centrifugal Mould

B - Spacer iron ring having width equal to the rotor core thickness.

C - End plates

The two end plates are joined together by four screws passing through holes in the spacer ring B.

d - Inner and Outer steel retaining rings.

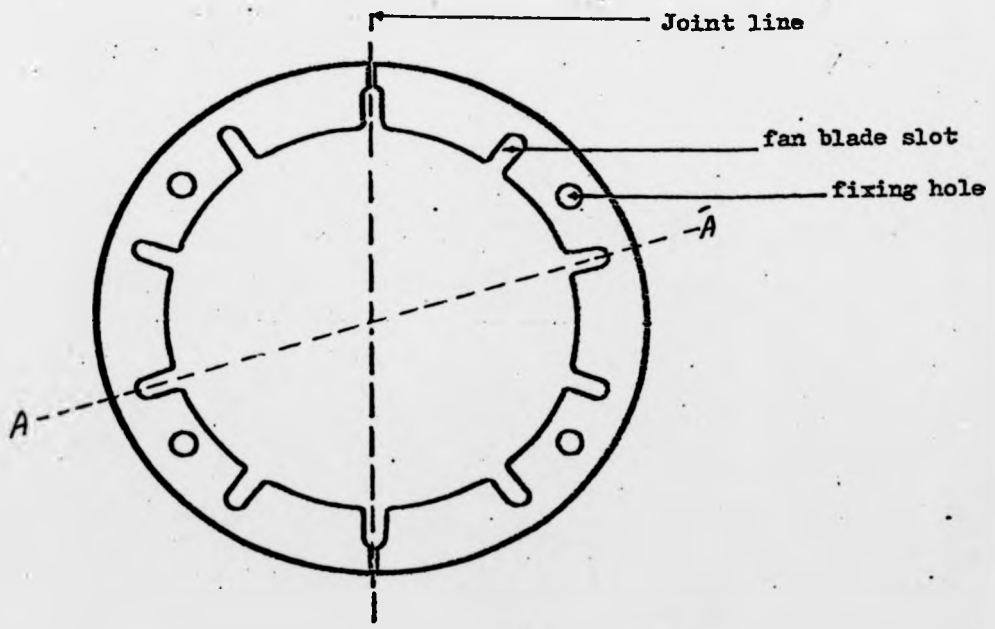

Fig (2.4b)- Top View of the spacer iron ring B.

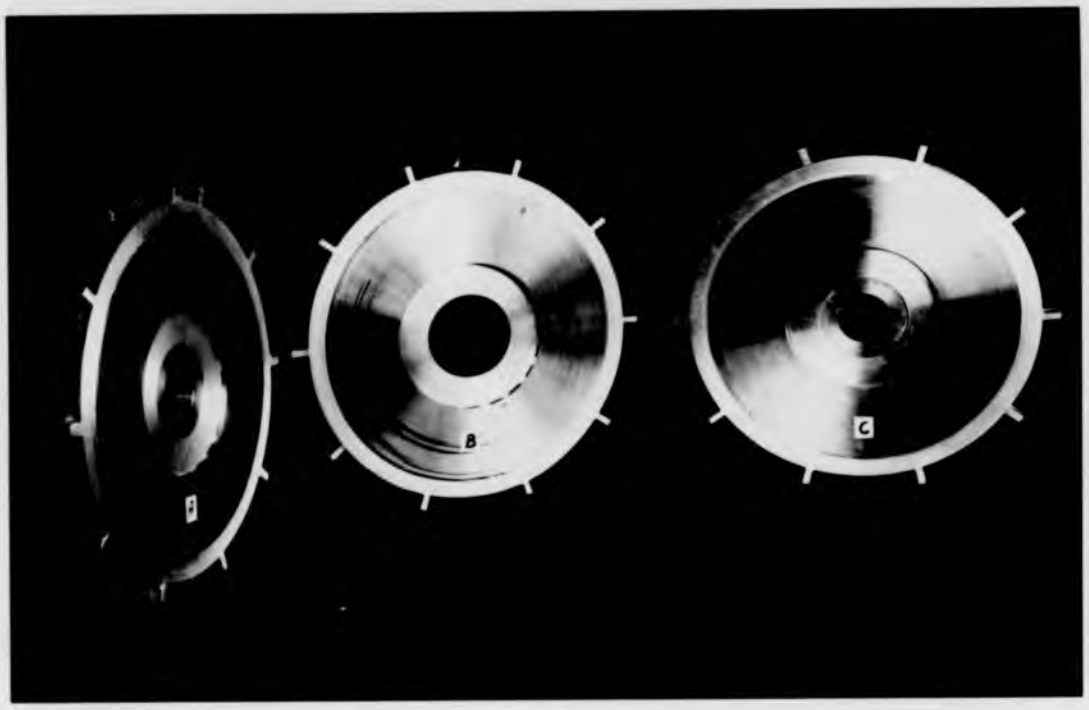

Fig.(2.5) - Planar Cage Induction Rotors

Rotor D is not shown since it is similar to rotor C in appearance.

Table - (2.3)

Rotor Designation	Rotor thickness x 10^{-3} m	Mass of the cage in each rotor.Kg	Rotor total mass in Kg.	Description	Motor's Total mass Kg.	Rotor's Moment of Inertia $Kg.m^2$
A	17.0	0.55	3.35	Single cage Solid Core 20 Unskewed bars	18.35	0.0154
B	27.35	0.80	4.71	Double cage Laminated core 20 unskewed bars on each cage	20.40	0.0215
C	17.25	0.50	3.43	Single cage Laminated core 18 bars skewed by one stator slot pitch	18.93	0.0158
D	17.25	0.60	3.50	Single cage Laminated core 20 unskewed bars	19.0	0.0161

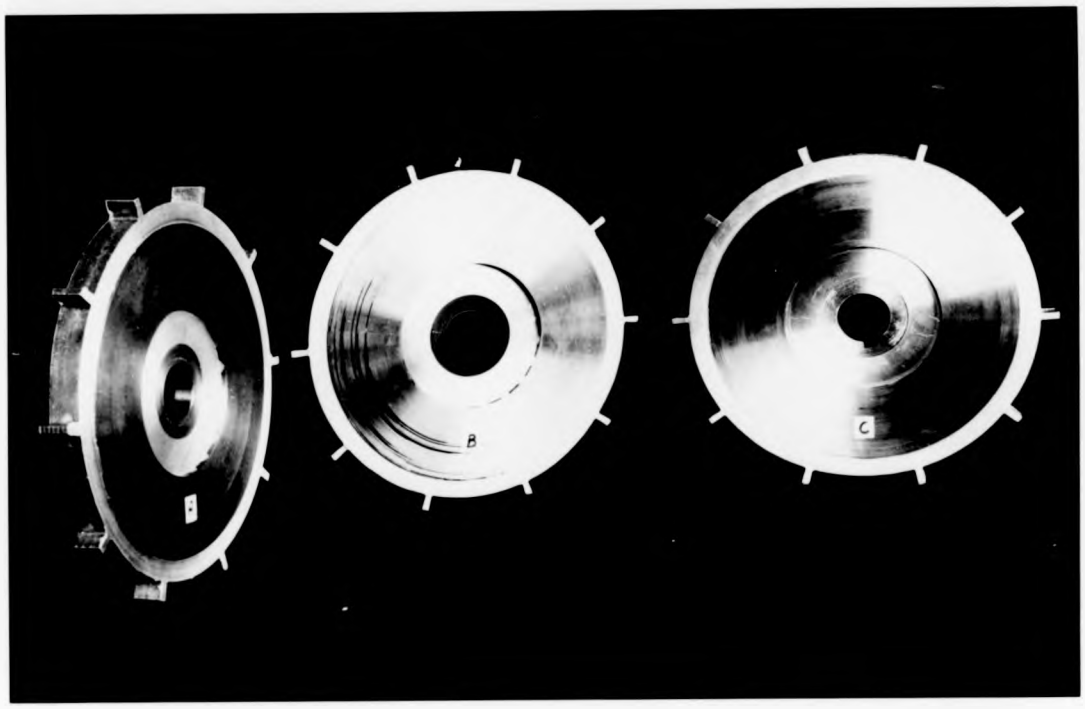

Fig.(2.5) - Planar Cage Induction Rotors

Rotor D is not shown since it is similar to rotor C in appearance.

Table - (2.3)

Rotor Designation	Rotor thickness x 10^{-3} m	Mass of the cage in each rotor.Kg	Rotor total mass in Kg.	Description	Motor's Total mass Kg.	Rotor's Moment of Inertia $Kg.m^2$
A	17.0	0.55	3.35	Single cage Solid Core 20 Unskewed bars	18.35	0.0154
B	27.35	0.80	4.71	Double cage Laminated core 20 unskewed bars on each cage	20.40	0.0215
C	17.25	0.50	3.43	Single cage Laminated core 18 bars skewed by one stator slot pitch	18.93	0.0153
D	17.25	0.60	3.50	Single cage Laminated core 20 unskewed bars	19.0	0.0161

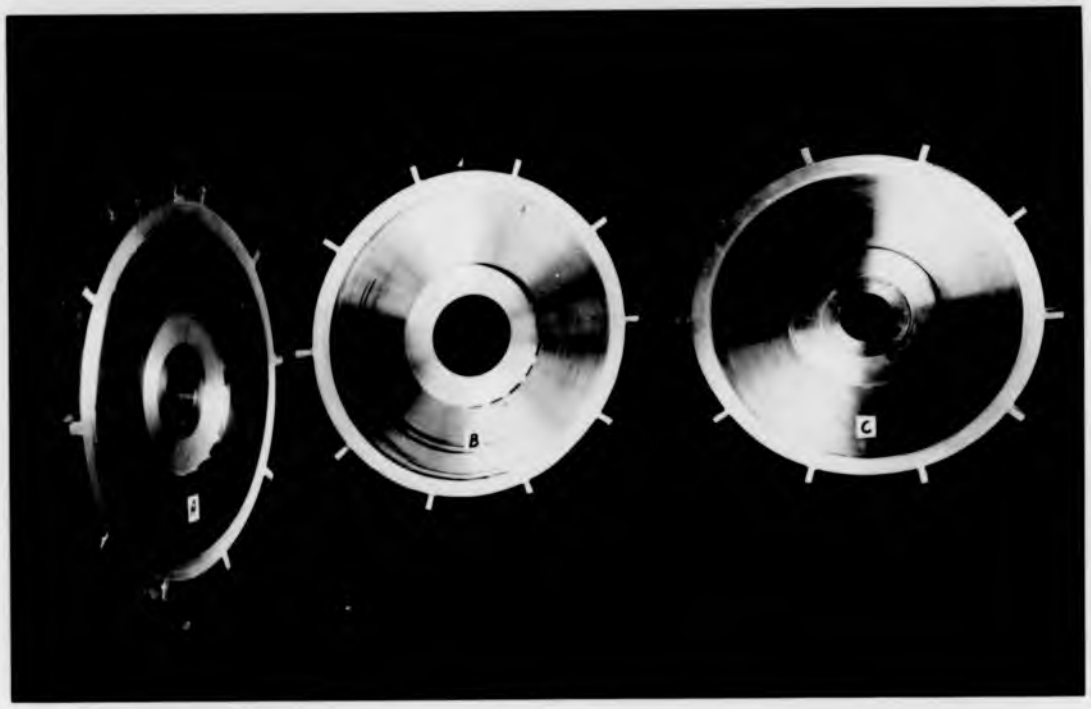

Fig.(2.5) - Planar Cage Induction Rotors

Rotor D is not shown since it is similar to rotor C in appearance.

Table - (2.3)

Rotor Designation	Rotor thickness $\times 10^{-3}$ m	Mass of the cage in each rotor.Kg	Rotor total mass in Kg.	Description	Motor's Total mass Kg.	Rotor's Moment of Inertia $Kg.m^2$
A	17.0	0.55	3.35	Single cage Solid Core 20 Unskewed bars	18.35	0.0154
B	27.35	0.80	4.71	Double cage Laminated core 20 unskewed bars on each cage	20.40	0.0215
C	17.25	0.50	3.43	Single cage Laminated core 18 bars skewed by one stator slot pitch	18.93	0.0158
D	17.25	0.60	3.50	Single cage Laminated core 20 unskewed bars	19.0	0.0161

2.2.6 Checking and Observations

After the casting is finished it is necessary to perform a number of tests on the product before considering it as satisfactory. The first easy and direct test is to examine the rotor visually. This type of check examines the exposed area like the end rings and the fans which are outside the laminations and the experienced person can draw some useful conclusions about the quality of the casting. A rough idea can be obtained about the condition of the bars inside the laminations using ultrasonic test .By sending signal through each bar and studying the reflected signal and the depth of reflection in comparison with that of the signal from a "standard bar."

A check on the temperature rise of the rotor during run-up test, noise and vibration gives a rough indication about the quality of castings and the goodness of the cage. Overheating of the rotor due to heavy overloads can bring about softening of the casting and fracture of a rotor bar under the influence of the centrifugal force. If a bar is therefore missing underneath the laminations this can cause periodic fluctuation of the stator current, pulsating humming and mechanical noise. The large number of trials made using this casting method showed that the possibility of a bar missing is very rare and none of the above symptoms showed up at all in the rotors produced.

It is perhaps advantageous that the rotors after casting are heat treated for 1-2 hours at 300-400°C. By doing so the insulation between the laminations and the cage can be increased and consequently the stray losses and the temprature rise of the rotor decreases.

It is important to get some insight into the mechanical rigidity of the aluminium cage. This can be achieved by carrying out an approximate stress analysis such as shown in Appendix A_1. This theory shows that the cage can run safely up to speeds of 32000 rev/min before the elastic limit is reached and it can be run to about three times this speed before it bursts.

Two experiments were carried out to test the rigidity of the aluminium

and the cage. In the first test a number of rectangular bars were cast out of pure and grain refined aluminium under exactly the same casting conditions applied in the cage casting. The bars were machined down to the shape shown in fig.(2.6a), keeping the length of the bar at least nine times its width to increase the sensitivity of the measurements. The standard tensile stress test is applied to these samples and the strain-stress curves for the two type of aluminium from no-load to beyond the maximum possible loading are shown in the same figure. It is clear that the ultimate tensile strenth of the grain refined aluminium is increased to twice its value without grain refining due to using a small amount of grain refiner. The second test involved the running of one of the rotors at speeds around 15000 rpm for fifteen minutes. Careful checks afterwards showed no signs of defects at the cage.

2.3 Conclusions

The rotor of the induction machine is the most important part of the machine, since it is the rotating part in which the energy conversion is taking place. It is therefore essential (especially in the case of axial field machines where the rotor is much thinner) to have a very rigid rotor which operates effectively and quietly. Brazing and welding techniques are difficult to apply in cage production for axial field machines. The cage in these machines must provide the following requirements: produce good induction torque, provide ventilating effect, enclose the laminations rigidly and provide the means of carrying the rotor on to the shaft. Due to the special shape of the rotor, the shaft has the special feature shown on page 96.

The author devised a new technique of rotor fixing using the aluminium inner end ring is found to be very effective [illegible] and contributes to an increase in the motor efficiency, decrease in the inertia, considerable reduction in rotor weight and consequently appreciable increase in power/weight ratio of the machine.

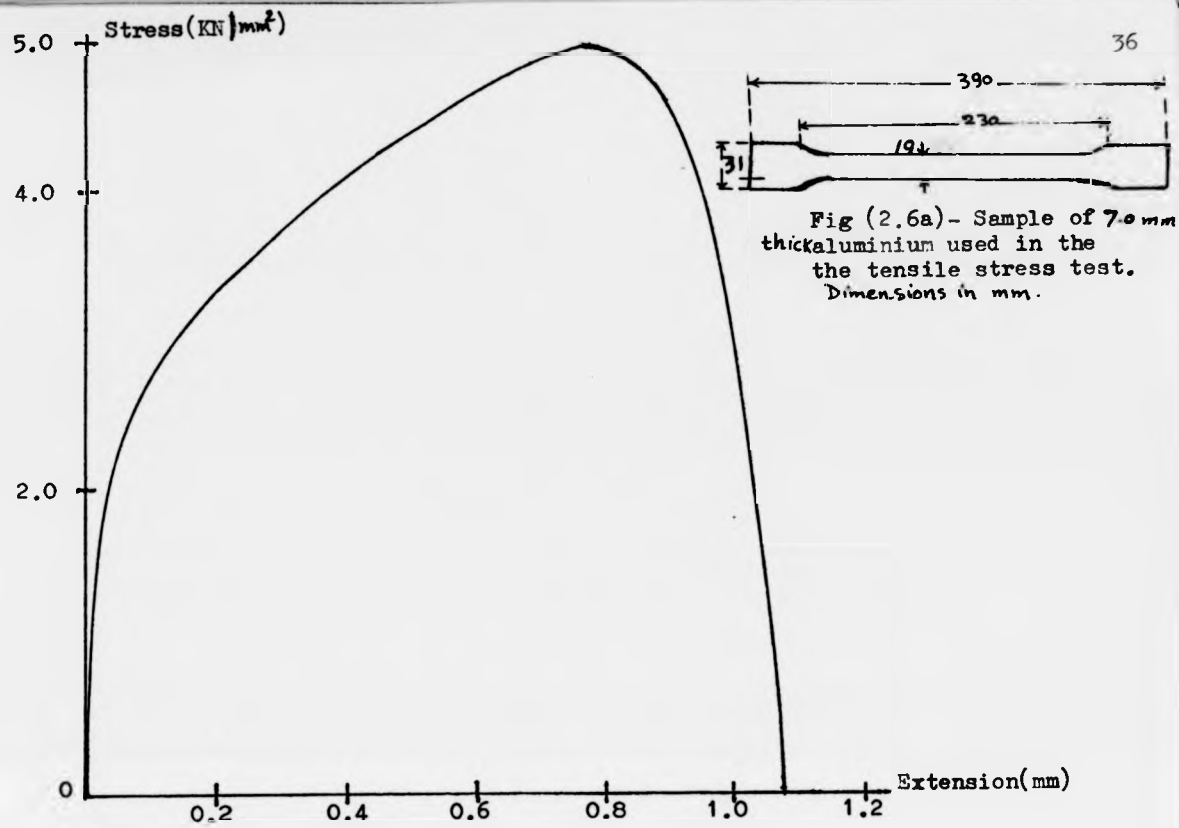

Fig (2.6a)- Sample of 7.0 mm thick aluminium used in the the tensile stress test. Dimensions in mm.

Fig (2.6b)- Tensile-Stress test curve for pure aluminium

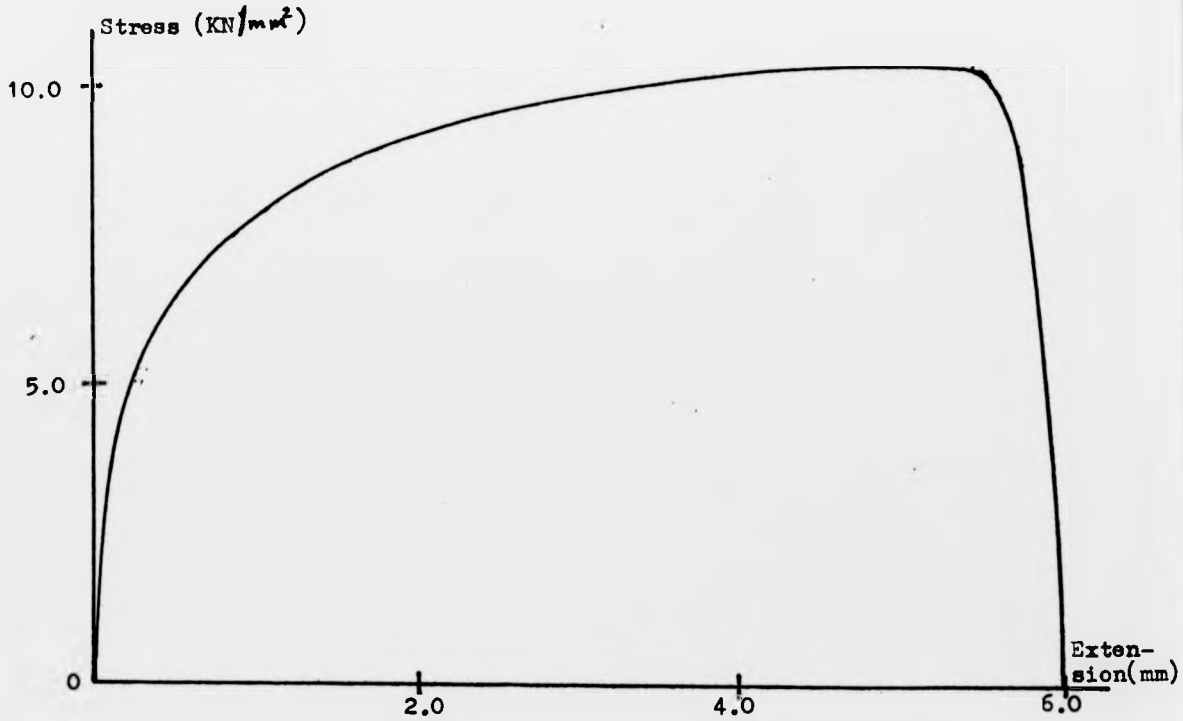

Fig. (2.6c)- Tensile-Stress curve for aluminium containing 0.2 %-wt of grain refiner

The centrifugal casting was found to be very successful in planar cage production even if it involves some extra efforts and designs. The casting method developed is suitable for rotor of any dimensions having any number of slots of any size and shape. More than one complete cage can be produced in a core by one casting process. The conditions for the best casting products are briefly: mould dipped in Foseco solvent and warmed up to 400°C, aluminium heated to 750°C, 0.2% aluminium weight of grain refiner added to molten metal prior to casting and finally speed of rotation of about 450 rev/min was found to be very suitable.

The rotors produced in this work are of high quality, making the machine stand a very good chance of competing with conventional motors in application requiring special features. The rotors are light, very rigid and were easily balanced.

CHAPTER 3

HARMONICS

3.1 Introduction

The study of harmonics in a machine is a necessary practice which can indicate how well the machine will perform. The origin of harmonics in the experimental machine are the winding distribution and the slotting of the stator surface.

Harmonics can produce disadvantageous effects. Some of these can be summarized as:

a - Distortion of the generated emf's of the supply.

b - Production of parasitic torques due to interaction of rotor and stator harmonics.

c - Introduction of vibration and noises.

d - Production of high frequency core losses in the teeth and pole faces.

The mmf harmonics do not directly cause harmonics in the terminal voltage, but they do influence its magnitude. In the case of mmf harmonic order 'k' it sets up a field of 'kp' poles rotating at speed 1/k of the synchronous speed with respect to the stator giving rise to a fundamental-frequency voltage in the windings rather than a harmonic voltage. This harmonic produces a torque having the same general shape as the fundamental and superimposed on it. If the harmonic is significant it may prevent the motor from exceeding about 1/k of the normal speed causing the motor to crawl. A similar effect can exist when stator-rotor mmf harmonics rotating together interact giving rise to synchronous crawling. The slot harmonics can produce harmonic torque in the same manner if an unwise rotor slot number has been chosen. For the present if the rotor slot number is chosen to be

44 instead of 20, the slot harmonic order 11 producing 44 poles will react with all the 44-bars in the rotor producing slot harmonic torque. If the rotor slots are chosen to be equal to stator slots the equal order harmonics rotating at the same speed in both stator and rotor will produce a synchronizing torque so that the rotor will remain at rest due to the cogging effect.

When the harmonics of the motor are to be considered, the equivalent circuit per phase can be extended to the mnemonic circuit of figure (3.1) suggested by Alger ref.3.1. This circuit shows that each harmonic field behaves as a separate motor connected in series with the fundamental, but creating its own independent rotor currents, torque, magnetizing reactance and number of poles. It starts with the series circuit of r_1 and x_1 the resistance and reactance of the stator winding. In series with r_1 and x_1 is the magnetizing reactance of the machine in parallel with the resistance and reactance of the rotor refered to the stator assuming only fundamental air gap flux.

The third part of the circuit represents the equivalent circuit of the magnetizing reactance of the machine and the secondary (rotor) parameters for air gap flux waves of certain harmonics.

This third part of the circuit can be used to take account of the two principal slot permeance harmonics (the 11th and 13th), the two principal phase belt harmonics (the 5th and 7th) and the two principal slot zig-zag harmonics (the 11th and 13th). The performance of the entire machine may be determined by first calculating the performance for the fundamental, and then calculating the effect of each harmonic in turn.

The aim of this chapter is to briefly study some aspects of the harmonics in the experimental machine, but no attempt is made to compensate for these harmonics in performance calculations. Successful attempts have been made to reduce the noise and vibration considerably by slot harmonic reduction using some practical means explained later.

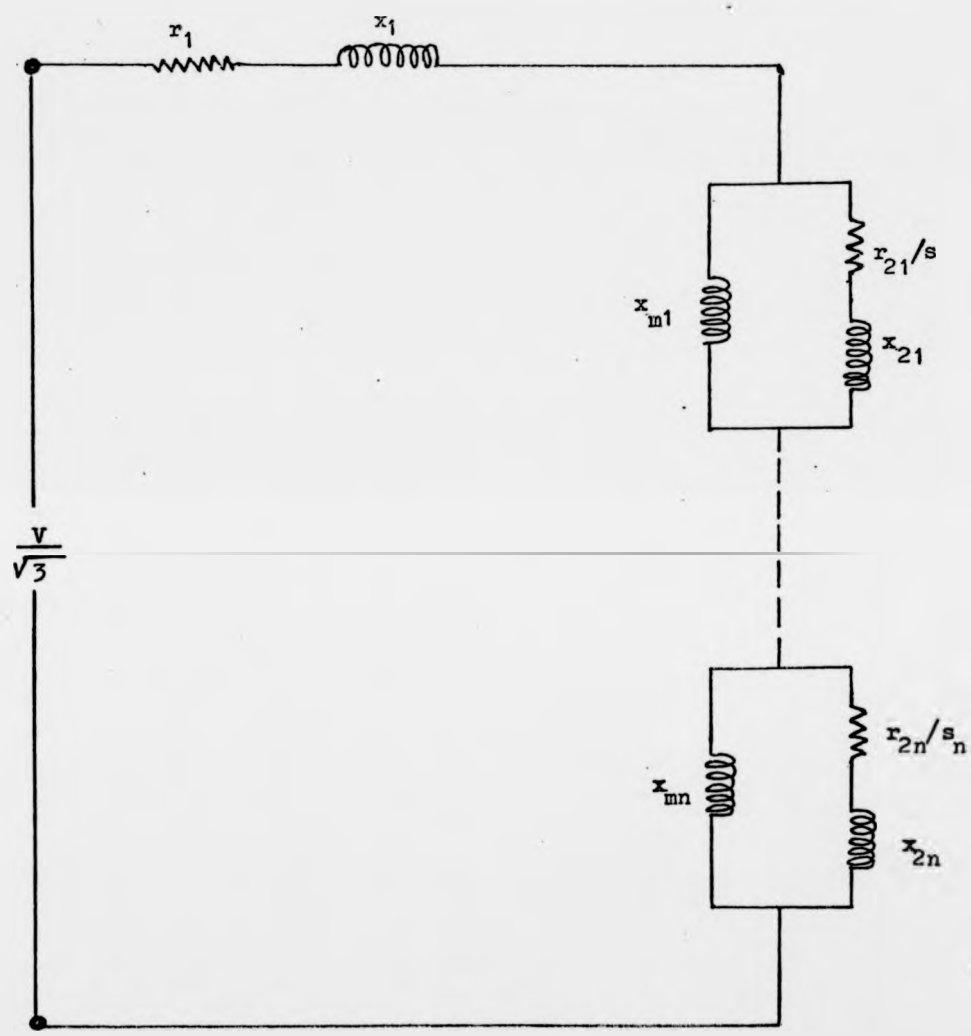

Fig.(3.1) - An extended per phase equivalent circuit of induction motor.

3.2 Stator M.M.F. distribution

The m.m.f. of a concentrated single coil in the stator fed with the current $i = I \cos\omega t$ is given ref.3.1, as;

$$M_k(\alpha) = \frac{2T.I \cos\omega t}{\pi} \sum_{k=1}^{\infty} \frac{1}{k} \sin\frac{k\rho\pi}{2} \cos k\alpha \quad \ldots\ldots\ldots\ldots\ldots 3.1$$

The kth term of this equation reveals that, the m.m.f wave has k times fundamental number of poles sinusoidally distributed around the periphery and alternate in time. This term can be written at any point and every instant of time as the sum of two equal constant magnitude m.m.fs revolving in opposite directions at the same speed of the original m.m.f giving that:

$$M_k(\alpha) = \frac{2T.I}{k} \sin\frac{k\rho\pi}{2} \left(\cos(kp\alpha - \omega t) + \cos(kp\alpha + \omega t)\right) \ldots\ldots 3.2$$

The m.m.f. of a single phase of N coils displaced by the slot pitch angle, α_d, in a machine with q slots per pole per phase is given by:

$$M_k(\alpha) = \frac{I.T.N}{\pi} \sum_{k=1}^{\infty} \frac{1}{k} \sin\frac{k\rho\pi}{2} \cdot \frac{\sin kq\alpha_d/2}{q.\sin k\alpha_d/2} \cdot \cos(kp\alpha \pm \omega t) \ldots 3.3$$

Considering a balanced double layer three phase winding the m.m.f per phase is:

$$M_{ph}(\alpha) = \frac{2I.T.N}{\pi} \sum_{k=1}^{\infty} \frac{1}{k} \sin\frac{k\rho\pi}{2} \cdot \frac{\sin kq\alpha_d/2}{q.\sin k\alpha_d/2} \cdot \cos(kp\alpha \pm \omega t) \ldots 3.4$$

where k = 1,3,5 .....odd harmonics.

It is a straightforward exercise to show that the resultant m.m.f wave for the experimental machine is given by (ref.3.1);

$$M_k(\alpha) = \frac{6I.T.N.}{\pi} \left(K_1 \cos(p\alpha - \omega t) + \sum_{k=1}^{\infty} (-1)^k \frac{K6k+1}{6k+1} \cos(p\alpha(6k+1) - \omega t) - \sum_{k=1}^{\infty} (-1)^k \frac{K6k-1}{6k-1} \cos(p\alpha(6k-1) + \omega t)\right) \ldots\ldots 3.5$$

where, K is the winding factor and (k= 1,2,3.....)

3.3 Reduction of the harmonics

It is a general engineering requirement to keep the amount of the harmonics in a machine as small as possible by reducing or suppressing them by well understanding the sources of these harmonics and better machine design. Some of the machine harmonics can be reduced as follows:

3.3.1 Stator mmf harmonics

These harmonics can be controlled by modifying the stator winding so as to cancel or reduce a number of specified harmonics. Harmonic study in the experimental machine shows that it is possible to follow the conventional calculation method used in radial machines in dealing with the distribution and pitch factors and the stator mmfs, ref.1.5.

3.3.1.1 Distribution factor

Coils comprising a phase are distributed in a number of slots per pole. The e.m.f. in adjacent coils will be out of phase by the slot pitch angle and the resultant will be less than the algebraic sum as follows:

$$\bar{E} = \frac{E}{q} \frac{\mathrm{Sin}(pq\alpha_d/2)}{\mathrm{Sin}(p\alpha_d/2)} \quad < E$$

where, the reduction factor,

$$K_d = \frac{\mathrm{Sin}(qp\alpha_d/2)}{q\mathrm{Sin}(p\alpha_d/2)}$$

is known as the distribution factor, and is the amount of the reduction in the resultant e.m.f. of a concentrated winding(E) when it is distributed.

For the kth harmonic, this factor becomes:

$$K_{dk} = \frac{\mathrm{Sin}(kpq\alpha_d/2)}{q\ \mathrm{Sin}(kp\alpha_d/2)}$$

For a uniformly distributed winding ($q \Rightarrow \infty$, $\alpha_d \Rightarrow 0$) this factor becomes:

$$Kdk = \frac{\mathrm{Sin}(kp\psi/2)}{kp\psi/2}$$

where $-\psi$ is the phase belt spread angle

The curve of this equation is a sine wave with rapidly diminishing amplitude. For a given phase-spread the values of Kdk alternate between positive and negative as the order of the harmonics increases and it never has the same value as that for the fundamental. Table(3.1) gives values of K_d for fundamental and harmonics up to 19 for a three phase machine having 1 to 10 slots per pole per phase and also for a uniformly distributed winding. Distributing the windings in a larger number of slots reduces the effect of the harmonics. But this does not affect the harmonics given by the formula:

$$k = 6q \pm 1$$

These harmonics are the slot harmonics and in the experimental machine (q=2) they are the 11th and 13th.

3.3.1.2 Pitch factor

In a full-pitch distributed winding, the resultant e.m.f. induced in each side of a coil will at every instant be equal in magnitude and directly in phase. If the windings are chorded, the effective e.m.fs on the two sides of each coil are not in phase since the coil spread is less or more than a pole pitch. The effective e.m.f of the fractional pitch coil for the fundamental is given by:

$$\bar{E} = \bar{E}\ \mathrm{Sin}\frac{(\alpha\pi)}{2} \qquad \angle \qquad \bar{E}$$

where $\bar{E}$ - effective e m f for a full-pole pitch winding

$\alpha = \frac{\text{Angle of spread of fractional pitch winding}}{\text{Angle of spread of full pole pitch winding}}$

k	Kdk (q) 1	2*	3	4	5	6	7	8	9	10	∞	$K_{\rho k}$ *	Kwk = Kdk . Kρk
1		0.9659	0.9598	0.9577	0.9567	0.9561	0.956	0.9556	0.9554	0.9553	0.9549	0.9659	0.9329
5		0.2588	-0.2176	0.2053	0.2000	0.1972	0.1955	0.1944	0.1937	0.1931	0.1910	0.2588	0.06698
7		-0.2588	-0.1774	-0.1576	-0.1494	-0.1453	-0.1428	-0.1413	-0.1402	-0.1395	-0.1364	-0.2588	0.06698
11		-0.9659	0.1774	-0.1261	-0.1095	-0.1017	-0.0974	-0.0948	-0.093	-0.0918	-0.0868	-0.9659	0.9329
13		-0.9659	0.2176	0.1261	0.1022	0.0920	0.08645	0.08312	0.0809	0.07945	0.0735	-0.9659	0.9329
17		-0.2588	0.9598	0.1576	0.1022	0.0837	0.07475	0.06968	0.06649	0.06433	0.0562	-0.2588	0.06698
19		0.2588	0.9598	-0.2053	-0.1095	-0.0837	-.0722	-0.066	-0.0621	-0.0596	-0.0503	0.2588	0.06698

Table (3.1) - Values of Kd, Kρ and Kw for different harmonics in induction motor.

* values for the experimental machine

k	Kdk (q) 1	2*	3	4	5	6	7	8	9	10	∞	$K_{\rho k}$ *	$K_{wk} = K_{dk} \cdot K_{\rho k}$
1		0.9659	0.9598	0.9577	0.9567	0.9561	0.956	0.9556	0.9554	0.9553	0.9549	0.9659	0.9329
5		0.2588	-0.2176	0.2053	0.2000	0.1972	0.1955	0.1944	0.1937	0.1931	0.1910	0.2588	0.06698
7		-0.2588	-0.1774	-0.1576	-0.1494	-0.1453	-0.1428	-0.1413	-0.1402	-0.1395	-0.1364	-0.2588	0.06698
11		-0.9659	0.1774	-0.1261	-0.1095	-0.1017	-0.0974	-0.0948	-0.093	-0.0918	-0.0868	-0.9659	0.9329
13		-0.9659	0.2176	0.1261	0.1022	0.0920	0.08645	0.08312	0.0809	0.07945	0.0735	-0.9659	0.9329
17		-0.2588	0.9598	0.1576	0.1022	0.0837	0.07475	0.06968	0.06649	0.06433	0.0562	-0.2588	0.06698
19		0.2588	0.9598	-0.2053	-0.1095	-0.0837	-.0722	-0.066	-0.0621	-0.0596	-0.0503	0.2588	0.06698

Table (3.1) - Values of Kd, $K\rho$ and Kw for different harmonics in induction motor.

* values for the experimental machine

The pitch factor for the kth harmonic is therefore given by:

$$K_{\rho k} = \text{Sin}\frac{Pk\epsilon}{2}$$

where $\epsilon = \alpha\pi$ is the chording angle(mechanical degrees)

By adjusting the pitch factor it is possible to reduce or eliminate certain harmonics. To eliminate the third harmonic and its odd multiples in a winding the chording angle must be $\pi/3$(to make $K_{\rho_3} = 0$). Following in a similar manner, chordings of $\pi/5$ and $\pi/7$ can eliminate the 5th and 7th harmonics which are equivalent to pitches of (4/5) and (6/7) of the full-pole pitch. The average of these two pitches is very nearly(5/6) which has pitch factors for 5th and 7th harmonics of 0.2588 and -0.2588 respectively.

Therefore a (5/6) pitch reduces the amplitude of these two harmonics in the voltage wave to about one-fourth of the amplitude they could have in a full-pitch winding using the same slot distribution. A pitch factor of (5/6) is employed in the stator windings of the experimental machine. Table (3.1) gives the pitch factors for a number of harmonics together with the winding factor which is taken as the product of the two above factors. This table shows also that the winding factor is a periodic function and that the slot harmonics have always winding factors equal to the fundamental.

3.3.2 Reduction of Slot Harmonics

Slot harmonics occur when one or both members of the machine are slotted, such that their surfaces are subjected to local variations of flux density. This variation in the flux density is mainly due to changes of the air-gap reluctance caused by the presence of the slot opening on one or both sides of the air-gap. The flux will therefore tuft at the tooth tips causing the field to contain ripples. This is as if there is superimposed upon the main flux an additional flux pulsating at a frequency of $(S_p \pm 1)f$, where S_p is number of slots per pole. Since the primary cause of this effect

is the variable reluctance of the gap (slot openings). it follows that if the reluctance due to slot opening is reduced by using nearly closed slots, the tooth ripples can be made small enough to be negligible. But this is not the case always, since sometimes as for instance the open slot design can simplify the stator manufacturing to a great extent and ease the winding process. Moreover it is almost impossible to produce semiclosed or closed slots by using the present manufacturing technique. It is therefore required to reduce these harmonics by employing some easy, cheap reliable means which can reduce the air gap reluctance variation due to slotting. There are a number of such means by which the tooth ripples can be effectively reduced and some of these are:

3.3.2.1 Slot combination

By this it means a suitable choice of the number of slots in the stator and rotor. This choice has to fulfil two conditions as nearly as possible. Firstly it has to obey the limitation due to the relation between the number of the slots and the number of poles in the machine and secondly a suitable relation between number of slots in the stator and rotor has to be established. The number of the slots in the stator is a well defined decision and its selection is limited by the number of poles and phases. The satisfactory relation between stator-rotor slots can be reached by proper selection of the number of slots in the rotor after the number of stator slots has been fixed. In a number of studies carried out by some investigators(Appleman (3.2), Kron (3.3), Alger(3.1))it is shown that unbalanced magnetic pull and rotor vibration can occur if the gap field contains two harmonic fields differing by two poles since the unbalanced magnetic pull depends on the product of the magnitudes of the two fields. It is shown also that if two fields differ by more than two poles, the effect is very small.

In appendix A2 the method used by Appleman is applied to the machine to show that the number of rotor bars employed in the present design is a suitable choice as far as the reduction of the above unbalanced magnetic pull is concerned.

3.3.2.2 Skewing

Skewing in both radial and axial field machines means that the slots are tilted at a certain angle relative to the unskewed slots which are at normal positions. Fig.(3.2a,b) shows the effect of skewing on the harmonic voltage induced in a rotor bar. At "a" the bar is shown under the effect of a harmonic flux density wave at certain instant of time with the bar unskewed. In this case the whole bar lies under the effect of the harmonic flux giving rise to a harmonic voltage in the bar in proportion to the harmonic flux density. But when the bar is so skewed that it covers at every moment two similar poles of the harmonic field at its ends fig.(3.2b), the voltage induced in part of the bar is accordingly cancelled by an equal and opposite voltage induced in the other part which is under a similar pole and consequently no current flows in the bar due to the harmonic field causing the field to skew out. In radial machines the skewing takes a spiral shape. The angle of skewing is related to the machine length, number of slots, machine diameter and the amount of skewing as a factor of the slot pitch angle and it is usually more than one slot pitch.

In axial machines the skewed bar has a curved shape as shown in fig(3.3) and is related to the number of slots and to main diameters of the machine. This type of skewing is found to be impractical to produce using the present production technique and can cause serious manufacturing problems.

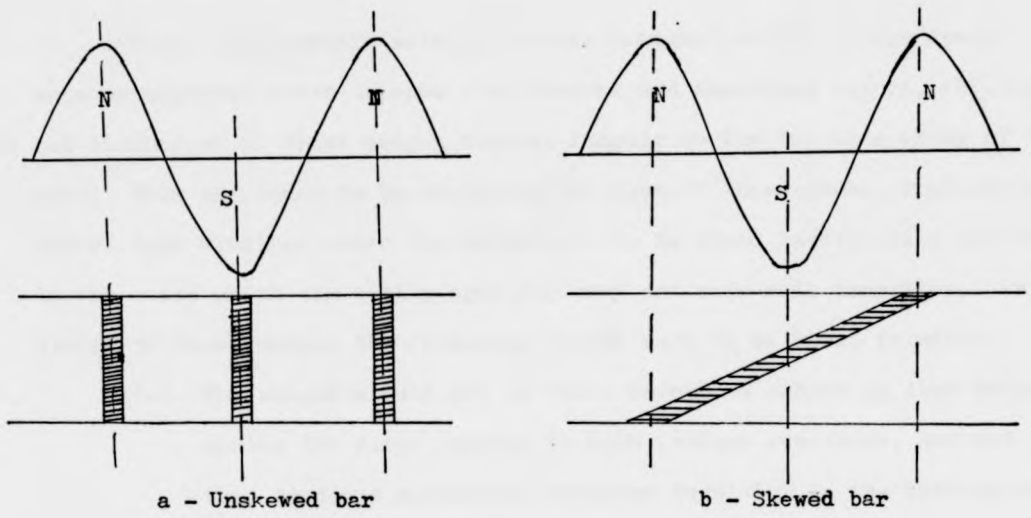

a - Unskewed bar b - Skewed bar

Fig.(3.2) - Effect of skewing on harmonic flux

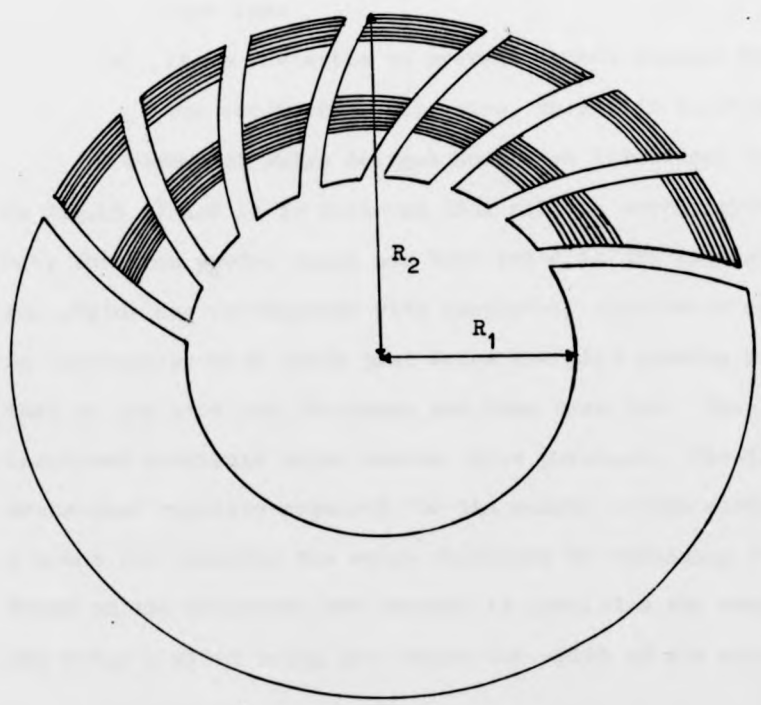

Fig.(3.3) - Ideal skewing in axial field machines

3.3.2.3 Magnetic slot wedges (MSW)

These are magnetic metallic pieces designed to fit in the spaces between adjacent teeth in open slot stators and sometimes rotors, ref.3.5. The shape and dimensions of these wedges depends largely on the top side shape of the slot. They are found to be useful in the case of three-phase, double-layer basket type windings where the coils have to be wound individually and inserted in the slots which are mostly open for easy and safe coil insertion. In the design of these wedges the following points have to be borne in mind:

(a) The wedges should not be thick enough to behave as flux bridges across the slots leading to high leakage reactance, and not too thin to cause mechanical problems resulting in the rubbing of the wedges between the rotor and stator faces.

(b) The wedges should not be too thick to appreciably increase the iron loss.

(c) It is advisable to prevent direct contact between the wedges and the teeth edges otherwise, they will short-circuit the laminations.

A number of wedge designs have been introduced by the author as shown in fig.(3.4) and it is believed that all are worth trying with the machine. Only the iron powder wedge has been tried in the present work. The slots in the stator are rectangular with completely open mouth causing the wedges to be rectangular with width just below the slot opening and length equal to that of the slot and thickness not less than 2mm. They are fixed on a rigid insulated substrate which serves three purposes. Firstly it gives the mechanical rigidity required for the wedges in the slots; Secondly it provides a means for changing the wedge thickness by machining it down while it is fixed on the substrate and thirdly it insulates the wedge from the slot edges, the wedge's width being just below the width of the substrate carrying it.

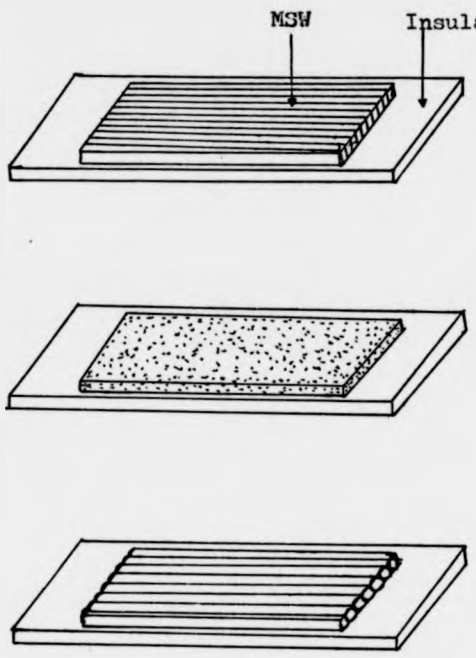

Fig.(3.4) - Possible designs of magnetic slot wedges

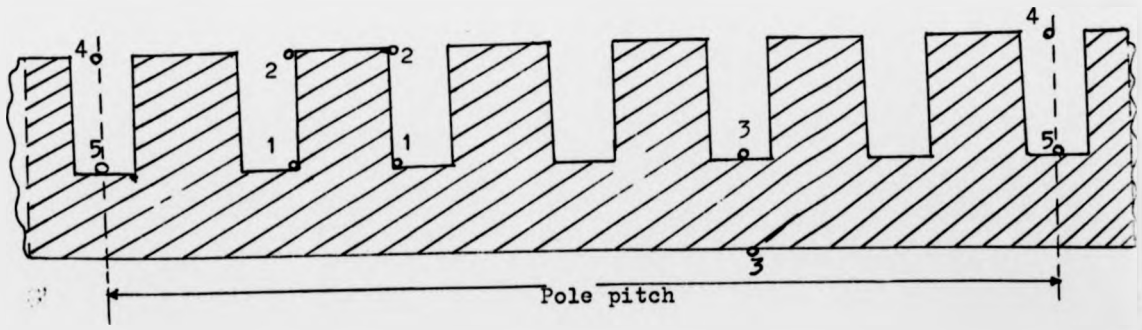

Fig.(3.5) - Search coils in the stator core

3.4 Harmonic measurements and Results

At the start of the work on harmonic measuremen ts it seemed that there was a need for a method of harmonic measurements at different places in the machine. This method must be rapid and must provide results of the total waveforms together with their harmonic analysis in the shape of plots which can be tabulated and kept for a long time.

An experimental method is therefore devised for measuring the harmonics in the flux waveforms by recording the e.m.fs induced in double turn search coils inserted at different points of the stator core and the air-gap as shown in fig.(3.5). Coils 1 and 2 detect the flux waveforms at the bottom and top of a single tooth; Coil 3 detect the flux waveform at the core, and finally coils 4 and 5 detect the flux waveforms at the top and bottom across a pole pitch of the machine since they extend a full-pole pitch covering slots(1-7). The measuring technique involves recording the resultant output waveform at each search coil using the Analog 7 tape recorder available in the Department. A large number of such waveforms can be recorded using one channel of the recorder. When using the recorder it is necessary to let it run for at least twenty seconds until it reaches its constant speed before any signal can be fed in. Applying the signal earlier than this time means recording the signal at different speeds and consequently the appearance of rather unexpected harmonics. The waveforms obtained on the tape are then analysed using Fourier Series harmonic analysis and some computerised subrountines to give output plots for the harmonics existing in the waveform logged to the computer. The method was first tested by analysing the waveform of a signal generator as shown in fig.(3.6). The spectra obtained in the tests are not line spectra owing to the fact that one period only of the waveform has been analysed. These spectra could be improved by analysing longer record lengths of the waveform. This method of harmonic analysis is aimed at observing the harmonics and the changes occuring in their order and amplitude in different experimental studies. The test method is divided in a number of parts as follows:

Fig.(3.6) - Testing the method of harmonic analysis

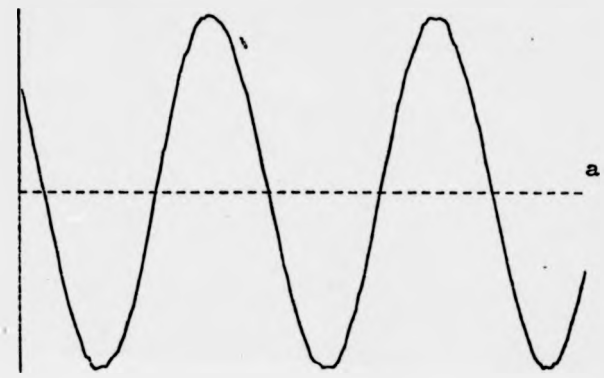

a - Signal generator waveform of 50Hz, fundamental frequency.

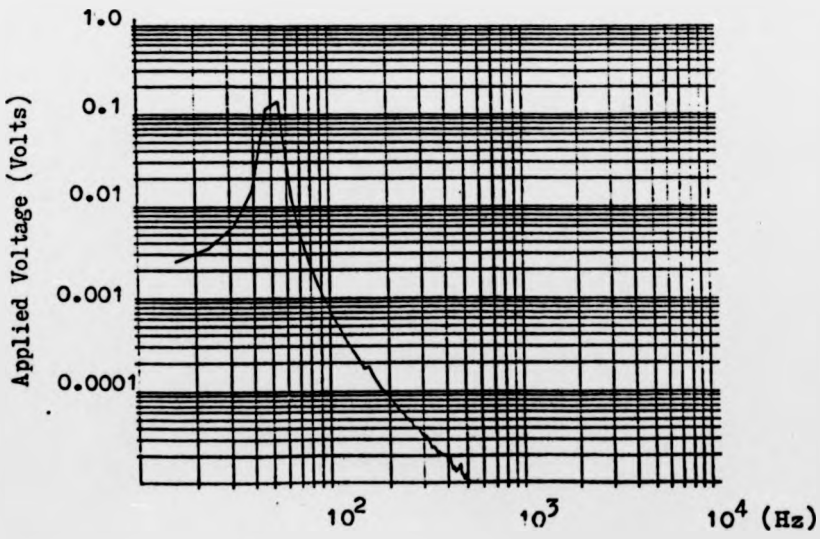

b - Harmonic analysis of a signal generator waveform.

part one is concerned mainly with the harmonics of the two stators only when there is no rotor, and this gives the harmonics in the stator m.m.f. The resultant waveforms at points(1,3,4) and their harmonic analysis are shown in fig.(3.7) at different air-gaps. The first waveforms are taken at zero air-gap(i.e the two stators are in complete contact). The rest of the waveforms are recorded at two air-gaps by separating the two stators 0.45 and 0.76 mm apart. These figures show clearly the damping effect of the gap reluctance in cancelling some of the harmonics. The test is then extended further to study the effect of the misalignment of the two stators relative to each other on the harmonic content. One of the stators is therefore fixed and the second rotated at intervals of one slot pitch (15^{o}) relative to the first and the flux waveform at the full pole pitch search coil is recorded using the same technique for three misalignment angles of 15^{o}, 30^{o}, and 45^{o}. The resultant waveforms and their analysis are shown in fig.(3.8). These are very important results since it can give a direct answer to the increase in the losses of the machine as the misalignment is increasing as shown in Chapter 6. Part two of the test is meant to show the effect of the rotor on the harmonic content. Therefore the same measuring method is repeated in the case of rotors D and C and the results are shown in Chapter 6.

The third part of the test is concerned with the effect of the magnetic slot wedges on harmonic content of the machine and the investigation of their effect in the noise level of the machine due to slot harmonic reduction and this is shown also in Chapter 6.

Results of fig.(3.7) show that increasing the air-gap can reduce the effect of some of the flux harmonics. This technique of harmonic reduction has been employed by Pensabene (1.2) in his pump drive motor to reduce the slot harmonic noise after the motor has started. But this is not always desirable since the increase in the air-gap length is accompanied always with an increase in magnetizing current and decrease in output power and efficiency.

part one is concerned mainly with the harmonics of the two stators only when there is no rotor, and this gives the harmonics in the stator m.m.f. The resultant waveforms at points(1,3,4) and their harmonic analysis are shown in fig.(3.7) at different air-gaps. The first waveforms are taken at zero air-gap(i.e the two stators are in complete contact). The rest of the waveforms are recorded at two air-gaps by separating the two stators 0.45 and 0.76 mm apart. These figures show clearly the damping effect of the gap reluctance in cancelling some of the harmonics. The test is then extended further to study the effect of the misalignment of the two stators relative to each other on the harmonic content. One of the stators is therefore fixed and the second rotated at intervals of one slot pitch (15^{o}) relative to the first and the flux waveform at the full pole pitch search coil is recorded using the same technique for three misalignment angles of 15^{o}, 30^{o}, and 45^{o}. The resultant waveforms and their analysis are shown in fig.(3.8). These are very important results since it can give a direct answer to the increase in the losses of the machine as the misalignment is increasing as shown in Chapter 6. Part two of the test is meant to show the effect of the rotor on the harmonic content. Therefore the same measuring method is repeated in the case of rotors D and C and the results are shown in Chapter 6.

The third part of the test is concerned with the effect of the magnetic slot wedges on harmonic content of the machine and the investigation of their effect in the noise level of the machine due to slot harmonic reduction and this is shown also in Chapter 6.

Results of fig.(3.7) show that increasing the air-gap can reduce the effect of some of the flux harmonics. This technique of harmonic reduction has been employed by Pensabene(1.2) in his pump drive motor to reduce the slot harmonic noise after the motor has started. But this is not always desirable since the increase in the air-gap length is accompanied always with an increase in magnetizing current and decrease in output power and efficiency.

part one is concerned mainly with the harmonics of the two stators only when there is no rotor, and this gives the harmonics in the stator m.m.f. The resultant waveforms at points(1,3,4) and their harmonic analysis are shown in fig.(3.7) at different air-gaps. The first waveforms are taken at zero air-gap(i.e the two stators are in complete contact). The rest of the waveforms are recorded at two air-gaps by separating the two stators 0.45 and 0.76 mm apart. These figures show clearly the damping effect of the gap reluctance in cancelling some of the harmonics. The test is then extended further to study the effect of the misalignment of the two stators relative to each other on the harmonic content. One of the stators is therefore fixed and the second rotated at intervals of one slot pitch (15°) relative to the first and the flux waveform at the full pole pitch search coil is recorded using the same technique for three misalignment angles of 15°, 30°, and 45°. The resultant waveforms and their analysis are shown in fig.(3.8). These are very important results since it can give a direct answer to the increase in the losses of the machine as the misalignment is increasing as shown in Chapter 6. Part two of the test is meant to show the effect of the rotor on the harmonic content. Therefore the same measuring method is repeated in the case of rotors D and C and the results are shown in Chapter 6.

The third part of the test is concerned with the effect of the magnetic slot wedges on harmonic content of the machine and the investigation of their effect in the noise level of the machine due to slot harmonic reduction and this is shown also in Chapter 6.

Results of fig.(3.7) show that increasing the air-gap can reduce the effect of some of the flux harmonics. This technique of harmonic reduction has been employed by Pensabene (1.2) in his pump drive motor to reduce the slot harmonic noise after the motor has started. But this is not always desirable since the increase in the air-gap length is accompanied always with an increase in magnetizing current and decrease in output power and efficiency.

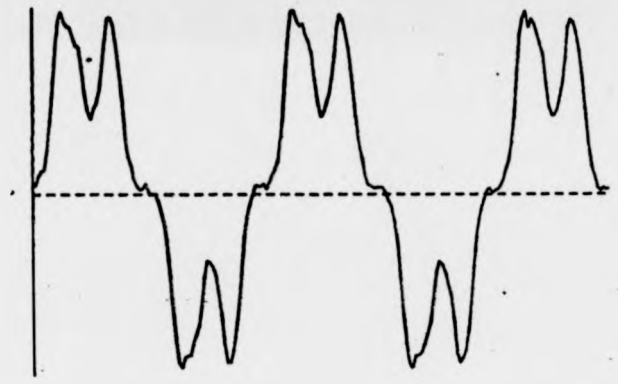

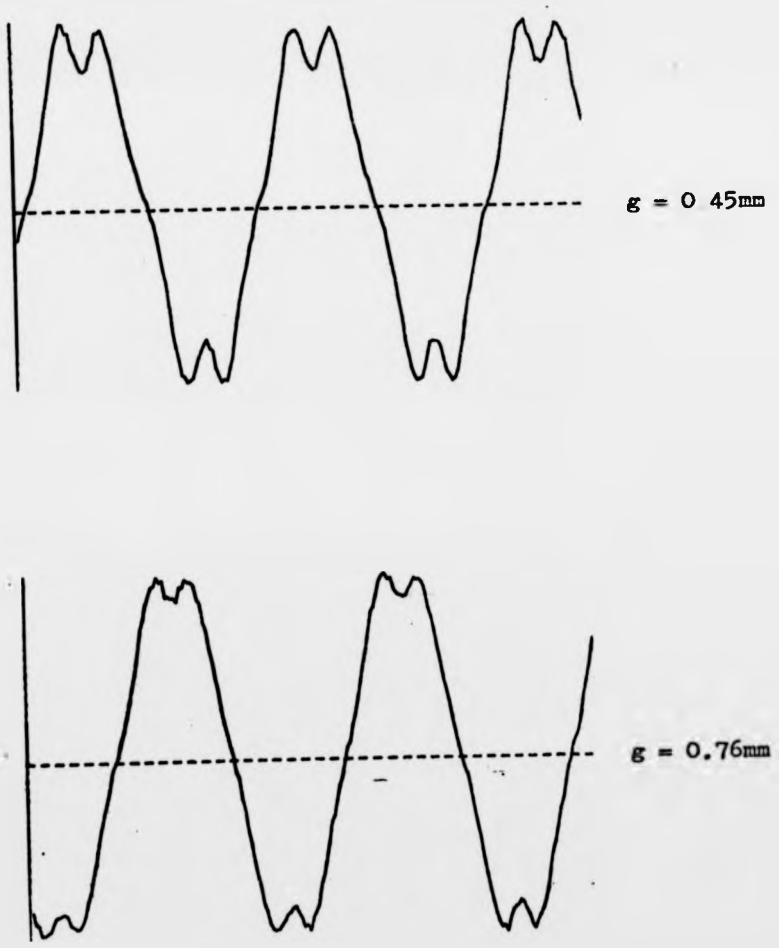

Fig.(3.7a) - Smoothing effect of air-gap reluctance on the teeth flux, search coil 2.

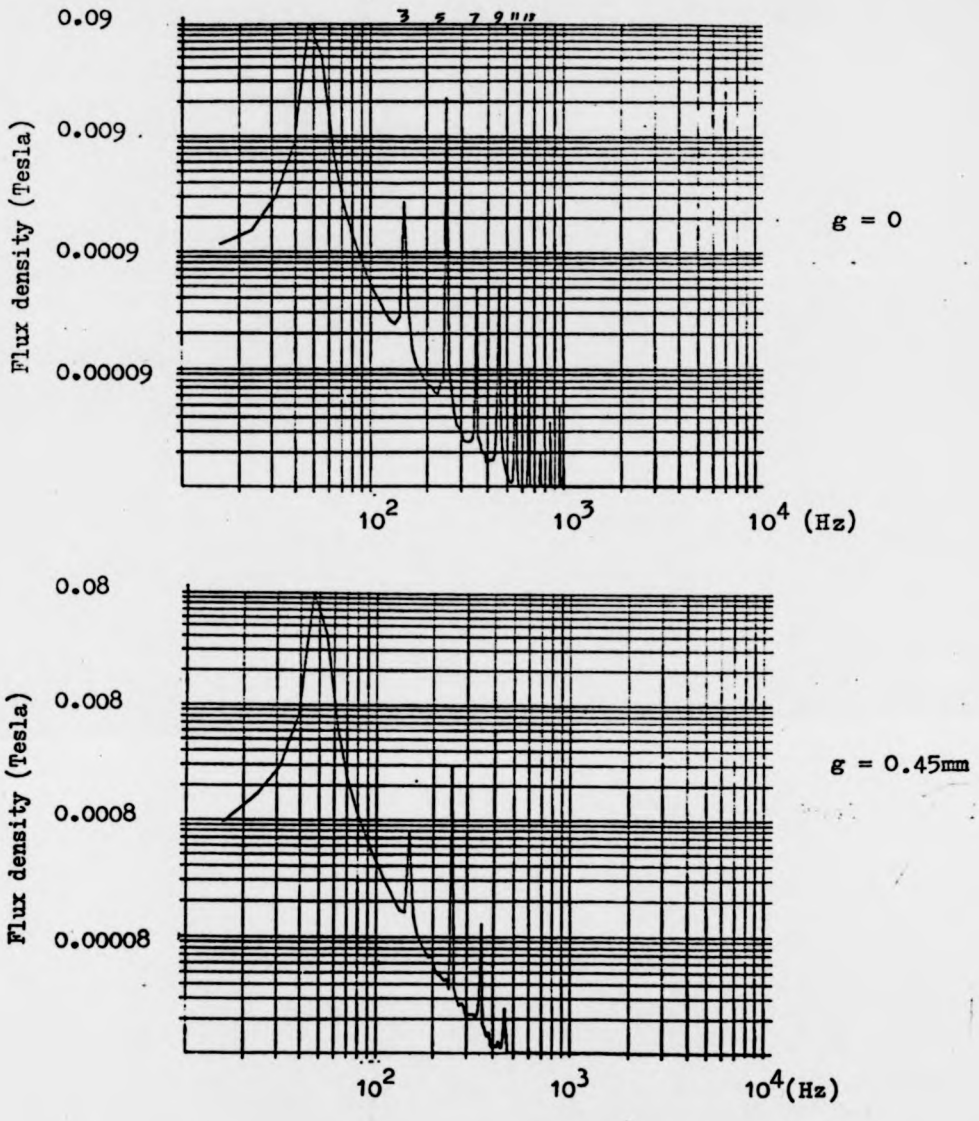

Fig.(3.7b) Waveform analysis of the teeth flux at different gaps.

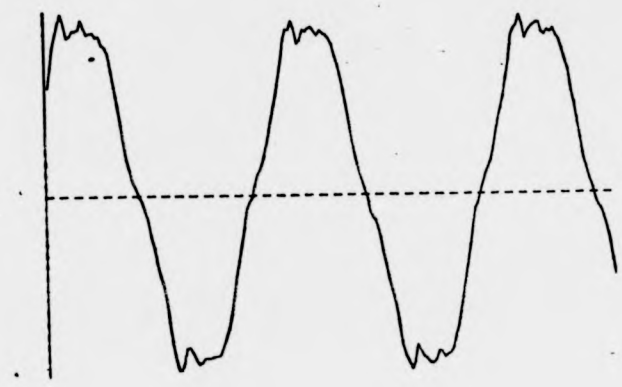

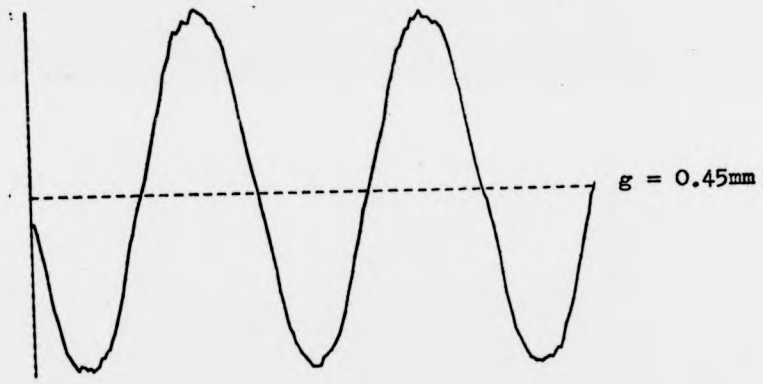

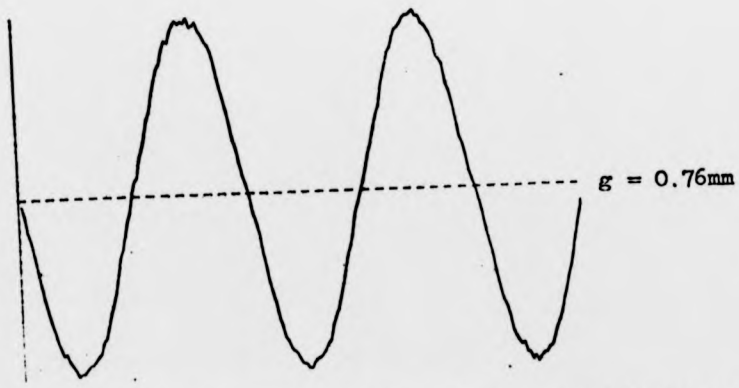

Fig.(3.7c) - Smoothing effect of air gap reluctance on the core flux, Search coil 3.

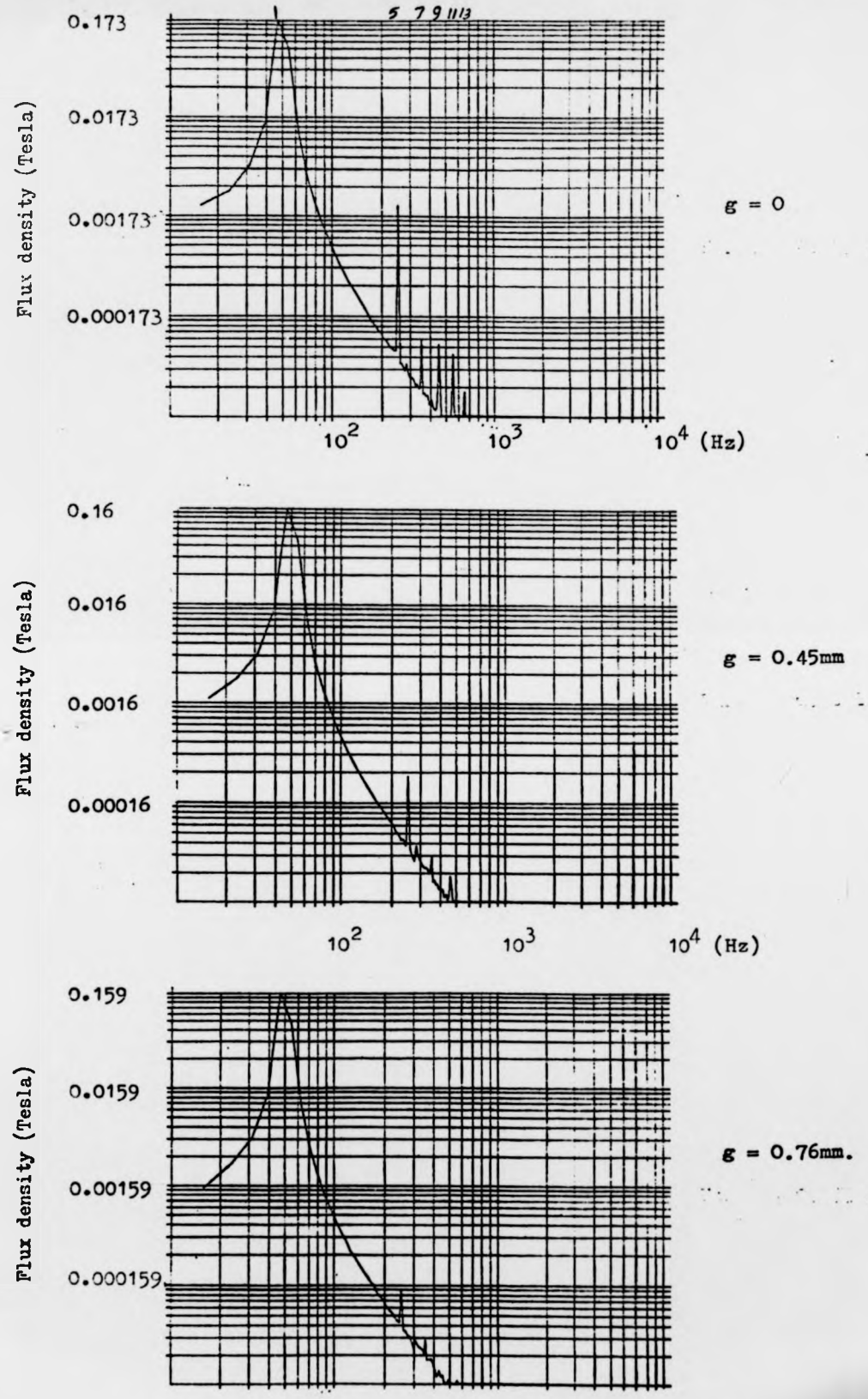

Fig.(3.7d) - Waveform analysis of the core flux at different gaps

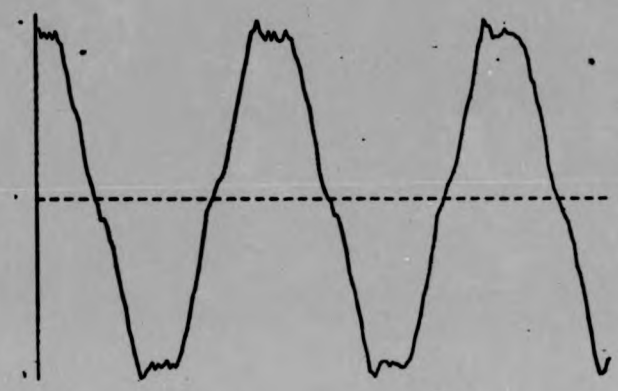

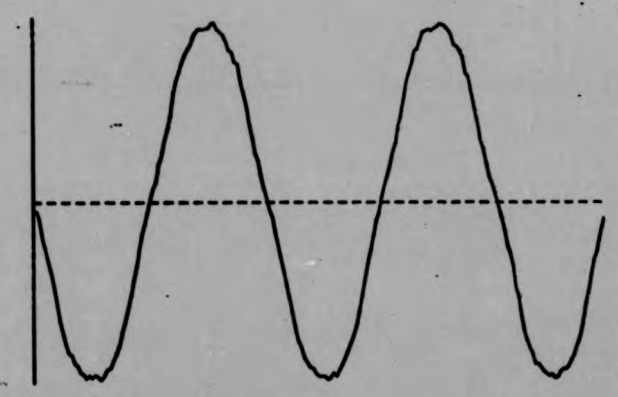

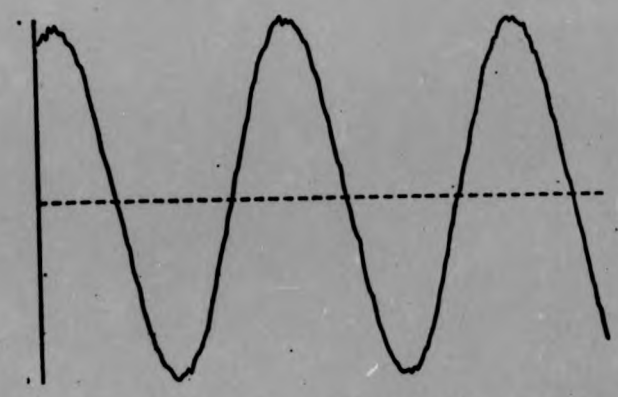

Fig. (3.7e) - Smoothing effect of air gap reluctance on the pole flux, search coil 4.

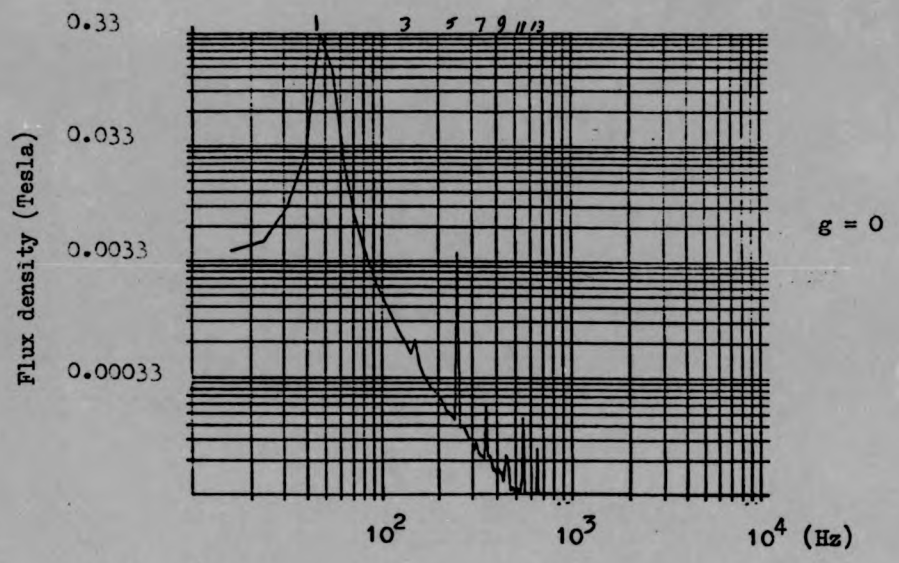

Fig.(3.7f) - Waveform analysis of the full pole pitch flux at different gaps

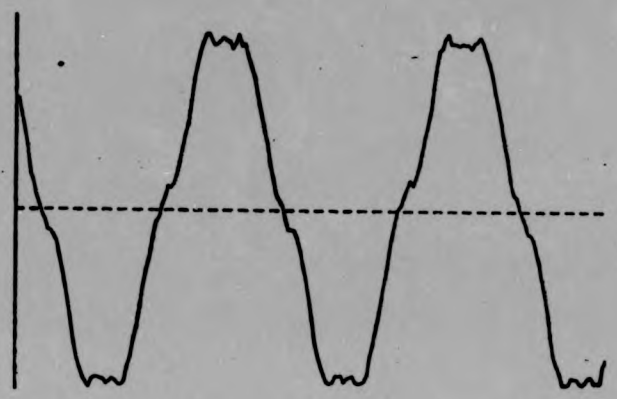

Pole flux waveform at

$\theta = 15^{\circ}$

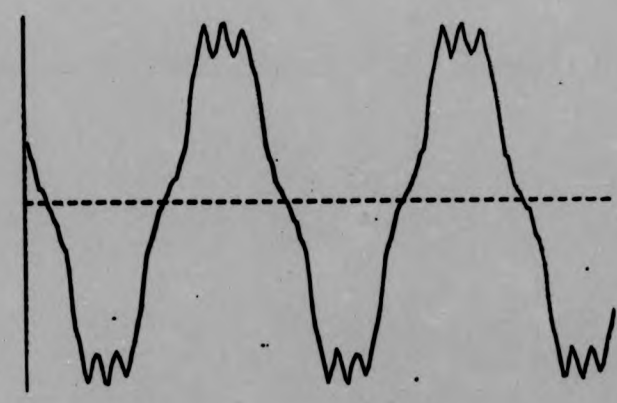

$\theta = 30^{\circ}$

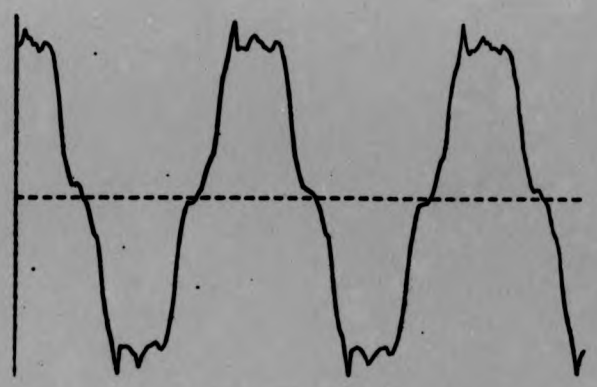

$\theta = 45^{\circ}$

Fig.(3.8a) - Pole flux waveform at different misalignments ($g = 0$), search coil 4.

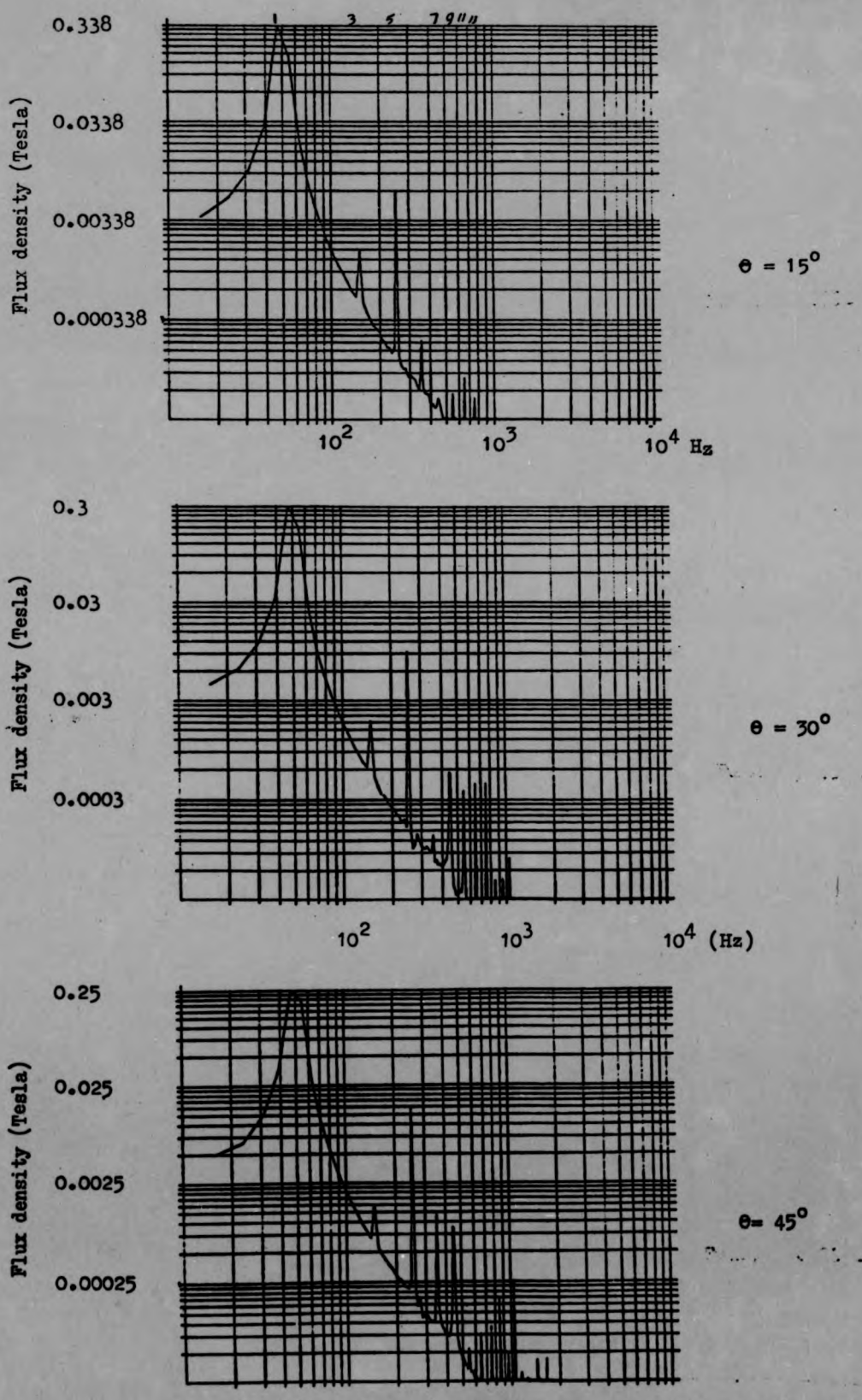

Fig.(3.8b) - Effect of the stator misalignment (θ) on the air-gap flux harmonic content (g=0)

The experiment showed that the perfect alignment is the position at which a north pole of one stator opposes a south pole of the other with the current and harmonics in the machine kept as small as possible. Fig.(3.7f) shows that harmonics in a pole pitch search coil when the stator are in perfect alignment and different gaps separate them with average phase input current of 0.68A at zero air gap lenth. Results of fig.(3.8) indicate that the harmonics increase sharply with the misalignment and so do the input currents. It was found that the minimum current position occurs at an alignment little different from the minimum harmonic position. It is decided therefore to use a position which gives both negligible harmonics and small balanced currents and this is the perfect aligned position. The harmonic in the resultant flux waveforms at the gap depends on the reaction between the magnetic circuit of the two stators. In the perfect alignment position the two waveforms are moving in phase giving rise to a resultant sinusoidal flux waveform. The misaligning of the stators causes the two waveforms to move out of phase with respect to each other by the misaligning angle arising in a waveform which is non-sinusoidal.

3.5 Fundamental Checkings

Before starting the harmonic measurements a number of checkings were made as shown below:

(a) The harmonics in the source voltage waveforms feeding the phases of the machine were checked by connecting two resistors of 23.3 KΩ and 0.2 KΩ in series across each two phases and the voltage waveform across the 0.2 KΩ resistor is analysed and the highest harmonic found to be less than 1% of the fundamental.

(b) The current balance of the source is checked by feeding the three phases into a circuit of three equal resistors(150Ω each) connected in delta through a three phase variac. Three ammeters connected between the variac and the resistors indicated currents of 1.46, 1.43, 1.45A.

(c) The current balance in the machine is checked by replacing the resistive loop in "b" by the three phases of the machine. The respective phases in the stators are connected in series and the final phases are star connected. The two stators perfectly aligned at zero air-gap and the currents recorded at the phases were 0.68, 0.65, 0.71A.

By carrying out such tests it is possible to segregate the machine's harmonics from those caused by external sources.

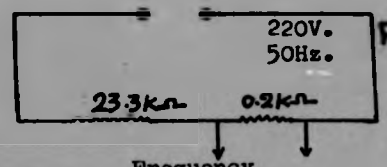

Fig.3.9a-Harmonic content of the mains waveform.

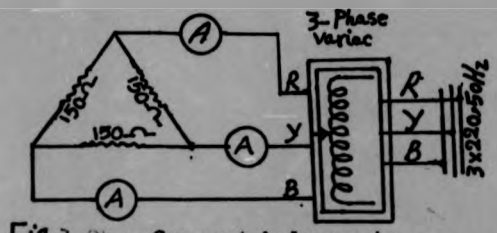

Fig.3.9b - Current balance in a three arms balanced resistive loop.

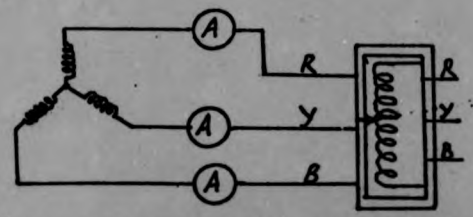

Fig.3.9c - Current balance in the three phases of the experimental machine.

CHAPTER 4

Air gap flux and equivalent circuit

4.1 Conformal transformation

To understand a machine closely it is essential to make a close study of the conditions under which the flux exists in the air-gap. This air-gap is usually a complex boundary such that it is not possible to use simple analytical methods to solve for the flux. The analytical method of conformal transformation is the most powerful method to use for field analysis of different boundary shapes.

The Schwarz- Christoffel transformation (SCT)ref4.1,used in this work, applies to problems having closed polygon boundaries. The solution for the field starts with mapping the actual configuration of the air-gap in the Z-plane where the flux and equipotential lines are not regular, straight and parallel, to a portion of a uniform rectangular field in a complex plane called the ζ-plane. The difficulty in this type of configuration, depends largely on the configuration's boundaries to be mapped, and mainly the number of right angles contained, since it is a technique involving right angles straightened up. It is found that two right angles is the maximum number of right angles which can exist in a configuration which involves no elliptic functions in the transformation, but only circular or hyperbolic functions. But when more than two right angles have to be straightened out, the integration may be a combination of elementary and elliptic functions of one of three kinds.

4.1.1 The transformation

The developed diagram of the induction machine to be mapped is shown in fig.(4.1) in the stator-rotor-stator configuration. It consists of two stators, each having a succession of completely open slots on each side of the rotor. The rotor is considered as a smooth plane surface opposing the

CHAPTER 4

Air gap flux and equivalent circuit

4.1 Conformal transformation

To understand a machine closely it is essential to make a close study of the conditions under which the flux exists in the air-gap. This air-gap is usually a complex boundary such that it is not possible to use simple analytical methods to solve for the flux. The analytical method of conformal transformation is the most powerful method to use for field analysis of different boundary shapes.

The Schwarz- Christoffel transformation (SCT)ref4.1,used in this work, applies to problems having closed polygon boundaries. The solution for the field starts with mapping the actual configuration of the air-gap in the Z-plane where the flux and equipotential lines are not regular, straight and parallel, to a portion of a uniform rectangular field in a complex plane called the ζ-plane. The difficulty in this type of configuration, depends largely on the configuration's boundaries to be mapped, and mainly the number of right angles contained, since it is a technique involving right angles straightened up. It is found that two right angles is the maximum number of right angles which can exist in a configuration which involves no elliptic functions in the transformation, but only circular or hyperbolic functions. But when more than two right angles have to be straightened out, the integration may be a combination of elementary and elliptic functions of one of three kinds.

4.1.1 The transformation

The developed diagram of the induction machine to be mapped is shown in fig.(4.1) in the stator-rotor-stator configuration. It consists of two stators, each having a succession of completely open slots on each side of the rotor. The rotor is considered as a smooth plane surface opposing the

Fig.(4.1) - Conformal transformation

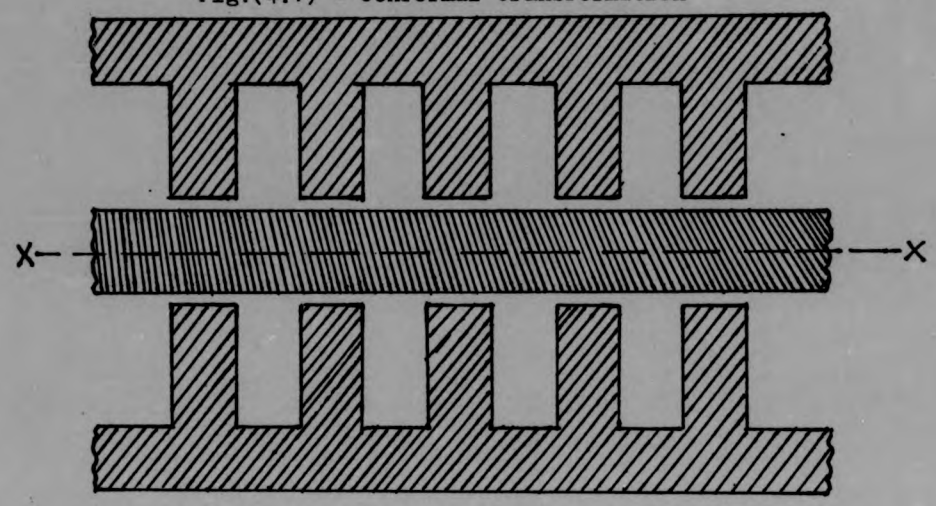

a - Developed diagram of the induction machine

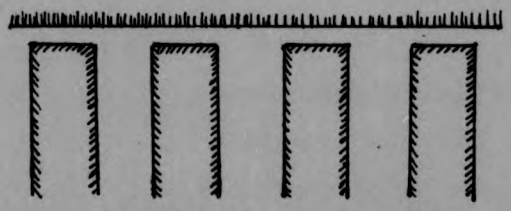

b - One side of the machine with infinite slot depth

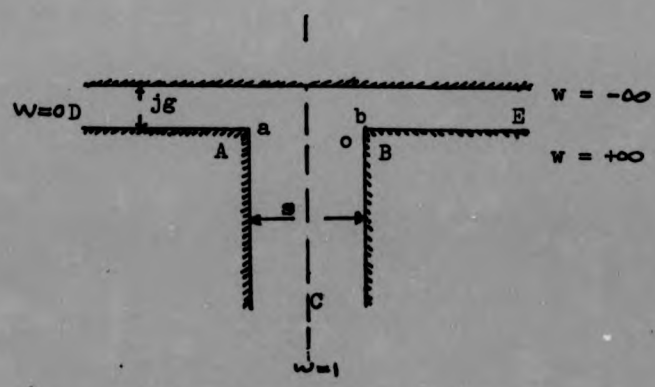

c - Single slot in the Z - Plane

slots. For the purpose of this transformation it is assumed that the slots are infinitely deep and only one slot has to be considered.

Fig.(4.2) by Coe(4.2) shows the variation of the flux-density at the centre of a slot bottom with the ratio d/s (slot depth/slot width) for values of (s/g) as parameters. The figure shows clearly that the flux drops sharply at the slot centre as d/s increases and it diminshes when this ratio increases above unity. It also shows that the drop in the flux gets sharper as the ratio s/g increases. Therefore,the first assumption is valid as long as the ratio of the slot depth to width is greater than unity (>2 in the experimental machine). The second assumption exists in most electrical machines where the air-gap is small compared with the width of an open slot.

Due to the symmetry of the machine about the xx-axis, only one half of the figure has to be considered as in fig (4.1b). Applying the first assumption, the configuration to be mapped is shown in fig.(4.1c). It consists of five corners with only two at A and B rectangular. After assigning values of w at E and D, there are remaining three more corners where values of w have to be fixed. Corners A and B can have arbitrary values 'a'and'b' with corner C having w = 1. It is to be noticed that 'a' is between w = 0 and w = 1 and 'b' is between w = 1 and w = $+\infty$. Fig.(4.1c) - becomes a closed polygon by joining the ends at D and C where w = 0 and w = 1, having five vertices ABCDE with corresponding angles, $3\pi/2$, $3\pi/2$,0,0 to be opened at E. Using SCT, the equation of transformation from the Z-plane to the upper half of the W-plane is given by:

$$\frac{dZ}{dw} = \bar{A}\,\frac{(w-a)^{\frac{1}{2}}\,(w-b)^{\frac{1}{2}}}{w(w-1)} \qquad \text{.....4.1}$$

4.1.2 Determination of the constants

The constants $\bar{A}$, a, and b can be found by crossing the air-gap at certain points in the Z-plane. This is equivalent in the W-plane to the

Fig.(4.1) - continue

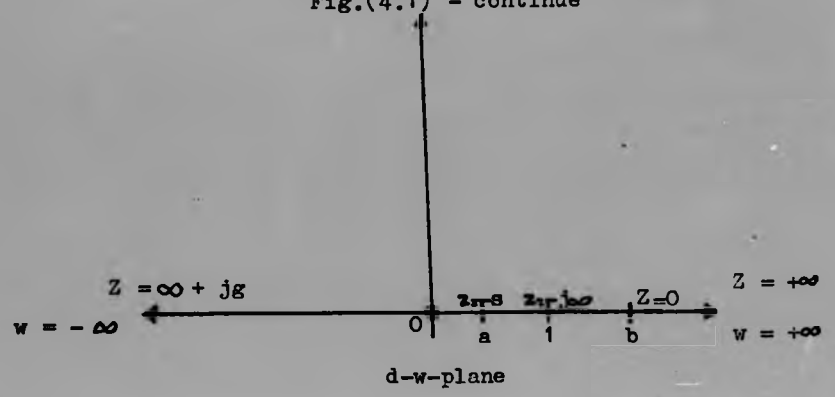

d-w-plane

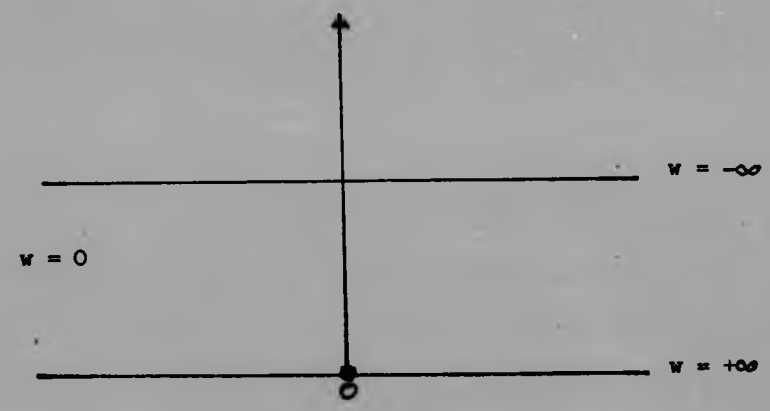

e - χ - Plane

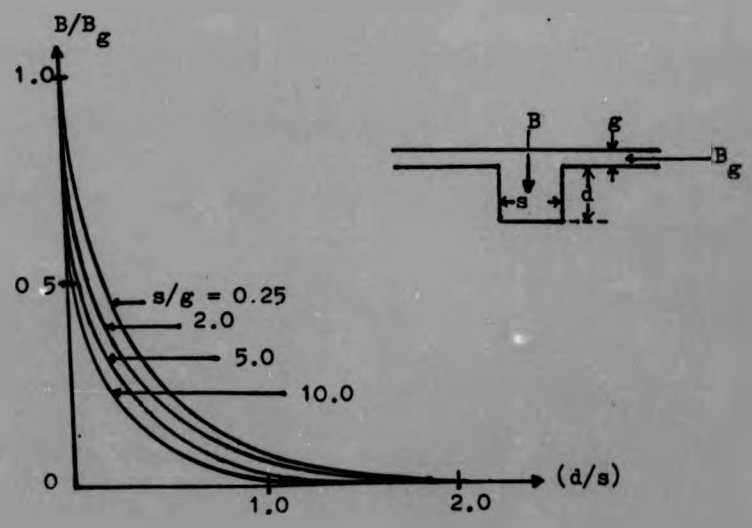

Fig.(4.2) - Flux density at the centre of a slot of finite depth by Coe,(analytical).

integration along large or small semicircles of a certain radius since this is a plane of semicircles. Crossing the air-gap as $Z \Rightarrow \infty$ is equal to the constant value of the air-gap length g including the direction. In the W-plane this is the integration along a large semicircle, ref.4.1;

$$w = R e^{j\theta} \qquad \text{and} \qquad dw = jR e^{j\theta}\, d\theta$$

Substituting these values in equation(4.1), gives:

$$dZ = \bar{A}\, \frac{(Re^{j\theta} - a)^{\frac{1}{2}} (Re^{j\theta} - b)^{\frac{1}{2}}}{Re^{j\theta} (Re^{j\theta} - 1)}\, jRe^{j\theta}\, d\theta$$

But as $R \Rightarrow \infty$ $\qquad Z \Rightarrow jg$ and

$$\bar{A} = \frac{g}{\pi} \qquad \ldots\ldots\ldots\ldots\ldots\ldots\ldots 4.2a$$

In the same manner crossing the air-gap as $Z \Rightarrow -\infty$ is equal to g and in the W-plane is equivalent to the integration along a small semicircle;

$$w = re^{j\theta} \qquad \text{and} \qquad dw = jre^{j\theta}\, d\theta \qquad \text{giving that;}$$

$$ab = 1 \qquad \ldots\ldots\ldots\ldots\ldots\ldots\ldots 4.2b$$

Substituting $\bar{A}$ in equation(4.1) gives:

$$dZ = \frac{g}{\pi} \frac{(w - a)^{\frac{1}{2}} (w - b)^{\frac{1}{2}}}{w(w - 1)}\, dw$$

The solution for this equation is obtained as follows:

$$\text{Let} \quad P^2 = \frac{(w - b)}{(w - a)} \qquad \ldots\ldots\ldots\ldots\ldots\ldots\ldots 4.2c$$

Therefore,

$$Z = \frac{2g}{\pi} \frac{(b + 1)^2 (b - 1) P^2}{(1 - P^2)(b^2 - P^2)(b + P^2)}\, dP$$

Using the method of partial fractions and with the help of Dwights' tables, ref.43;

$$Z = \frac{g}{\pi}\left(\ln\left|\frac{1 + P}{1 - P}\right| - \ln\left|\frac{b + P}{b - P}\right| - 2\frac{(b - 1)}{\sqrt{b}} \cdot \tan^{-1}\frac{P}{\sqrt{b}}\right) \ldots\ldots 4.3$$

integration along large or small semicircles of a certain radius since this is a plane of semicircles. Crossing the air-gap as $Z \Rightarrow \infty$ is equal to the constant value of the air-gap length g including the direction. In the W-plane this is the integration along a large semicircle, Ref. 4.1;

$$w = R e^{j\theta} \qquad \text{and} \qquad dw = jR e^{j\theta}\, d\theta$$

Substituting these values in equation(4.1), gives:

$$dZ = \bar{A}\, \frac{(Re^{j\theta} - a)^{\frac{1}{2}} (Re^{j\theta} - b)^{\frac{1}{2}}}{Re^{j\theta} (Re^{j\theta} - 1)}\, jRe^{j\theta}\, d\theta$$

But as $R \Longrightarrow \infty$ $\quad Z \Longrightarrow jg$ and

$$\bar{A} = \frac{g}{\pi} \qquad \ldots\ldots\ldots\ldots\ldots\ldots\ldots 4.2a$$

In the same manner crossing the air-gap as $Z \Longrightarrow -\infty$ is equal to g and in the W-plane is equivalent to the integration along a small semicircle;

$$w = re^{j\theta} \qquad \text{and} \qquad dw = jre^{j\theta}\, d\theta \qquad \text{giving that;}$$

$$ab = 1 \ldots\ldots\ldots\ldots\ldots\ldots\ldots 4.2b$$

Substituting $\bar{A}$ in equation(4.1) gives:

$$dZ = \frac{g}{\pi}\, \frac{(w - a)^{\frac{1}{2}} (w - b)^{\frac{1}{2}}}{w(w - 1)}\, dw$$

The solution for this equation is obtained as follows:

$$\text{Let} \quad P^2 = \frac{(w - b)}{(w - a)} \qquad \ldots\ldots\ldots\ldots\ldots\ldots 4.2c$$

Therefore,

$$Z = \frac{2g}{\pi}\, \frac{(b + 1)^2 (b - 1)\, P^2}{(1 - P^2)\, (b^2 - P^2)(b + P^2)}\, dP$$

Using the method of partial fractions and with the help of Dwights' tables, Ref. 45;

$$Z = \frac{g}{\pi}\left(\ln\left|\frac{1 + P}{1 - P}\right| - \ln\left|\frac{b + P}{b - P}\right| - 2\,\frac{(b - 1)}{\sqrt{b}} \cdot \tan^{-1}\frac{P}{\sqrt{b}}\right) \ldots\ldots 4.3$$

The constant of integration is equal to zero by choosing the origin such that P = 0 at that point. From equation (4.3) when P = 0, Z is also zero, but w = b indicating that the origin in the Z-plane is at the point B. Values of b and a can be found by substituting w = a in equation (4.2c) giving that P = ∞ and putting this value in equation (4.3) gives:

$$Z = \frac{g}{\pi}\left(-2\frac{(b-1)}{\sqrt{b}}\pi\right), \text{ But at } w = a \quad Z = -s + o \text{ (Fig.4.1c)}$$

$$\text{Therefore} \qquad \frac{b-1}{\sqrt{b}} = s/g$$

Solving this equation for b gives:

$$b = \frac{(2 + (s/g)^2) + \sqrt{(2 + (s/g)^2)^2 - 4}}{2} \quad \ldots\ldots\ldots\ldots\ldots 4.4$$

4.1.3 Slot flux-density distribution

The transformation from the W-plane where the field is shown to be circular to the χ-plane where the field is regular and parallel, ref.4.1, given by;

$$\chi = \frac{\bar{V}}{\pi}\log w \quad \ldots\ldots\ldots\ldots\ldots\ldots 4.5$$

where $\bar{V}$ is the potential difference between two surfaces to be considered. The flux density at any point between these two surfactes is given by:

$$B = \mu_o \left|\frac{d\chi}{dz}\right|$$

By using the mathematical chain-rule it is possible to show that:

$$B = \frac{\mu_o \bar{V}}{g}\left|\frac{(w-1)}{(w-a)^{\frac{1}{2}}(w-b)^{\frac{1}{2}}}\right| \quad \ldots\ldots\ldots\ldots 4.6a$$

The maximum value of this flux occurs at the air-gap "g" towards the corners D and E of fig.(4.1c) where w = 0 and $\pm\infty$ giving uniform flux density ($B_{max} = \mu_o \frac{\bar{V}}{g}$)
The flux density at any point is therefore given by;

$$B = \left|\frac{(w-1)}{(w-a)^{\frac{1}{2}}(w-b)^{\frac{1}{2}}}\right| B_{max} \quad \ldots\ldots\ldots\ldots 4.6b$$

The full curve in Fig.(4.3) shows the flux density in the slot according to the above equation.

The amount of the drop of the flux at the slot is given by (ref.4.1) as:

$$\phi_1 = \int_{-\infty}^{+\infty} (B_{max} - B)\, dx$$

Using equations 4.6b and 4.1 in the above integration and with the help of Fig.(4.1d) it is possible to show that;

$$\phi_1 = \frac{g}{\pi} \int_{\infty}^{-\infty} \left(\frac{(w-1)^{\frac{1}{2}} (w-b)^{\frac{1}{2}}}{w(w-1)} \right) dw$$

Substituting equation 4.2c in the above equation and integrating gives;

$$\phi_1 = \frac{2g}{\pi} \left(\frac{(b-1)}{\sqrt{b}} \left(\tan^{-1}\sqrt{b} - \tan^{-1}\frac{1}{\sqrt{b}}\right) - \ln \frac{(b+1)^2}{4B} \right) B_{max} \quad \ldots 4.6$$

where,

$$\tan^{-1}\sqrt{b} - \tan^{-1}\frac{1}{\sqrt{b}} = \tan^{-1}\left(\frac{s}{2g}\right)$$

and

$$\frac{(b+1)^2}{4b} = 1 + \frac{s^2}{4g^2}$$

Therefore equation (4.6c) becomes:

$$\phi_1 = g\gamma B_{max} \quad \ldots\ldots\ldots\ldots\ldots\ldots 4.7a$$

where,

$$\gamma = \frac{4}{\pi}\left(\left(\frac{s}{2g}\right) \tan^{-1}\left(\frac{s}{2g}\right) - \ln\left(1 + \frac{s^2}{4g^2}\right)^{\frac{1}{2}}\right) \quad \ldots\ldots\ldots\ldots\ldots 4.7b$$

The flux in a slot pitch $(t + s)$ is therefore reduced from the uniform value of $(t + s)B_{max}$ for a smooth air-gap to a new value $(t + s - \gamma g)B_{max}$ for the slotted gap, and the ratio between these two fluxes is known as the Carter coefficient given by:

$$K_c = \frac{(t+s)}{(t+s-\gamma g)} > 1 \quad \ldots\ldots\ldots\ldots\ldots\ldots 4.8a$$

The amplitude of the flux drop at the centre of the slot is given by:

$$B_c = 2\beta B_{max} \quad \ldots\ldots\ldots\ldots\ldots\ldots\ldots\ldots\ldots 4.8b$$

where,

$$\beta = \left(0.5 - \frac{\sqrt{b}}{(1+b)}\right) \quad \ldots\ldots\ldots\ldots\ldots\ldots\ldots\ldots 4.8c$$

Values of β as function of s/g have been plotted in fig.(4.4) using equations (4.4) and (4.8c).

The amount of the drop of the flux at the slot is given by (ref.4.1) as:

$$\phi_1 = \int_{-\infty}^{+\infty} (B_{max} - B)\, dx$$

Using equations 4.6b and 4.1 in the above integration and with the help of Fig.(4.1d) it is possible to show that;

$$\phi_1 = \frac{g}{\pi} \int_{\infty}^{-\infty} \left(\frac{(w-1)^{\frac{1}{2}} (w-b)^{\frac{1}{2}}}{w(w-1)} \right) dw$$

Substituting equation 4.2c in the above equation and integrating gives;

$$\phi_1 = \frac{2g}{\pi} \left(\frac{(b-1)}{\sqrt{b}} \left(\tan^{-1}\frac{1}{\sqrt{b}} - \tan^{-1}\frac{1}{\sqrt{b}}\right) - \ln \frac{(b+1)^2}{4B} \right) B_{max} \quad \ldots 4.6$$

where,

$$\tan^{-1}\frac{1}{\sqrt{b}} - \tan^{-1}\frac{1}{\sqrt{b}} = \tan^{-1}\left(\frac{s}{2g}\right)$$

and

$$\frac{(b+1)^2}{4b} = 1 + \frac{s^2}{4g^2}$$

Therefore equation (4.6c) becomes:

$$\phi_1 = g\gamma B_{max} \quad \ldots\ldots\ldots\ldots\ldots\ldots 4.7a$$

where,

$$\gamma = \frac{4}{\pi}\left(\left(\frac{s}{2g}\right) \tan^{-1}\left(\frac{s}{2g}\right) - \ln\left(1 + \frac{s^2}{4g^2}\right)^{\frac{1}{2}}\right) \quad \ldots\ldots\ldots\ldots\ldots 4.7b$$

The flux in a slot pitch $(t + s)$ is therefore reduced from the uniform value of $(t + s)B_{max}$ for a smooth air-gap to a new value $(t + s - \gamma g)B_{max}$ for the slotted gap, and the ratio between these two fluxes is known as the Carter coefficient given by:

$$K_c = \frac{(t+s)}{(t+s-\gamma g)} > 1 \quad \ldots\ldots\ldots\ldots\ldots\ldots 4.8a$$

The amplitude of the flux drop at the centre of the slot is given by:

$$B_c = 2\beta B_{max} \quad \ldots\ldots\ldots\ldots\ldots\ldots\ldots\ldots\ldots 4.8b$$

where,

$$\beta = \left(0.5 - \frac{\sqrt{b}}{(1+b)}\right) \quad \ldots\ldots\ldots\ldots\ldots\ldots\ldots 4.8c$$

Values of β as function of s/g have been plotted in fig.(4.4) using equations (4.4) and (4.8c).

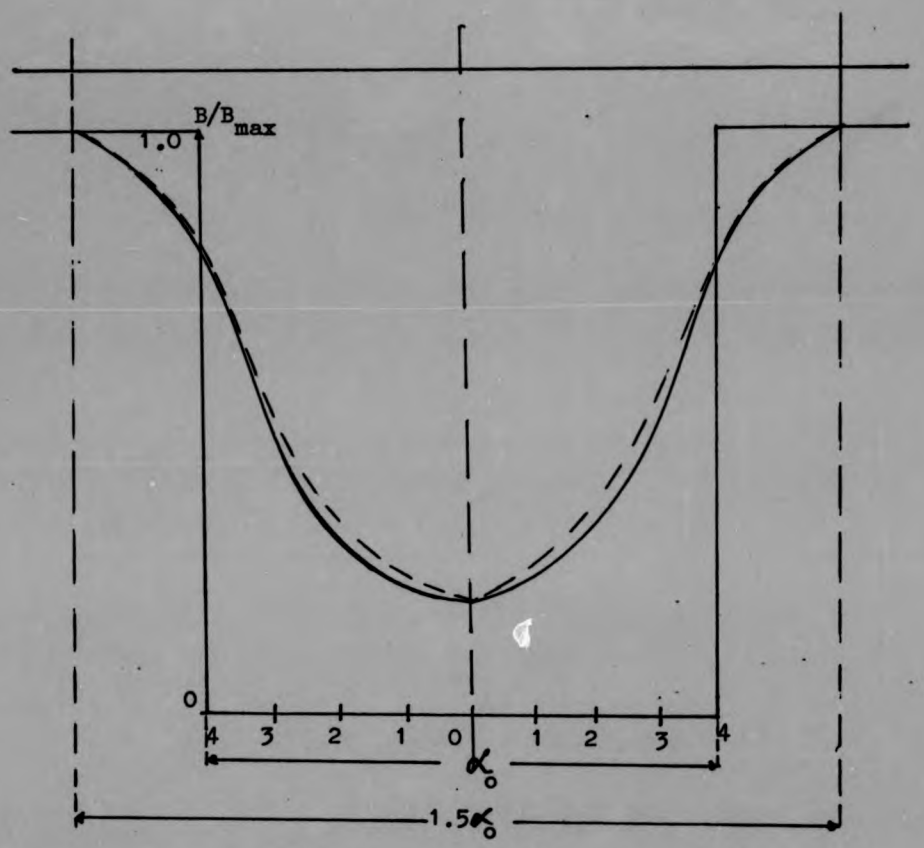

Fig.(4.3) - Flux drop curve at the slot.
Full curve - Conformal transformation
Dashed curve - Heller's formula

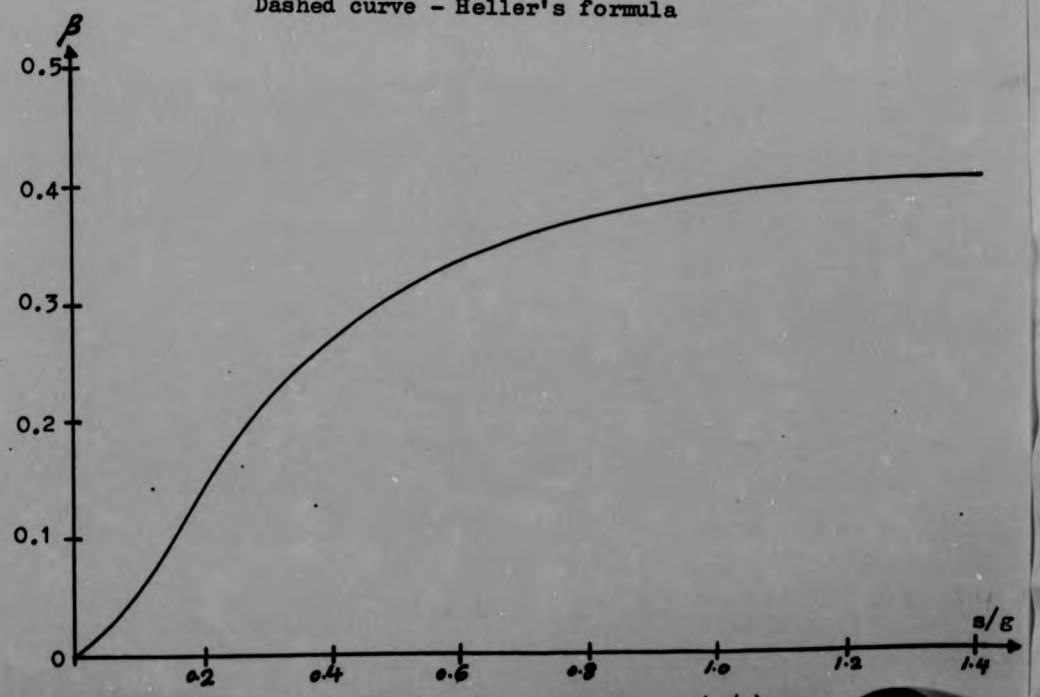

Fig.(4.4) - β as function of (s/ε)

4.1.4 Magnetic air gap conductance

It is shown in fig.(4.3) that the slot opening in the machine affects the magnetic distribution up to $0.75\alpha_o$ from the centre of the slot where α_o is the slot opening angle and it stays uniform above this angular distance. Using Hellers formula, ref.4.4, the magnetic induction density over the slot pitch in terms of the angular displacement can be approximated as:

$$B(\alpha) = (1 - \beta - \beta \cos \frac{\pi \alpha}{0.75\alpha_o}) B_{max} \qquad 0 < \alpha < 0.75\alpha_o \ldots 4.9a$$

$$B(\alpha) = B_{max} \qquad 0.75\alpha_o < \alpha < \alpha_d \ldots 4.9b$$

where α_d is the slot pitch angle, and β is defined in 4.8.C;

$$\alpha_o = \frac{2s}{D} \quad \text{(rad./sec.)}$$

$$\alpha_d = \frac{2(t + s)}{D} \quad \text{for any diameter D.}$$

The mean magnetic induction density over the slot pitch using these values of induction is given by:

$$B_s = \frac{2}{\alpha_d} \int_0^{0.5\alpha_d} B d\alpha$$

Therefore

$$B_s = \frac{(t + s) - 1.5\beta s}{(t + s)} \cdot B_{max}$$

giving a new expression for the Carter coefficient as:

$$K_c = \frac{(t + s)}{(t + s) - 1.5\beta s} \ldots\ldots\ldots\ldots\ldots\ldots 4.10$$

The flux density of a smooth air-gap between rotor and stator is given by:

$$B = \frac{\text{Magnetic potential difference}}{g}$$

But when the air-gap is not smooth, that is when one side of the air-gap or both are slotted, the air-gap is no longer uniform and the flux density is given by:

$$B(\alpha) = \frac{1}{g(\alpha)} = f(\alpha)$$

assuming unit magnetic potential difference.

The function $f(\alpha)$ is a periodic function with a period of α_d and has the values given in equation 4.9. If the number of the stator slots is z and the origin is taken at the stator slot axis, this function can be written in the Fourier series form as:

$$f(\alpha) = a_o - \sum_{n=1}^{\infty} a_n \cos nz\alpha \quad \text{.....4.11a}$$

where $$a_o = \frac{2}{\alpha_d} \int_0^{0.5\alpha_d} f(\alpha)\,d\alpha$$

$$a_n = \frac{4}{\alpha_d} \int_0^{0.5\alpha_d} f(\alpha) \cos \frac{n\pi\alpha}{\alpha_d/2}\, d\alpha$$

Therefore,

$$a_o = \frac{2}{\alpha_d} \left(\int_0^{0.75\alpha_o} (1-\beta-\beta\cos\frac{\pi\alpha}{0.75\alpha_o})\,d\alpha + \int_{0.75\alpha_o}^{0.5\alpha_d} d\alpha \right) \cdot B_{max}$$

$$a_n = \frac{4}{\alpha_d} \left(\int_0^{0.75\alpha_o} (1-\beta-\beta\cos\frac{\pi\alpha}{0.75\alpha_o})\cos\frac{2n\pi\alpha}{\alpha_d}\,d\alpha + \int_{0.75\alpha_o}^{0.5\alpha_d} \cos\frac{2n\pi\alpha}{\alpha_d}\,d\alpha \right) \cdot B_{max}$$

giving that $$a_o = 1/K_c \cdot g \qquad (\text{since } B_{max} = 1/g)$$

$$a_n = \frac{\beta}{g} F_n(\alpha_o/\alpha_d)$$

where,

$$F_n(\alpha_o/\alpha_d) = \frac{1}{n} \frac{4}{\pi} \left(0.5 + \frac{(n\alpha_o/\alpha_d)^2}{(0.9 - 2(n\alpha_o/\alpha_d)^2)}\right) \sin 1.5\pi(n\frac{\alpha_o}{\alpha_d}) \quad \text{..4.11b}$$

Substituting these values in equation 4.11a, gives that:

$$f(\alpha) = \left(\frac{1}{K_c \cdot g} - \frac{\beta}{g} \sum_{n=1}^{\infty} F_n \cos nz\alpha\right)$$

But $f(\alpha) = \frac{1}{g(\alpha)}$ is the magnetic conductance.

The magnetic conductance of the air-gap is therefore given by:

$$\frac{1}{g(\alpha)} = \frac{1}{g}\left(\frac{1}{K_c} - \beta\sum_{n=1}^{\infty} F_n \cos nz\alpha\right) \quad \ldots\ldots\ldots\ldots 4.11c$$

4.2 Effective air gap length

The reduction in the air-gap flux can also be explained in terms of the increase in the physical air-gap length "g" due to slotting to a larger air-gap length known as the effective or magnetic air-gap length. This new air-gap length is given by:

$$\bar{g} = K_c g \quad \ldots\ldots\ldots\ldots\ldots 4.12a$$

β is shown to be constant for a given value of "s/g", equation 4.8c, therefore Kc depends on the tooth to slot ration "s/t".

In radial air-gap machines this ratio is constant along the active length of the machine. In the experimental machine however the slot width is made constant along machine's active length in the radial direction, but the tooth width is varying from a minimum at D_1 to its largest value at D_2. Therefore the ratio t/s is varying as a function of the radius and consequently causing K_c in equation 4.10 to vary as follows:

$$\text{since} \quad (t + s) = \frac{2\pi R}{z}$$

$$\text{From equation 4.10} \quad K_c = \frac{2\pi R/z}{\frac{2\pi R}{z} - 1.5\, s}$$

$$= \frac{2\pi R}{2\pi R - 1.5 z \beta s}$$

Therefore to calculate the effective air-gap length and to account for such a variation, the average value of the air-gap length has to be found as:

$$\bar{g} = \frac{2}{(D_2 - D_1)} \int_{D_1/2}^{D_2/2} K_c \cdot g \cdot dR$$

$$\vartheta = \frac{2\pi}{(D_2 - D_1)} \int_{D_1/2}^{D_2/2} \frac{2\pi R}{2\pi R - 1.5z\beta s} dR$$

giving that $\bar{g} = K_{ce} \cdot g$

Where the effective Carter coefficient is given by:

$$K_{ce} = \left(1 + \frac{(1.5z\beta s)}{\pi(D_2 - D_1)} \ln \frac{(\pi D_2 - 1.5z\beta s)}{(\pi D_1 - 1.5z\beta s)}\right) \quad \ldots\ldots\ldots 4.12b$$

The second term in this equation represents the amount of the increase in the air-gap length through the factor β which is a function of s/g. For a closed or semiclosed slot machine β is very small and therefore this factor falls to zero in the above equation making the effective Carter Coefficient almost equal to unity.

In the present machine the ratio s/g is quite large due to the requirement of the stator open slots and consequently the effective Carter Coefficient is expected to be much higher than unity. Fig.(4.5a) shows the variation of Carter Coefficient as a function of the machine's diameter for values of the physical air-gap length as parameter. Fig.(4.5b) shows the average Carter Coefficient as a function of the slot opening for a given machine diameter.

4.3 Air-gap Permeance

The two stators of the experimental machine are designed with the slots completely open. Therefore in any flux calculation it is essential to include the deviation of the gap permeance from being uniform due to the slotting. Fig.(4.6) shows a portion of the air-gap "R δR δα" having a rectangular shape of radial length dR at radius R from the centre subtending an angle dα. The permeance of this element per unit machine's active length is given by

$$dP_r = \frac{\mu_o . R . dR . d\alpha}{g(\alpha)}$$

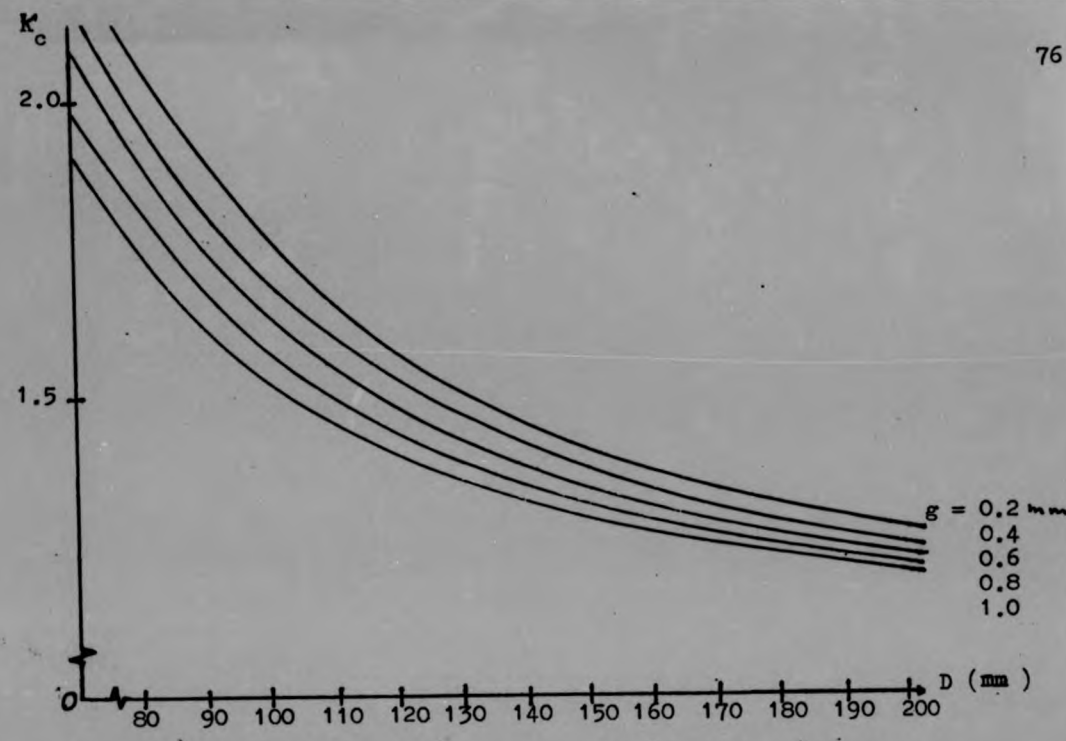

Fig.(4.5a) - Carter's coefficient as a function of the machine diameter for different values of air-gap.

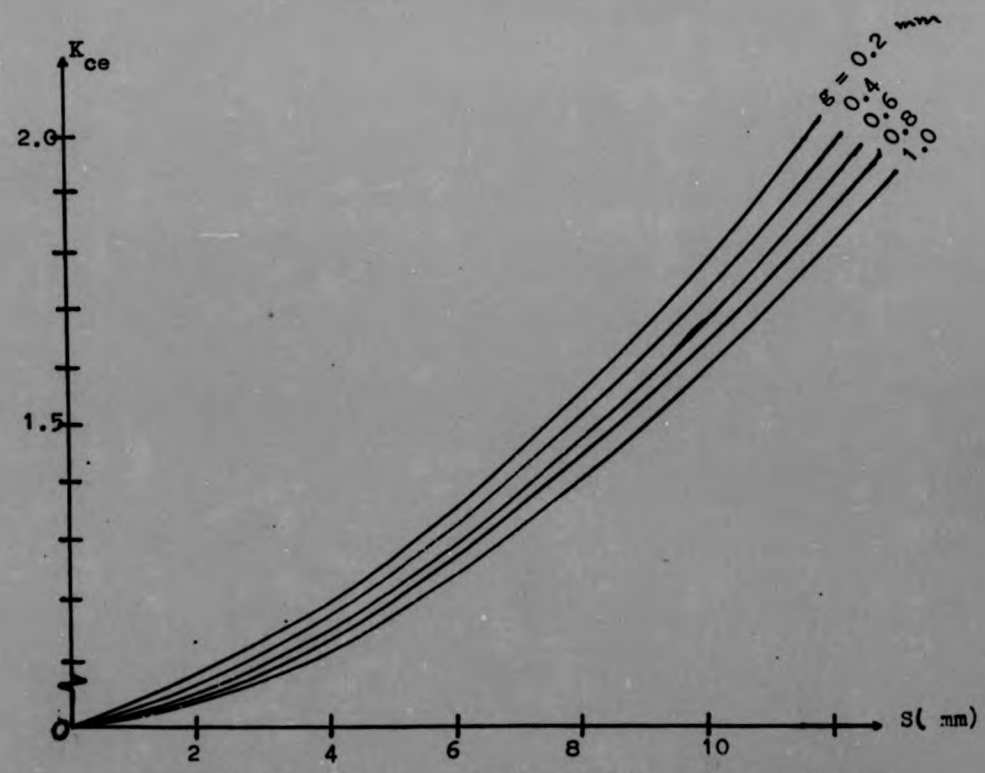

Fig.(4.5b) - Average Carter's coefficient as a function of machine's slot-opening for different values of air-gap.

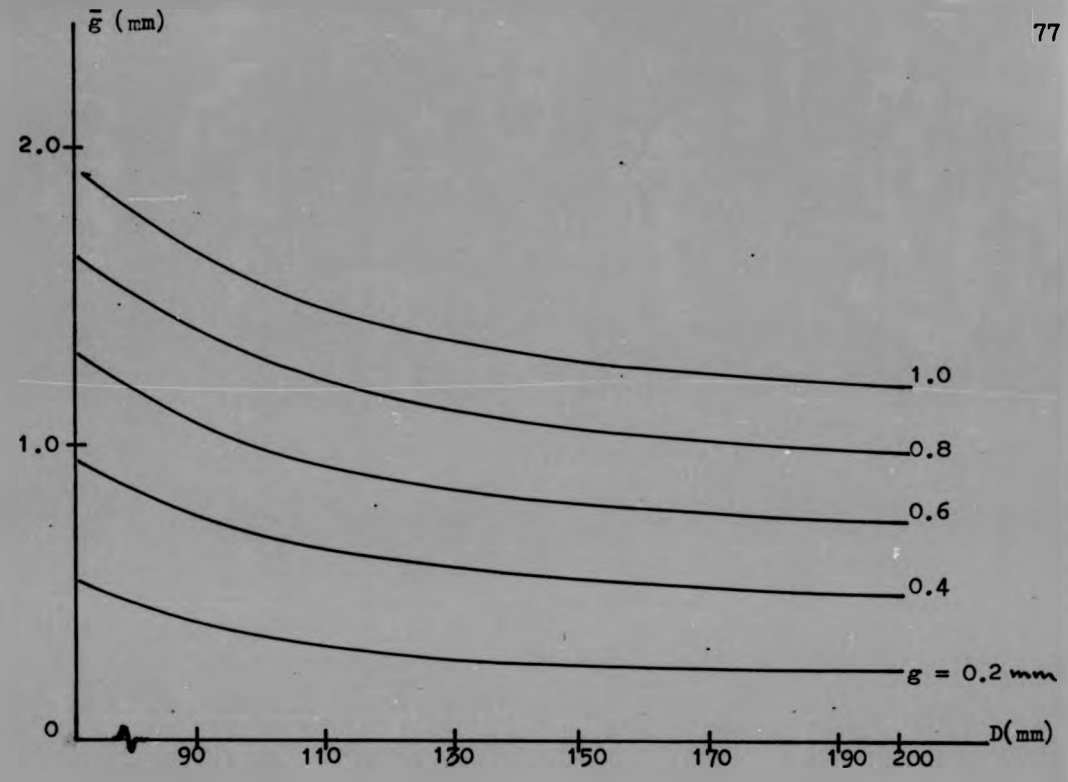

Fig.(4.5c) - Magnetic air-gap as a function of the machine's diameter for different air-gaps.

Table(4.1) - Values of F for the harmonics up to the fifth

α_o/α_d $s/(s+t)$	1	2	3	4	5
0.1	0.295	0.282	0.262	0.235	0.203
0.2	0.564	0.47	0.328	0.221	0.0023
0.3	0.786	0.492	0.236	0.0425	-0.023
0.4	0.94	0.443	0.0576	-0.0323	0
0.5	0.9995	0.260	-0.0375	0	0.00175
0.6	0.9836	0.085	-0.0277	0.0128	-0.0067
0.7	1.12	-0.293	0.0109	-0.0056	0.00342
0.8	0.886	-0.0646	0.0164	-0.00423	0
0.9	0.709	-0.0415	-0.00218	0.00545	-0.00205
1.0	0.5207	0	-0.112	0	0.00231

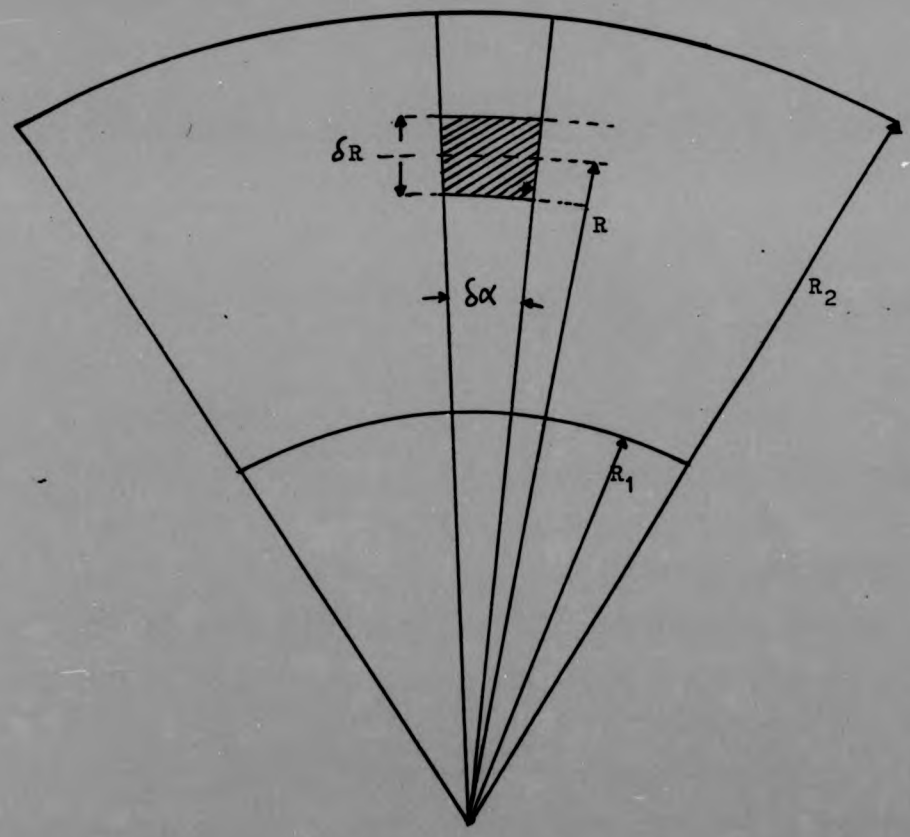

Fig.(4.6) - Element R.δR.δα of the air-gap

where

$$\frac{d\alpha}{g(\alpha)} = \frac{1}{g}\left(\frac{1}{K_c} - \beta \sum_{n=1}^{\infty} F_n \cos nz\alpha\right)$$

and g is the physical air gap of the machine(sum of both sides).

Therefore,

$$dP_r = \frac{\mu_o}{g}\left(\frac{1}{K_c} - \beta \sum_{n=1}^{\infty} F_n \cos nz\alpha\right) RdR$$

The total permeance can be obtained by integrating this equation between the limits $D_1/2$ and $D_2/2$, giving:

$$P_r = \frac{\mu_o(D_2^2 - D_1^2)}{8g}\left(\left(1 - \frac{3\beta zs}{\pi(D_2 + D_1)}\right) - \beta \sum_{n=1}^{\infty} F_n \cos nz\alpha\right) \quad \ldots.4.13$$

4.4 Air-gap flux

Since the practical machine is operating in the additive mode, the mmfs of the two stators are adding together and the magnetic circuit is similar to that in radial machines, with one difference that the flux lines cross the air gap four times to complete one magnetic circulation. The derivation of an expression which can represent the actual gap flux as near as possible is an essential task in machine analysis since the performance equations of any machine depend fully on the air-gap flux.

The analysis is similar to that employed by Gupta and Capaldi(4.5,1.5), in that it depends on the principle that the air-gap flux can be expressed as the product of the permeance of the gap with the mmf acting across it between the two stators. In the analysis the following general idealisations are made:

1. The iron laminations exhibit infinite permeability, hence the magnetic circuit is linear and effect of hystersis in the flux distribution is negligible.
2. The currents in each slot are concentrated at the intersection of the slot centre line and the stator surface.

3. The effect of slotting is included by calculating the resultant conductance of the air-gap.
4. Flux crosses the air-gap axially in straight lines and continues circumferentially in the stators.
5. Due to the machine's construction, the magnetic surfaces of the rotor and stators are parallel.
6. Since the machine is double sided, the flux is crossing the gap twice at each side giving rise to a larger effective air-gap in this type of machines.

Therefore multiplying equation(4.13) by equation(3.5) term by term gives the air-gap flux as a function of time and the angle α. This angle represents any position in the air-gap relative to the stator slot centre axis of phase A carrying the current Icoswt.

The air-gap flux is therefore:

$$\phi_\alpha = \frac{\mu_o(D_2^2 - D_1^2)}{8g}\left((1 - \frac{3\beta zs}{\pi(D_2+D_1)}) - \beta\sum_{n=1}^{\infty} F_n \cos nz\alpha\right)\cdot$$

$$\frac{6\bar{N}I}{\pi}\left(K_1\cos(p\alpha - wt) \pm \sum_{k=1}^{\infty} K_{6k\pm1}\cos((6k\pm1)p\alpha \pm wt)\right)$$

$$\phi_\alpha = \frac{3\mu_o(D_2^2 - D_1^2)I\bar{N}}{4\pi g}\cdot\left(K_1(1 - \frac{3\beta zs}{(D_2+D_1)})\cos(p\alpha - wt) \pm K_{6k\pm1}(1 - \frac{3\beta zs}{\pi(D_2+D_1)})\cdot\right.$$

$$\sum_{k=1}^{\infty}\cos((6k\pm1)p\alpha \pm wt) - \beta K_1\sum_{n=1}^{\infty} F_n \cos nz\alpha\cdot\cos(p\alpha - wt) \mp \beta K_{6k\pm1}\cdot$$

$$\left.\sum_{k=1}^{\infty}\sum_{n=1}^{\infty} F_n \cos nz\alpha\cdot\cos((6k\pm1)p\alpha \pm wt)\right)$$

$$\Phi_{\alpha} = C\cdot I\cos(p\alpha - wt) - D\cdot I\sum_{n=1}^{\infty} F_n \cos nz\alpha \cdot \cos(p\alpha - wt)$$

$$\pm \frac{I\cdot OK_{6k \pm 1}}{K_1} \sum_{k=1}^{\infty} \cos((6k \pm 1)p\alpha \pm wt)$$

$$\mp \frac{D\cdot I}{K_1} K_{6k \pm 1} \sum_{k=1}^{\infty}\sum_{n=1}^{\infty} F_n \cos nz\alpha \cdot \cos((6k \pm 1)p\alpha \pm wt) \quad .....4.14a$$

where,

$$C = \frac{3\mu_o(D_2^2 - D_1^2)\acute{N}K_1}{4\pi g}\left(1 - \frac{3\beta_{zs}}{\pi(D_2 + D_1)}\right)$$

$$D = \frac{3\mu_o(D_2^2 - D_1^2)\acute{N}K_1\beta}{4\pi g}$$

The total flux per pole is therefore found by integrating $\Phi_{\alpha} d\alpha$ between the limits $-\pi/2p$ to $+\pi/2p$ as:

$$\Phi_T = \frac{2IC}{p}\cos wt + DI\sum_{n=1}^{\infty}\frac{2F_n}{p\left((nz/p)^2 - 1\right)}\cos wt \pm \frac{I\cdot CK_{6k\pm 1}}{K_1}\sum_{k=1}^{\infty}\frac{2}{p(6k\pm 1)}\cos wt$$

$$\pm \frac{D\cdot IK_{6k \pm 1}}{K_1}\sum_{k=1}^{\infty}\sum_{n=1}^{\infty}\frac{2F_n}{p\left((nz/p(6k\pm 1))^2 - 1\right)}\cos wt \quad .....4.14b$$

It is shown earlier that the harmonic content of the stator mmf is small and can be neglected without introducing important effects in the calculations. Therefore considering the fundamental only, equation 4.14b becomes:

$$\Phi_T = \left(\frac{2IC}{p} + DI\sum_{n=1}^{\infty}\frac{2F_n}{p\left((nz/p)^2 - 1\right)}\right)\cos wt \quad ....4.15$$

$$\Phi_\alpha = C\,I\cos(p\alpha - wt) - D\,I\sum_{n=1}^{\infty} F_n \cos nz\alpha \cdot \cos(p\alpha - wt)$$

$$\pm \frac{I\,O\,K_{6k \pm 1}}{K_1} \sum_{k=1}^{\infty} \cos((6k \pm 1)p\alpha \pm wt)$$

$$\mp \frac{D\,I}{K_1} K_{6k \pm 1} \sum_{k=1}^{\infty}\sum_{n=1}^{\infty} F_n \cos nz\alpha \cdot \cos((6k \pm 1)p\alpha \pm wt) \quad \ldots\ldots 4.14a$$

where,

$$C = \frac{3\mu_o(D_2^2 - D_1^2)\,\bar{N}K_1}{4\pi g}\left(1 - \frac{3\beta zs}{\pi(D_2 + D_1)}\right)$$

$$D = \frac{3\mu_o(D_2^2 - D_1^2)\,\bar{N}K_1\beta}{4\pi g}$$

The total flux per pole is therefore found by integrating $\Phi_\alpha d\alpha$ between the limits $-\pi/2p$ to $+\pi/2p$ as:

$$\Phi_T = \frac{2IC}{p}\cos wt + DI\sum_{n=1}^{\infty}\frac{2F_n}{p\left((nz/p)^2 - 1\right)}\cos wt \pm \frac{I\,C\,K_{6k\pm 1}}{K_1}\sum_{k=1}^{\infty}\frac{2}{p(6k\pm 1)}\cos wt$$

$$\pm \frac{D\,I\,K_{6k \pm 1}}{K_1}\sum_{k=1}^{\infty}\sum_{n=1}^{\infty}\frac{2F_n}{p\left((nz/p(6k\pm 1))^2 - 1\right)}\cos wt \quad \ldots\ldots\ldots 4.14b$$

It is shown earlier that the harmonic content of the stator mmf is small and can be neglected without introducing important effects in the calculations. Therefore considering the fundamental only, equation 4.14b becomes:

$$\Phi_T = \left(\frac{2IC}{p} + DI\sum_{n=1}^{\infty}\frac{2F_n}{p\left((nz/p)^2 - 1\right)}\right)\cos wt \quad \ldots\ldots 4.15$$

The function F_n is given by equation 4.11 as a function of (s/t+s) the slot opening/slot pitch ratio. This function has a constant value in radial machines, since the above ratio is constant along the machine's active length. In axial field machines however this function is no longer constant due to the variation in the ratio (s/t+s) along the machine's active length and its amplitude decays sinusoidally. Table(4.1) shows values of F_n up to the 5th harmonic. Comparing these values at slot opening angle/slot pitch angle in range 0.36 - 0.72 (which is the variation in this ratio along the experimental machine's active length) the following conclusions can be reached;

a. The amplitudes of the harmonics other than the first in the given ratio range are negligible.

b. The first harmonic has the same order of amplitude at this ratio range. It is therefore possible to simplify the problem by chosing an average value of 0.97 for this function.

Putting this value of F_n in equation 4.15, the total flux becomes:

$$\Phi_T = \frac{2I}{p}\left(C + \frac{\bar{D}}{((z/p)^2 - 1)}\right) \cos wt \quad \ldots\ldots\ldots 4.16$$

where, $\bar{D} = \dfrac{2.91\,\mu_o(D_2^2 - D_1^2)\beta N K_1}{4\pi g}$

The peak flux density at t = 0 is therefore given by:

$$B_p = \frac{\pi}{2}\,\frac{\Phi_T}{A_p}$$

where, $A_p = \dfrac{\pi(D_2^2 - D_1^2)}{16}$ pole area

and $$B_p = \frac{8I}{(D_2^2 - D_1^2)}\left(C + \frac{\bar{D}}{((z/p)^2 - 1)}\right)$$

The flux density as a function of α is therefore given by:

$$B = C_1 I\cos(p\alpha - wt) + \bar{C}_1 I\left(\cos\left((z+p)\alpha - wt\right) + \cos\left((z-p)\alpha + wt\right)\right) \quad \ldots 4.17$$

where,

$$C_1 = \frac{8C}{(D_2^2 - D_1^2)} \qquad \text{and} \qquad \bar{C}_1 = \frac{8\bar{D}}{(D_2^2 - D_1^2)\left((z/p)^2 - 1\right)}$$

4.5 Equivalent circuit

The equivalent circuit for one phase of the machine is shown in fig.(4.7), together with its parameters for each rotor introduced in Table 4.2. The power delivered to the air-gap by the stator windings (air-gap power P_g) can be interpreted in two parts, one as ohmic loss in the rotor and is "$\bar{s}P_g$" and the other as the mechanical power developed by the shaft as $(1 - \bar{s})P_g$. The gross mechanical power at the shaft is;

$$P = I_2^2 r_2 \left(\frac{1 - \bar{s}}{\bar{s}}\right) \quad \ldots\ldots\ldots\ldots 4.18$$

To find the net output power it is necessary to account for the total losses in the machine. The circuit of fig.(4.7) can be simplified by omitting the resistance r_o which represents the iron loss and can be deducted as power loss.

The power of equation 4.18 is a result of the sum of torques developed due to the interaction of the current in each bar with the air-gap magnetic induction. By considering a small element dR of a bar at radius R, the elemental e.m.f is given by:

$$e = B_\alpha . dR . R(-\bar{s}w_s)$$

where $(-\bar{s}w_s)$ is the speed at which the bars are moving backward relative to the rotating field. The e.m.f of a complete bar is therefore given by:

$$E_b = \frac{-\bar{s}w\,(D_2^2 - D_1^2)}{8p}\left(C_1 I\cos(p\alpha - wt) + D_1 I\left(\cos\left((z+p)\alpha - wt\right) + \cos\left((z-p)\alpha + wt\right)\right.\right.$$

Fig.(4.7) - Equivalent circuit per phase of the experimental machine.

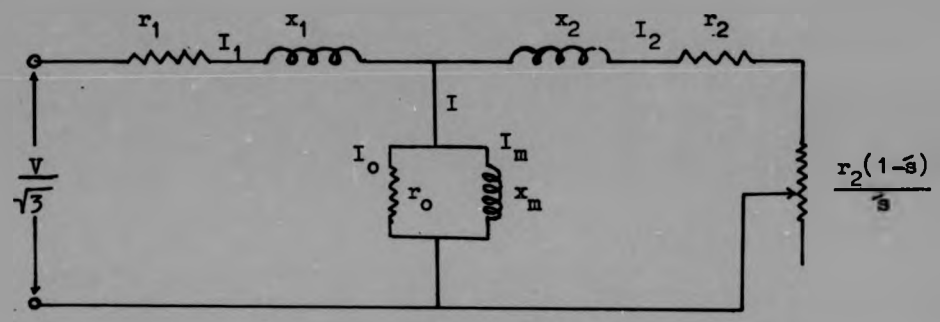

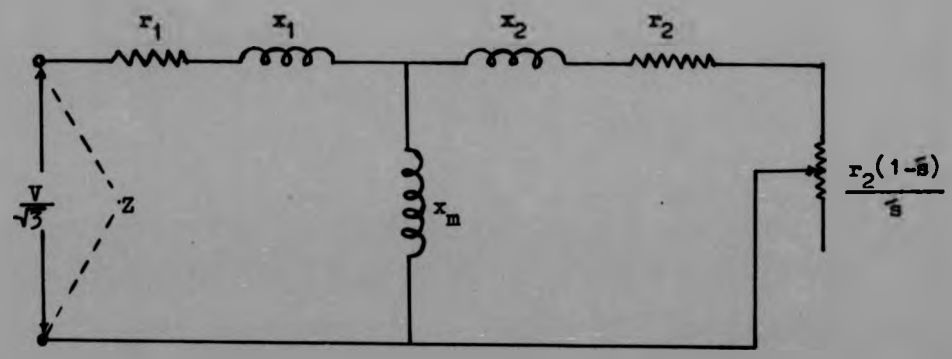

$$Z = \frac{r_1\left((r_2/\bar{s})^2 + (x_2 + x_m)^2\right) + \left((r_2/\bar{s})(x_2 + x_m)x_m - x_2 x_m r_2/\bar{s}\right)}{\left((r_2/\bar{s})^2 + (x_2 + x_m)^2\right)} + j$$

$$\frac{x_1\left((r_2/\bar{s})^2 + (x_2 + x_m)^2\right) + \left((r_2/\bar{s})^2 x_m + (x_2 + x_m)x_2 x_m\right)}{\left((r_2/\bar{s})^2 + (x_2 + x_m)^2\right)}$$

Table 4.2 - Machine parameters with different rotors

	g(physical gap) = 0.5mm $\bar{g}$(Magnetic gap) = 0.75mm					g = 0.7mm $\bar{g}$ = 1.05mm					g = 0.9mm $\bar{g}$ = 1.35mm				
Motor designation	x_1	x_2	r_1(75°C)	r_2(75°C)	X_m	x_1	x_2	r_1(75°C)	r_2(75°C)	X_m	x_1	x_2	r_1(75°C)	r_2(75°C)	X_m
A	3.1	3.1	1.54	1.910	29.63	3.1	3.1	1.54	1.91	23.77	3.1	3.1	1.54	1.91	20.39
B(end rings not separated)	3.4	3.4	1.54	1.470	38.14	3.4	3.4	1.54	1.47	32.14	3.4	3.4	1.54	1.47	26.68
B(end rings separated	3.4	3.4	1.54	1.585	32.23	3.4	3.4	1.54	1.585	27.21	3.4	3.4	1.54	1.585	24.07
D	4.07	4.07	1.54	1.95	38.5	4.07	4.07	1.54	1.95	32.0	4.07	4.07	1.54	1.95	27.0
C	4.2	4.2	1.54	2.41	34.27	4.2	4.2	1.54	2.41	27.08	4.2	4.2	1.54	2.41	22.64
C(4mm machined from each end ring)	4.2	4.2	1.54	2.72	34.60	4.2	4.2	1.54	2.72	28.59	4.2	4.2	1.54	2.72	21.46
C(7mm machined from each end ring)	4.2	4.2	1.54	3.2	34.60	4.2	4.2	1.54	3.2	29.2	4.2	4.2	1.54	3.2	21.6
D(stator slots filled with SMW)	4.76	4.76	1.54	1.90	41.0	4.76	4.76	1.54	1.90	33 09	4.76	4.76	1.54	1.90	27.67

Where, $w_s = w/p$

$$\text{or } E_b = -\frac{swI}{p}\left(C\cos(p\alpha - wt) + \frac{D}{((z/p)^2 - 1)}\left(\cos((z+p)\alpha - wt) + \cos((z-p)\alpha + wt)\right)\right)$$

The impedance of each bar is taken to be $Z_b = (r + jsx)$ and includes portions of the end rings joined to the bar.

The current in the bar is therefore given by:

$$i_b = -\frac{wI}{pZ_b}\left(C\cos(p\alpha - \theta_b) + \frac{D}{((z/p)^2 - 1)}\left(\cos((z+p)\alpha - \theta_b) + \cos((z-p)\alpha - \theta_b)\right)\right) \quad ..4.19$$

where $|Z_b| = \left((r/s)^2 + x^2\right)^{\frac{1}{2}}$

and $\tan\theta_b = \frac{sx}{r}$ is the bar load impedance phase angle

r and x are the bar load resistance and reactance at standstill.

The torque on the element is therefore:

$$dT = B_\alpha . i_b . RdR$$

The total torque on a single bar can be obtained by integrating the above equation between the limits of D1/2 and D2/2 giving that

$$T_b = \frac{(D_2^2 - D_1^2)}{8} B_\alpha . i_b$$

Substituting values of B_α and i_b,

$$T_b = \left(CI\cos(p\alpha - wt) + \frac{DI}{((z/p)^2 - 1)}\left(\cos((z+p)\alpha - wt) + \cos((z-p)\alpha + wt)\right)\right.\cdot$$

$$\left. -\frac{wI}{pZ_b}\left(C\cos(p\alpha - \theta_b) + \frac{D}{((z/p)^2 - 1)}\left(\cos((z+p)\alpha - \theta_b) + \cos((z-p)\alpha + wt)\right)\right)\right.$$

$$T_b = \frac{wC^2I^2}{pZ_b}\cos p\alpha\cdot\cos(p\alpha-\theta_b) + \frac{wCDI^2}{pZ_b\left((z/p)^2-1\right)}\Big(\cos(p\alpha-\theta_b)\cdot\cos(z+p)\alpha + \cos(p\alpha-\theta_b)\cdot\cos(z+p)\alpha\Big) + \frac{wCDI^2}{pZ_b\left((z/p)^2-1\right)}\Big(\cos p\alpha\cdot\cos\big((z+p)\alpha-\theta_b\big) + \cos p\alpha\cdot\cos\big((z-p)\alpha-\theta_b\big) + \frac{wD^2I^2}{pZ_b\left((z/p)^2-1\right)^2}\Big(\cos\big((z+p)\alpha-\theta_b\big)\cdot\cos(z+p)\alpha + \cos\big((z+p)\alpha-\theta_b\big)\cos(z-p)\alpha + \cos\big((z-p)\alpha-\theta_b\big)\cos(z+p)\alpha + \cos\big((z-p)\alpha-\theta_b\big)\cdot\cos(z-p)\alpha\Big) \quad \ldots\ldots\ldots\ldots 4.20$$

The peak torque is given by integrating equation 4.20 between 0 and π/p giving that

$$T_{b(p)} = \frac{wI^2}{pZ_b}\,\frac{\pi}{2p}\left(C^2 + \frac{2D^2}{\left((z/p)^2-1\right)}\right)\cos\theta_b$$

But $$\cos\theta_b = \frac{r/s}{\left((r/s)^2+x^2\right)^{\frac{1}{2}}}$$

Thus $$T_{av.} = \frac{wI^2}{p^2Z_b}\left(C^2 + \frac{2D^2}{\left((z/p)^2-1\right)}\right)\cdot\frac{r/s}{\left((r/s)^2+x^2\right)^{\frac{1}{2}}}$$

and the total torque for the machine of n_b bars is:

$$T_t = \left(\frac{wI}{pZ_b}\right)^2\left(C^2 + \frac{2D^2}{\left((z/p)^2-1\right)}\right)\cdot\frac{pn_br}{2sw} \text{ Nm} \quad \ldots\ldots\ldots 4.21a$$

The total output power can be stated;

$$P_t = w_r T_t \qquad w_r = (1-s)w$$

giving $$P_t = \left(\frac{wI}{pZ_b}\right)^2\left(C^2 + \frac{2D^2}{\left((z/p)^2-1\right)}\right)\frac{(1-s)n_br}{2ms} \text{ watts/phase} \quad \ldots\ldots\ldots 4.21b$$

where m is the number of phases in the machine and I is the peak phase current.

The power output of equation 4.21b calculated from the machine's parameters must be equal to the power output of equation 4.18 calculated from equivalent circuit parameters. Therefore by equalising the two equations, the turns ratio is found to be:

$$T_r = \frac{\left(C + \frac{D}{((z/p)^2 - 1)}\right)}{\left(C^2 + \frac{2D^2}{((z/p)^2 - 1)}\right)^{\frac{1}{2}}} (4pNK_1) \sqrt{m/n_b} \quad \ldots\ldots\ldots 4.22$$

Therefore the secondary parameters of the equivalent circuit r_2, x_2 referred to the primary are given by:

$$r_2 = T_r^2 r$$

$$x_2 = T_r^2 x$$

where r and x are components of the bar load impedance and can be written as the sum of the bar and portion of the end ring as;

$$r = r_b + \tfrac{1}{2} r_e$$

$$x = x_b + \tfrac{1}{2} x_e$$

and shown in A_3 as a function of frequency.

4.6 Saturation

The magnetization curves of the machine at three values of air-gap lengths are shown in fig.(4.8). The straight line tangent to the lower portion of the curve is the air-gap line indicating the mmf required to overcome the air-gap reluctance. Under very small saturation the air-gap line and magnetization curve would coincide. The departure of the curve from the air-gap line is an indication of the level of saturation* in the machine. Using the magnetization curve for 0.5mm air gap length at 220V, the magnetizing reactance is found to be 38Ω, while in the non-saturated region it is 50.4Ω. The average flux density is about 0,4 wb/m^2 and the level of saturation is about 23%. The saturation can be accounted for by expressing the performance equations in terms of the magnetizing reactance:

$$X_m = 4NK_1 w \left(C + \frac{D}{((z/p)^2 - 1)}\right)$$

* level of saturation (ref.3.4). = $\frac{\text{Total mmf - air gap mmf}}{\text{Total mmf}} = \frac{A - B}{A}$

4.6 Saturation

The magnetization curves of the machine at three values of air-gap lengths are shown in fig.(4.8). The straight line tangent to the lower portion of the curve is the air-gap line indicating the mmf required to overcome the air-gap reluctance. Under very small saturation the air-gap line and magnetization curve would coincide. The departure of the curve from the air-gap line is an indication of the level of saturation* in the machine. Using the magnetization curve for 0.5mm air gap length at 220V, the magnetizing reactance is found to be 38Ω, while in the non-saturated region it is 50.4Ω. The average flux density is about 0.4 wb/m^2 and the level of saturation is about 23%. The saturation can be accounted for by expressing the performance equations in terms of the magnetizing reactance:

$$X_m = 4NK_1 w \left(C + \frac{D}{((z/p)^2 - 1)}\right)$$

* level of saturation (ref.3.4). = $\frac{\text{Total mmf - air gap mmf}}{\text{Total mmf}} = \frac{A - B}{A}$

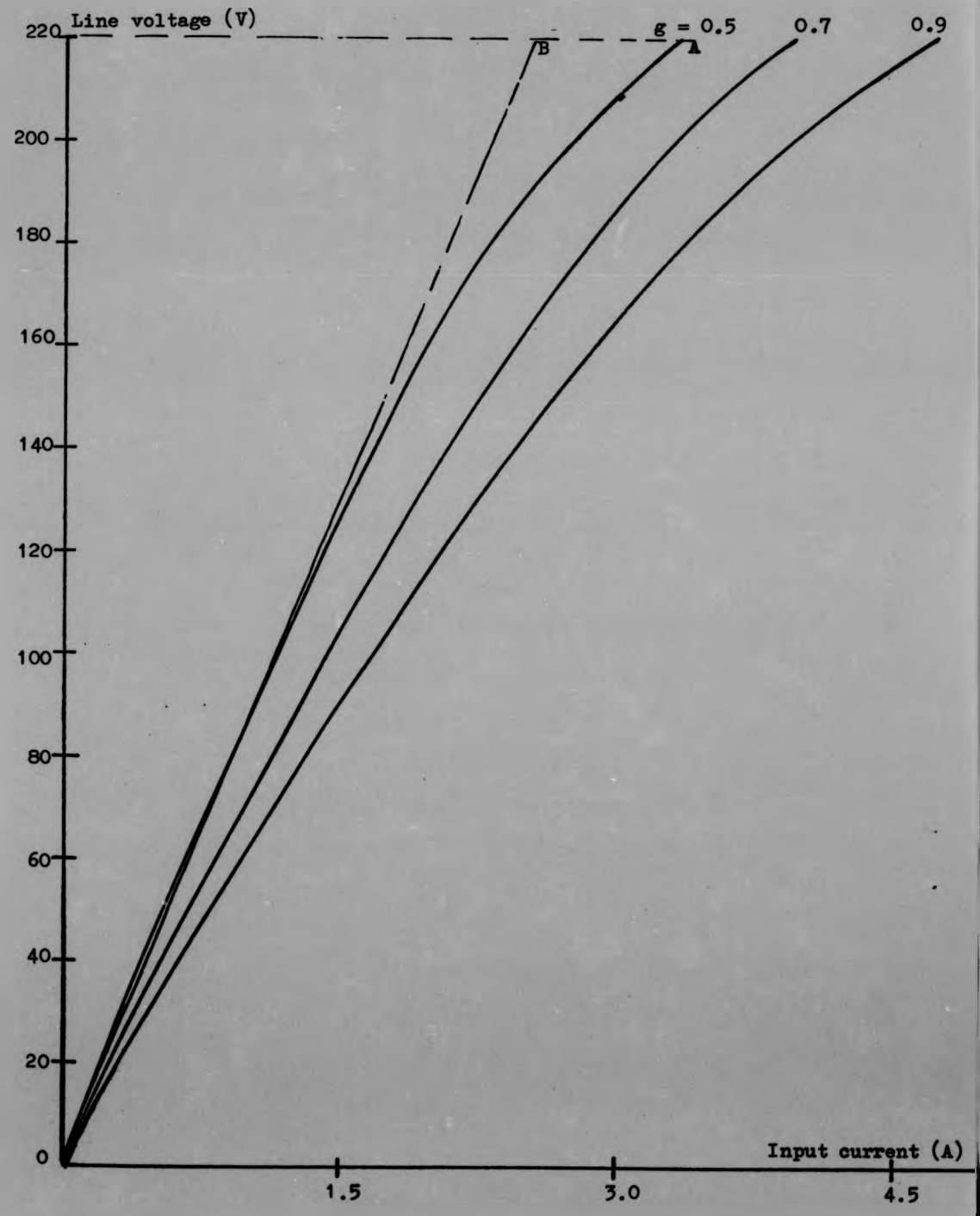

Fig.(4.8) - Magnetization curve of the motor operated with rotor D at three values of air-gap length.

CHAPTER 5

EXPERIMENTAL MACHINE AND MEASURING TECHNIQUES

5.1 Details of the Experimental Machine

Due to the single and double cage rotor production it is now possible to produce two sizes of the machine having the same external diameter of 240mm and axial lengths of 98 and 110mm respectively as shown in A5.

5.1.1 Stators

The experimental machine consists of two similar stators each having the distributed winding shown in Fig.5.0. The respective phases in the stators are connected in series and the final phases are star connected. Each stator has the following details:

Inner and outer diameters - 85 and 170mm.

Total depth of the core - 33mm.

Slots - 24, Non skewed, rectangular completely open.

Slot depth - 19mm, slot width - 8mm.

Slot width/Tooth width - 0.615 at D_2

and 3.05 at D_1

Core depth at the back of the slots - 14mm.

Winding - 3 phase, 4 pole, double layer, star connected,

20 turns per coil, 5/6 chorded rectangular coils

Resistance 0.77Ω/phase at 75°C

Each stator is made out of 33 meters length steel strip known as Losil 800 of 0.5mm thickness. This is a low silicon non-oriented steel material with comparatively low losses combined with good permeability characteristics for machine design. The strip is covered with a thin layer of inorganic material chemically and thermally bonded on to the steel base. The coating is heat and oil resistant and can withstand the annealing temperature. One of the problems which occurred was the difficulty of getting the required strip width. Therefore the required width had to be cut from a 120mm width strip supplied by

Fig.5.0 - Stator winding distribution (3 phase, 4-pole, double layer, 5/6 full pitch, 24 slots, 20 turns/coil and star connected) wire gauge 1.25 mm diameter.

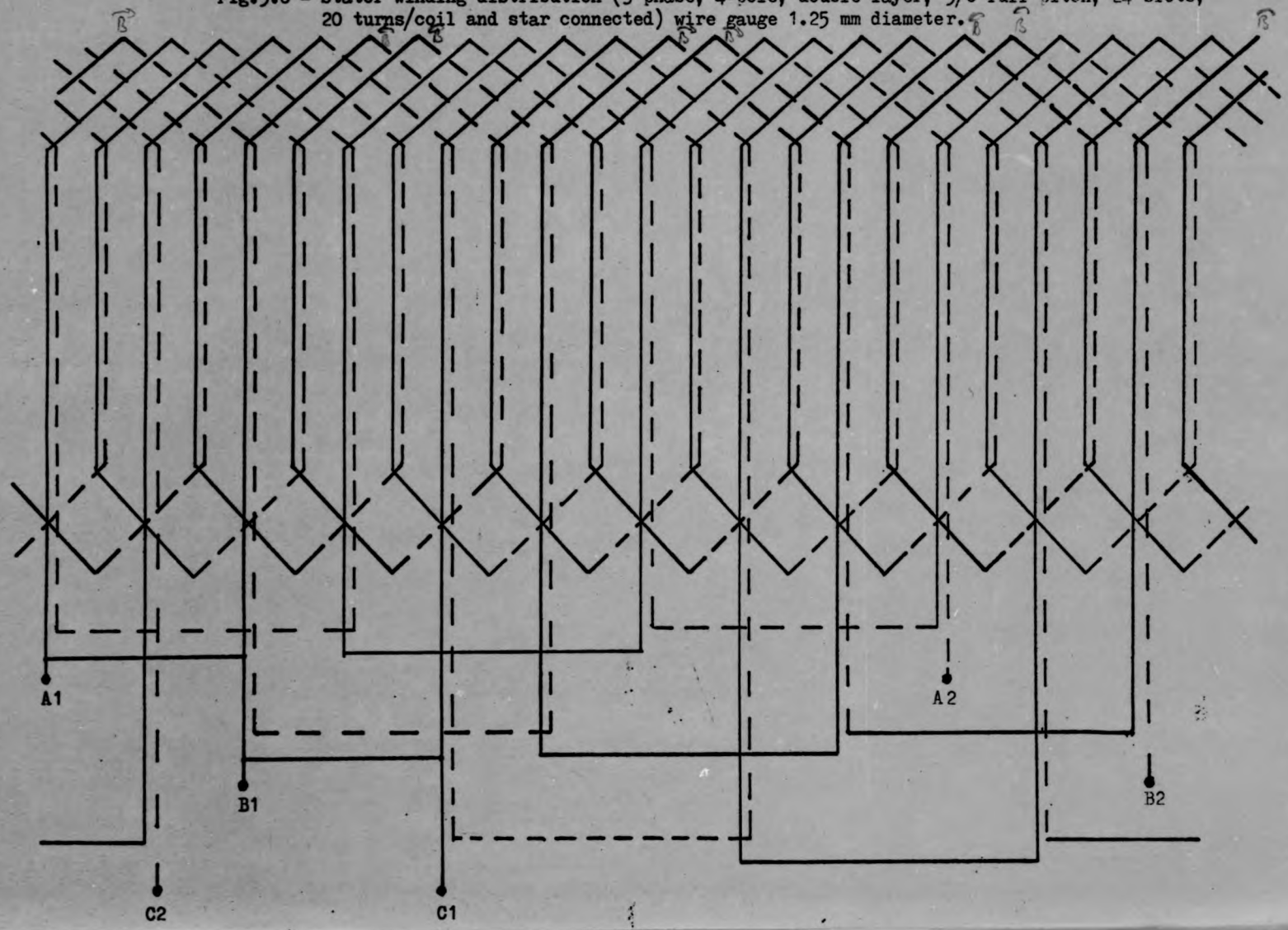

Fig.5.0 - Stator winding distribution (3 phase, 4-pole, double layer, 5/6 full pitch, 24 slots, 20 turns/coil and star connected) wire gauge 1.25 mm diameter.

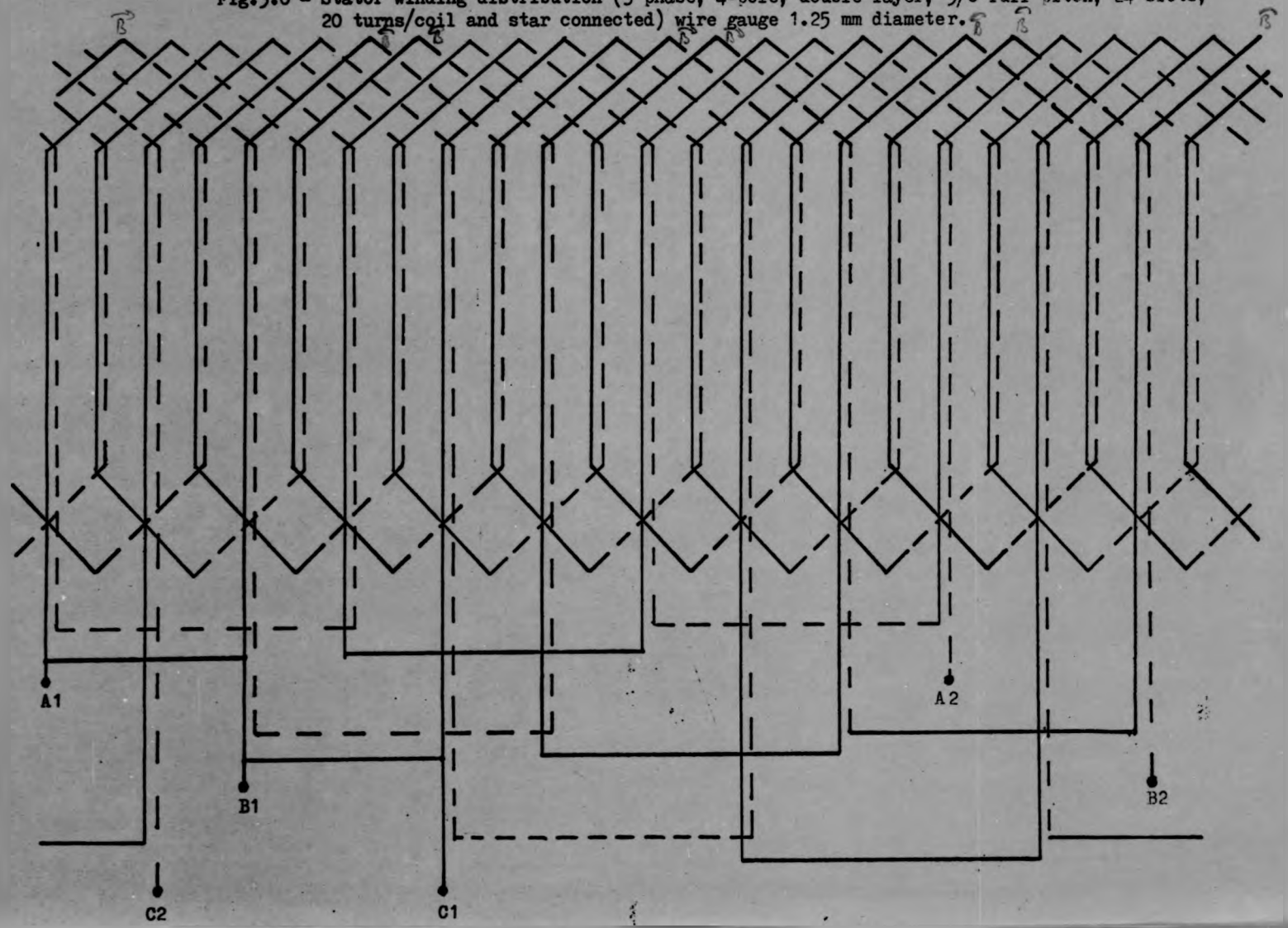

British Steel. The slitting of the steel to the required widths introduced a big problem especially that it is found that the slitting machines in use at a number of companies consulted can not handle such an amount of steel. After a long search the problem has been solved when the author modified an electric stamping machine existed in the department to a strip cutter, and good strips were cut to the required specification.

Each stator is wound in the shape of a spiral spring around a steel disc using Jig W shown in Fig.(5.3). After finishing the winding, the strip end is soldered to the last turn and a steel ring is heated and dropped over the core. When it is cooled the ring shrinks and clamps the core. The inner disc and the outer ring are then machined down to the required thickness. The steel coil is then transferred to Jig M of Fig.(5,3) for slot opening. Following this is the strain relief process which is achieved by annealing. Fig.(5.3b) shows one of the stators in Jig M after the slots have been cut.

5.1.2 Rotors

Four rotors have been made of the same steel strip in the shape of flat discs and they are designated A,B,C,and D all having the same diameter as the stators. Rotor A is a single cage with 20 normal slots made of three solid cast iron rings inserted together to give thickness of 17mm and inertia of 0.0154 $Kg.m^2$. Rotor B is a double cage - each cage consisting of 20 normal slots separated by thin steel bridge and having a total thickness of 28mm and inertia of 0.0215 $Kg.m^2$. Rotor C is a single cage of 18 slots skewed one slot pitch having thickness of 17.25mm and inertia of 0.0158 $Kg.m^2$. Rotor D is a single cage - with 20 normal slots extending radially, having a thickness of 17.25mm side to side and inertia 0.0161 $Kg.m^2$. A fifth rotor could be a reluctance rotor produced by machining the laminations at certain places of the rotor D to produce the saliency required. Three of the four experimental rotors are shown in chapter 2.

5.2 Mechanical design features

5.2.1 Skewing

It is found, ref.1.5, that due to the disc shape of the machine the skewing theoretically follows a curved line. In practice this is very difficult to achieve and consequently the skewing used in the present design is a linear skewing of one stator slot pitch (15^{o}) with the slots running straight from the outer surface of the rotor radially to its inner surface and tilted from the normal slot position.

To achieve such skewing, the rotor is adjusted vertically under the milling machine with the drill pointing towards the rotor centre. To produce the required skewing, the centre of the rotor is displaced along the horizontal axis a linear distance (R_2 Sin α) equal to the skewing angle required causing the drill to tilt relative to the first position by the skewing angle. This is shown in fig.(5.1) for one slot pitch in the 18-bars single cage rotor.

5.2.2 Fixing Techniques

In the experimental machine there are two parts which have to be fixed mechanically, these include the supporting of the rotor core carrying the cage on the steel shaft and the fixing of the stators in the end plates. Suitable fixing of the rotor on the shaft is a very important requirement in this type of machine and it can effect the construction of the rotor.

In a number of axial field machine designs which the author has encountered, special thought and design are always devoted to the method of fixing the rotor onto the shaft. In most of these designs, complicated methods involving a lot of design efforts have been used. Moreover they often cause increases in iron loss and higher rotor inertia. The fixing technique used in the present design offers the following advantages:

(a) The technique is rigid enough to stand the expected axial forces on the rotor and to limit any bending caused by such forces.

(b) The technique is straightforward with no complications and the fixing

Fig.(5.1) - Skewing in an axial field machine -

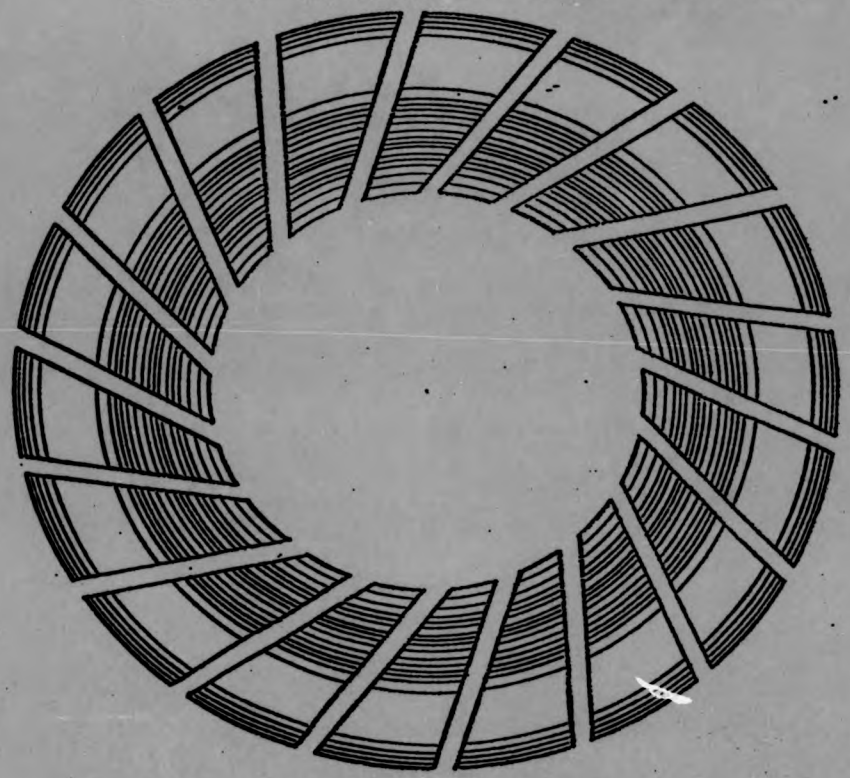

a - Skewed bar rotor

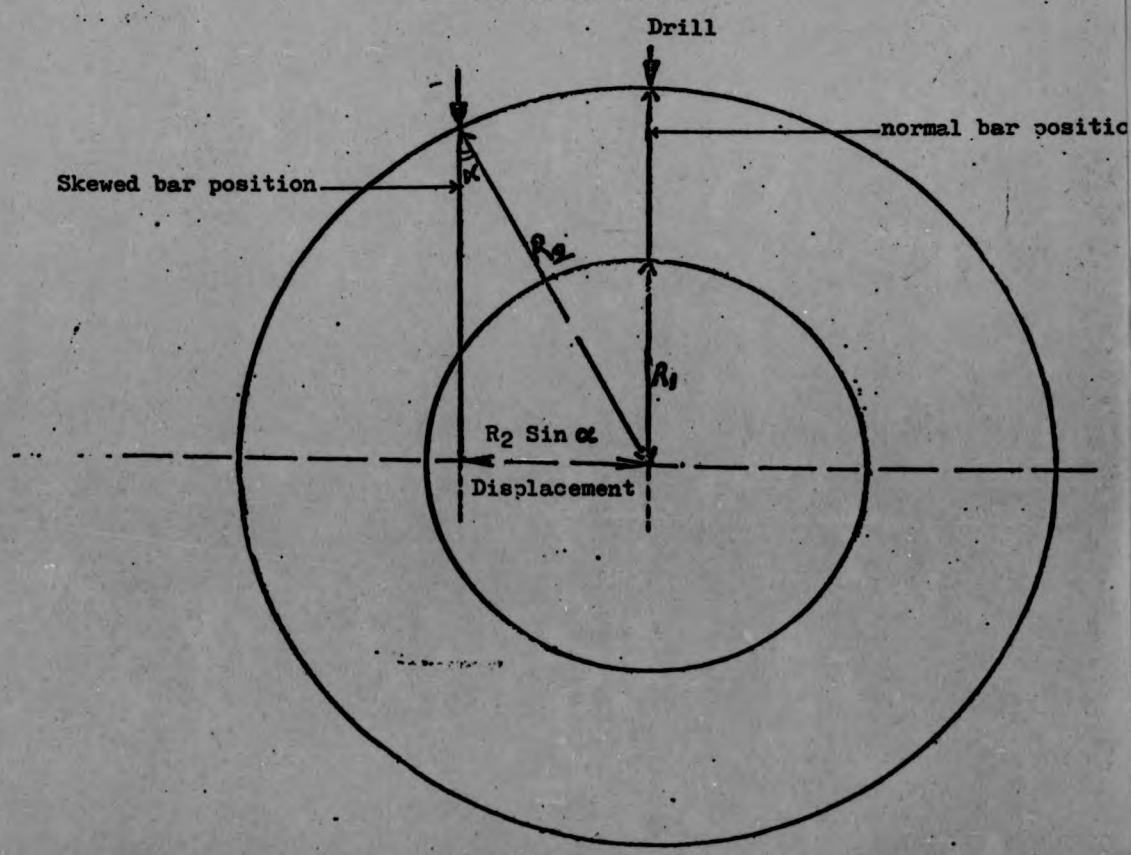

b - The process of skewing

means do not extend beyond the rotor surface in the axial direction, except at the central part of the machine.

(c) No external bolts or rings are required in the technique. These bolts and rings can be serious sources of power loss and vibrations at different speeds.

The rotor fixing technique depends heavily on two parts of the rotor; these are the massive aluminium inner end ring and the inner surface of the core at the central diameter. The aluminium at the centre is bored out and a steel bush with a key way having a thickness just below the aluminium thickness is cooled in liquid nitrogen and dropped in . As the bush expands it becomes a tight fit in the aluminium ring.

A steel shaft is made to the required dimensions carrying on one side a round shoulder made as an integral part with the shaft, with diameter just below 85mm and thickness of 4mm. The other side of the shaft is supplied with a similar shoulder movable on a thread on the shaft and clamping against the other side of the aluminium ring. The two shoulders are made to fit into the inner diameter of the rotor and enclose a key and are locked by a locknut at the back of the movable shoulder as shown in fig.(5.2a).

The fixing of the stator cores into the end-plates is another important requirement. Unsuitable fixing of the cores can cause similar problems as in the case of the rotors. Therefore any fixing technique must fulfil the above requirements. The end-plates employed have a cup shape with dimensions just sufficient to accommodate the stator cores. Initially six radial holes were drilled and tapped in each end-plate and grub screws were used to press against the outer surface of the core and are located in recesses made in the outer ring of the core.

When the motor was given the first experimental run it seemed to be quiet, smooth and noiseless but after running for a period of time some noises started to appear and increased until rubbing between the stator and rotor occurred. It was noticed that the noise started at high voltages and increased

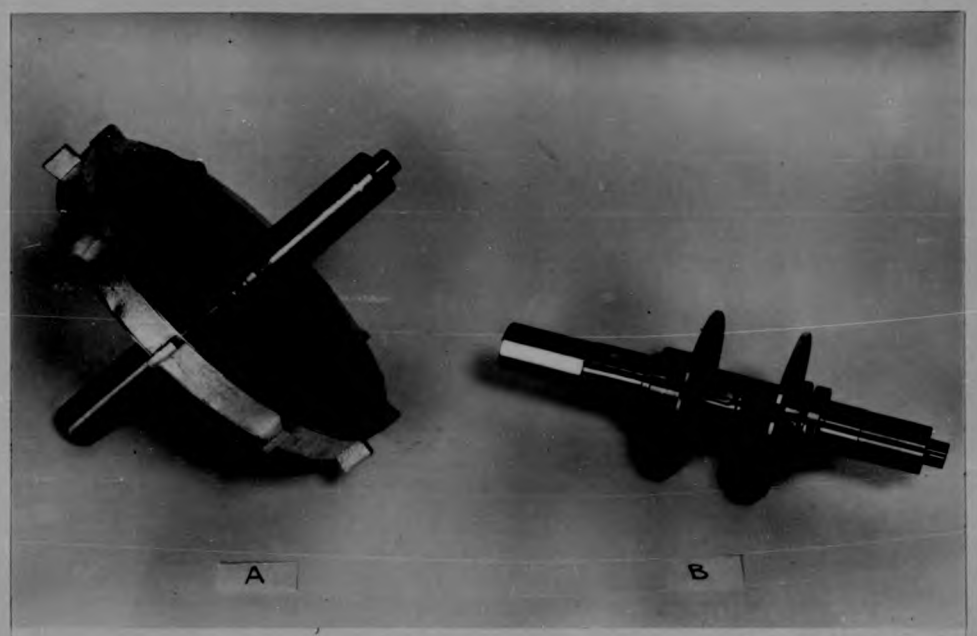

Fig. (5.2a) A - Complete rotor with solid shaft

B - The fixing assembly

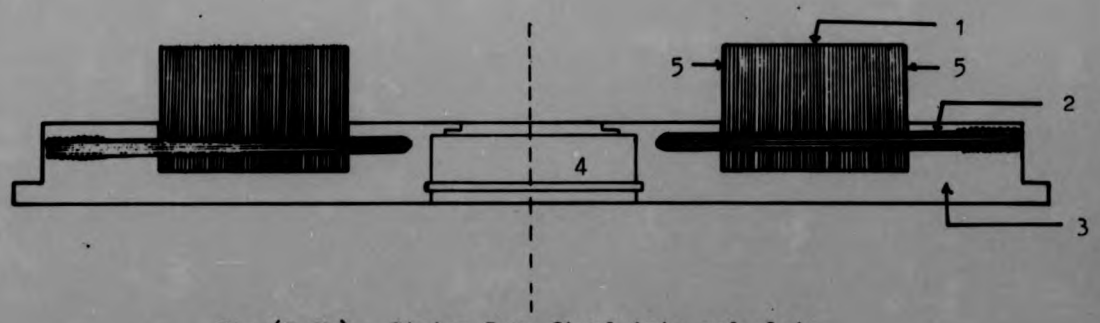

Fig.(5.2b) - Stator Core fixed into end-plate.

1. - Stator laminated core.
2. - Hardened steel screw for fixing the stator core into the end-plate.
3. - Aluminium end-plate.
4. - Bearing.
5. - Outer and inner steel retaining rings.

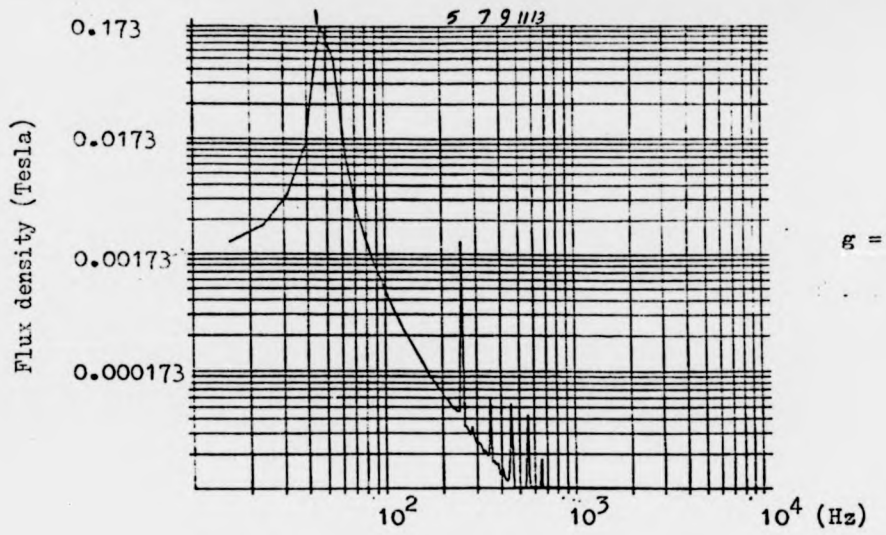

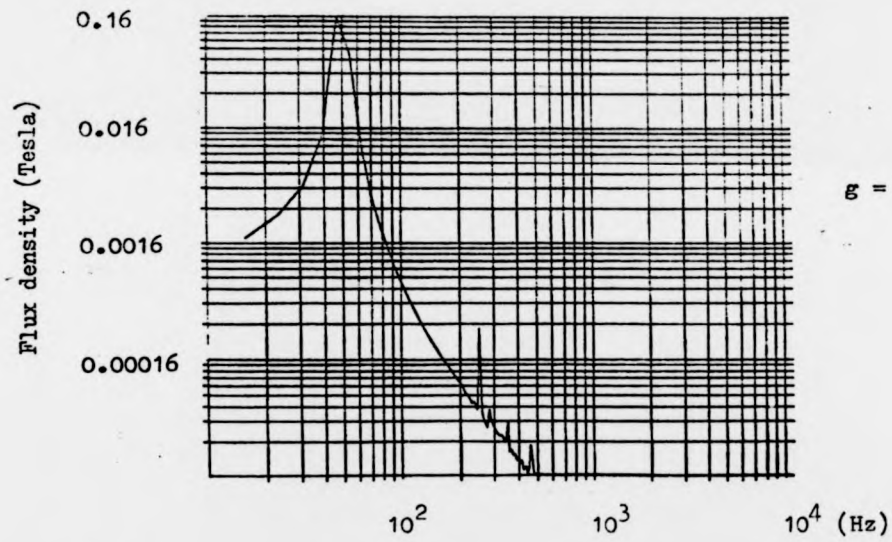

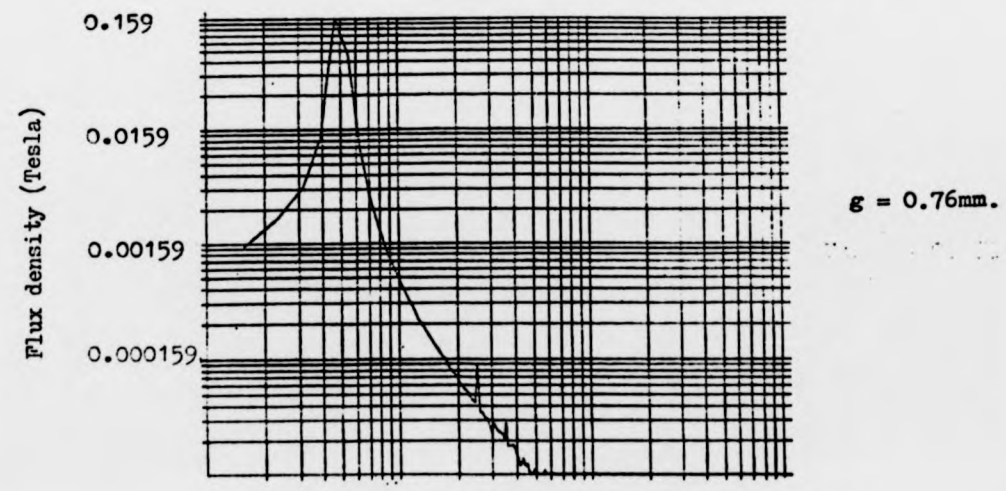

Fig.(3.7d) - Waveform analysis of the core flux at different gaps

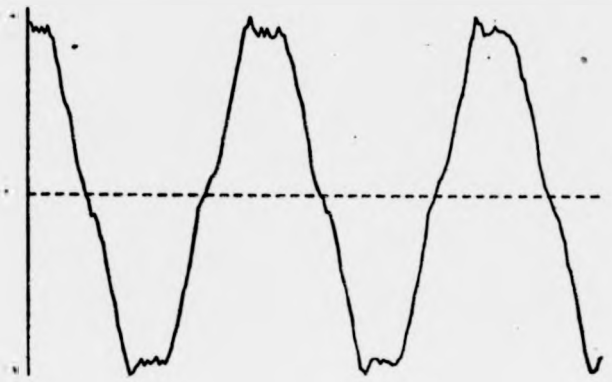

Pole flux waveform
at g = 0

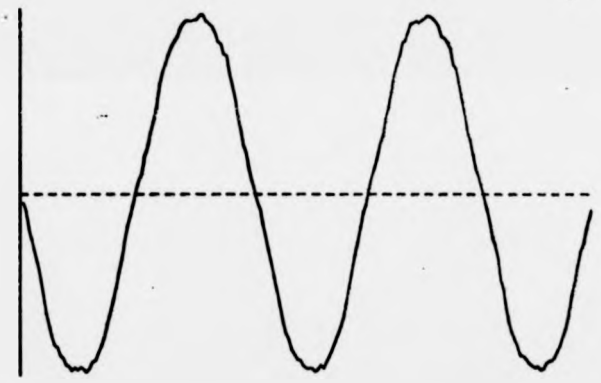

g = 0.45mm

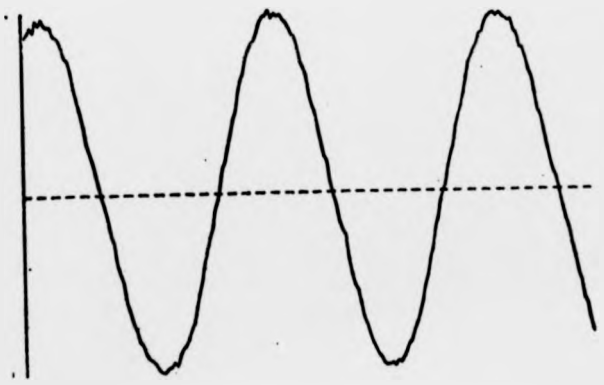

g = 0.76mm

Fig. (3.7c) - Smoothing effect of air gap reluctance on the pole flux, search coil 4.

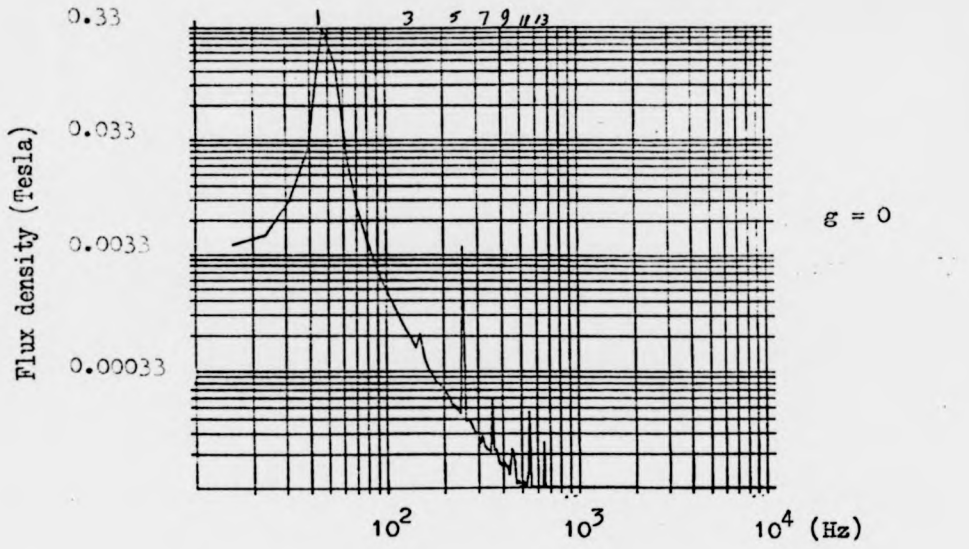

Fig.(3.7f) - Waveform analysis of the full pole pitch flux at different gaps

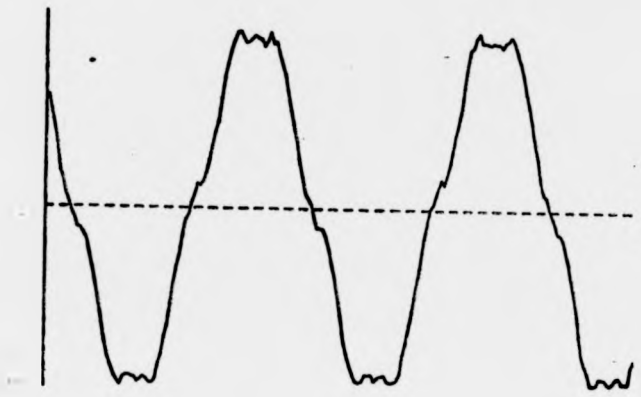

Pole flux waveform at
$\theta = 15^{\circ}$

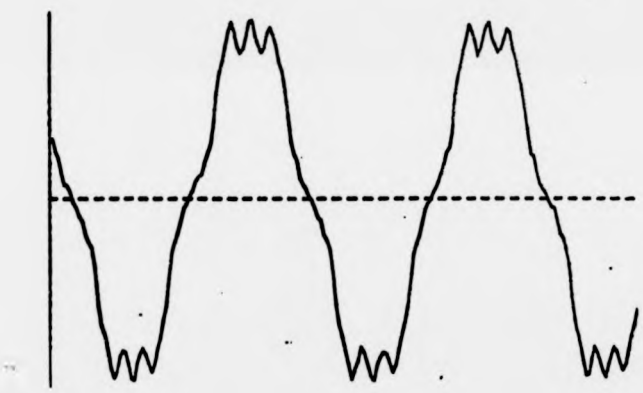

$\theta = 30^{\circ}$

$\theta = 45^{\circ}$

Fig.(3.8a) - Pole flux waveform at different misalignments (g = 0), search coil 4.

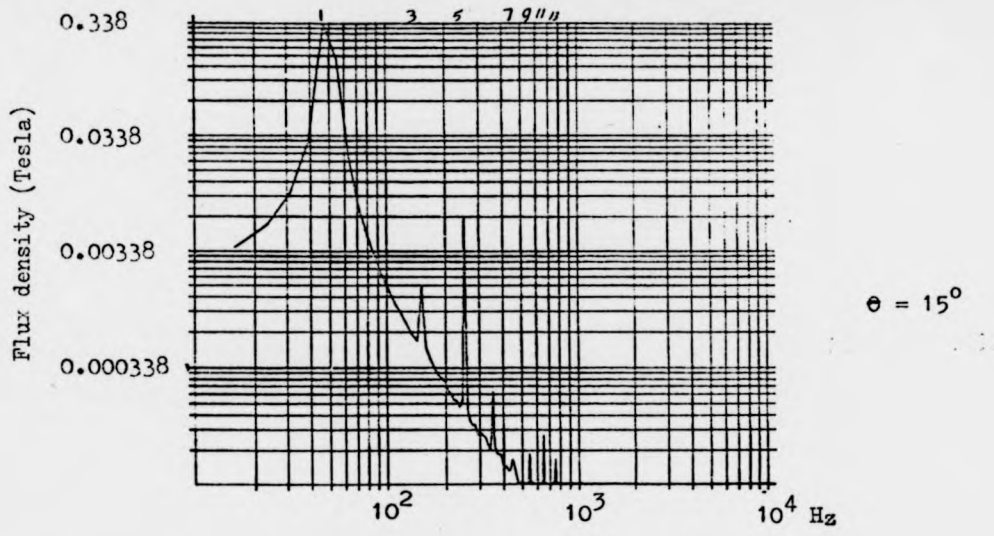

Fig.(3.8b) - Effect of the stator misalignment (θ) on the air-gap flux harmonic content (ε=0)

The experiment showed that the perfect alignment is the position at which a north pole of one stator opposes a south pole of the other with the current and harmonics in the machine kept as small as possible. Fig.(3.7f) shows that harmonics in a pole pitch search coil when the stator are in perfect alignment and different gaps separate them with average phase input current of 0.68A at zero air gap lenth. Results of fig.(3.8) indicate that the harmonics increase sharply with the misalignment and so do the input currents. It was found that the minimum current position occurs at an alignment little different from the minimum harmonic position. It is decided therefore to use a position which gives both negligible harmonics and small balanced currents and this is the perfect aligned position. The harmonic in the resultant flux waveforms at the gap depends on the reaction between the magnetic circuit of the two stators. In the perfect alignment position the two waveforms are moving in phase giving rise to a resultant sinusoidal flux waveform. The misaligning of the stators causes the two waveforms to move out of phase with respect to each other by the misaligning angle arising in a waveform which is non-simusoidal.

3.5 Fundamental Checkings

Before starting the harmonic measurements a number of checkings were made as shown below:

(a) The harmonics in the source voltage waveforms feeding the phases of the machine were checked by connecting two resistors of 23.3 KΩ and 0.2 KΩ in series across each two phases and the voltage waveform across the 0.2 KΩ resistor is analysed and the highest harmonic found to be less than 1% of the fundamental.

(b) The current balance of the source is checked by feeding the three phases into a circuit of three equal resistors(150Ω each) connected in delta through a three phase variac. Three ammeters connected between the variac and the resistors indicated currents of 1.46, 1.43, 1.45A.

(c) The current balance in the machine is checked by replacing the resistive loop in "b" by the three phases of the machine. The respective phases in the stators are connected in series and the final phases are star connected. The two stators perfectly aligned at zero air-gap and the currents recorded at the phases were 0.68, 0.65, 0.71A.

By carrying out such tests it is possible to segregate the machine's harmonics from those caused by external sources.

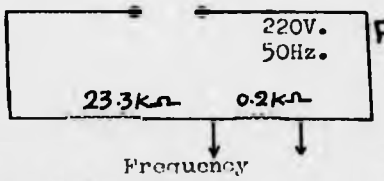

Fig.3.9a-Harmonic content of the mains waveform.

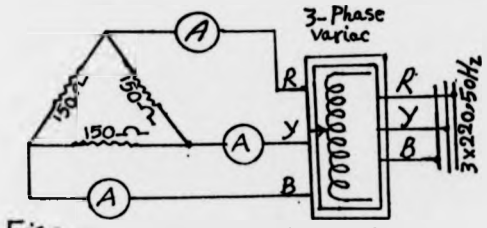

Fig.3.9b - Current balance in a three arms balanced resistive loop.

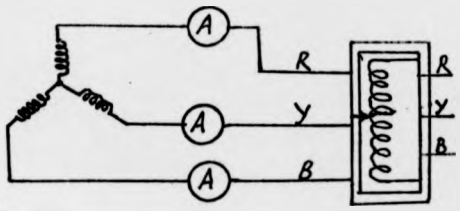

Fig.3.9c - Current balance in the three phases of the experimental machine.

CHAPTER 4

Air gap flux and equivalent circuit

4.1 Conformal transformation

To understand a machine closely it is essential to make a close study of the conditions under which the flux exists in the air-gap. This air-gap is usually a complex boundary such that it is not possible to use simple analytical methods to solve for the flux. The analytical method of conformal transformation is the most powerful method to use for field analysis of different boundary shapes.

The Schwarz- Christoffel transformation (SCT)ref1.1,used in this work, applies to problems having closed polygon boundaries. The solution for the field starts with mapping the actual configuration of the air-gap in the Z-plane where the flux and equipotential lines are not regular, straight and parallel, to a portion of a uniform rectangular field in a complex plane called the ζ-plane. The difficulty in this type of configuration, depends largely on the configuration's boundaries to be mapped, and mainly the number of right angles contained, since it is a technique involving right angles straightened up. It is found that two right angles is the maximum number of right angles which can exist in a configuration which involves no elliptic functions in the transformation, but only circular or hyperbolic functions. But when more than two right angles have to be straightened out, the integration may be a combination of elementary and elliptic functions of one of three kinds.

4.1.1 The transformation

The developed diagram of the induction machine to be mapped is shown in fig.(4.1) in the stator-rotor-stator configuration. It consists of two stators, each having a succession of completely open slots on each side of the rotor. The rotor is considered as a smooth plane surface opposing the

Fig.(4.1) - Conformal transformation

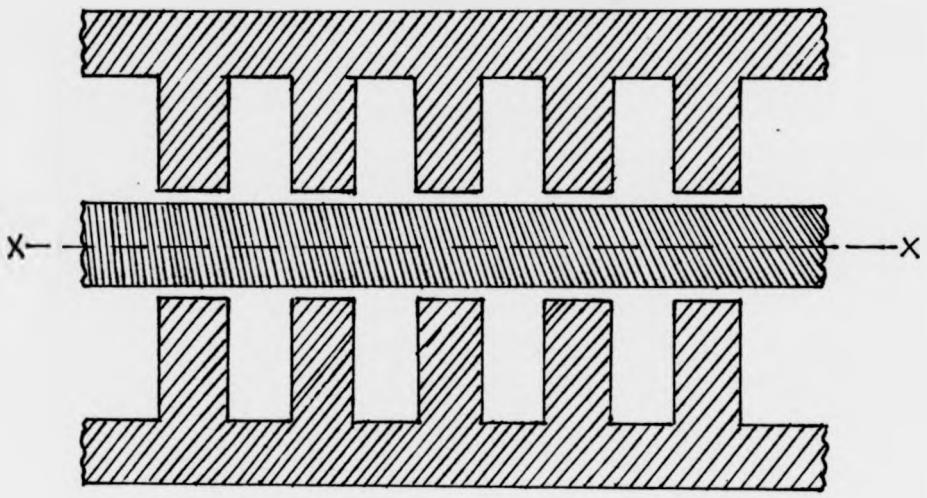

a - Developed diagram of the induction machine

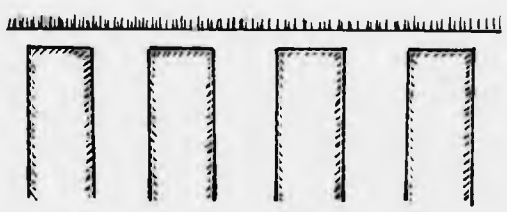

b - One side of the machine with infinite slot depth

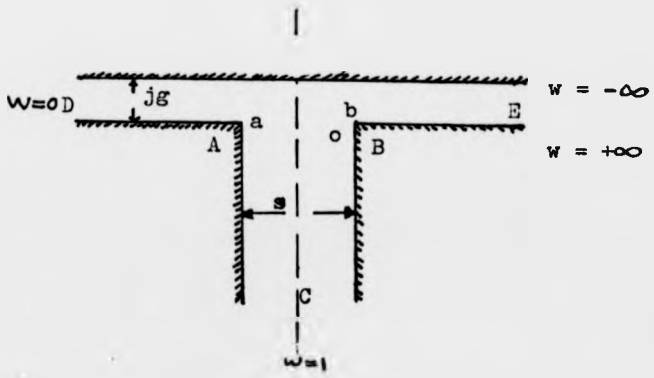

c - Single slot in the Z - Plane

slots. For the purpose of this transformation it is assumed that the slots are infinitely deep and only one slot has to be considered.

Fig.(4.2) by Coe(4.2) shows the variation of the flux-density at the centre of a slot bottom with the ratio d/s (slot depth/slot width) for values of (s/g) as parameters. The figure shows clearly that the flux drops sharply at the slot centre as d/s increases and it diminshes when this ratio increases above unity. It also shows that the drop in the flux gets sharper as the ratio s/g increases. Therefore, the first assumption is valid as long as the ratio of the slot depth to width is greater than unity (>2 in the experimental machine). The second assumption exists in most electrical machines where the air-gap is small compared with the width of an open slot.

Due to the symmetry of the machine about the xx-axis, only one half of the figure has to be considered as in fig (4.1b). Applying the first assumption, the configuration to be mapped is shown in fig.(4.1c). It consists of five corners with only two at A and B rectangular. After assigning values of w at E and D, there are remaining three more corners where values of w have to be fixed. Corners A and B can have arbitrary values 'a' and 'b' with corner C having w = 1. It is to be noticed that 'a' is between w = 0 and w = 1 and 'b' is between w = 1 and w = $+\infty$. Fig.(4.1c) - becomes a closed polygon by joining the ends at D and C where w = 0 and w = 1, having five vertices ABCDE with corresponding angles, $3\pi/2$, $3\pi/2$,0,0 to be opened at E. Using SCT, the equation of transformation from the Z-plane to the upper half of the W-plane is given by:

$$\frac{dZ}{dw} = \bar{A}\,\frac{(w-a)^{\frac{1}{2}}\,(w-b)^{\frac{1}{2}}}{w(w-1)} \qquad \text{.....4.1}$$

4.1.2 Determination of the constants

The constants $\bar{A}$, a, and b can be found by crossing the air-gap at certain points in the Z-plane. This is equivalent in the W-plane to the

Fig.(4.1) - continue

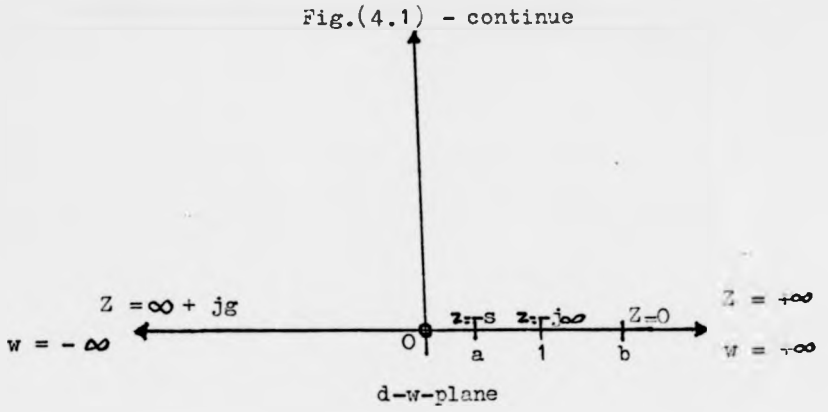

d-w-plane

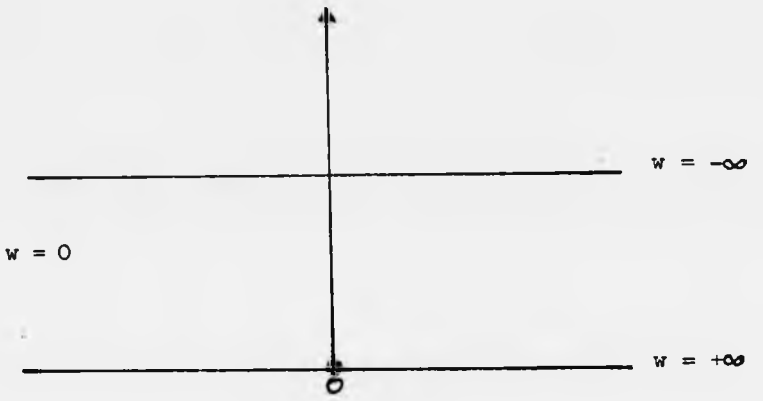

e - χ - Plane

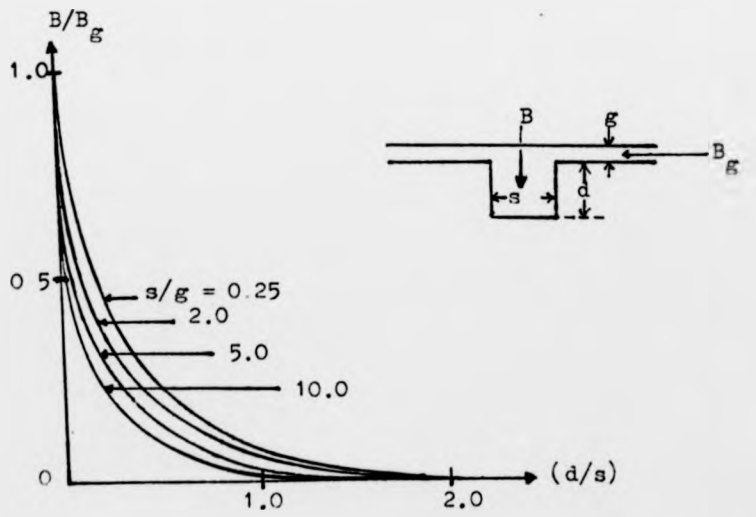

Fig.(4.2) - Flux density at the centre of a slot of finite depth by Coe, (analytical).

integration along large or small semicircles of a certain radius since this is a plane of semicircles. Crossing the air-gap as $Z \Rightarrow \infty$ is equal to the constant value of the air-gap length g including the direction. In the W-plane this is the integration along a large semicircle, ref.4.1;

$$w = Re^{j\theta} \qquad \text{and} \qquad dw = jRe^{j\theta}\, d\theta$$

Substituting these values in equation(4.1), gives:

$$dZ = \bar{A}\,\frac{(Re^{j\theta} - a)^{\frac{1}{2}}\,(Re^{j\theta} - b)^{\frac{1}{2}}}{Re^{j\theta}\,(Re^{j\theta} - 1)}\, jRe^{j\theta}\, d\theta$$

But as $R \Rightarrow \infty$ $\qquad Z \Rightarrow jg$ and

$$\bar{A} = \frac{g}{\pi} \qquad \ldots\ldots\ldots\ldots\ldots\ldots\ldots\ldots 4.2a$$

In the same manner crossing the air-gap as $Z \Rightarrow -\infty$ is equal to g and in the W-plane is equivalent to the integration along a small semicircle:

$$w = re^{j\theta} \qquad \text{and} \qquad dw = jre^{j\theta}\, d\theta \qquad \text{giving that;}$$

$$ab = 1 \qquad \ldots\ldots\ldots\ldots\ldots\ldots\ldots\ldots 4.2b$$

Substituting $\bar{A}$ in equation(4.1) gives:

$$dZ = \frac{g}{\pi}\,\frac{(w - a)^{\frac{1}{2}}\,(w - b)^{\frac{1}{2}}}{w(w - 1)}\, dw$$

The solution for this equation is obtained as follows:

$$\text{Let} \quad P^2 = \frac{(w - b)}{(w - a)} \qquad \ldots\ldots\ldots\ldots\ldots\ldots\ldots\ldots 4.2c$$

Therefore,

$$Z = \frac{2g}{\pi}\,\frac{(b + 1)^2\,(b - 1)\,P^2}{(1 - P^2)\,(b^2 - P^2)(b + P^2)}\, dP$$

Using the method of partial fractions and with the help of Dwights' tables, ref.43;

$$Z = \frac{g}{\pi}\left(\ln\left|\frac{1 + P}{1 - P}\right| - \ln\left|\frac{b + P}{b - P}\right| - 2\,\frac{(b - 1)}{\sqrt{b}} \cdot \tan^{-1}\frac{P}{\sqrt{b}}\right) \ldots\ldots 4.3$$

integration along large or small semicircles of a certain radius since this is a plane of semicircles. Crossing the air-gap as $Z \Rightarrow \infty$ is equal to the constant value of the air-gap length g including the direction. In the W-plane this is the integration along a large semicircle, ref.4.1;

$$w = Re^{j\theta} \qquad \text{and} \qquad dw = jRe^{j\theta}\, d\theta$$

Substituting these values in equation(4.1), gives:

$$dZ = \bar{A}\,\frac{(Re^{j\theta} - a)^{\frac{1}{2}}\,(Re^{j\theta} - b)^{\frac{1}{2}}}{Re^{j\theta}\,(Re^{j\theta} - 1)}\, jRe^{j\theta}\, d\theta$$

But as $R \Longrightarrow \infty$ $\qquad Z \Longrightarrow jg$ and

$$\bar{A} = \frac{g}{\pi} \qquad \ldots\ldots\ldots\ldots\ldots\ldots\ldots\ldots 4.2a$$

In the same manner crossing the air-gap as $Z \Longrightarrow -\infty$ is equal to g and in the W-plane is equivalent to the integration along a small semicircle:

$$w = re^{j\theta} \qquad \text{and} \qquad dw = jre^{j\theta}\, d\theta \qquad \text{giving that;}$$

$$ab = 1 \qquad \ldots\ldots\ldots\ldots\ldots\ldots\ldots\ldots 4.2b$$

Substituting $\bar{A}$ in equation(4.1) gives:

$$dZ = \frac{g}{\pi}\,\frac{(w - a)^{\frac{1}{2}}\,(w - b)^{\frac{1}{2}}}{w(w - 1)}\, dw$$

The solution for this equation is obtained as follows:

$$\text{Let} \quad P^2 = \frac{(w - b)}{(w - a)} \qquad \ldots\ldots\ldots\ldots\ldots\ldots\ldots\ldots 4.2c$$

Therefore,

$$Z = \frac{2g}{\pi}\,\frac{(b + 1)^2\,(b - 1)\,P^2}{(1-P^2)\,(b^2 - P^2)(b+P^2)}\, dP$$

Using the method of partial fractions and with the help of Dwights' tables, ref.43;

$$Z = \frac{g}{\pi}\left(\ln\left|\frac{1 + P}{1 - P}\right| - \ln\left|\frac{b + P}{b - P}\right| - 2\,\frac{(b - 1)}{\sqrt{b}} \cdot \tan^{-1}\frac{P}{\sqrt{b}}\right) \ldots\ldots 4.3$$

The constant of integration is equal to zero by choosing the origin such that P = 0 at that point. From equation (4.3) when P = 0, Z is also zero, but w = b indicating that the origin in the Z-plane is at the point B. Values of b and a can be found by substituting w = a in equation (4.2c) giving that P = ∞ and putting this value in equation (4.3) gives:

$$Z = \frac{g}{\pi}\left(-2\frac{(b-1)}{\sqrt{b}}\pi\right), \text{ But at } w = a \quad Z = -s + o \text{ (Fig.4.1c)}$$

$$\text{Therefore} \qquad \frac{b-1}{\sqrt{b}} = s/g$$

Solving this equation for b gives:

$$b = \frac{(2 + (s/g)^2) + \sqrt{(2 + (s/g)^2)^2 - 4}}{2} \quad \ldots\ldots\ldots\ldots\ldots 4.4$$

4.1.3 Slot flux-density distribution

The transformation from the W-plane where the field is shown to be circular to the χ-plane where the field is regular and parallel, ref.4.1, given by;

$$\chi = \frac{\bar{V}}{\pi}\log w \quad \ldots\ldots\ldots\ldots\ldots\ldots 4.5$$

where $\bar{V}$ is the potential difference between two surfaces to be considered. The flux density at any point between these two surfactes is given by:

$$B = \mu_o \left|\frac{d\chi}{dz}\right|$$

By using the mathematical chain-rule it is possible to show that:

$$B = \frac{\mu_o \bar{V}}{g}\left|\frac{(w-1)}{(w-a)^{\frac{1}{2}}(w-b)^{\frac{1}{2}}}\right| \quad \ldots\ldots\ldots\ldots 4.6a$$

The maximum value of this flux occurs at the air-gap "g" towards the corners D and E of fig.(4.1c) where w = 0 and $\pm\infty$ giving uniform flux density ($B_{max} = \mu_o \frac{\bar{V}}{g}$)

The flux density at any point is therefore given by;

$$B = \left|\frac{(w-1)}{(w-a)^{\frac{1}{2}}(w-b)^{\frac{1}{2}}}\right| B_{max} \quad \ldots\ldots\ldots\ldots 4.6b$$

The full curve in Fig.(4.3) shows the flux density in the slot according to the above equation.

The constant of integration is equal to zero by choosing the origin such that P = 0 at that point. From equation (4.3) when P = 0, Z is also zero, but w = b indicating that the origin in the Z-plane is at the point B. Values of b and a can be found by substituting w = a in equation (4.2c) giving that P = ∞ and putting this value in equation (4.3) gives:

$$Z = \frac{g}{\pi}\left(-2\frac{(b-1)}{\sqrt{b}}\pi\right), \text{ But at } w = a \quad Z = -s + o \text{ (Fig.4.1c)}$$

$$\text{Therefore} \qquad \frac{b-1}{\sqrt{b}} = s/g$$

Solving this equation for b gives:

$$b = \frac{(2 + (s/g)^2) + \sqrt{(2 + (s/g)^2)^2 - 4}}{2} \quad \ldots\ldots\ldots\ldots\ldots 4.4$$

4.1.3 Slot flux-density distribution

The transformation from the W-plane where the field is shown to be circular to the χ-plane where the field is regular and parallel, ref.4.1, given by;

$$\chi = \frac{\bar{V}}{\pi}\log w \quad \ldots\ldots\ldots\ldots\ldots\ldots 4.5$$

where $\bar{V}$ is the potential difference between two surfaces to be considered. The flux density at any point between these two surfactes is given by:

$$B = \mu_o \left|\frac{d\chi}{dz}\right|$$

By using the mathematical chain-rule it is possible to show that:

$$B = \frac{\mu_o \bar{V}}{g}\left|\frac{(w-1)}{(w-a)^{\frac{1}{2}}(w-b)^{\frac{1}{2}}}\right| \quad \ldots\ldots\ldots\ldots 4.6a$$

The maximum value of this flux occurs at the air-gap "g" towards the corners D and E of fig.(4.1c) where w = 0 and $\pm\infty$ giving uniform flux density ($B_{max} = \mu_o \frac{\bar{V}}{g}$)
The flux density at any point is therefore given by;

$$B = \left|\frac{(w-1)}{(w-a)^{1/2}(w-b)^{1/2}}\right| B_{max} \quad \ldots\ldots\ldots\ldots 4.6b$$

The full curve in Fig.(4.3) shows the flux density in the slot according to the above equation.

The amount of the drop of the flux at the slot is given by (ref.4.1) as:

$$\phi_1 = \int_{-\infty}^{+\infty} (B_{max} - B)\, dx$$

Using equations 4.6b and 4.1 in the above integration and with the help of Fig.(4.1d) it is possible to show that;

$$\phi_1 = \frac{g}{\pi} \int_{0}^{-\infty} \left(\frac{(w-1)^{\frac{1}{2}} (w-b)^{\frac{1}{2}}}{w(w-1)} \right) dw$$

Substituting equation 4.2c in the above equation and integrating gives;

$$\phi_1 = \frac{2g}{\pi} \left(\frac{(b-1)}{\sqrt{b}} \left(\tan^{-1}\sqrt{b} - \tan^{-1}\frac{1}{\sqrt{b}}\right) - \ln \frac{(b+1)^2}{4b} \right) B_{max} \quad \ldots 4.6$$

where,

$$\tan^{-1}\sqrt{b} - \tan^{-1}\frac{1}{\sqrt{b}} = \tan^{-1}\left(\frac{s}{2g}\right)$$

and

$$\frac{(b+1)^2}{4b} = 1 + \frac{s^2}{4g^2}$$

Therefore equation (4.6c) becomes:

$$\phi_1 = g\gamma B_{max} \quad \ldots\ldots\ldots\ldots\ldots\ldots 4.7a$$

where,

$$\gamma = \frac{4}{\pi}\left(\left(\frac{s}{2g}\right)\tan^{-1}\left(\frac{s}{2g}\right) - \ln\left(1 + \frac{s^2}{4g^2}\right)^{\frac{1}{2}}\right) \quad \ldots\ldots\ldots\ldots 4.7b$$

The flux in a slot pitch $(t + s)$ is therefore reduced from the uniform value of $(t + s)B_{max}$ for a smooth air-gap to a new value $(t + s - \gamma g)B_{max}$ for the slotted gap, and the ratio between these two fluxes is known as the Carter coefficient given by:

$$K_c = \frac{(t+s)}{(t+s-\gamma g)} > 1 \quad \ldots\ldots\ldots\ldots\ldots 4.8a$$

The amplitude of the flux drop at the centre of the slot is given by:

$$B_c = 2\beta B_{max} \quad \ldots\ldots\ldots\ldots\ldots\ldots\ldots\ldots 4.8b$$

where,

$$\beta = \left(0.5 - \frac{\sqrt{b}}{(1+b)}\right) \quad \ldots\ldots\ldots\ldots\ldots\ldots 4.8c$$

Values of β as function of s/g have been plotted in fig.(4.4) using equations (4.4) and (4.8c).

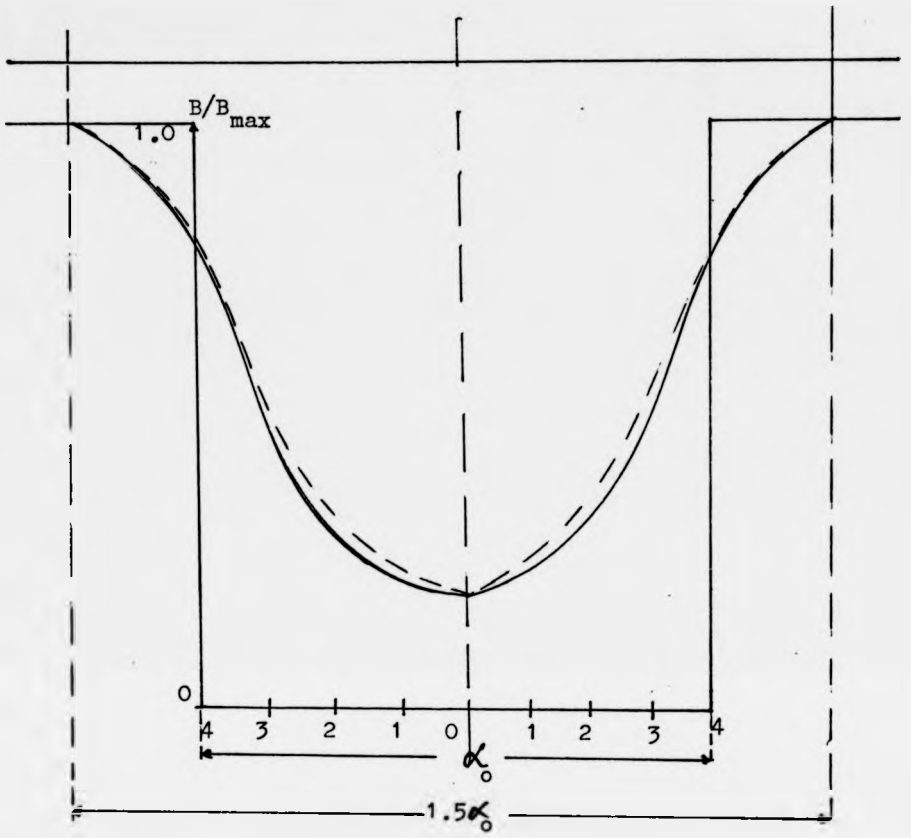

Fig.(4.3) - Flux drop curve at the slot.
Full curve - Conformal transformation
Dashed curve - Heller's formula

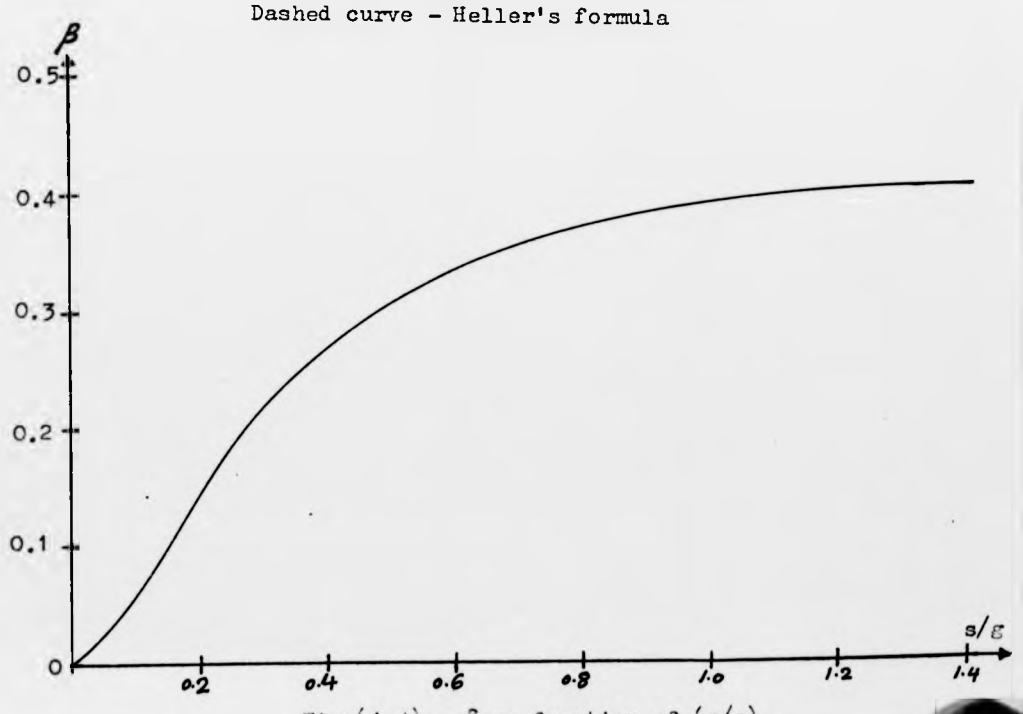

Fig.(4.4) - β as function of (s/ε)

4.1.4 Magnetic air gap conductance

It is shown in fig.(4.3) that the slot opening in the machine affects the magnetic distribution up to $0.75\alpha_o$ from the centre of the slot where α_o is the slot opening angle and it stays uniform above this angular distance. Using Hellers formula, ref.4.4, the magnetic induction density over the slot pitch in terms of the angular displacement can be approximated as:

$$B(\alpha) = (1 - \beta - \beta \cos \frac{\pi\alpha}{0.75\alpha_o}) B_{max} \qquad 0 < \alpha < 0.75\alpha_o \ldots\ldots 4.9a$$

$$B(\alpha) = B_{max} \qquad 0.75\alpha_o \leq \alpha < \alpha_d \ldots\ldots 4.9b$$

where α_d is the slot pitch angle, and β is defined in 4.8.C;

$$\alpha_o = \frac{2s}{D} \quad (\text{rad./sec.})$$

$$\alpha_d = \frac{2(t + s)}{D} \qquad \text{for any diameter D.}$$

The mean magnetic induction density over the slot pitch using these values of induction is given by:

$$B_s = \frac{2}{\alpha_d} \int_0^{0.5\alpha_d} B d\alpha$$

Therefore $$B_s = \frac{(t + s) - 1.5\beta s}{(t + s)} \cdot B_{max}$$

giving a new expression for the Carter coefficient as:

$$K_c = \frac{(t + s)}{(t + s) - 1.5\beta s} \ldots\ldots\ldots\ldots\ldots\ldots 4.10$$

The flux density of a smooth air-gap between rotor and stator is given by:

$$B = \frac{\text{Magnetic potential difference}}{g}$$

But when the air-gap is not smooth, that is when one side of the air-gap or both are slotted, the air-gap is no longer uniform and the flux density is given by:

$$B(\alpha) = \frac{1}{g(\alpha)} = f(\alpha)$$

assuming unit magnetic potential difference.

The function $f(\alpha)$ is a periodic function with a period of α_d and has the values given in equation 4.9. If the number of the stator slots is z and the origin is taken at the stator slot axis, this function can be written in the Fourier series form as:

$$f(\alpha) = a_o - \sum_{n=1}^{\infty} a_n \cos nz\alpha \quad \text{.....4.11a}$$

where $$a_o = \frac{2}{\alpha_d} \int_0^{0.5\alpha_d} f(\alpha)\, d\alpha$$

$$a_n = \frac{4}{\alpha_d} \int_0^{0.5\alpha_d} f(\alpha) \cos \frac{n\pi\alpha}{\alpha_d/2}\, d\alpha$$

Therefore,

$$a_o = \frac{2}{\alpha_d} \left(\int_0^{0.75\alpha_o} (1-\beta-\beta \cos \frac{\pi\alpha}{0.75\alpha_o})\, d\alpha + \int_{0.75\alpha_o}^{0.5\alpha_d} d\alpha \right) \cdot B_{max}$$

$$a_n = \frac{4}{\alpha_d} \left(\int_0^{0.75\alpha_o} (1-\beta-\beta \cos \frac{\pi\alpha}{0.75\alpha_o}) \cos \frac{2n\pi\alpha}{\alpha_d}\, d\alpha + \int_{0.75\alpha_o}^{0.5\alpha_d} \cos \frac{2n\pi\alpha}{\alpha_d}\, d\alpha \right) \cdot B_{max}$$

giving that

$$a_o = 1/K_c \cdot g \qquad (\text{since } B_{max} = 1/g)$$

$$a_n = \frac{\beta}{g} F_n(\alpha_o/\alpha_d)$$

where,

$$F_n(\alpha_o/\alpha_d) = \frac{1}{n} \frac{4}{\pi} \left(0.5 + \frac{(n\alpha_o/\alpha_d)^2}{(0.9 - 2(n\alpha_o/\alpha_d)^3}\right) \sin 1.5\pi(n\frac{\alpha_o}{\alpha_d}) \quad \text{..4.11b}$$

Substituting these values in equation 4.11a, gives that:

$$f(\alpha) = \left(\frac{1}{K_c \cdot g} - \frac{\beta}{g} \sum_{n=1}^{\infty} F_n \cos nz\alpha\right)$$

But $f(\alpha) = \frac{1}{g(\alpha)}$ is the magnetic conductance.

The magnetic conductance of the air-gap is therefore given by:

$$\frac{1}{g(\alpha)} = \frac{1}{g}\left(\frac{1}{K_c} - \beta\sum_{n=1}^{\infty} F_n \cos nz\alpha\right) \quad \ldots\ldots\ldots\ldots 4.11c$$

4.2 Effective air gap length

The reduction in the air-gap flux can also be explained in terms of the increase in the physical air-gap length "g" due to slotting to a larger air-gap length known as the effective or magnetic air-gap length. This new air-gap length is given by:

$$\bar{g} = K_c g \quad \ldots\ldots\ldots\ldots\ldots 4.12a$$

β is shown to be constant for a given value of "s/g", equation 4.8c, therefore Kc depends on the tooth to slot ration "s/t".

In radial air-gap machines this ratio is constant along the active length of the machine. In the experimental machine however the slot width is made constant along machine's active length in the radial direction, but the tooth width is varying from a minimum at D_1 to its largest value at D_2. Therefore the ratio t/s is varying as a function of the radius and consequently causing K_c in equation 4.10 to vary as follows:

$$\text{since} \quad (t + s) = \frac{2\pi R}{z}$$

$$\text{From equation 4.10} \quad K_c = \frac{2\pi R/z}{\frac{2\pi R}{z} - 1.5\,s}$$

$$= \frac{2\pi R}{2\pi R - 1.5 z \beta s}$$

Therefore to calculate the effective air-gap length and to account for such a variation, the average value of the air-gap length has to be found as:

$$\bar{g} = \frac{2}{(D_2 - D_1)} \int_{D_1/2}^{D_2/2} K_c . g . dR$$

$$\mathcal{G} = \frac{2\pi}{(D_2 - D_1)} \int_{D_1/2}^{D_2/2} \frac{2\pi R}{2\pi R - 1.5z\beta s} dR$$

giving that $\bar{g} = K_{ce} \cdot g$

Where the effective Carter coefficient is given by:

$$K_{ce} = \left(1 + \frac{(1.5z\beta s)}{\pi(D_2 - D_1)} \ln \frac{(\pi D_2 - 1.5z\beta s)}{(\pi D_1 - 1.5z\beta s)}\right) \quad \ldots\ldots\ldots 4.12b$$

The second term in this equation represents the amount of the increase in the air-gap length through the factor β which is a function of s/g. For a closed or semiclosed slot machine β is very small and therefore this factor falls to zero in the above equation making the effective Carter Coefficient almost equal to unity.

In the present machine the ratio s/g is quite large due to the requirement of the stator open slots and consequently the effective Carter Coefficient is expected to be much higher than unity. Fig.(4.5a) shows the variation of Carter Coefficient as a function of the machine's diameter for values of the physical air-gap length as parameter. Fig.(4.5b) shows the average Carter Coefficient as a function of the slot opening for a given machine diameter.

4.3 Air-gap Permeance

The two stators of the experimental machine are designed with the slots completely open. Therefore in any flux calculation it is essential to include the deviation of the gap permeance from being uniform due to the slotting. Fig.(4.6) shows a portion of the air-gap "$R\delta R\delta\alpha$" having a rectangular shape of radial length dR at radius R from the centre subtending an angle $d\alpha$. The permeance of this element per unit machine's active length is given by

$$dP_r = \frac{\mu_o . R . dR . d\alpha}{g(\alpha)}$$

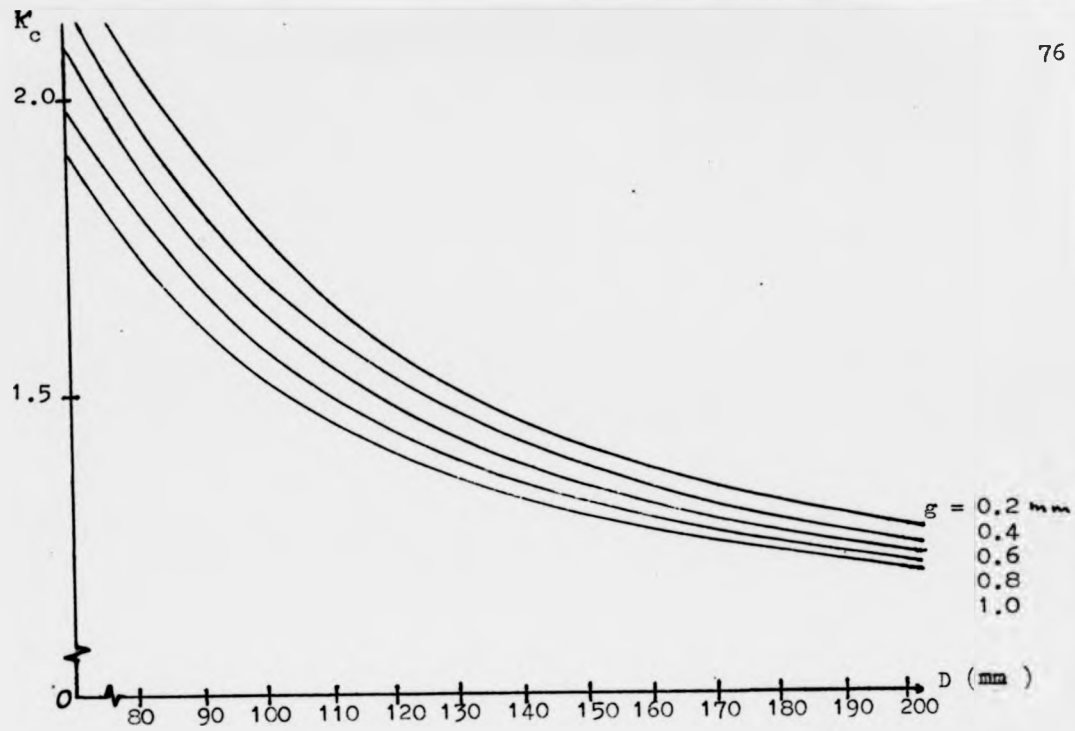

Fig (4.5a) - Carter's coefficient as a function of the machine diameter for different values of air-gap.

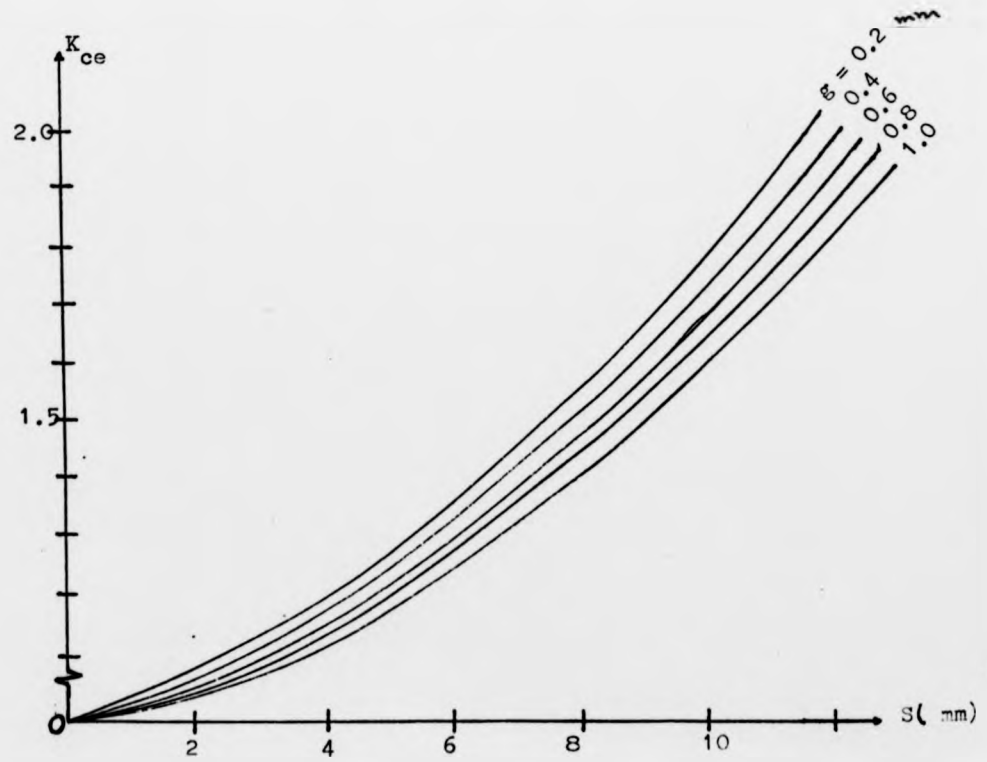

Fig.(4.5b) - Average Carter's coefficient as a function of machine's slot-opening for different values of air-gap.

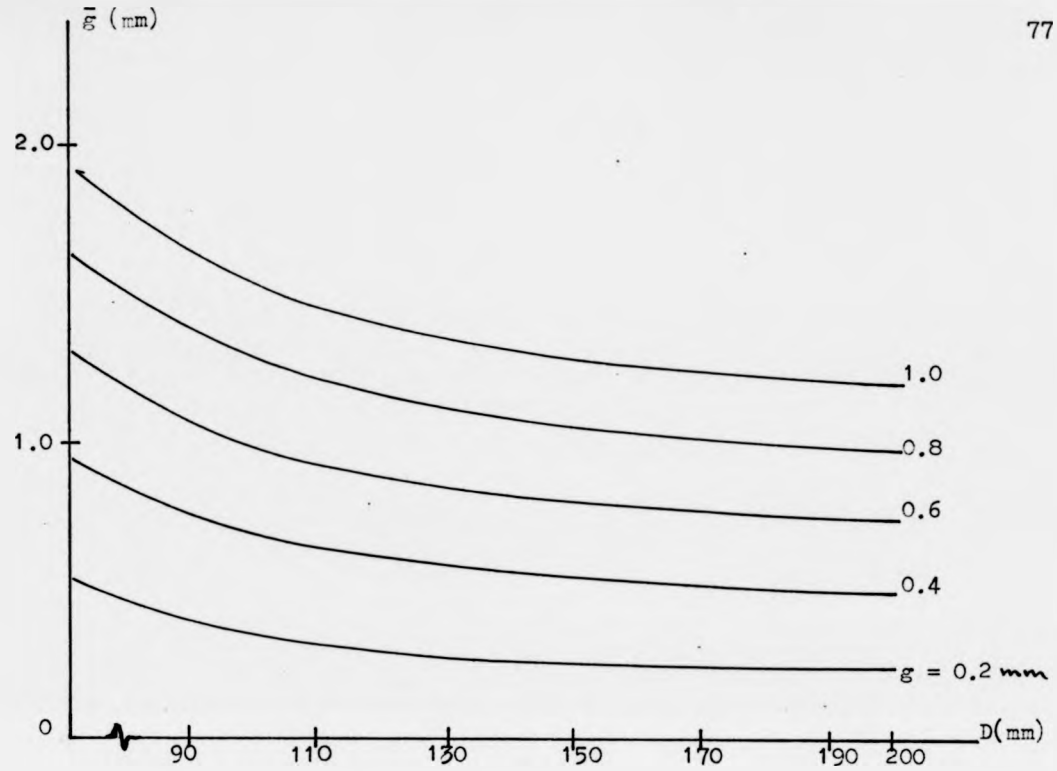

Fig.(4.5c) - Magnetic air-gap as a function of the machine's diameter for different air-gaps.

Table(4.1) - Values of F for the harmonics up to the fifth

$\alpha_o/\pi d$ $s/(s+t)$	1	2	3	4	5
0.1	0.295	0.282	0.262	0.235	0.203
0.2	0.564	0.47	0.328	0.221	0.0023
0.3	0.786	0.492	0.236	0.0425	-0.023
0.4	0.94	0.443	0.0576	-0.0323	0
0.5	0.9995	0.260	-0.0375	0	0.00175
0.6	0.9836	0.085	-0.0277	0.0128	-0.0067
0.7	1.12	-0.293	0.0109	-0.0056	0.00342
0.8	0.886	-0.0646	0.0164	-0.00423	0
0.9	0.709	-0.0415	-0.00218	0.00545	-0.00205
1.0	0.5207	0	-0.112	0	0.00231

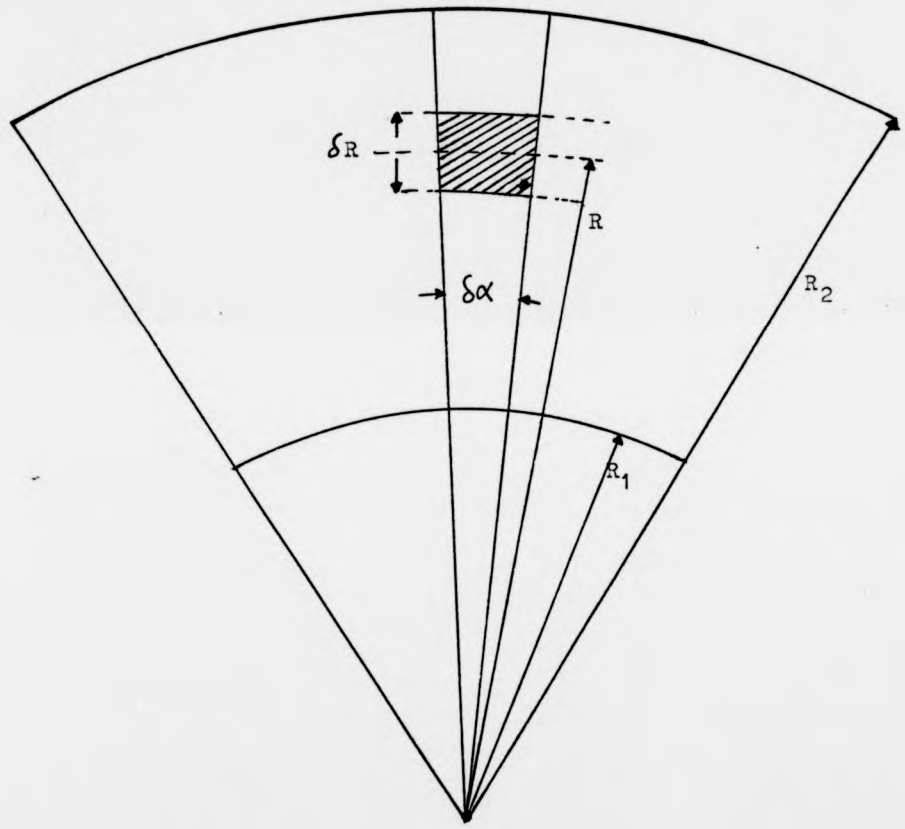

Fig.(4.6) - Element R.δR.δα of the air-gap

where

$$\frac{d\alpha}{g(\alpha)} = \frac{1}{g}\left(\frac{1}{K_c} - \beta \sum_{n=1}^{\infty} F_n \cos nz\alpha\right)$$

and g is the physical air gap of the machine(sum of both sides).

Therefore,

$$dP_r = \frac{\mu_o}{g}\left(\frac{1}{K_c} - \beta \sum_{n=1}^{\infty} F_n \cos nz\alpha\right) RdR$$

The total permeance can be obtained by integrating this equation between the limits $D_1/2$ and $D_2/2$, giving:

$$P_r = \frac{\mu_o(D_2^2 - D_1^2)}{8g}\left(\left(1 - \frac{3\beta_{zs}}{\pi(D_2 + D_1)}\right) - \beta \sum_{n=1}^{\infty} F_n \cos nz\alpha\right) \quad \ldots.4.13$$

4.4 Air-gap flux

Since the practical machine is operating in the additive mode, the mmfs of the two stators are adding together and the magnetic circuit is similar to that in radial machines, with one difference that the flux lines cross the air gap four times to complete one magnetic circulation. The derivation of an expression which can represent the actual gap flux as near as possible is an essential task in machine analysis since the performance equations of any machine depend fully on the air-gap flux.

The analysis is similar to that employed by Gupta and Capaldi(4.5,1.5), in that it depends on the principle that the air-gap flux can be expressed as the product of the permeance of the gap with the mmf acting across it between the two stators. In the analysis the following general idealisations are made:

1. The iron laminations exhibit infinite permeability, hence the magnetic circuit is linear and effect of hystersis in the flux distribution is negligible.
2. The currents in each slot are concentrated at the intersection of the slot centre line and the stator surface.

3. The effect of slotting is included by calculating the resultant conductance of the air-gap.
4. Flux crosses the air-gap axially in straight lines and continues circumferentially in the stators.
5. Due to the machine's construction, the magnetic surfaces of the rotor and stators are parallel.
6. Since the machine is double sided, the flux is crossing the gap twice at each side giving rise to a larger effective air-gap in this type of machines.

Therefore multiplying equation(4.13) by equation(3.5) term by term gives the air-gap flux as a function of time and the angle α. This angle represents any position in the air-gap relative to the stator slot centre axis of phase A carrying the current Icoswt.

The air-gap flux is therefore:

$$\phi_\alpha = \frac{\mu_o(D_2^2 - D_1^2)}{8g}\left((1 - \frac{3\beta zs}{\pi(D_2+D_1)}) - \beta\sum_{n=1}^{\infty} F_n \cos nz\alpha \right)\cdot$$

$$\frac{6\bar{N}I}{\pi}\left(K_1\cos(p\alpha - wt) \pm \sum_{k=1}^{\infty} K_{6k\pm1}\cos((6k\pm1)p\alpha \pm wt)\right)$$

$$\phi_\alpha = \frac{3\mu_o(D_2^2 - D_1^2)I\bar{N}}{4\pi g}\cdot\Big(K_1(1 - \frac{3\beta zs}{(D_2+D_1)})\cos(p\alpha - wt) \pm K_{6k\pm1}(1 - \frac{3\beta zs}{\pi(D_2+D_1)})\cdot$$

$$\sum_{k=1}^{\infty}\cos((6k\pm1)p\alpha \pm wt) - \beta K_1\sum_{n=1}^{\infty} F_n \cos nz\alpha\cdot\cos(p\alpha - wt) \mp \beta K_{6k\pm1}\cdot$$

$$\sum_{k=1}^{\infty}\sum_{n=1}^{\infty} F_n \cos nz\alpha\cdot\cos((6k\pm1)p\alpha \pm wt)\Big)$$

$$\Phi_\alpha = C\cdot I\cos(p\alpha - wt) - D\cdot I\sum_{n=1}^{\infty} F_n \cos n\alpha \cdot \cos(p\alpha - wt)$$

$$\pm \frac{I\cdot K_{6k \pm 1}}{K_1} \sum_{k=1}^{\infty} \cos((6k \pm 1)p\alpha \pm wt)$$

$$\mp \frac{D\cdot I}{K_1} K_{6k \pm 1} \sum_{k=1}^{\infty}\sum_{n=1}^{\infty} F_n \cos nz\alpha \cdot \cos((6k \pm 1)p\alpha \pm wt) \quad .....4.14a$$

where,

$$C = \frac{3\mu_o(D_2^2 - D_1^2)\,\bar{N}K_1}{4\pi g}\left(1 - \frac{3\beta_{zs}}{\pi(D_2 + D_1)}\right)$$

$$D = \frac{3\mu_o(D_2^2 - D_1^2)\,\bar{N}K_1\beta}{4\pi g}$$

The total flux per pole is therefore found by integrating $\Phi_\alpha\, d\alpha$ between the limits $-\pi/2p$ to $+\pi/2p$ as:

$$\Phi_T = \frac{2IC}{p}\cos wt + DI\sum_{n=1}^{\infty}\frac{2F_n}{p((nz/p)^2 - 1)}\cos wt \pm \frac{ICK_{6k\pm 1}}{K_1}\sum_{k=1}^{\infty}\frac{2}{p(6k\pm 1)}\cos wt$$

$$\pm \frac{DIK_{6k \pm 1}}{K_1}\sum_{k=1}^{\infty}\sum_{n=1}^{\infty}\frac{2F_n}{p((nz/p(6k\pm 1))^2 - 1)}\cos wt \quad .....4.14b$$

It is shown earlier that the harmonic content of the stator mmf is small and can be neglected without introducing important effects in the calculations. Therefore considering the fundamental only, equation 4.14b becomes:

$$\Phi_T = \left(\frac{2IC}{p} + DI\sum_{n=1}^{\infty}\frac{2F_n}{p((nz/p)^2 - 1)}\right)\cos wt \quad ....4.15$$

$$\Phi_\alpha = C\,I\cos(p\alpha - wt) - D\,I\sum_{n=1}^{\infty} F_n \cos nz\alpha \cdot \cos(p\alpha - wt)$$

$$\pm \frac{I\,OK_{6k \pm 1}}{K_1} \sum_{k=1}^{\infty} \cos((6k \pm 1)p\alpha \pm wt)$$

$$\mp \frac{D\,I}{K_1} K_{6k \pm 1} \sum_{k=1}^{\infty} \sum_{n=1}^{\infty} F_n \cos nz\alpha \cdot \cos((6k \pm 1)p\alpha \pm wt) \quad .....4.14a$$

where,

$$C = \frac{3\mu_o(D_2^2 - D_1^2)\,\acute{N}K_1}{4\pi g}\left(1 - \frac{3\beta zs}{\pi(D_2 + D_1)}\right)$$

$$D = \frac{3\mu_o(D_2^2 - D_1^2)\,\acute{N}K_1\beta}{4\pi g}$$

The total flux per pole is therefore found by integrating $\Phi_\alpha d\alpha$ between the limits $-\pi/2p$ to $+\pi/2p$ as:

$$\Phi_T = \frac{2IC}{p}\cos wt + DI\sum_{n=1}^{\infty} \frac{2F_n}{p\left((nz/p)^2 - 1\right)}\cos wt \pm \frac{LCK_{6k\pm 1}}{K_1}\sum_{k=1}^{\infty} \frac{2}{p(6k\pm 1)}\cos wt$$

$$\pm \frac{DIK_{6k \pm 1}}{K_1}\sum_{k=1}^{\infty}\sum_{n=1}^{\infty} \frac{2F_n}{p\left((nz/p(6k\pm 1))^2 - 1\right)}\cos wt \quad .....4.14b$$

It is shown earlier that the harmonic content of the stator mmf is small and can be neglected without introducing important effects in the calculations. Therefore considering the fundamental only, equation 4.14b becomes:

$$\Phi_T = \left(\frac{2IC}{p} + DI\sum_{n=1}^{\infty} \frac{2F_n}{p\left((nz/p)^2 - 1\right)}\right)\cos wt \quad ....4.15$$

The function F_n is given by equation 4.11 as a function of (s/t+s) the slot opening/slot pitch ratio. This function has a constant value in radial machines, since the above ratio is constant along the machine's active length. In axial field machines however this function is no longer constant due to the variation in the ratio (s/t+s) along the machine's active length and its amplitude decays sinusoidally. Table(4.1) shows values of F_n up to the 5th harmonic. Comparing these values at slot opening angle/slot pitch angle in range 0.36 - 0.72 (which is the variation in this ratio along the experimental machine's active length) the following conclusions can be reached;

a. The amplitudes of the harmonics other than the first in the given ratio range are negligible.

b. The first harmonic has the same order of amplitude at this ratio range. It is therefore possible to simplify the problem by chosing an average value of 0.97 for this function. Putting this value of F_n in equation 4.15, the total flux becomes:

$$\Phi_T = \frac{2I}{p}\left(C + \frac{\bar{D}}{((z/p)^2 - 1)}\right) \cos wt \quad \ldots\ldots\ldots 4.16$$

where, $\bar{D} = \dfrac{2.91\,\mu_o(D_2^2 - D_1^2)\beta N K_1}{4\pi g}$

The peak flux density at t = 0 is therefore given by:

$$B_p = \frac{\pi}{2}\,\frac{\Phi_T}{A_p}$$

where, $A_p = \dfrac{\pi(D_2^2 - D_1^2)}{16}$ pole area

and $$B_p = \frac{8I}{(D_2^2 - D_1^2)}\left(C + \frac{\bar{D}}{((z/p)^2 - 1)}\right)$$

The flux density as a function of α is therefore given by:

$$B = C_1 I\cos(p\alpha - wt) + \bar{C}_1 I\left(\cos\left((z+p)\alpha - wt\right) + \cos\left((z-p)\alpha + wt\right)\right) \quad \ldots 4.17$$

where,

$$C_1 = \frac{8C}{(D_2^2 - D_1^2)} \qquad \text{and} \qquad \bar{C}_i = \frac{8\bar{D}}{(D_2^2 - D_1^2)\left((z/p)^2 - 1\right)}$$

4.5 Equivalent circuit

The equivalent circuit for one phase of the machine is shown in fig.(4.7), together with its parameters for each rotor introduced in Table 4.2. The power delivered to the air-gap by the stator windings (air-gap power P_g) can be interpreted in two parts, one as ohmic loss in the rotor and is "$\bar{s}P_g$" and the other as the mechanical power developed by the shaft as $(1 - \bar{s})P_g$. The gross mechanical power at the shaft is;

$$P = I_2^2\, r_2 \left(\frac{1 - \bar{s}}{\bar{s}}\right) \quad \ldots\ldots\ldots\ldots 4.18$$

To find the net output power it is necessary to account for the total losses in the machine. The circuit of fig.(4.7) can be simplified by omitting the resistance r_o which represents the iron loss and can be deducted as power loss.

The power of equation 4.18 is a result of the sum of torques developed due to the interaction of the current in each bar with the air-gap magnetic induction. By considering a small element dR of a bar at radius R, the elemental e.m.f is given by:

$$e = B_\alpha .\, dR .\, R(-\bar{s}w_s)$$

where $(-\bar{s}w_s)$ is the speed at which the bars are moving backward relative to the rotating field. The e.m.f of a complete bar is therefore given by:

$$E_b = \frac{-\bar{s}w\,(D_2^2 - D_1^2)}{8p}\left(C_1 I\cos(p\alpha - wt) + D_1 I\left(\cos\left((z+p)\alpha - wt\right) + \cos\left((z-p)\alpha + wt\right)\right.\right.$$

Fig.(4.7) - Equivalent circuit per phase of the experimental machine.

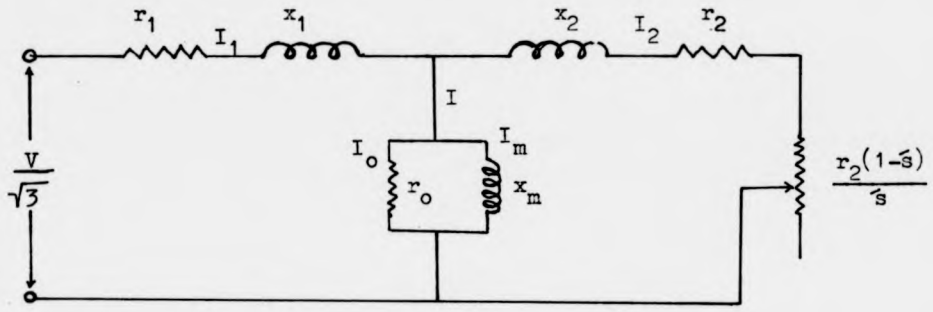

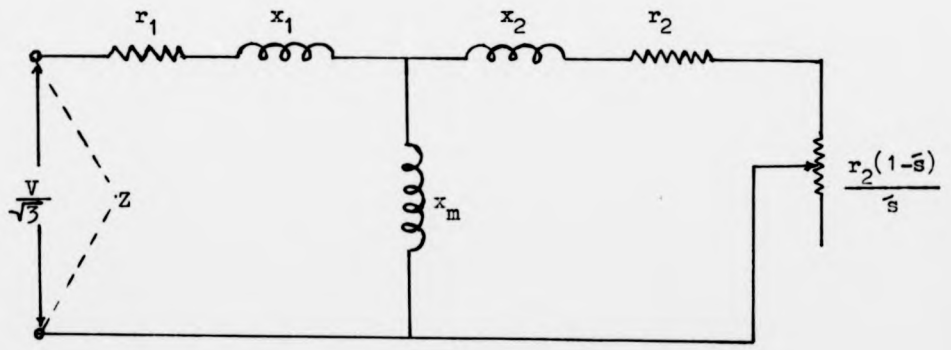

$$Z = \frac{r_1\left((r_2/\bar{s})^2 + (x_2 + x_m)^2\right) + \left((r_2/\bar{s})(x_2 + x_m)x_m - x_2 x_m r_2/\bar{s}\right)}{\left((r_2/\bar{s})^2 + (x_2 + x_m)^2\right)} + j$$

$$\frac{x_1\left((r_2/\bar{s})^2 + (x_2 + x_m)^2\right) + \left((r_2/\bar{s})^2 x_m + (x_2 + x_m)x_2 x_m\right)}{\left((r_2/\bar{s})^2 + (x_2 + x_m)^2\right)}$$

Table 4.2 - Machine parameters with different rotors

	g(physical gap) = 0.5mm $\bar{g}$(Magnetic gap) = 0.75mm					g = 0.7mm $\bar{g}$ = 1.05mm					g = 0.9mm $\bar{g}$ = 1.35mm				
Motor designation	x_1	x_2	r_1(75°C)	r_2(75°C)	X_m	x_1	x_2	r_1(75°C)	r_2(75°C)	X_m	x_1	x_2	r_1(75°C)	r_2(75°C)	X_m
A	3.1	3.1	1.54	1.910	29.63	3.1	3.1	1.54	1.91	23.77	3.1	3.1	1.54	1.91	20.39
B(end rings not separated)	3.4	3.4	1.54	1.470	38.14	3.4	3.4	1.54	1.47	32.14	3.4	3.4	1.54	1.47	26.68
B(end rings separated	3.4	3.4	1.54	1.585	32.23	3.4	3.4	1.54	1.585	27.21	3.4	3.4	1.54	1.585	24.07
D	4.07	4.07	1.54	1.95	38.5	4.07	4.07	1.54	1.95	32.0	4.07	4.07	1.54	1.95	27.0
C	4.2	4.2	1.54	2.41	34.27	4.2	4.2	1.54	2.41	27.08	4.2	4.2	1.54	2.41	22.64
C(4mm machined from each end ring)	4.2	4.2	1.54	2.72	34.60	4.2	4.2	1.54	2.72	28.59	4.2	4.2	1.54	2.72	21.46
C(7mm machined from each end ring)	4.2	4.2	1.54	3.2	34.60	4.2	4.2	1.54	3.2	29.2	4.2	4.2	1.54	3.2	21.6
D(stator slots filled with SMW)	4.76	4.76	1.54	1.90	41.0	4.76	4.76	1.54	1.90	33 09	4.76	4.76	1.54	1.90	27.67

Where, $w_s \doteq w/p$

or $E_b = -\frac{'swI}{p}\left(C\cos(p\alpha - wt) + \frac{D}{((z/p)^2 - 1)}\left(\cos((z+p)\alpha - wt) + \cos((z-p)\alpha + wt)\right)\right)$

The impedance of each bar is taken to be $Z_b = (r + j'x)$ and includes portions of the end rings joined to the bar.

The current in the bar is therefore given by:

$$i_b = -\frac{wI}{p^2 Z_b}\left(C\cos(p\alpha - \theta_b) + \frac{D}{((z/p)^2 - 1)}\left(\cos((z+p)\alpha - \theta_b) + \cos((z-p)\alpha - \theta_b)\right)\right) \quad ..4.19$$

where $|Z_b| = \left((r/s)^2 + x^2\right)^{\frac{1}{2}}$

and $\tan\theta_b = \frac{'sx}{r}$ is the bar load impedance phase angle

r and x are the bar load resistance and reactance at standstill.

The torque on the element is therefore:

$$dT = B_\alpha . i_b . RdR$$

The total torque on a single bar can be obtained by integrating the above equation between the limits of D1/2 and D2/2 giving that

$$T_b = \frac{(D_2^2 - D_1^2)}{8} B_\alpha \cdot i_b$$

Substituting values of B_α and i_b,

$$T_b = \left(CI\cos(p\alpha - wt) + \frac{DI}{((z/p)^2 - 1)}\left(\cos((z+p)\alpha - wt) + \cos((z-p)\alpha + wt)\right) \cdot \right.$$

$$\left. -\frac{wI}{pZ_b}\left(C\cos(p\alpha - \theta_b) + \frac{D}{((z/p)^2 - 1)}\left(\cos((z+p)\alpha - \theta_b) + \cos((z-p)\alpha + wt)\right)\right)\right)$$

$$T_b = \frac{wC^2I^2}{pZ_b}\cos p\alpha\cdot\cos(p\alpha - \theta_b) + \frac{wCDI^2}{pZ_b\left((z/p)^2-1\right)}\left(\cos(p\alpha-\theta_b)\cdot\cos(z+p)\alpha + \cos(p\alpha-\theta_b)\cdot\cos(z+p)\alpha\right) + \frac{wCDI^2}{pZ_b\left((z/p)^2-1\right)}\left(\cos p\alpha\cdot\cos\left((z+p)\alpha-\theta_b\right) + \cos p\alpha\cdot\cos\left((z-p)\alpha-\theta_b\right) + \frac{wD^2I^2}{pZ_b\left((z/p)^2-1\right)^2}\left(\cos\left((z+p)\alpha-\theta_b\right)\cdot\cos(z+p)\alpha + \cos\left((z+p)\alpha-\theta_b\right)\cos(z-p)\alpha + \cos\left((z-p)\alpha-\theta_b\right)\cdot\cos(z+p)\alpha + \cos\left((z-p)\alpha-\theta_b\right)\cdot\cos(z-p)\alpha\right) \quad \ldots\ldots\ldots\ldots\ldots\ldots\ldots\ldots\ldots\ldots\ldots\ldots 4.20$$

The peak torque is given by integrating equation 4.20 between 0 and π/p giving that

$$T_{b(p)} = \frac{wI^2}{pZ_b}\,\frac{\pi}{2p}\left(C^2 + \frac{2D^2}{\left((z/p)^2-1\right)}\right)\cos\theta_b$$

But $$\cos\theta_b = \frac{r/s}{\left((r/s)^2 + x^2\right)^{\frac{1}{2}}}$$

Thus $$T_{av.} = \frac{wI^2}{p^2Z_b}\left(C^2 + \frac{2D^2}{\left((z/p)^2-1\right)}\right)\cdot\frac{r/s}{\left((r/s)^2 + x^2\right)^{\frac{1}{2}}}$$

and the total torque for the machine of n_b bars is:

$$T_t = \left(\frac{wI}{pZ_b}\right)^2\left(C^2 + \frac{2D^2}{\left((z/p)^2-1\right)}\right)\cdot\frac{pn_br}{2sw} \text{ Nm} \quad \ldots\ldots\ldots 4.21a$$

The total output power can be stated;

$$P_t = w_r T_t \qquad w_r = (1-s)w$$

giving $$P_t = \left(\frac{wI}{pZ_b}\right)^2\left(C^2 + \frac{2D^2}{\left((z/p)^2-1\right)}\right)\frac{(1-s)n_br}{2ms} \text{ watts/phase} \quad \ldots\ldots\ldots 4.21b$$

where m is the number of phases in the machine and I is the peak phase current.

The power output of equation 4.21b calculated from the machine's parameters must be equal to the power output of equation 4.18 calculated from equivalent circuit parameters. Therefore by equalising the two equations, the turns ratio is found to be:

$$T_r = \frac{\left(C + \frac{D}{((z/p)^2 - 1)}\right)}{\left(C^2 + \frac{2D^2}{((z/p)^2 - 1)}\right)^{\frac{1}{2}}} (4p\pi K_1) \sqrt{m/n_b} \quad \ldots\ldots\ldots 4.22$$

Therefore the secondary parameters of the equivalent circuit r_2, x_2 referred to the primary are given by:

$$r_2 = T_r^2 r$$

$$x_2 = T_r^2 x$$

where r and x are components of the bar load impedance and can be written as the sum of the bar and portion of the end ring as;

$$r = r_b + \tfrac{1}{2} r_e$$

$$x = x_b + \tfrac{1}{2} x_e$$

and shown in A_3 as a function of frequency.

4.6 Saturation

The magnetization curves of the machine at three values of air-gap lengths are shown in fig.(4.8). The straight line tangent to the lower portion of the curve is the air-gap line indicating the mmf required to overcome the air-gap reluctance. Under very small saturation the air-gap line and magnetization curve would coincide. The departure of the curve from the air-gap line is an indication of the level of saturation* in the machine. Using the magnetization curve for 0.5mm air gap length at 220V, the magnetizing reactance is found to be 38Ω, while in the non-saturated region it is 50.4Ω. The average flux density is about 0.4 wb/m^2 and the level of saturation is about 23%. The saturation can be accounted for by expressing the performance equations in terms of the magnetizing reactance:

$$X_m = 4NK_1 w \left(C + \frac{D}{((z/p)^2 - 1)}\right)$$

* level of saturation (ref.3.4) = $\frac{\text{Total mmf - air gap mmf}}{\text{Total mmf}} = \frac{A - B}{A}$

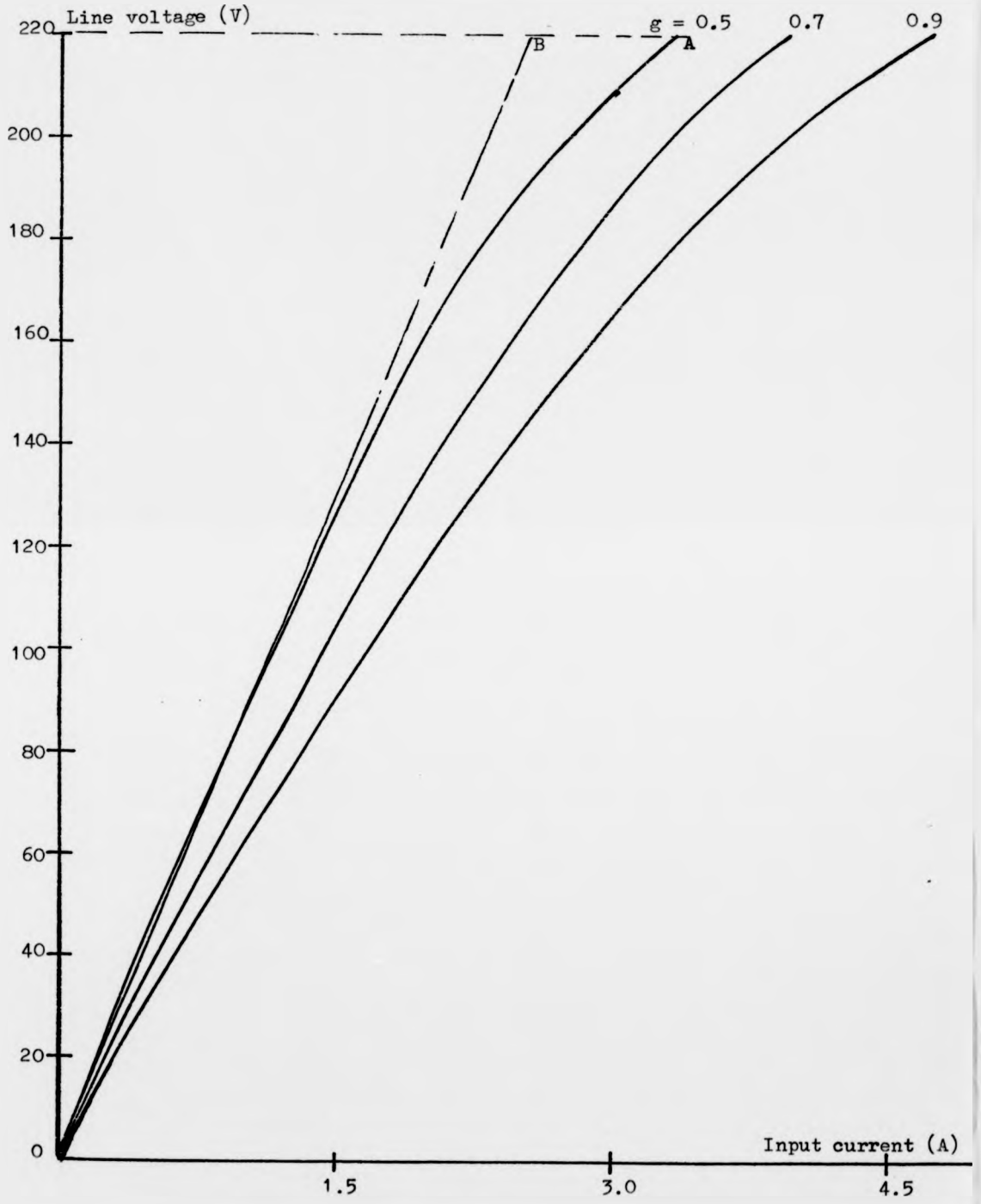

Fig.(4.8) - Magnetization curve of the motor operated with rotor D at three values of air-gap length.

CHAPTER 5

EXPERIMENTAL MACHINE AND MEASURING TECHNIQUES

5.1 Details of the Experimental Machine

Due to the single and double cage rotor production it is now possible to produce two sizes of the machine having the same external diameter of 240mm and axial lengths of 98 and 110mm respectively as shown in A5.

5.1.1 Stators

The experimental machine consists of two similar stators each having the distributed winding shown in Fig.5.0. The respective phases in the stators are connected in series and the final phases are star connected. Each stator has the following details:

Inner and outer diameters - 85 and 170mm.

Total depth of the core - 33mm.

Slots - 24, Non skewed, rectangular completely open.

Slot depth - 19mm, slot width - 8mm.

Slot width/Tooth width - 0.615 at D_2

and 3.05 at D_1

Core depth at the back of the slots - 14mm.

Winding - 3 phase, 4 pole, double layer, star connected,

20 turns per coil, 5/6 chorded rectangular coils

Resistance 0.77Ω/phase at 75°C

Each stator is made out of 33 meters length steel strip known as Losil 800 of 0.5mm thickness. This is a low silicon non-oriented steel material with comparatively low losses combined with good permeability characteristics for machine design. The strip is covered with a thin layer of inorganic material chemically and thermally bonded on to the steel base. The coating is heat and oil resistant and can withstand the annealing temperature. One of the problems which occurred was the difficulty of getting the required strip width. Therefore the required width had to be cut from a 120mm width strip supplied by

Fig.5.0 - Stator winding distribution (3 phase, 4-pole, double layer, 5/6 full pitch, 24 slots, 20 turns/coil and star connected) wire gauge 1.25 mm diameter.

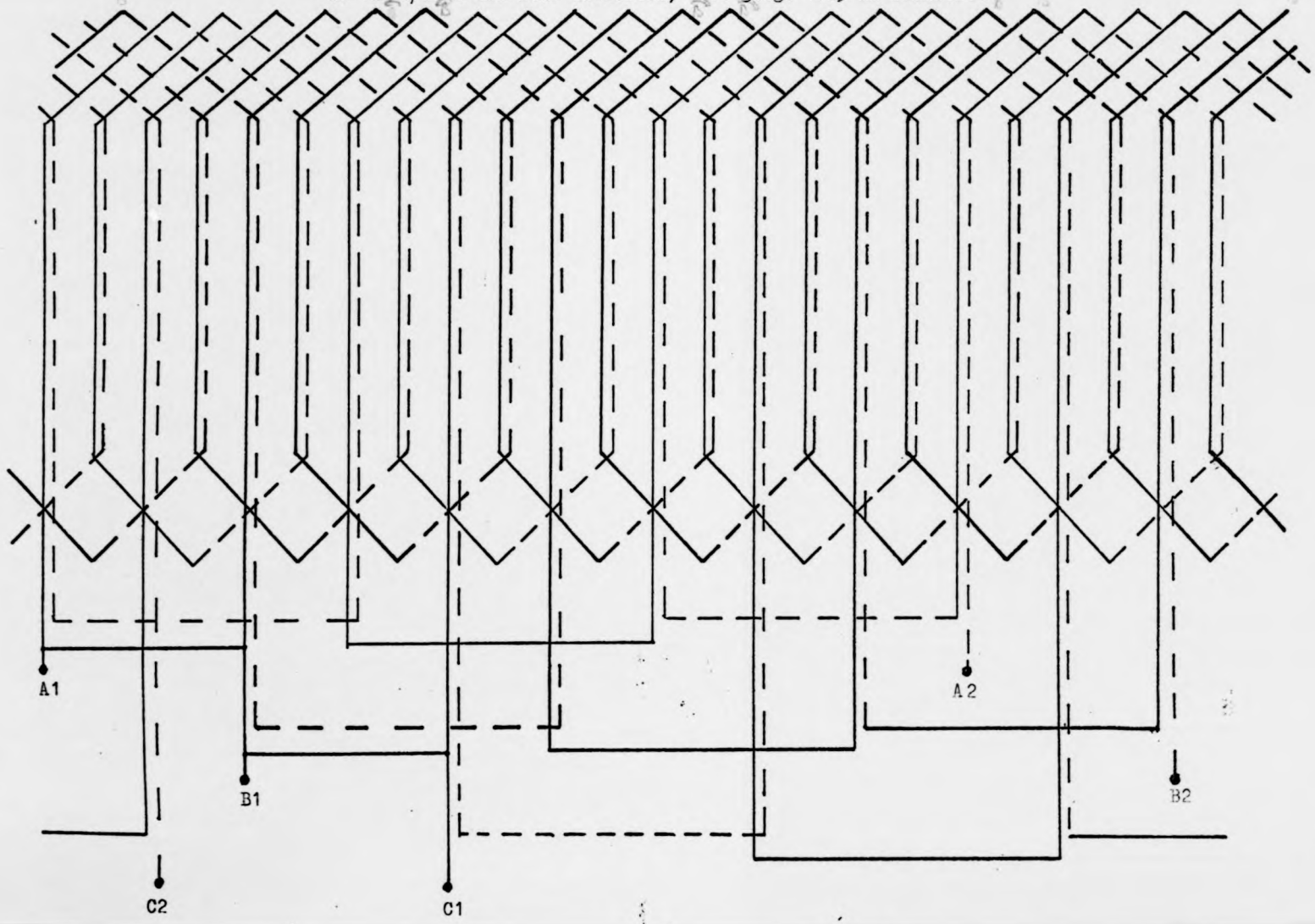

British Steel. The slitting of the steel to the required widths introduced a big problem especially that it is found that the slitting machines in use at a number of companies consulted can not handle such an amount of steel. After a long search the problem has been solved when the author modified an electric stamping machine existed in the department to a strip cutter, and good strips were cut to the required specification.

Each stator is wound in the shape of a spiral spring around a steel disc using Jig W shown in Fig.(5.3). After finishing the winding, the strip end is soldered to the last turn and a steel ring is heated and dropped over the core. When it is cooled the ring shrinks and clamps the core. The inner disc and the outer ring are then machined down to the required thickness. The steel coil is then transferred to Jig M of Fig.(5,3) for slot opening. Following this is the strain relief process which is achieved by annealing. Fig.(5.3b) shows one of the stators in Jig M after the slots have been cut.

5.1.2 Rotors

Four rotors have been made of the same steel strip in the shape of flat discs and they are designated A,B,C,and D all having the same diameter as the stators. Rotor A is a single cage with 20 normal slots made of three solid cast iron rings inserted together to give thickness of 17mm and inertia of 0.0154 $Kg.m^2$. Rotor B is a double cage - each cage consisting of 20 normal slots separated by thin steel bridge and having a total thickness of 28mm and inertia of 0.0215 $Kg.m^2$. Rotor C is a single cage of 18 slots skewed one slot pitch having thickness of 17.25mm and inertia of 0.0158 $Kg.m^2$. Rotor D is a single cage - with 20 normal slots extending radially, having a thickness of 17.25mm side to side and inertia 0.0161 $Kg.m^2$. A fifth rotor could be a reluctance rotor produced by machining the laminations at certain places of the rotor D to produce the saliency required. Three of the four experimental rotors are shown in chapter 2.

5.2 Mechanical design features

5.2.1 Skewing

It is found, ref. 1.5, that due to the disc shape of the machine the skewing theoretically follows a curved line. In practice this is very difficult to achieve and consequently the skewing used in the present design is a linear skewing of one stator slot pitch (15^{o}) with the slots running straight from the outer surface of the rotor radially to its inner surface and tilted from the normal slot position.

To achieve such skewing, the rotor is adjusted vertically under the milling machine with the drill pointing towards the rotor centre. To produce the required skewing, the centre of the rotor is displaced along the horizontal axis a linear distance (R_2 Sin α) equal to the skewing angle required causing the drill to tilt relative to the first position by the skewing angle. This is shown in fig.(5.1) for one slot pitch in the 18-bars single cage rotor.

5.2.2 Fixing Techniques

In the experimental machine there are two parts which have to be fixed mechanically, these include the supporting of the rotor core carrying the cage on the steel shaft and the fixing of the stators in the end plates. Suitable fixing of the rotor on the shaft is a very important requirement in this type of machine and it can effect the construction of the rotor.

In a number of axial field machine designs which the author has encountered, special thought and design are always devoted to the method of fixing the rotor onto the shaft. In most of these designs, complicated methods involving a lot of design efforts have been used. Moreover they often cause increases in iron loss and higher rotor inertia. The fixing technique used in the present design offers the following advantages:

(a) The technique is rigid enough to stand the expected axial forces on the rotor and to limit any bending caused by such forces.

(b) The technique is straightforward with no complications and the fixing

Fig.(5.1) - Skewing in an axial field machine

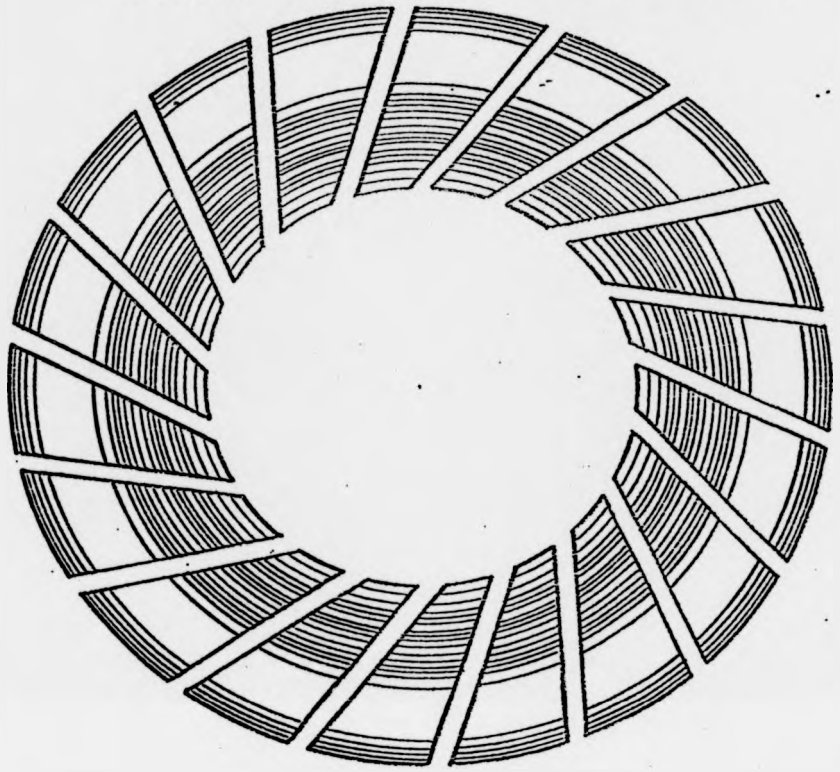

a - Skewed bar rotor

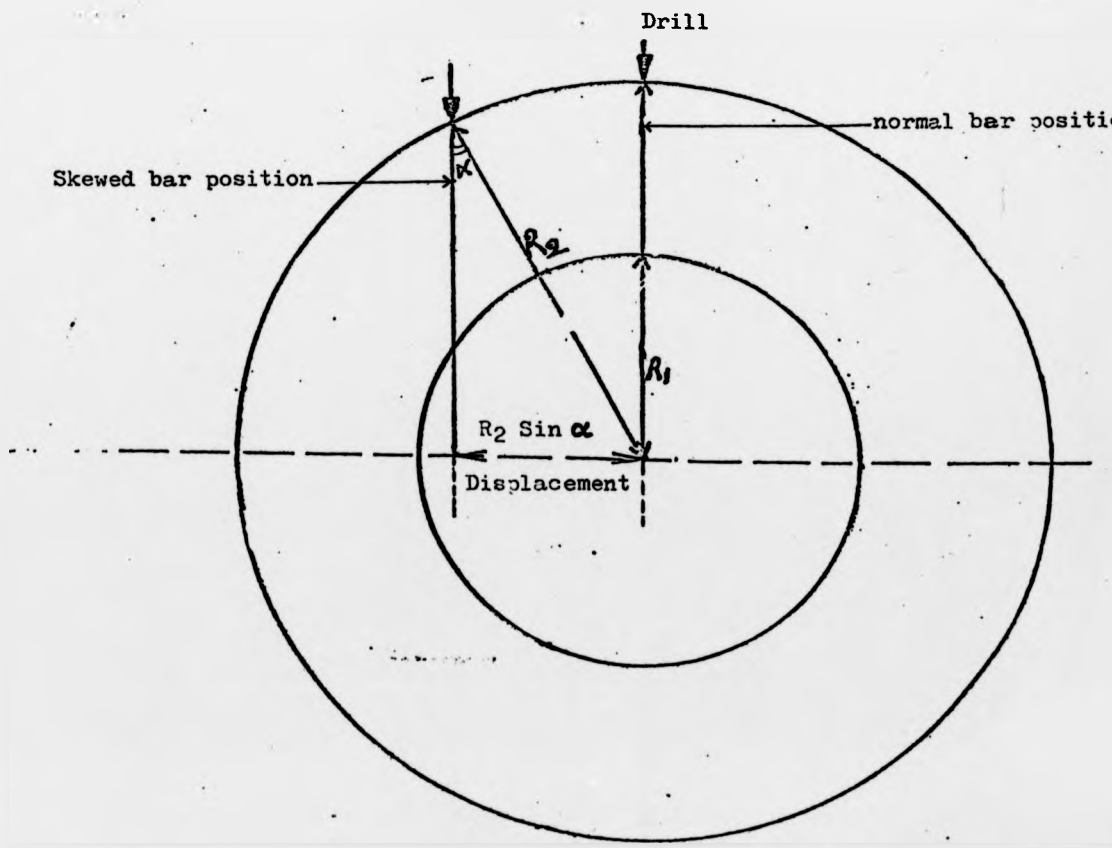

b - The process of skewing

means do not extend beyond the rotor surface in the axial direction, except at the central part of the machine.

(c) No external bolts or rings are required in the technique. These bolts and rings can be serious sources of power loss and vibrations at different speeds.

The rotor fixing technique depends heavily on two parts of the rotor; these are the massive aluminium inner end ring and the inner surface of the core at the central diameter. The aluminium at the centre is bored out and a steel bush with a key way having a thickness just below the aluminium thickness is cooled in liquid nitrogen and dropped in . As the bush expands it becomes a tight fit in the aluminium ring.

A steel shaft is made to the required dimensions carrying on one side a round shoulder made as an integral part with the shaft, with diameter just below 85mm and thickness of 4mm. The other side of the shaft is supplied with a similar shoulder movable on a thread on the shaft and clamping against the other side of the aluminium ring. The two shoulders are made to fit into the inner diameter of the rotor and enclose a key and are locked by a locknut at the back of the movable shoulder as shown in fig.(5.2a).

The fixing of the stator cores into the end-plates is another important requirement. Unsuitable fixing of the cores can cause similar problems as in the case of the rotors. Therefore any fixing technique must fulfil the above requirements. The end-plates employed have a cup shape with dimensions just sufficient to accommodate the stator cores. Initially six radial holes were drilled and tapped in each end-plate and grub screws were used to press against the outer surface of the core and are located in recesses made in the outer ring of the core.

When the motor was given the first experimental run it seemed to be quiet, smooth and noiseless but after running for a period of time some noises started to appear and increased until rubbing between the stator and rotor occurred. It was noticed that the noise started at high voltages and increased

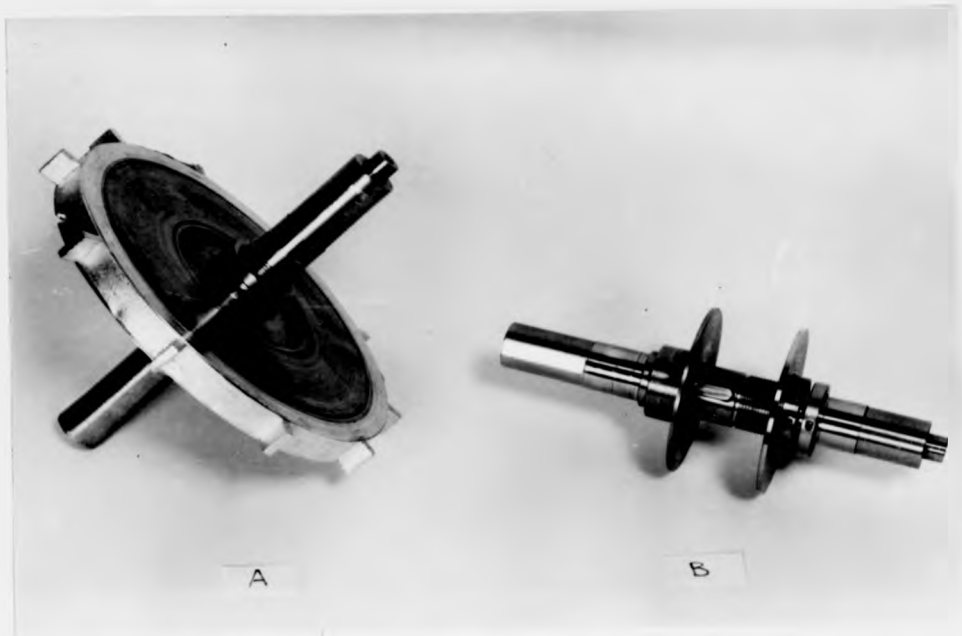

Fig. (5.2a) A - Complete rotor with solid shaft

B - The fixing assembly

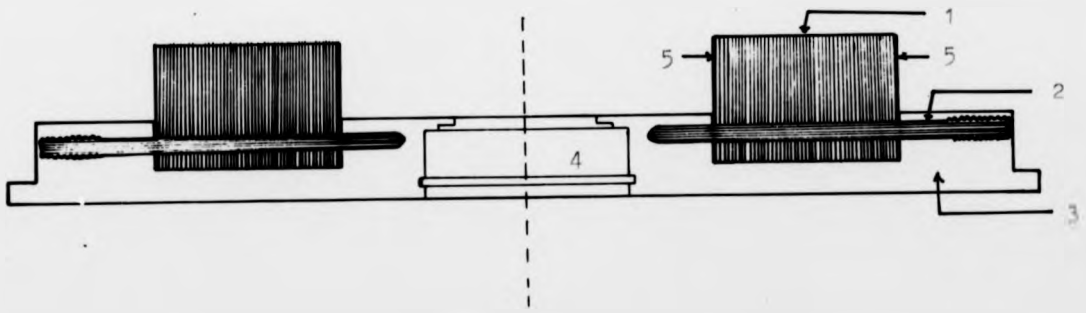

Fig.(5.2b) - Stator Core fixed into end-plate.

1. - Stator laminated core.
2. - Hardened steel screw for fixing the stator core into the end-plate.
3. - Aluminium end-plate.
4. - Bearing.
5. - Outer and inner steel retaining rings.

A B

Fig. (5.2a) A - Complete rotor with solid shaft

B - The fixing assembly

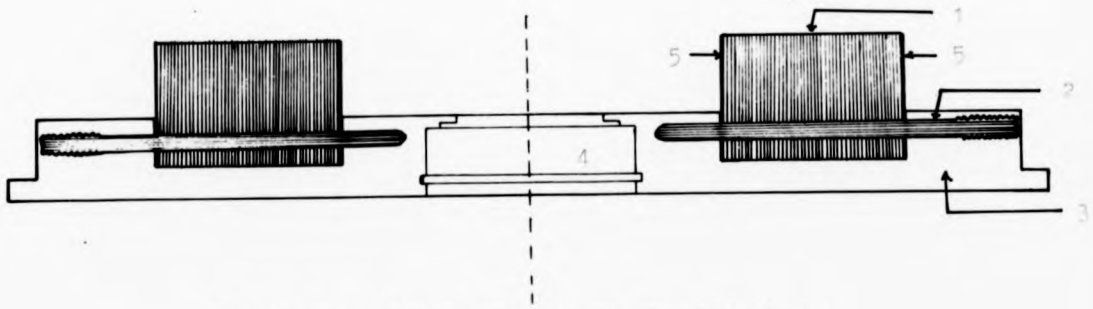

Fig.(5.2b) - Stator Core fixed into end-plate.

1. - Stator laminated core.
2. - Hardened steel screw for fixing the stator core into the end-plate.
3. - Aluminium end-plate.
4. - Bearing.
5. - Outer and inner steel retaining rings.

rapidly with the voltage to an extent that it was impossible to run the motor. A careful and continuous study of the noise by the author showed that due to the fixing technique used in fixing the stator core on to the end-plate, there is a possibility that the core can move axially inside its housing. At high voltages where the air-gap field is high one of the cores or both suffer a certain movement giving rise to noises due to magnetic pull. This magnetic pull urges the pulling out of the core until touching between the surfaces occurs. To cure this problem the six radial holes at each end plate are extended radially into the laminations to cross to the inner edge of the housing as shown in fig.(5.2b). Special steel screws have been prepared for this purpose. The screws are heated and quenched in oil for hardening and to form a skin of oxide which can help in insulating them from the laminations. This technique was found to be successful even if it can affect the iron loss.

5.2.3 The Jigs

In order to manufacture the two stators and the four rotors properly, it is necessary to use two steel jigs. These jigs are called as W and M according to their functions.

Jig W - fig.(5.3a) is designed for winding the steel strips using the lathe. It consists of a shaft with a disc shoulder welded to it having three equi-spaced tapped holes. Two end plates of diameter larger than the core diameter each having three holes to match those in the shoulder were prepared. The end plates are designed to fit on the shaft and are separated from each other by a central bush having a length equal to the required thickness of the core to be wound. This technique of using a central bush provides the means of freely winding any core by only changing the bush. To start winding the strip a cut is made in the bush to accommodate the starting end of the strip which is thinned down and soldered to the bush. This jig is also used for carrying and

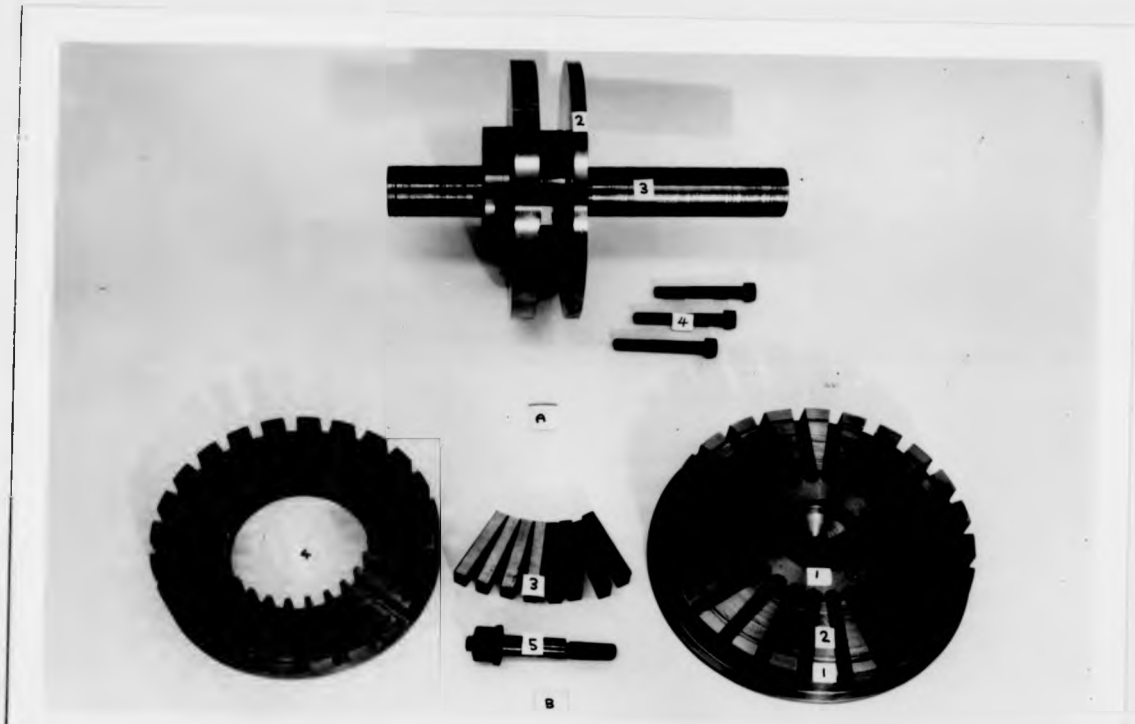

Fig.(5.3)

A - Jig W (winding jig)

B1 - Jig M (slot cutting jig)

B2,4 - Stator core after slot cutting

B3,5 - Solid inserters and fixing screw

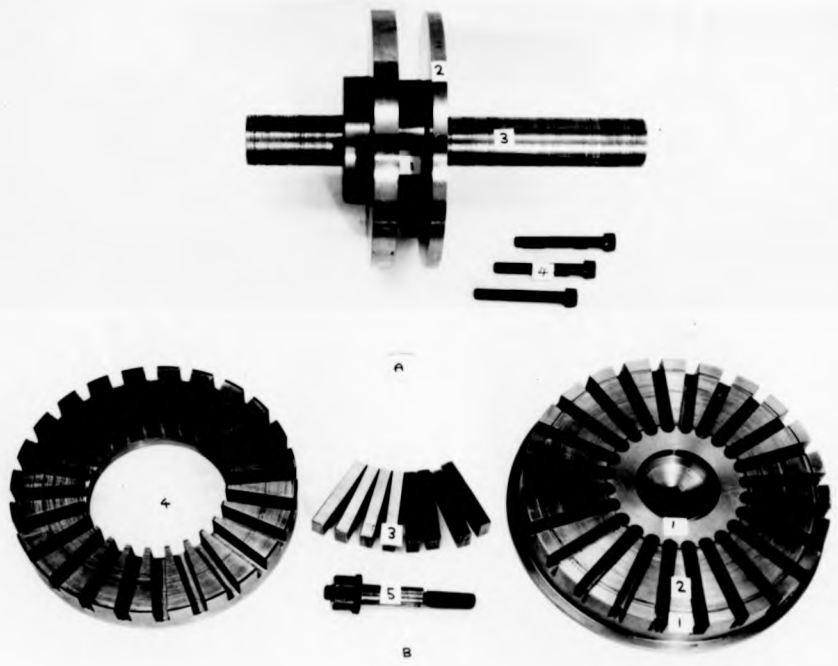

Fig.(5.3)

A - Jig W (winding jig)

B1 - Jig M (slot cutting jig)

B2,4 - Stator core after slot cutting

B3,5 - Solid inserters and fixing screw

supporting the rotor core during radial hole opening.

Jig M is designed for slot milling across the stator face to produce the required slot number in each stator. This jig has a cup shape shown in fig.(5.3b) It consists of a central hub to fit into the inner diameter of the stator core and an external rim in which the outer surface of the core is fitted. It is also supplied with a single slotted cover to clamp over the core and expose the area at which the slotting has to be done. It is also helpful to insert some rectangular steel pieces in every slot opened to provide rigidity to the coil after removing it from the jig.

5.2.4 Ventilation

The process of cooling a machine is a matter of first importance, as the rating of any machine depends greatly on proper ventilation especially if it is a continuously rated machine. Cooling is a process of heat dissipation within a machine by conduction, convection and radiation and it can be an art rather than a science. It depends on the shape and the size of the machine and the ambient at which it has to be operated. The ventilation method used in this machine is a combination of radial, axial and circumferential ventilation acting on the back of stator cores, the faces of laminations exposed at the air-gap and on the winding overhangs. Such type of ventilation is illustrated by the design shown in fig.(5.4). It consists of two parts: Firstly passage ways in the end plates allow cold air from outside to pass into the hot parts of the machine, and secondly the rotor carries ten aluminium blades which in rotating circulate the air very efficiently. The rotation of the blades causes the air to circulate radially and circumferentially. On the left hand side of the motor, the blades draw air through the left hand vents at the back of the stator core. The air at this inlet divides in four paths passing through channels 4mm deep cut in the end plates underneath the core. Two paths extend radially towards the inner and outer overhangs and the other two go circumferentially.

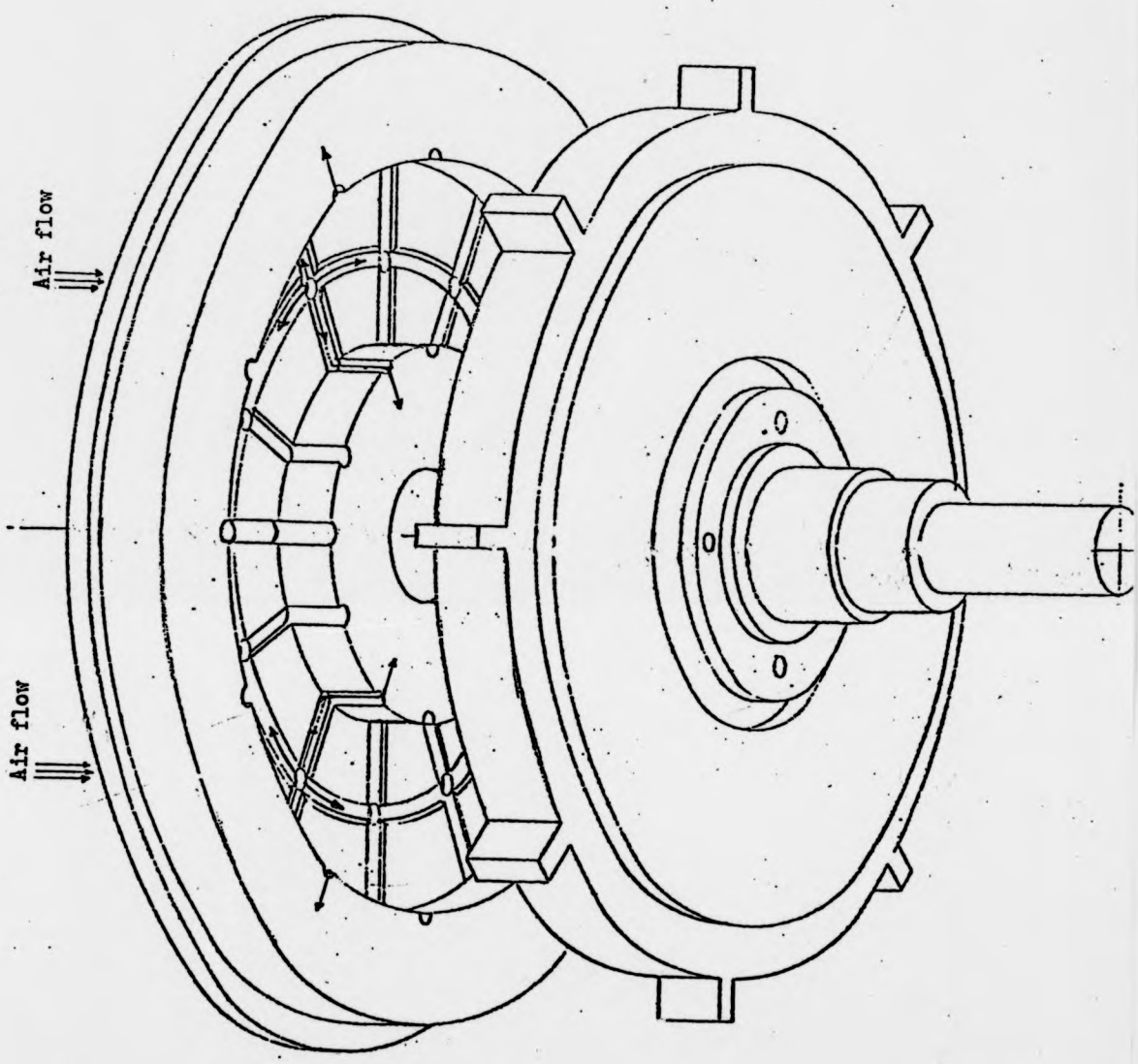

Fig.(5.4) - Ventilation in the experimental machine

All these air-currents come out at openings in the overhangs to circulate inside the motor and rush out through openings in the case. The fans also draw air through the case openings and pass it over the interior stator and rotor surfaces. The passageways through stator slots can provide additional ventilation by increasing the volume of the cooling air passing through the machine. The air in these passageways is in a direct contact with the windings making the cooling process more effective. The case and end plates help the cooling process by dissipating heat by radiation and convection.

5.3 Experimental Equipment and Measuring Techniques

5.3.1 Speed

The use of mechanical tachometers and stroboscopes has been avoided since it is necessary that the speed readings must be accurate and straightforward. An electronic stroboscope was designed to give a direct reading of the speed as the machine is loaded. It consists of an aluminium disc with sixty equally spaced slots fitted to the shaft of the motor. The disc runs in a split cut in a plastic block between a source of light and a light sensitive photo-transistor. The passing of successive slots produces output pulses which are amplified and used to trigger a digital counter.

5.3.2 Torque

A modified ASEA ring torductor has been used for accurate torque measurements after calibrating against applied weights. It consists of a stator of three rings of windings each having four poles distributed around the steel shaft acting as a solid rotor. The central ring is excited with alternating current and acts as the primary of a transformer with the outer as secondaries. When torque is applied to the shaft, principle stresses at 45^{o} to the axis of the shaft are created. These cause an increase in permeability in the direction of tension, and a decrease in permeability in the direction of compression. The change in the permeability of the shaft material causes distortion in the symmetrical distribution of the magnetic field at the primary in proportion to the

applied stress and the resultant fluxes through the poles induce secondary voltages. This is very useful device for shaft torque measurement, since it is very rigid and requires no direct contact to the rotating shaft. Fig.(5.5) shows the calibration curve of the device.

5.3.3 Air-gap Flux

This is calculated by measuring the induced e.m.f. in a full pitched search coil of two turns of thin wire placed in the slots at the air-gap face. Search coils are also used on a single tooth and at the core for flux measurements and harmonic analysis, search coils 2, 3, 4 of fig.3.5.

5.3.4 Temperature

A number of NiCr/N.Al thermocouple sensors are inserted at different spots of the stator core and the temperature is recorded continuously during the tests. The sensor must be put at points away from any air-draughts and at the hottest points of the machine. It is difficult to reach the thermocouple at the central part of the machine which is believed to be the hottest spot inside the machine. The temperature of the winding at the bottom of a slot at the outer overhang is measured and to account for the temperature of the centre, 20°C is added to every temperature reading to determine a safety limit (130°C) within which the machine can operate. The enamelled copper wire employed in the stator winding is 1.25mm diameter (bare) and is covered with insulation of class F and grade M.

5.3.5 Inertia

The moment of inertia I is measured by fixing the rotor between two centres and allowing it to rotate on a horizontal axis. A weight "m" is hanged at height "h" on a thread wound round the shaft and allowed to fall freely. The moment of inertia (ref.5.1) is given by:

$$I = mr^2 \frac{N}{N+n}\left(\frac{gt^2}{2h} - 1\right) \quad \ldots\ldots\ldots\ldots 5.1$$

Fig (5.5) - Torductor Calibration

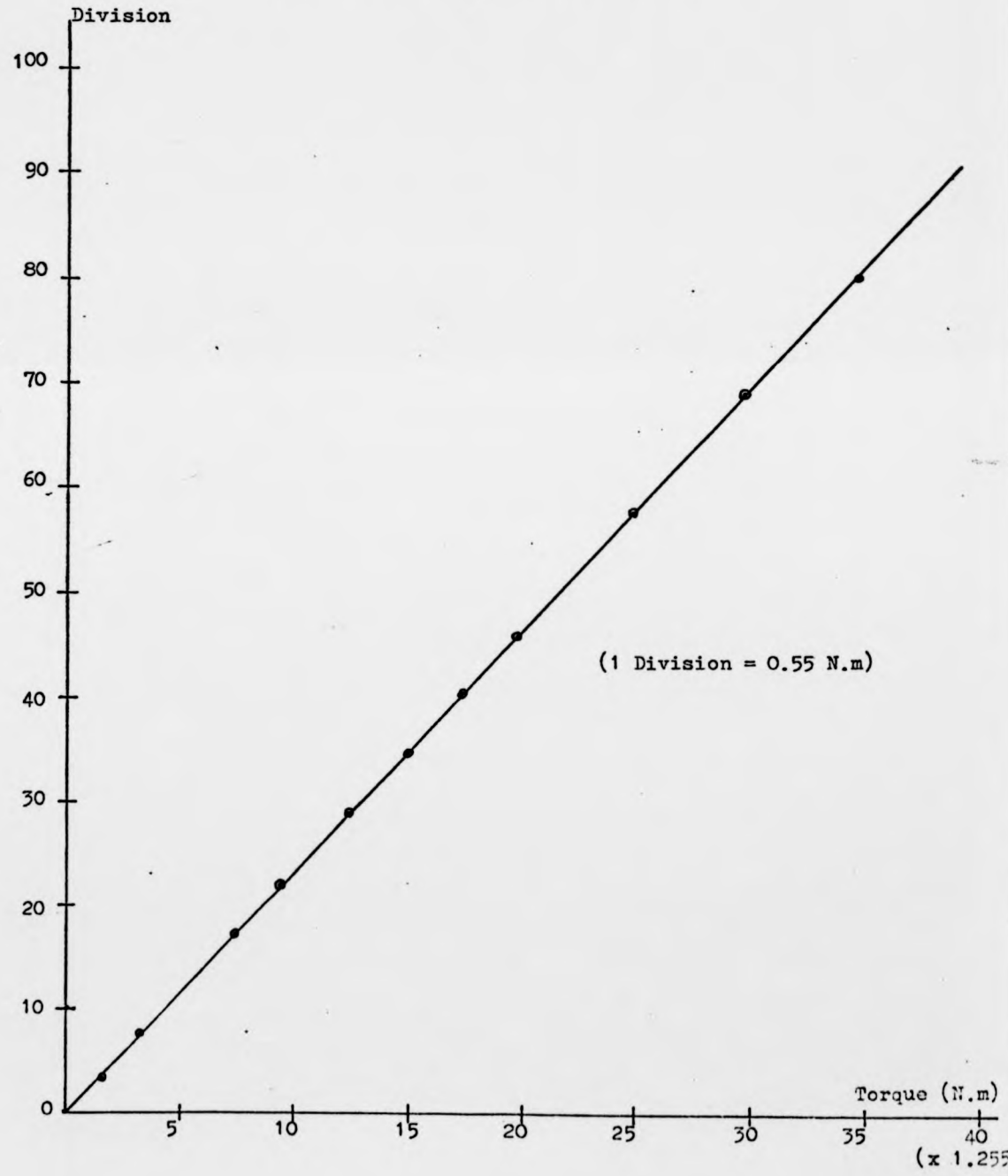

where N - number of revolutions the rotor turns after the weight "m" has reached the floor.

n - number of revolutions the rotor turns before the weight reaches the floor

r - radius of the shaft

t - time taken by the weight to reach the floor

g - Acceleration due to gravity.

The effect of the friction at the two ends is considered in the formula by counting number of revolutions the rotor turns after the weight has reached the floor

5.4 Unbalanced Magnetic Pull (UMP)

5.4.1 Introduction

It is necessary that wide studies of UMP should be made for any motor to understand how the machine's characteristics can be improved. In 1963 Von Kaehne(5.2) reported in his survey on unbalanced magnetic pull that an increase of 1.5 KW in output has been achieved in a 2-pole 15 KW induction motor by better understanding the UMP. By carrying on such an investigation it is also possible to detect the amount of change in size and weight which can be obtained by changing some of the motor's dimensions and the type of materials used in the design.

Knowing the magnitude of the pull it is possible to obtain sufficient information about the required stiffness of the mechanical assembly, in particular the shaft, necessary to limit the deflection caused by the pull to a safe value. In the experimental machine if the shaft or the shoulders which support the cage on the shaft are too weak, the deflection can cause rubbing between the rotor and stator faces. But on the other hand if they are too stiff, the physical dimensions and weight of the machine will be excessive. The magnetic pull caused by the eccentricity of the rotor in the air-gap is one of the important areas of study in this machine. The word eccentricity used in this text means "axial eccentricity". The supporting

area of the rotor on the shaft is very limited causing the UMP due to this type of eccentricity to be very effective. There are a number of possible reasons for eccentricity of the rotor. The mechanical reasons include inaccurate positioning of the rotor with respect to the stators, rough surface finish of the stator, shaft deflection due to weight of the rotor or external pull and overhanging weight and finally abnormal wear of sleeve bearings and other bearing failures. These causes give rise to stationary eccentricity. Rotating eccentricity can exist as a result of unbalance of the rotating assembly due to rough surface finish and non-vertical mounting of the rotor on the shaft through the key-way. There are electromagnetic reasons also for this type of eccentricity, such as, non-suitable combinations of stator and rotor slots and unbalance due to a fault in the supply or in machine windings (this include, un-symmetrical supply, short-circuited turns or coils which cause dissymmetries in the magnetic circuits).

In the experimental machine only static eccentricity is expected since the two sides of the rotor under test can be skimmed to a true finish surface. In radial machines static eccentricity occurs when rotor and stator axes are not coincident. This occurs in axial field machines when the line passing through the middle plane of the rotor perpendicular to the shaft does not fall in the central plane of the air-gap between the two stators.

5.4.2 Unbalanced Magnetic Pull Calculations

When the air-gaps on both sides of the rotor are not in electromagnetic equilibrium, the magnetic attraction between the rotor face and the stator at the smallest air-gap side per unit area is given by equation(A4.5) as:

$$f = \frac{B_w^2}{2\mu_o}\left(1 - \frac{1}{\mu_r}\right) \quad N/m^2 \quad \ldots\ldots\ldots\ldots 5.2a$$

where μ_r – is the relative permeability of the laminations

$B\alpha$ – is the flux density in the air gap ($g_o$mm) on each side of the motor given on page 83 as:

$$B\alpha = I(C_1 \cos P\alpha + \acute{C}_1(\cos(z + p)\alpha + \cos(z - p)\alpha) \quad (t = 0) \quad \ldots\ldots\ldots 5.2b$$

Considering an elemental radial portion dR of rotor face at radius R, subtending an angle of width $d\alpha$, the force on this element is therefore given by:

$$f = \frac{B^2}{2\mu_o}\left(1 - \frac{1}{\mu_r}\right) RdR\, d\alpha \quad \ldots\ldots\ldots\ldots 5.3$$

If any eccentricity is introduced in conjunction with rotor position in the air-gap as shown in Fig.(5.7a), the air gap g_1 on one side becomes smaller than the air gap g_2 on the other side.

The small air gap length $g_1 = go(1 - e)$

and the large air gap length $g_2 = go(1 + e)$

where $e = \frac{\text{Larger air-gap - Smaller air gap}}{\text{Sum of air gaps}}$

or $e = \frac{g_2 - g_1}{2go}$ as shown in Fig.(5.7a)

But fig.(5.6) shows that the flux density is inversely proportional to the air-gap length for the same magnetising current. Therefore the flux density on the side of the larger air-gap length is given by:

$$B_2 = \frac{B\alpha}{(1 + e)}$$

and the flux density on the side of the smaller air-gap length is given by:

$$B_1 = \frac{B\alpha}{(1 - e)}$$

From equation (5.3) the attraction force on the larger gap side is given by:

$$F_2 = \frac{B_2^2}{2\mu_o}\left(1 - \frac{1}{\mu_r}\right) RdR\, d\alpha \quad \ldots\ldots\ldots\ldots 5.4a$$

and the attraction force on the smaller gap side is given by:

$$F_1 = \frac{B_1^2}{2\mu_o}\left(1 - \frac{1}{\mu_r}\right) RdR\, d\alpha \quad \ldots\ldots\ldots\ldots 5.4b$$

Subtracting equation (5.4a from equation (5.4b) gives the one side magnetic pull on the elemental area "RdRdα" as:

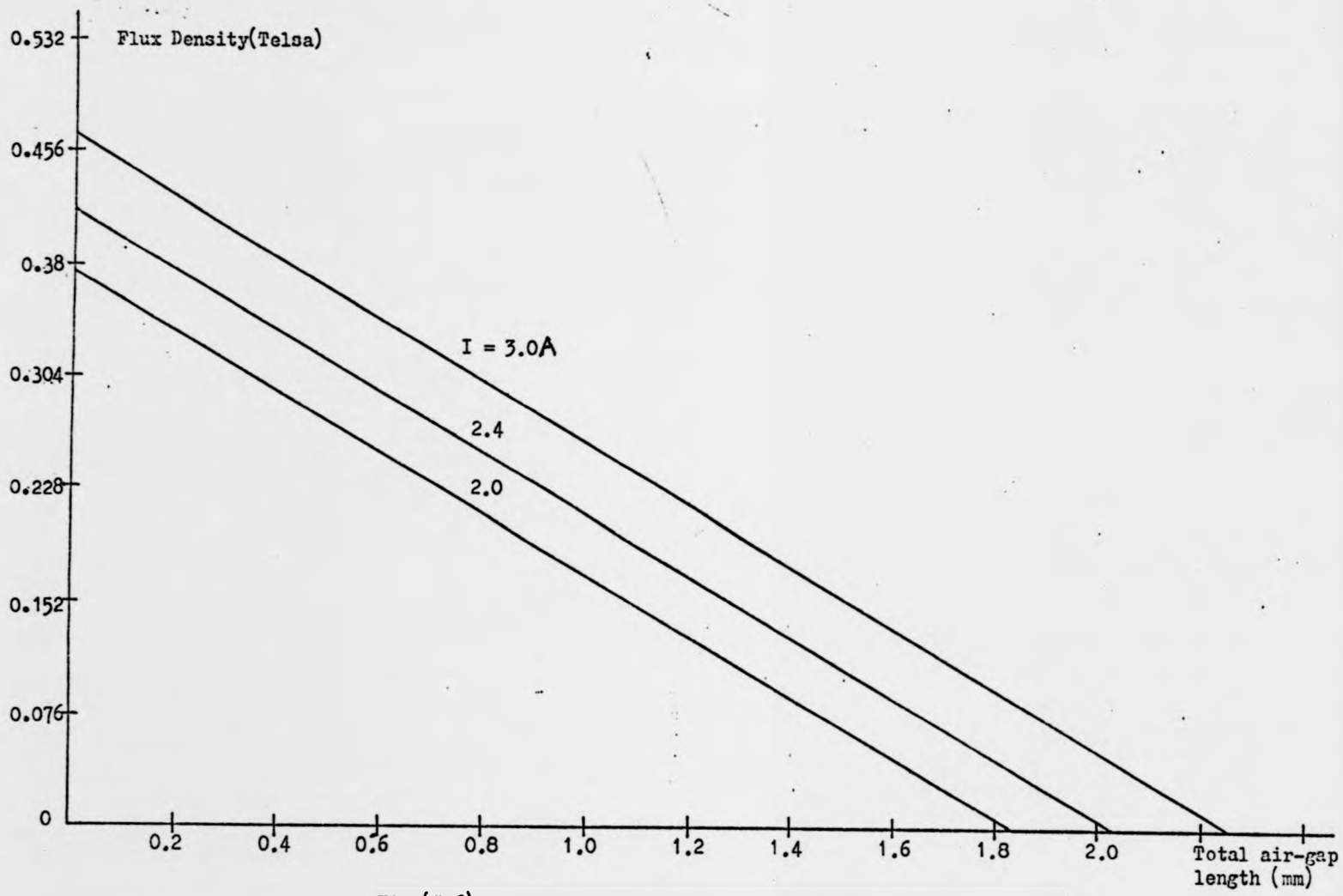

Fig.(5.6) Air-gap flux density as a function of the gap length for constant input current(*experimental*).

$$F = \frac{1}{2\mu_o}\left(1 - \frac{1}{\mu_r}\right)\left(B_1^2 - B_2^2\right) RdRd\alpha$$

The total one side magnetic pull on the element can be found by integrating the above equation between the limits D1/2 and D2/2, given that:

$$F = \frac{(D_2^2 - D_1^2)}{16\mu_o}\left(\frac{1}{(1-e)^2} - \frac{1}{(1+e)^2}\right)\left(1 - \frac{1}{\mu_r}\right) B_\alpha^2\, d\alpha \quad \text{.....5.5}$$

The total one side magnetic pull on the rotor is therefore found by integrating equation (5.5) between the limits $-\frac{\pi}{2P}$ to $+\frac{\pi}{2P}$ as:

$$F = 2p\,\frac{(D_2^2 - D_1^2)}{16\mu_o}\left(1 - \frac{1}{\mu_r}\right)\frac{4e}{(1-e^2)^2} I^2 \int_{-\frac{\pi}{2P}}^{+\frac{\pi}{2P}} \left(C_1\cos p\alpha + \bar{C}(\cos(z-p)\alpha + \cos(z+p)\alpha\right)^2 d\alpha$$

giving that

$$F = 2p\,\frac{(D_2^2 - D_1^2)}{16\mu_o}\,\frac{4e}{(1-e^2)^2}\,\frac{\pi}{2p}\,(C_1^2 + 2\bar{C}_1^2)\,\left(1 - \frac{1}{\mu_r}\right) I^2$$

$$F = \frac{4\pi\left(1 - \frac{1}{\mu_r}\right)}{\mu_o(D_2^2 - D_1^2)}\left(C^2 + \frac{2D^2}{(z/p)^2 - 1)^2}\right)\frac{4e}{(1-e^2)^2} I^2 \quad \text{.....5.6}$$

where C_1, $\bar{C}_1$, C, $\bar{C}$ and D are given in Chapter 4, pp.81, 83.

Equation 5.6 can be expressed in terms of the line voltage as:

$$F = \frac{4\pi\left(1 - \frac{1}{\mu_r}\right)}{\mu_o(D_2^2 - D_1^2)}\left(C^2 + \frac{2D^2}{(z/p)^2 - 1)^2}\right)\frac{4e}{(1-e^2)^2}\,\frac{2V^2}{3z_t^2} \quad \text{.....5.7}$$

where z_t is the impedance per phase of the machine under no load and V is the line voltage.

5.4.3. Analytical results and Discussion

The magnetic pull has been studied at two different air-gaps for different applied voltages with the eccentricity as parameter. Fig.(5.7a) shows the one-sided pull as a function of the applied voltage, for eccentricities (0.05 - 0.9) and air-gap length of 0.5mm. The magnetic pull is proportional to the square of the applied voltage. It is possible to see that the UMP increases more sharply as the eccentricity increases. This means that for a given applied voltage the pull approaches∞ due to any sudden increase in the eccentricity. This can be observed more closely by comparing the two curves of eccentricities 0.1 and 0.6 noticing that the increase in the pull when eccentricity changes from 0.1 to 0.2 is less pronounced than that when eccentricity changes from 0.6 to 0.7.

Fig.(5.7b) shows the one sided pull for twice air-gap length and the results are considerable reduction in the pull. In practice the behaviour is expected to be as follows: At low magnetic inductions the pull increases with the square of the applied voltage. As saturation commences the UMP becomes linear for a short while, since saturation limits the flux density in the iron in the region of smallest gap length. At a critical induction at the knee of the saturation curve, the UMP reaches its maximum values and then decreases for higher values of applied voltage due to the sharp reduction in the permeability. Previous investigators accounted for saturation by considering an effective increase in the air-gap and using the new air-gap in determining an equivalent eccebtricity which in turn replaces the actual eccentricity in the formula for UMP. In the present calculation the effect of saturation is taken account of by introducing the relative permeability of the magnetic material in the formula for UMP. Using the flux density in equation (5.2b) means including the effect of the slotting. Slotting reduces the air-gap flux but concentrates it over the tooth region.

Fig.(5.7c,d) shows the pull drawn as a function of the eccentricity for a

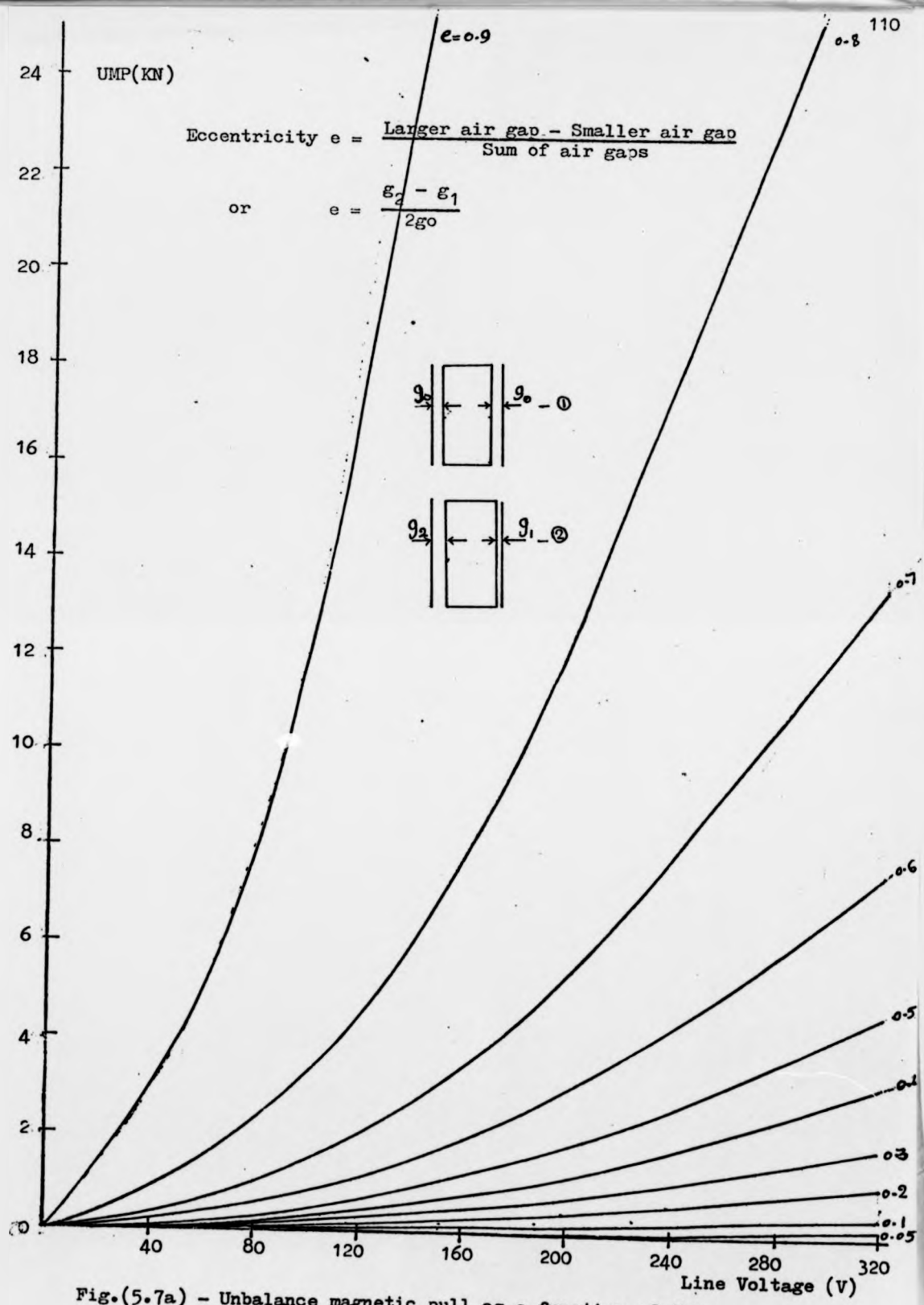

Fig.(5.7a) - Unbalance magnetic pull as a function of the applied voltage for fixed eccentricities (g=0.5mm)
(Theoritical Curves)

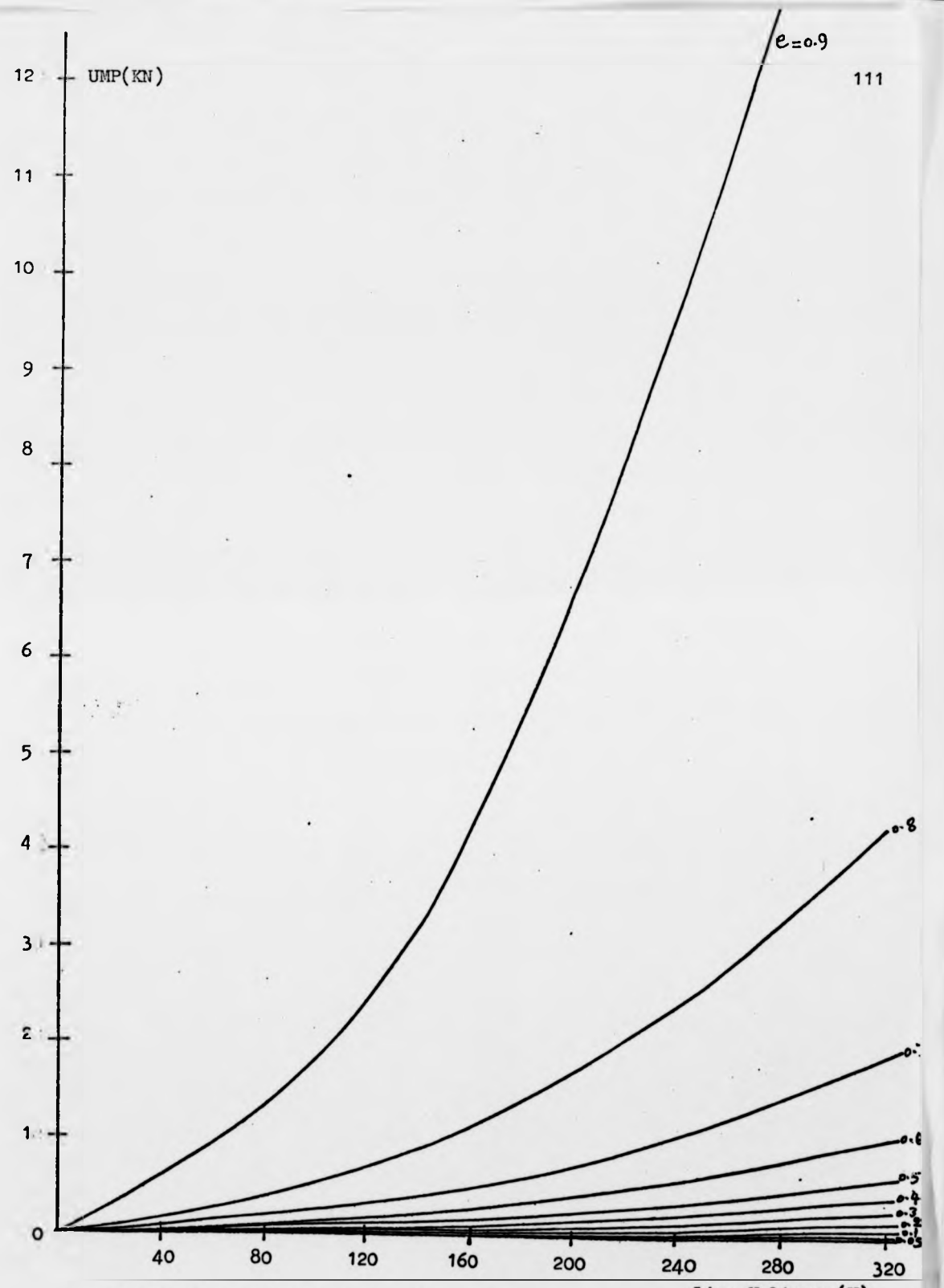

Fig.(5.7b) - Unbalance magnetic pull as a function of the applied voltage for fixed eccentricities (g=1.00mm) (Theoritical Curves)

constant air-gap flux or a constant applied voltage at two air gap lengths. For a voltage of 220 Volts and air-gap 0.5mm the pull is linear up to eccentricity of 0.4 and the rate of increase is linear. The pull is then increased more than linear at higher eccentricities aporoaching infinity.

When the voltage is increased to 310 Volts the pull increases linearly up to eccentricity of 0.3 and then deviates and approaches infinity. Comparing the pull at two different air-gaps at the same voltage and eccentricity, it is found that the increase in the air-gap length by a factor of two causes a reduction in the pull by a factor of four. By considering the pull equation and results of fig.(5.7) it is possible to see easily that as "e" increases the one side magnetic pull increases rapidly and it reaches very large values as eccentricity approaches unity.

All these considerations indicate the essential need for a rigid rotor design and a satisfactory fixing method. At the same time it demonstrates the requirement for a stator core rigidly housed in end plate. Any looseness will cause unacceptable magnetic effects. There is no comparable problem in radial machines, due to the closed cylindrical features of the stator.

5.5 UMP Measurement

Any type of unbalanced magnetic pull existing in the machine no matter what its origin is, will cause the rotor to suffer bending towards one side of the air-gap, so that any mechanical measurement of the force must start with the rotor.

A number of measuring methods have been attempted by the author as follows:

(1) Force measurements at the rotor surface using strain gauges attached to the rotor face at different places in the air-gap and taking the output through the shaft to slip-rings. This method was found to be impractical due to the following disadvantages and difficulties:

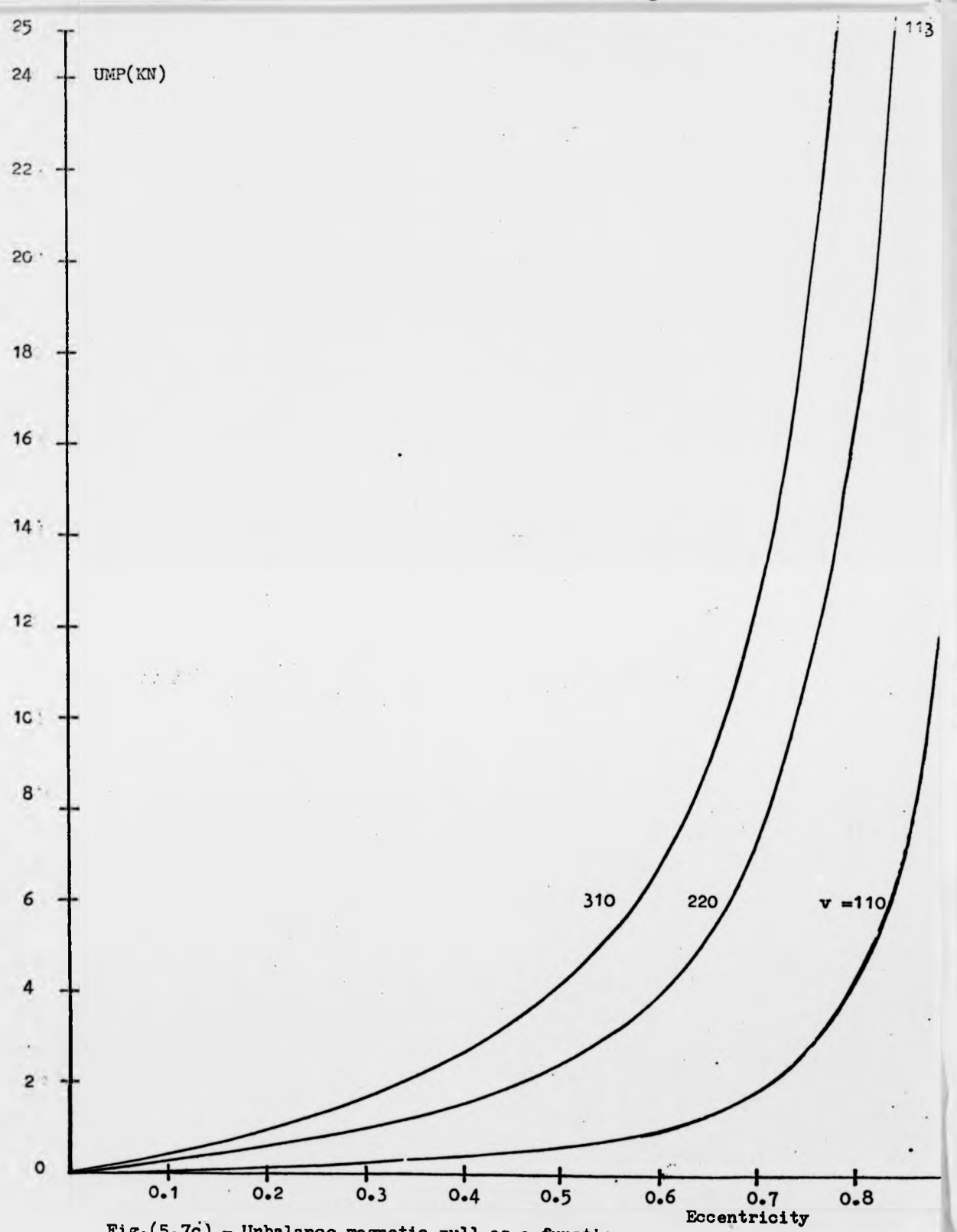

Fig.(5.7c) - Unbalance magnetic pull as a function of the eccentricity for constant applied voltage (g=0.5mm) (Theoritical Curves)

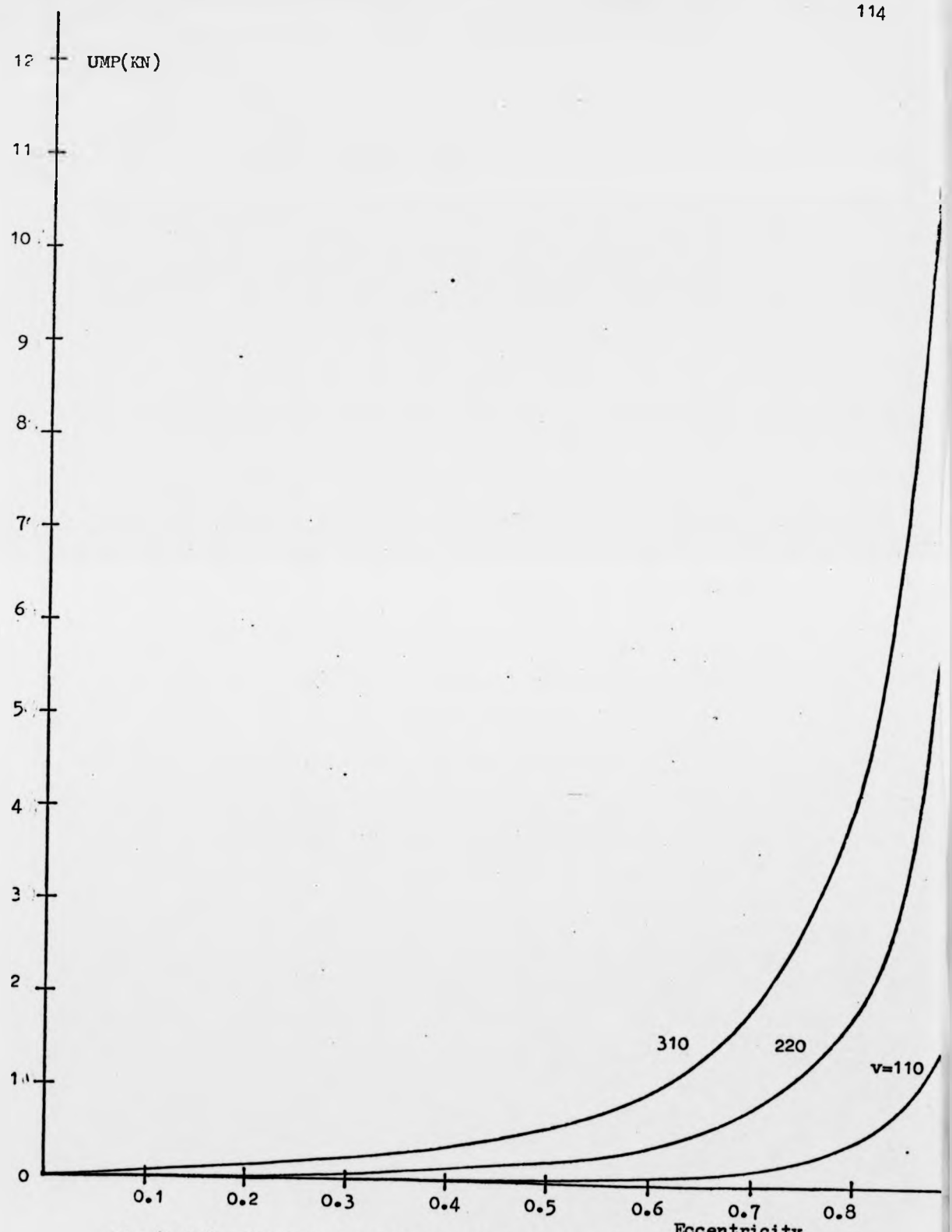

Fig.(5.7d) - Unbalance magnetic pull as a function of the eccentricity for constant applied voltage (g = 1.00mm)
(Theoritical curves)

heating at the rotor face can alter the guage outputs giving false readings; effect of the alternating field on the guage wire; and finally the output is taken from the guages through slip rings fixed to the shaft which causes high noise to signal ratio.

(2) Use of the capacitive effect between rotor and stator surfaces; The stator and rotor behave as two parallel plane surfaces, a structure which directly initiates the idea of using the change of capacitance between the two planes as a function of their separation. A number of problems exist making the apllication rather difficult. It involves the use of two conductive circular copper plates attached to the rotor and stator surfaces and consequently there exists the problem of passing current to the rotor plate. Heating of the plates and other alternating field effects gives rise to difficult problems.

Therefore owing to the difficulties involved in the two methods mentioned above it has been decided to measure the force exerted on the rotor mechanically using a transducer. The transducer designed for this purpose is shown in fig.(5.8). It consists of a central steel shaft which is pressed continuously in a direction opposite to the applied forces by a fine retaining spring. The shaft has on one end a fine ball-bearing which is in continuous contact with the rotating surface whose magnetic pull is to be measured. The bearing is free to rotate in the same direction as the surface. The advantage expected from the use of the bearing is to reduce the friction between the shaft and the rotating surface. On the other end of the shaft is attached a sharp adjustable head pressing against a thin steel strip supporting a strain guage on its opposite side. Therefore by using this transducer it is possible to transfer any mechanical force exerted on the head by the rotor to an electrical signal. The transducer gives an output signal whichever way the rotor bends. The zero adjustment can be achieved by adjusting the sharp head on the shaft and a fine

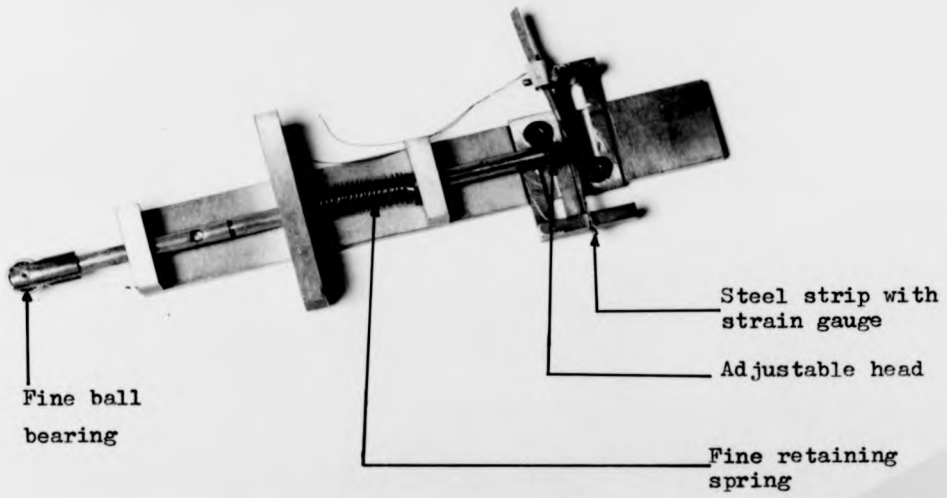

Fig.(5.8) - Force transducer

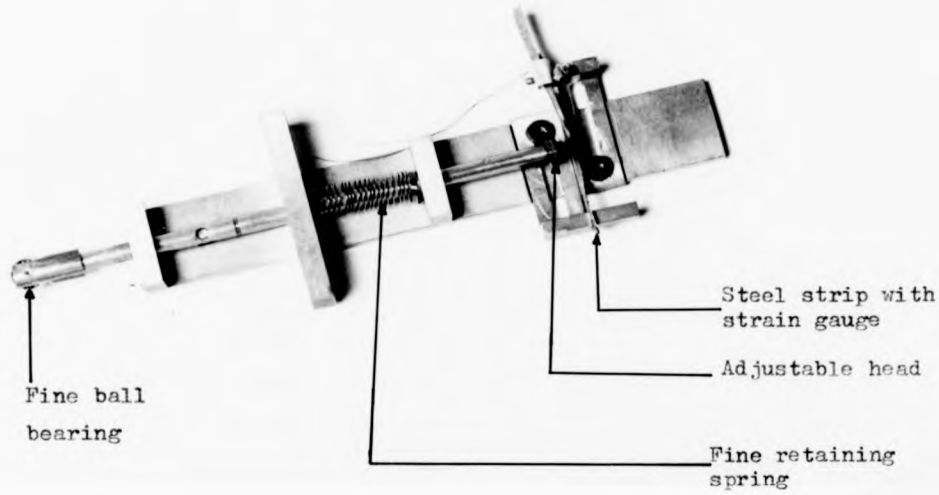

Fig (5 8) - Force transducer

resistance on the electrical bridge used for unbalance detection in which the working strain gauge is one arm. No experimental measurements could be made due to time shortage, but it is proposed to persue this work in the future.

5.6 Single sided applications

One of the most desirable features of the machine is that it is suited very well for applications requiring a flat shaped motor, especially when it is operating as a single sided-machine. Some of these include the use of the machine as a single phase driving pump motor, or to directly drive the brush in a floor polishing machine. The removal of one of the stators provides the space required for coupling the load to the rotor face including the magnetic return path and at the same time to keep the motor to the required thickness. The use of single phase winding and the removal of one stator reduces the power output and increases the UMP considerably. The power output can be increased using a double cage rotor and employing more copper in the stator by increasing the number of the coils per pole and also increasing the number of turns per coil. The problem of increased UMP can be overcome by the following techniques:

(a) Mechanically; using a rigid shaft rotating in a bush bearing supported by a thrust bearing.

(b) Magnetically; The one sided magnetic pull can be partially reduced by producing a force acting directly on the rotor in opposition to it. Rustecki (ref.1.4) used a set of electromagnet poles arranged in a circle on the stator end plate opposite to the rotor, with the magnets magnetised axially (this is known in magnetic levitation as the normal flux system). Simple calculations on the motor showed that the motor can produce a thrust force of about 160N and that the ferro-magnetic attraction force on the rotor is in excess of 2KN. It is therefore required that the repulsion force produced by any technique must have the same order of magnitude as the ferro-magnetic attraction force and the drag must be much below the motor thrust force, (perhaps in the order of 20%)giving rise to a lift/drag ratio

of about 60. The above arrangement can give rise to a drag force much greater than the thrust force causing the motor to stall. As an alternative the author suggests the arrangement shown in Fig. 5.9a using permanent magnet poles. The system employed is known as the "null flux" system in which the rotor rotates between two magnetic pole arrangements of figure 5.9a. It has been shown (ref.5.3, 5.4) that this system can give enhanced lift/drag ratio over the normal flux system. These references showed also that by using high coercivity magnets, small separations and suitable conducting ring thickness, it is possible to arrive at a "null flux" system having low drag force and considerable lift force which can be attractive in the present work. Extensive experimental investigation is required to explore the effects of different types and shapes of permanent magnets, the separations and the different aluminium ring thickness with respect to the skin depth. The experimental investigation can be improved by employing a copper ring instead of aluminium and it can yield a system operating at low drag force and reasonable lift force below the characteristic velocity (the velocity at which the maximum drag force occurs, shown as Vo in figure 5.9b).

5.6.1 Forces acting on the end ring

It is well known, ref.(5.3,5.4,5.5) that there are two types of forces acting on the end ring. These are the repulsion force described above and the drag force which tries to slow the rotor down. The repulsion force is the lift force in electro-magnetic suspension systems used in transport applications. The drag force varies in a rather complicated way with the speed of the conducting surface, and is suited for the present application with some precautions. Fig.(5.9b) shows the two forces as a function of speed. The drag increases rapidly at starting and reaches a maximum value at relatively

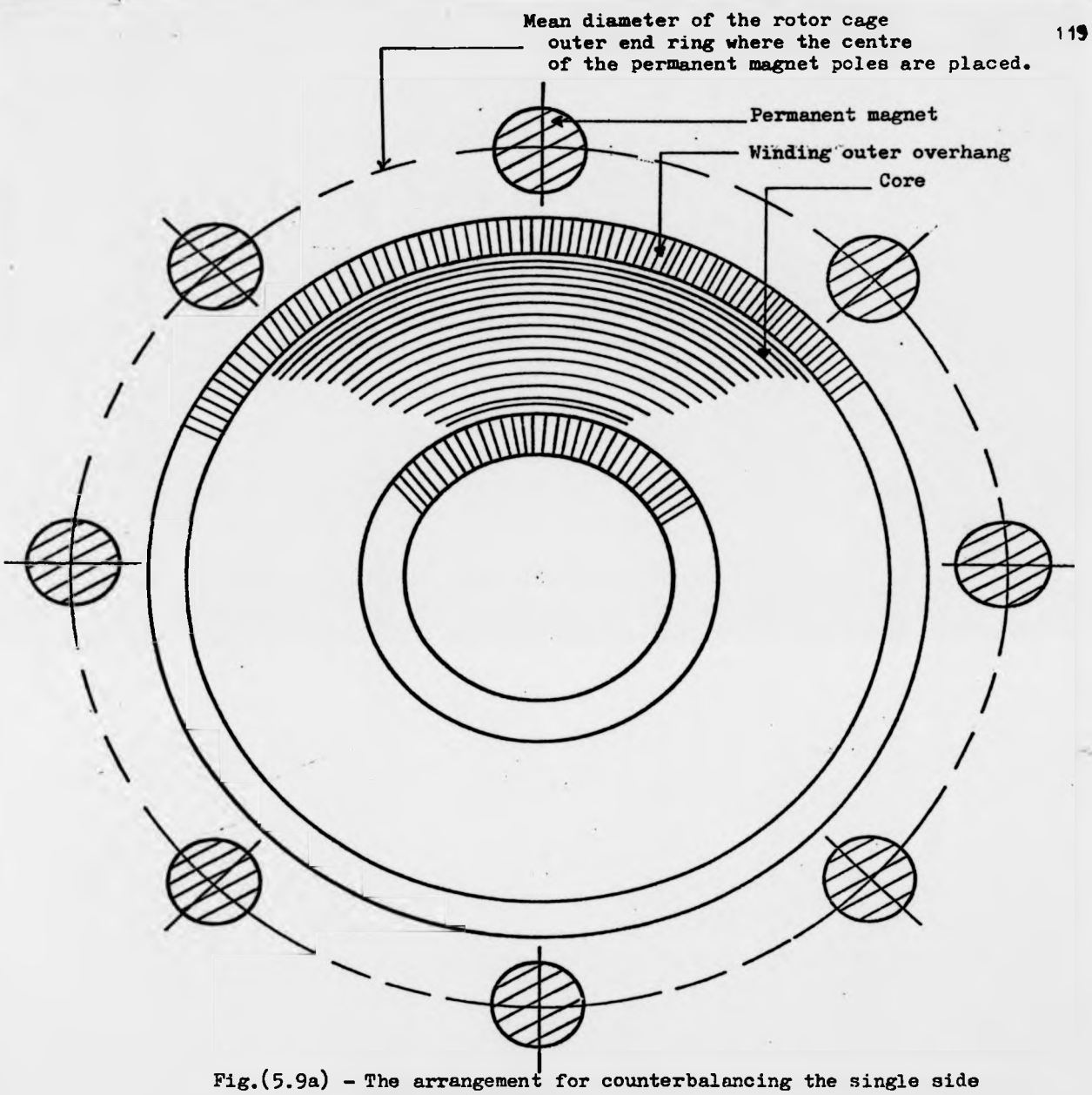

Fig.(5.9a) - The arrangement for counterbalancing the single side pull on the rotor.

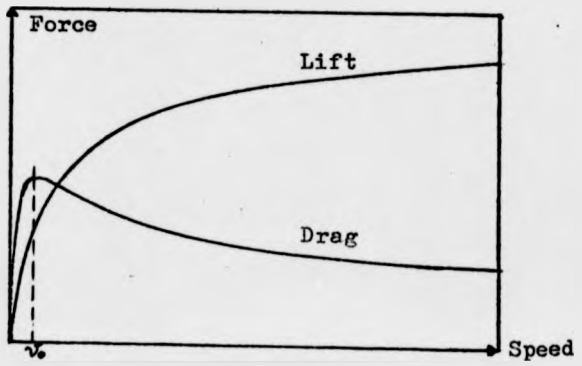

Fig (5.9b) - Drag and lift forces as function of the speed of rotation.

low speeds. It then decays sharply. The lift increases linearly with speed at starting and then increases less than linearly until it reaches an almost constant value at high speeds. Therefore it is possible to conclude that at full speed the force acting on the end ring is mainly replusive in opposition to the UMP direction which acts on the laminated core of the rotor.

The precaution needed to be considered is at starting where the drag is maximum, even if there is a good possibility that the motor can overcome such a drag. If it is difficult to start the motor under the drag, it is advisable to consider a design in which the magnets are movable in the axial direction. Therefore when starting the motor the magnets are pulled out until the motor passes the critical speed of maximum drag and then pushed home and locked for minimum distance from the end ring.

CHAPTER 6

Experimental results

6.1 Introduction

The results in this chapter are introduced in three main sections covering different tests and studies on the motor. It is hoped to introduce a brief insight into the general practical behaviour of the motor in connection with iron loss, performance characteristics with different rotors and changes and improvements achieved by introducing a number of factors such as relative position of the stators, number of cages, cage resistance, skewing and MSW. The functions of skewing and MSW are investigated by studying their effect on the performance characteristics, harmonic content and noise level of the machine.

6.2 Iron loss and Friction and windage loss

It is useful to have some insight into the iron losses occurring in different parts of the motor and the way they can be changed. The shape of the motor and its construction provide a number of possible tests for iron loss under different conditions. It is possible to measure the static iron loss(iron loss with no rotational movement) in the two stators from minimum air-gap to any required value in a manner similar to the transformer tests. The transformer in this case is the two stators with either air in between or a rotor core of magnetic material. The test started with no rotor between the stators and with a certain air-gap. Recordings were made of the input power, current, flux density and temperature of the winding up to the rated voltage. The iron loss is taken as the input power less the total ohmic loss, taking into account the resistance change with temperature rise. The test is then repeated with the rotor core without conductive cage inserted between the stators leaving an air-gap on each side half that used

in the stator-stator configuration. The static iron loss in the rotor alone is therefore found from the difference between the two power readings at each voltage. Following the same testing method the power loss in each rotor is found. This method can also be used to detect any change in the magnetic properties of the rotor core material by measuring change in its iron loss due to any external processing done on the material such as annealing and to decide whether it is beneficial or not.

6.2.1 Driving test

In this test the experimental machine is coupled to a 3 kw d.c motor the joint being made with a hollow steel shaft which is part of the torductor unit, and is supported at the middle by a self aligning bearing arrangement. The field and armature windings of the d.c motor are fed from a 240V d.c supply. The test consists of running the set once with the rotor without cage and again when the cage is inserted to find the increase in friction and windage losses due to the conductive cage together with the fan blades. The test can be used to find the fundamental frequency and high frequency losses. This can be done by running the set again with the a.c motor energised at the rated voltage, recording the a.c input to the a.c motor and the d.c input to the drive motor. Substracting the copper loss and the friction and windage from the a.c input gives the curve shown in fig.6.3a at rated voltage and mains frequency. It is not possible to obtain the exact behaviour at synchronous speed. At this speed the a.c input falls since the only input power is due to the stators losses and the pulsations. The power taken by the driving machine increases abruptly. In practice such behaviour is very difficult to notice due to the small changes in the power such that an accurate and sensitive arrangement is essential.

6.2.2 Results

Tests on the stators alone showed that iron loss depends heavily on the relative angular alignment between the two stators. It is therefore necessary to optimise the most suitable position for the stators to give as small iron loss as possible, negligible harmonics and smallest balanced currents in the three phases. The transformer test method was found to be a suitable tool for such experimental optimisation.

Fig.(6.1) shows the iron loss as a function of the misalignment between the two stators with an air-gap of 0.6mm and no rotor present. (In (a) the power loss is plotted as a function of the gap flux density at three different misalignment angles. In (b) the gap flux density is kept constant at a voltage of 100 Volts and the misalignment is increased in steps of 2^{o} up to 68^{o}, every time recording input power, currents and winding temperature. It is shown that the loss is increasing with increasing misalignment, fluctuating between large values when slots in the stators oppose and smaller values when teeth oppose slots, but the loss is increasing continuously with misalignment compared with the perfectly aligned position.

Fig.(6.2) shows the iron loss in the stators and rotors for perfect alignment as a function of gap flux density for different air-gaps. The iron loss in the stator at rated voltage and air gaps of 0,0.4,0.6mm is shown in (a) to be 42, 62, and 80 watts respectively. The increase in the loss could be due to a reduction in the flux leakage as the two stators separate causing an increase in the useful flux and naturally an increase in the iron loss. In (b) the losses in the single cage laminated and solid cores are shown to be 16.5 and 120 watts respectively. It is found that the loss in the rotor laminated core is always less than that in the stator cores and that the loss in the solid core is considerable compared to those in the stator and rotor laminated cores. These are losses in the rotors when they

Fig.(6.1a) - Stator iron loss as a function of the gap flux density for fixed misalignment angle (g = 0.6mm)

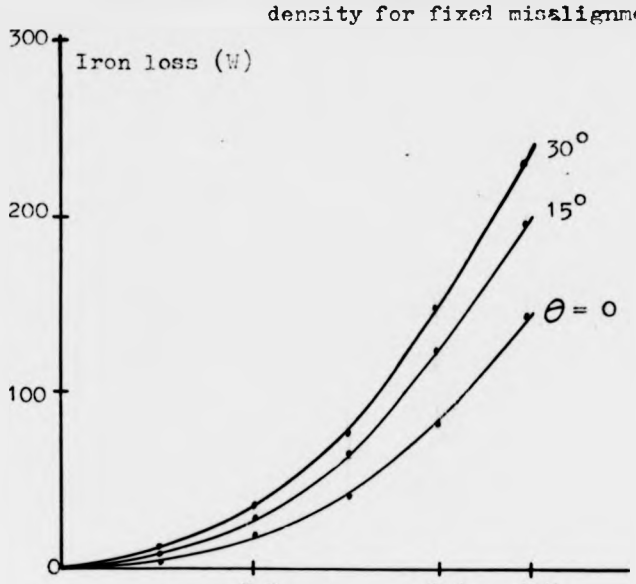

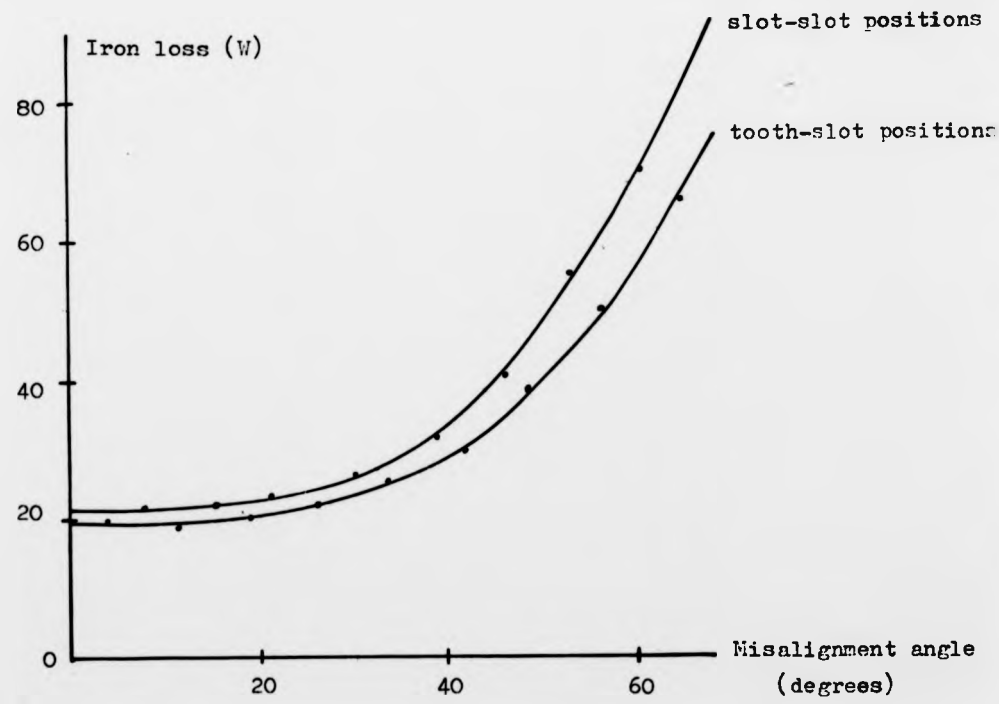

Fig.(6.1b) - Stator iron loss as a function of misalignment angle for constant flux density.
(g = 0.6mm, V = 100 Volts)

Fig.(6.2a) - Stator iron loss for different gap lengths and perfect alignment ($\theta = 0$)

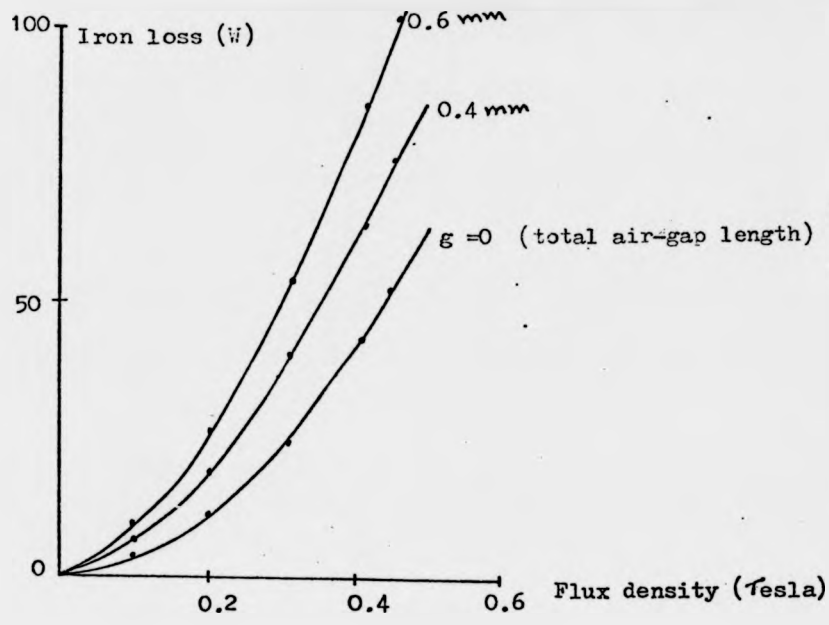

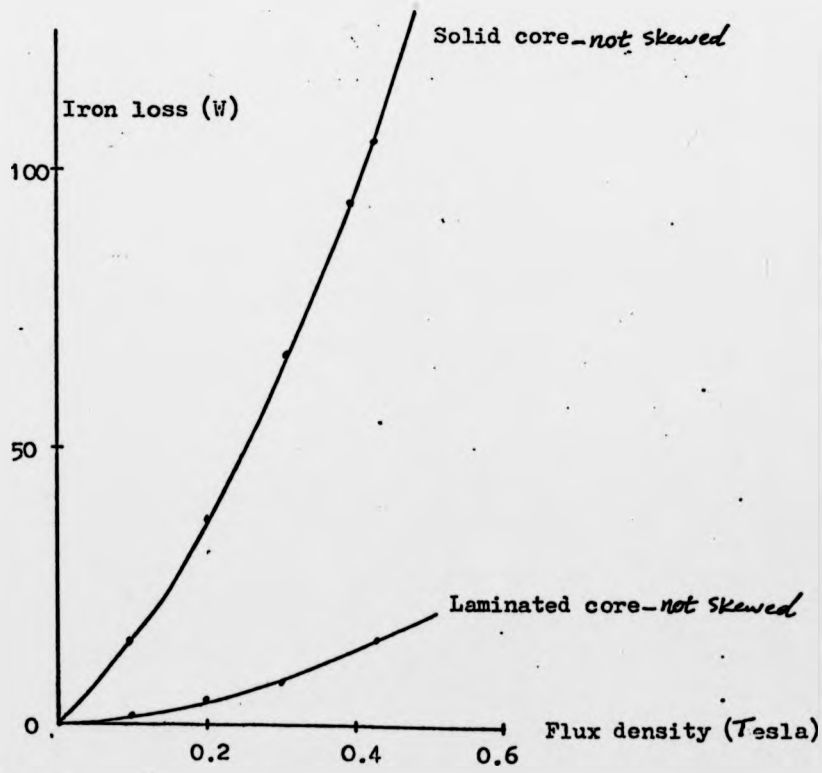

Fig.(6.2b) - Iron loss in the single cage laminated and solid rotor cores.

are stationary, but when the cores run near synchronous speed (slip of 0.08) these losses decrease dramatically since they depend on the square of rotor frequency. Some results of the driving test are shown in fig.(6.3). In (a) the friction and windage losses with the single cage laminated core is shown. The F & W curve is almost proportional to the speed. In (b) results for the double cage rotor are shown.

6.3 Annealing

Winding the steel strip into a spiral spring, dropping the inner and outer steel rings around the cores, holes and slot openings through laminated layers are all sources of a complex system of stresses applied to the metal. This type of cold metal work in addition to changing mechanical properties also changes the physical properties of the metal such that there is a detrimental effect on the magnetic properties. Therefore it is always required to restore the undeformed, relaxed condition after processing. There is an energy barrier which opposes such a relaxation which can be overcome by heating the metal to a suitable temperature, for a certain period of time under specified conditions in a process known as annealing. The second aim in annealing in the present work is that it is hoped that by heating the laminations it might cause the individual layers to displace from each other thus helping to break the shorting between layers which occur during machining and consequently reducing the iron loss. The type of steel stripes used is coated with a thin heat resistive layer which stand the annealing temperature. The cost of the strip is found to be almost twice that of the non-coated strip of the same magnetic properties. It is therefore worthwhile to carry out an experimental investigation to show how necessary is the thermal coated layer on the strips especially that there is no clear answer to this problem as far as the author is aware. The experiment performed is a comparison test of the iron loss in one magnetic

Fig.(6.3a) - Driving test on single cage (laminated) rotor.

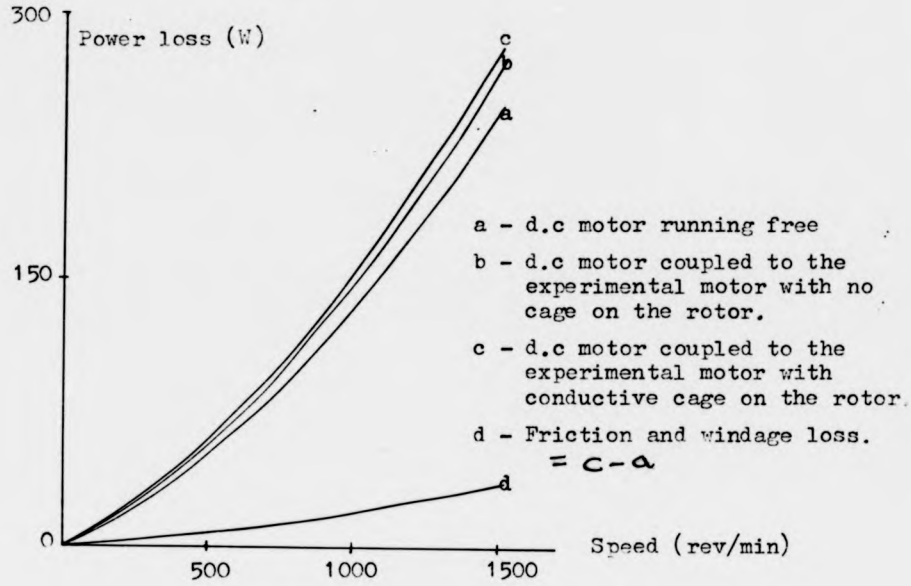

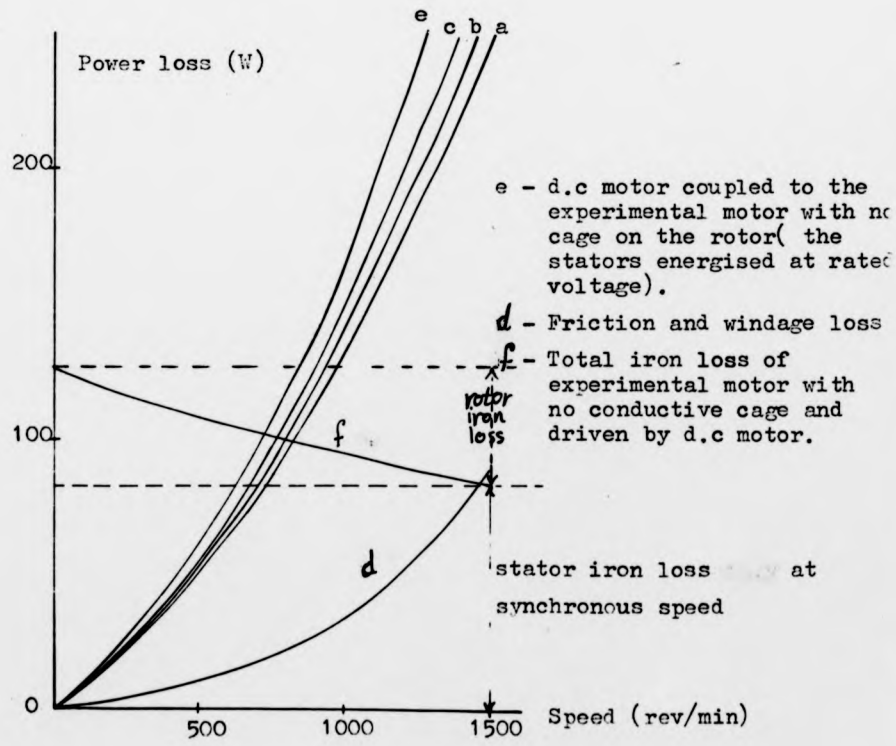

Fig.(6.3b) - Driving test on double cage motor

material at different conditions and it is approached as follows:

6.3.1 Experimental assessment

The experiment is a modified form of the Epstein square test. It consists of a square made of four identical magnetizing coils each in the shape of a solenoid 0.19m long wound with 635 turns of heavy gauge enamelled wire connected in series to form the primary winding, fig.604a. Each primary coil has on its centre, a single layer coil of thin enamelled wire of 500 turns. These coils are connected in series to form the secondary winding. The magnetic material used in the test consists of strips of the same steel employed in the prototype machine having (0.0005 x 0.5 x 0.25 m) dimensions with no coating layer. The strips were arranged in four bundles, each of fourteen steel strips, assembled in the shape of a complete square to form a closed magnetic circuit with the corners overlapped and clamped to give minimum reluctance. The electrical circuit used in the tests is shown in fig. 6.4b.

The requirement of a constant flux (V/f = Const.) throughout the test is achieved by using the generalised machine set available at the laboratory. It consists of a slip ring induction machine mechanically coupled to a d.c. machine, the speed of which can be controlled from (1500-3000) rev/min. The windings of the induction machine are connected to give a two-pole, three-phase machine of 240V rated voltage. By controlling the speed of the d.c. motor, an output with a frequency range of (0 - 100)Hz is obtained at the slip rings. The condition (V/f = Const.) is achieved by taking the output through a variable autotransformer. When the frequency (f) is changed the output voltage (V) at the secondary terminals has to be adjusted to give the same ratio. The test is repeated three times under exactly identical conditions with respect to the constant flux and the volume of the air-gap inside the coils, but with different combinations of steel strips. Comparing the iron loss as a function of the frequency which is conducted as follows;

a - The fourteen strips in each bundle are uninsulated and pressed together to be in complete contact in a single bundle and with

Fig.6.4 - Epstein square test

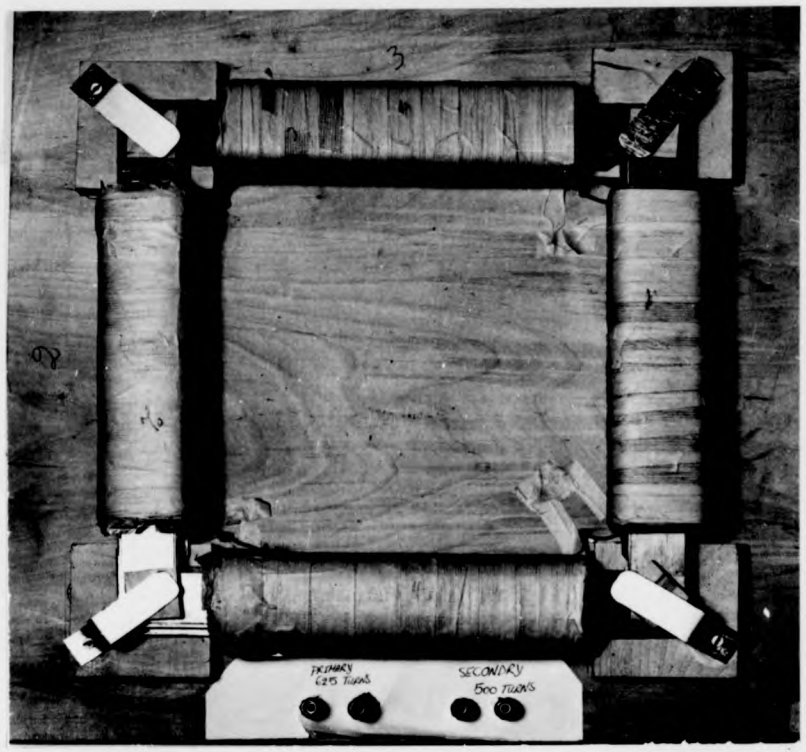

a - Epstein square built by the author

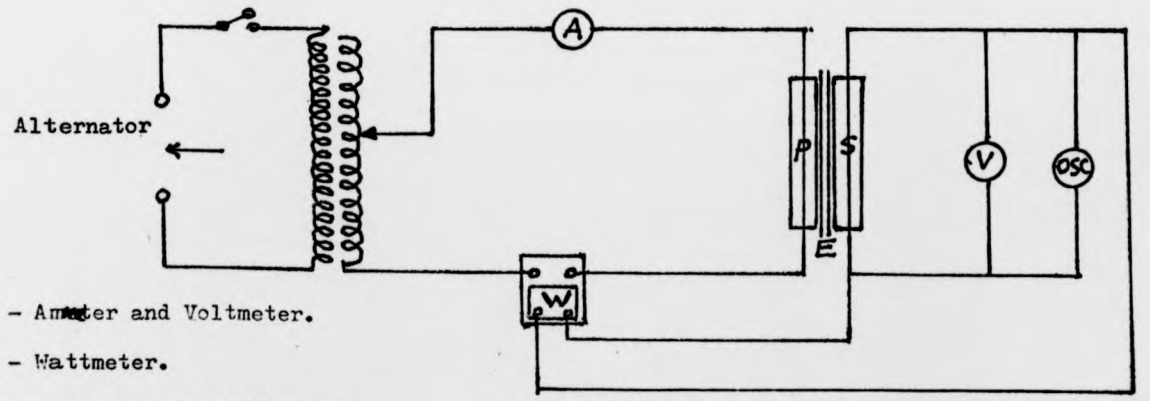

A,V - Ammeter and Voltmeter.

W - Wattmeter.

OSC - Cathode ray Oscilloscope.

E - Epstein square.

P,S - Primary and Secondary of E.

b - The circuit used in Epstein square test
(- based on BS601: part 5/1973)

Fig.6.4 - Epstein square test

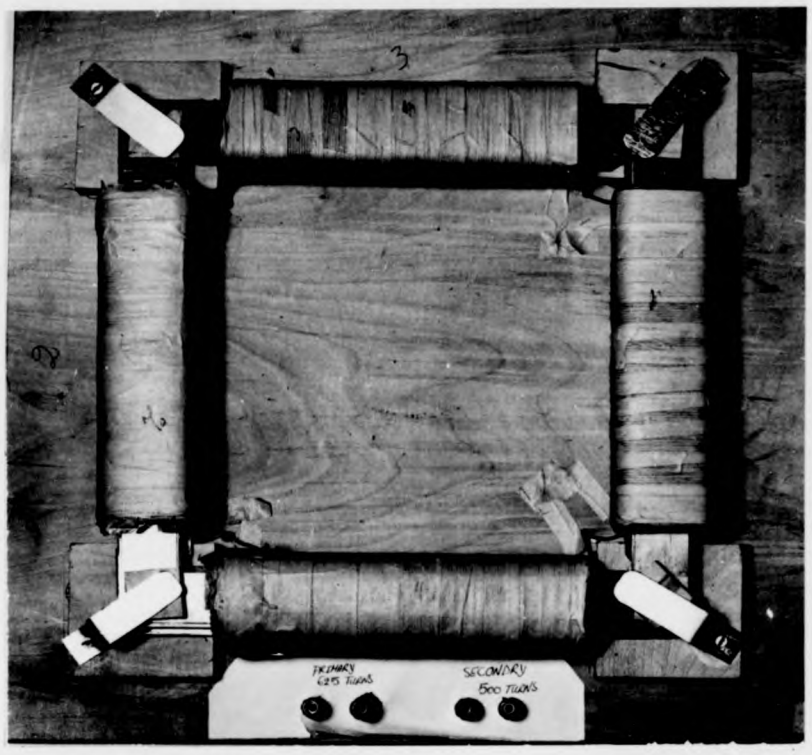

a - Epstein square built by the author

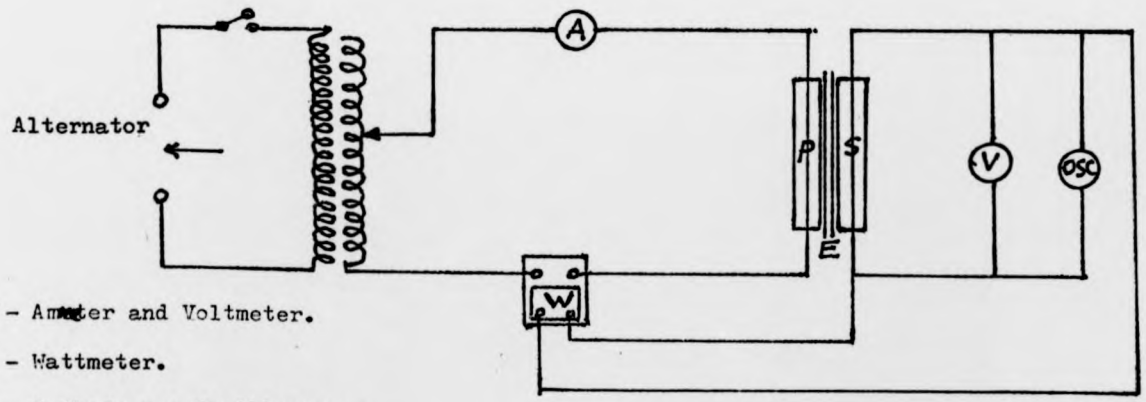

A,V - Ammeter and Voltmeter.

W - Wattmeter.

OSC - Cathode ray Oscilloscope.

E - Epstein square.

P,S - Primary and Secondary of E.

b - The circuit used in Epstein square test
(- based on BS601: part 5/1973)

Fig.6.4 - Epstein square test

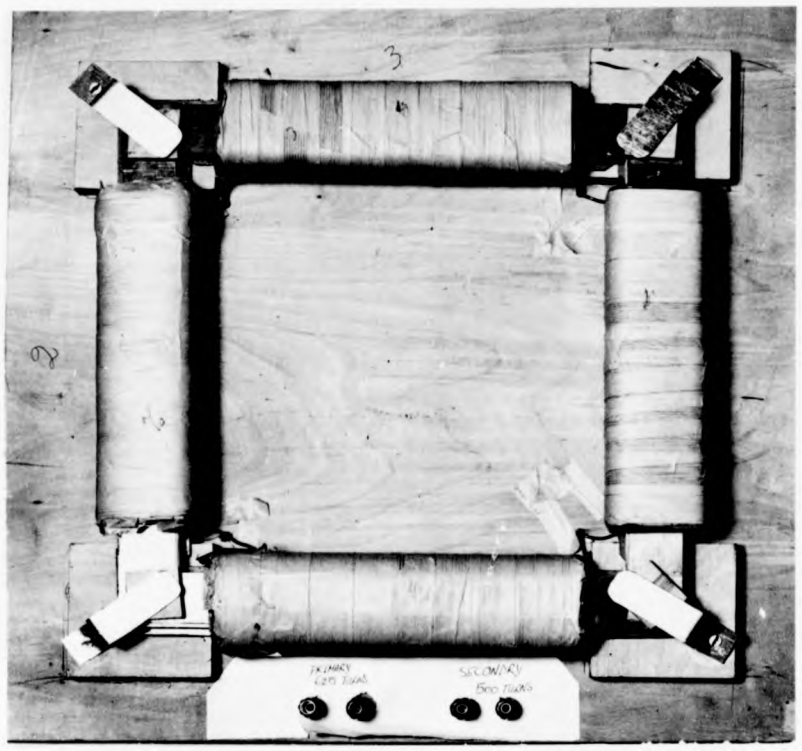

a - Epstein square built by the author

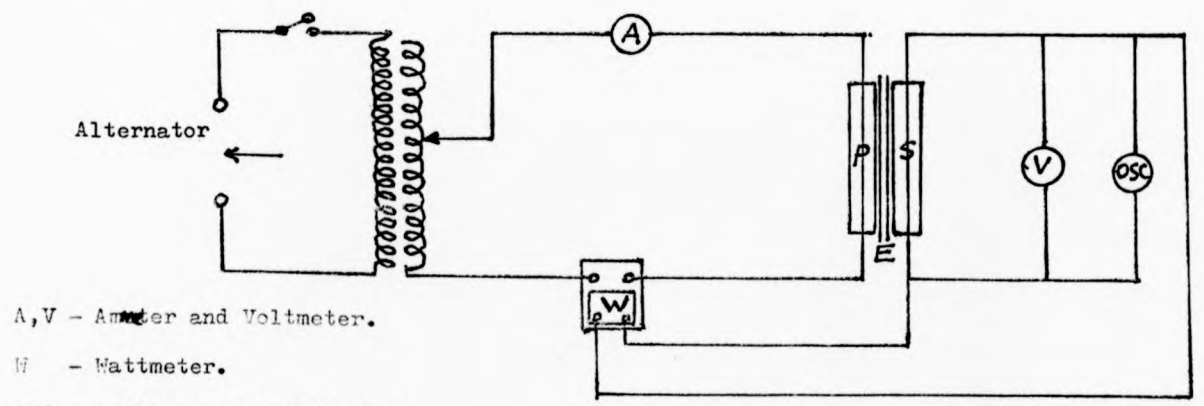

A,V - Ammeter and Voltmeter.

W - Wattmeter.

OSC - Cathode ray Oscilloscope.

E - Epstein square.

P,S - Primary and Secondary of E.

b - The circuit used in Epstein square test
(- based on BS601: part 5/1973)

others in the neighbouring bundles.

b - (a) is repeated with the strips insulated completely from each other.

c - The fourteen strips in each bundle are now replaced by a solid rectangular bar of steel having the same volume as the fourteen strips pressed together.

The conditions in (a) and (b) simulate the practical conditions in the slip wound rotor or stator in respect of eddy current loss. The waveform of the alternator output is checked continuously and is found to be reasonably sinusoidal except at frequencies below 12 Hz.

6.3.2 Results

The curves in fig.(6.4) show the total input power to the square as a function of the frequency. The ohmic loss in the coils is neglected in tests 'a' and 'b'. In test 'c' the temperature of the coil is recorded continuously and the copper loss is deducted from each power reading.

Fig.(6.4c) - shows the loss curves at two constant values of flux when the strips are not insulated and in complete contact.

Fig.(6.4d) - shows the results for completely insulated strips under the same conditions as in the previous figure.

Fig.(6.4e) - shows the results when the strip bundles are replaced by equivalent solid bars.

Comparing figures 6.4e and 6.4d shows that to reduce the eddy current power loss in a solid element, it has to be laminated into thin layers parallel to the magnetic field. The reduction in the power is found to be of the order of twenty times at 100 Hz and seventeen times at 50 Hz. Comparing figures 6.4d and 6.4c shows that there are no big discrepancies in the power loss in the experimental frequency range. This is of great importance in connection with the cost of the machine since the cost of the non-coated steel strip is

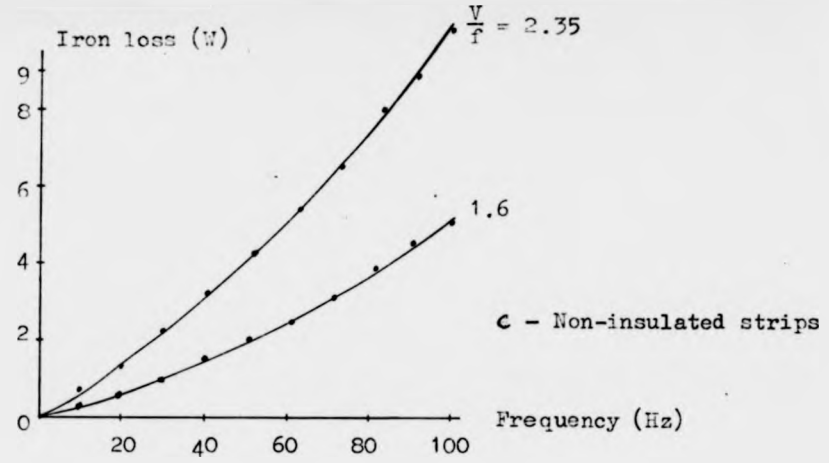

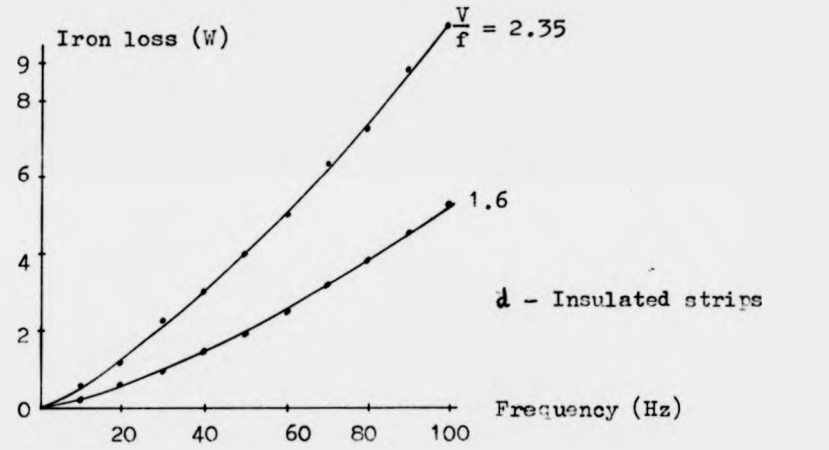

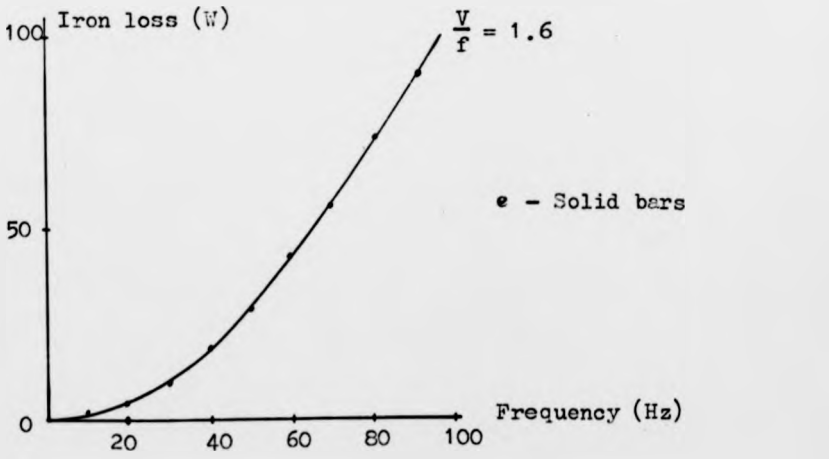

Fig.(6.4) - Iron loss as a function of the frequency at constant flux showing effect of the insulation between the steel strips.

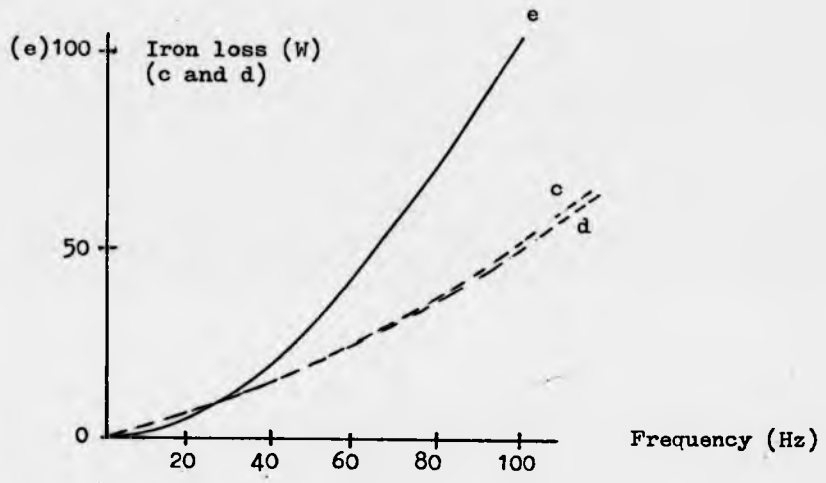

Fig.(6.4f) - Comparison between the iron loss curves of figure (6.4 c,d,e)

6.57

barely half the cost of the coated steel employed in constructing the experimental machine. This similarity in results could be due to the oxide layer formed on the strip which acts as a good insulator or because the strips are not in a perfect contact or a mix of both. In this machine it is advantageous to use as thin strips in core winding as possible whereas in conventional machines the sheets of steel have got to be thick enough to stand the stamping and cutting processes. Using thin strips reduces the loss in individual strip considerably and provides much easier winding and more rigid cores and at the same time it reduces the mechanical and magnetic stresses. Fig.(6.4e) suggests also that the use of a solid rotor made of cast iron involves high power loss. To reduce the power loss the rotor is constructed of three solid rings of 0.14, 0.14, 0.145m radial thickness inserted together. It is expected that such a design is acceptable in reluctance type machines.

6.4 Performance test

This section of the work is aimed to investigate the effect of a number of factors on the machine through the study of the performance characteristics and detecting the changes occurring. It is required to study the efficiency, output power, power factor and starting characteristics with each rotor and to investigate the effect of changing the air gap, cage resistance and some other factors shown later. The performance characteristics are studied by performing a load test with each rotor, using a Ward-Leonard system. The complete test rig together with the electric circuit used in the test are shown in fig. (6.5a,b). The disc motor was loaded by a d.c. machine which can be operated as a motor or a generator, with its output balanced against another d.c. machine which can be made to generate or motor by controlling the field current. By using this arrangement it was possible to control the loading very smoothly and over a wide range. The overloading of the motor is avoided as much as possible to prevent any damage to the winding since the motor is required for further tests and studies in the

Fig.(6.5) - Test rig

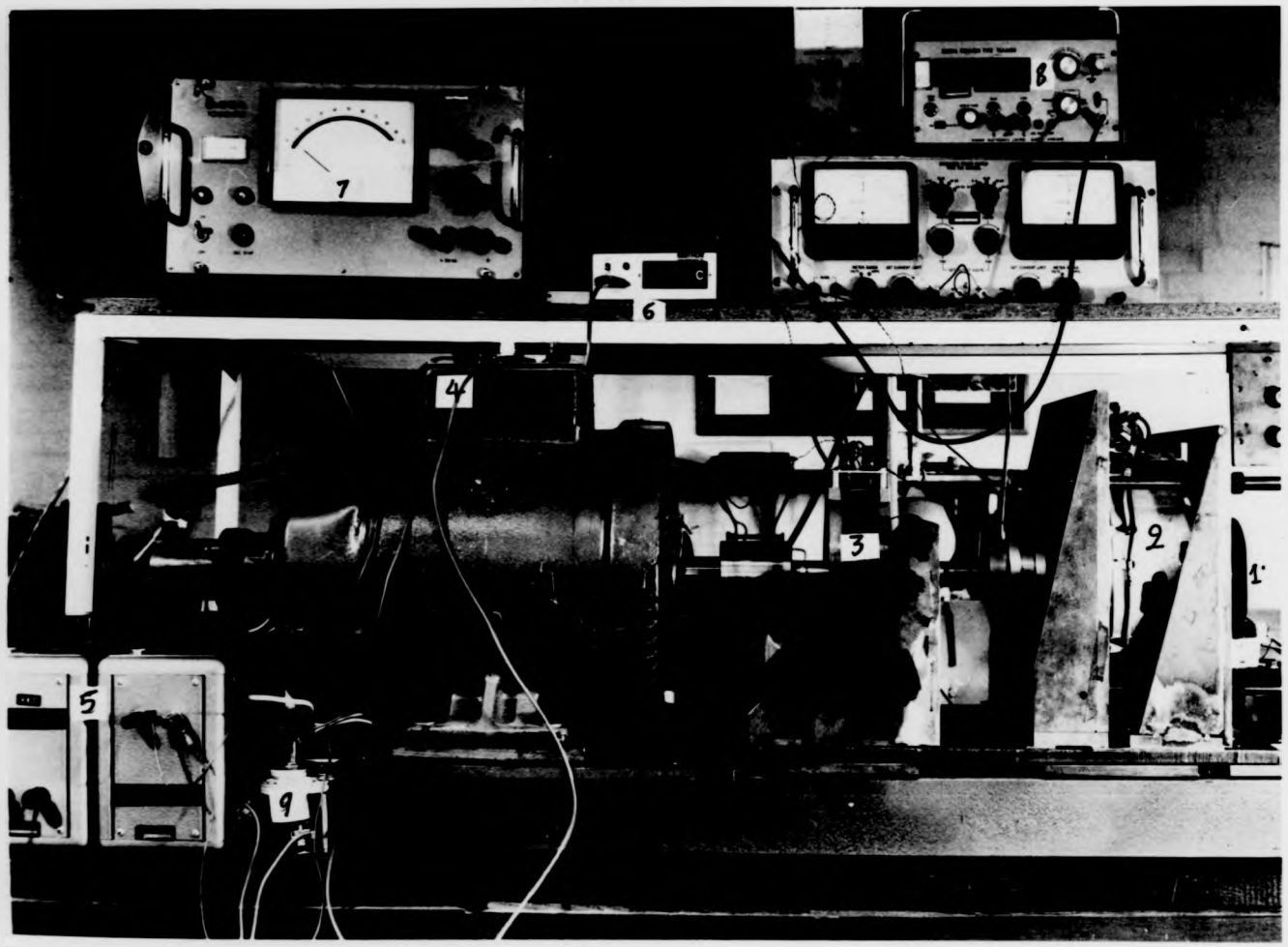

1. Speed measuring arrangement
2. Experimental machine
3. Torductor
4. d.c machine (generator/motor)
5. Field controls
6. Thermometer and thermocouple
7. Torque measuring meter
8. Digital counter
9. Isolator switch between the rotors of the d.c machines.

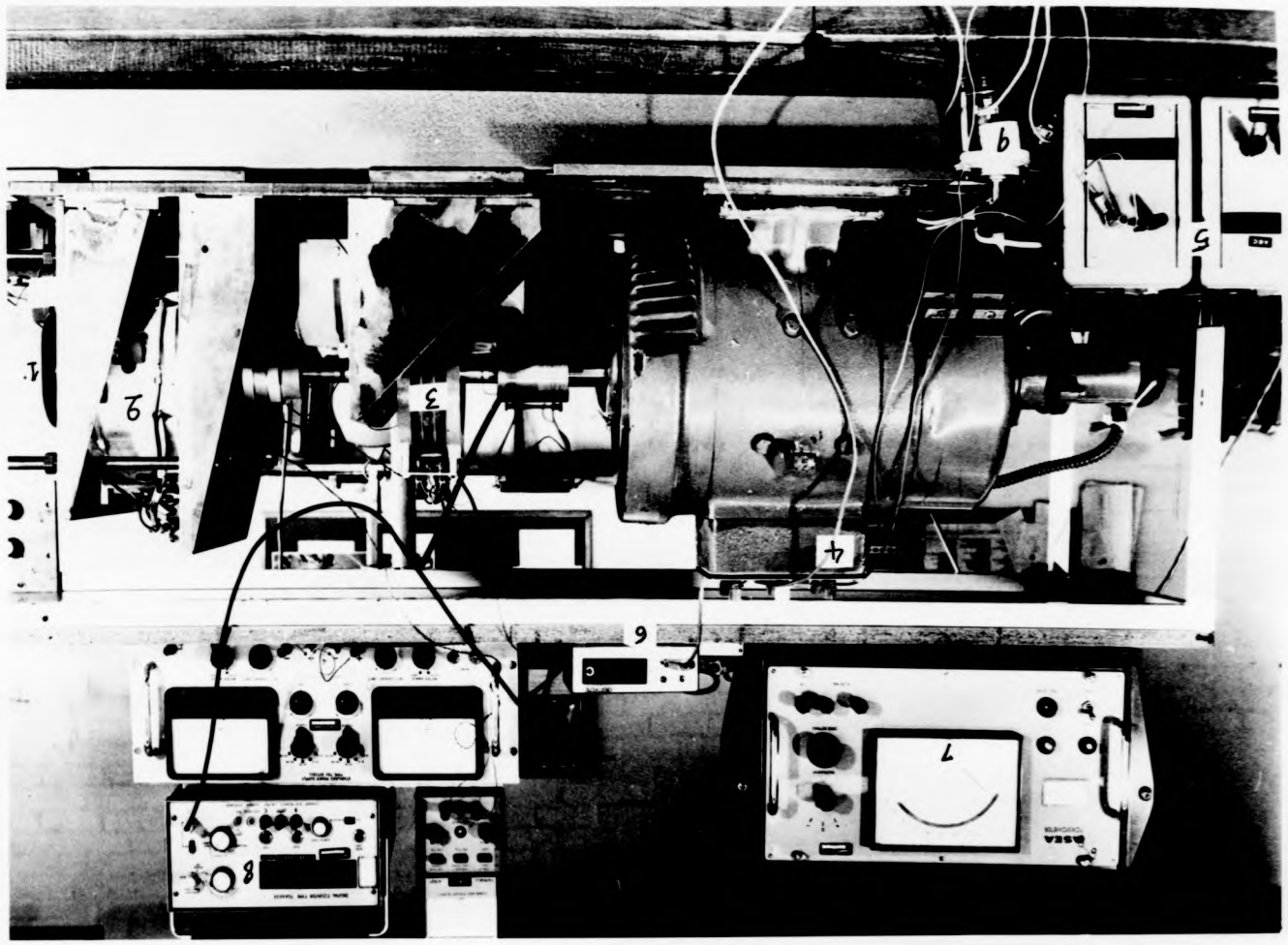

Fig.(6.5a - Test rig

1. Speed measuring arrangement
2. Experimental machine
3. Torductor
4. d.c machine (generator/motor)
5. Field controls
6. Thermometer and thermocouple
7. Torque measuring meter
8. Digital counter
9. Isolator switch between the rotors of the d.c machines.

Fig.(6.5) - Test rig

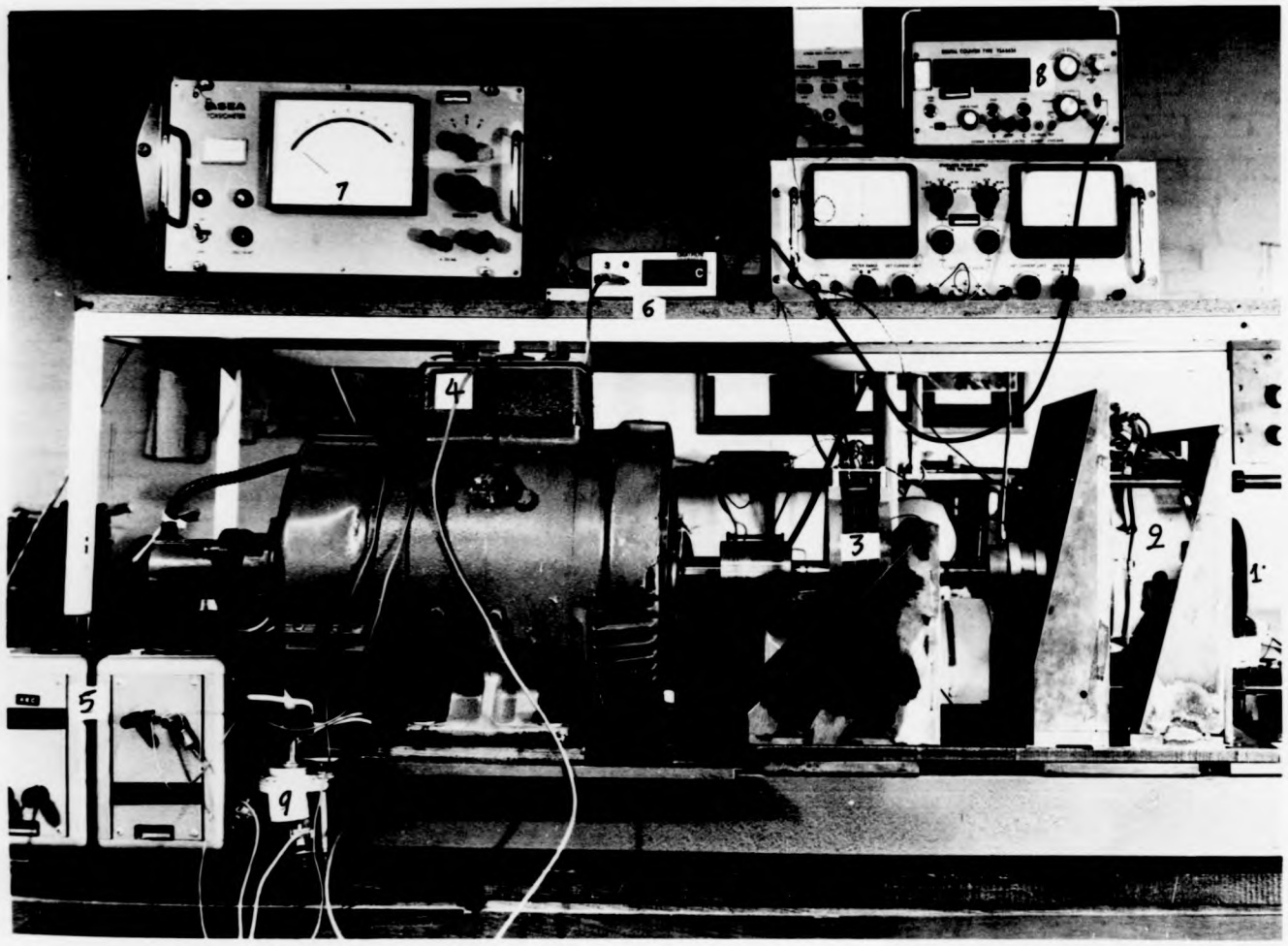

1. Speed measuring arrangement
2. Experimental machine
3. Torductor
4. d.c machine (generator/motor)
5. Field controls
6. Thermometer and thermocouple
7. Torque measuring meter
8. Digital counter
9. Isolator switch between the rotors of the d.c machines.

Fig.6.5b – Circuit diagram of the experimental rig of figure 6.7

1 – 3 – Phase variac.

2abc – Electric bulb, slotted disc and photo-transistor

3 – Digital counter.

4 – 3 – Phase induction motor (experimental machine)

5,6 – Tordllctor and Torque-meter.

7,8 – d.c. motors (240V., 6Kw and 6.75Kw)

9 – AC/DC variable **rectifier.**

10 – 3 – Phase Alternator (230V., 3KVA)

A, W1, W2 – Ammeters and Wattmeters.

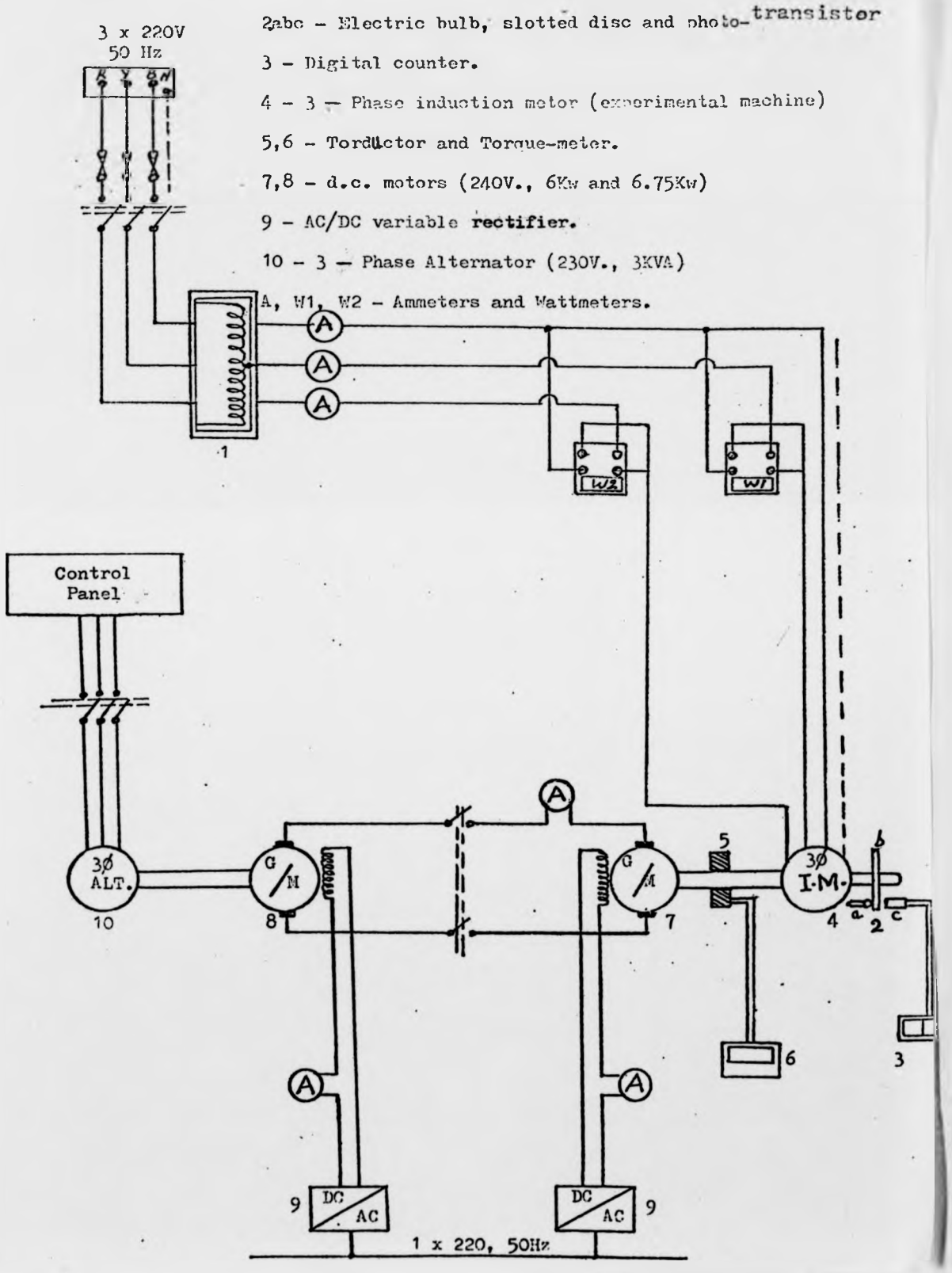

near future. No work has been done on the reluctance type machine and the work is concentrated on the induction machine only since the production of a good induction machine means indirectly the possibility of having a satisfactory reluctance motor. The load test was performed on every rotor at three air gap lengths of 0.5, 0.7 and 0.9 mm. The exact air gap length is obtained by using ready made space washers of specified thickness. The friction and windage loss was measured every time the air gap required changing to compensate for any change in this power when the motor is disassembled. To take any set of readings the system is allowed to run for a few minutes to reach the steady state before readings are taken. When the rated values are required the motor is continuously loaded and the steady state temperature of the winding is recorded until a loading is reached which causes a temperature rise near the safe limit (see p.102) of the winding insulation. The values of the current, power output and torque are then taken as the rated values of the motor. The same arrangement of fig.(6.5) is used to measure the starting characteristics. This has been done by locking the hollow shaft possing through the torductor in a place between the torductor and the loading motor. The torque, current and temperature rise were recorded as the voltage was increased step by step as high as possible.

6.4.1 Test results

Fig.(6.6) shows the performance of the motor fitted with rotor D at three air gaps. This includes curves for efficiency, power factor and output power as functions of the speed. Only the speed range (1000 - 1500 rev/min) is shown, since it covers the range of the experimental study. It shows the maximum values attained and moreover it simplifies the plotting. The rated current of the machine is found to be about 6.25A which is equivalent to a current density of $5A/mm^2$. Increasing the gap is found to reduce the magnetizing reactance and has no effect on the other parameters. The machine parameters at the three air gaps are measured for the same rated current for

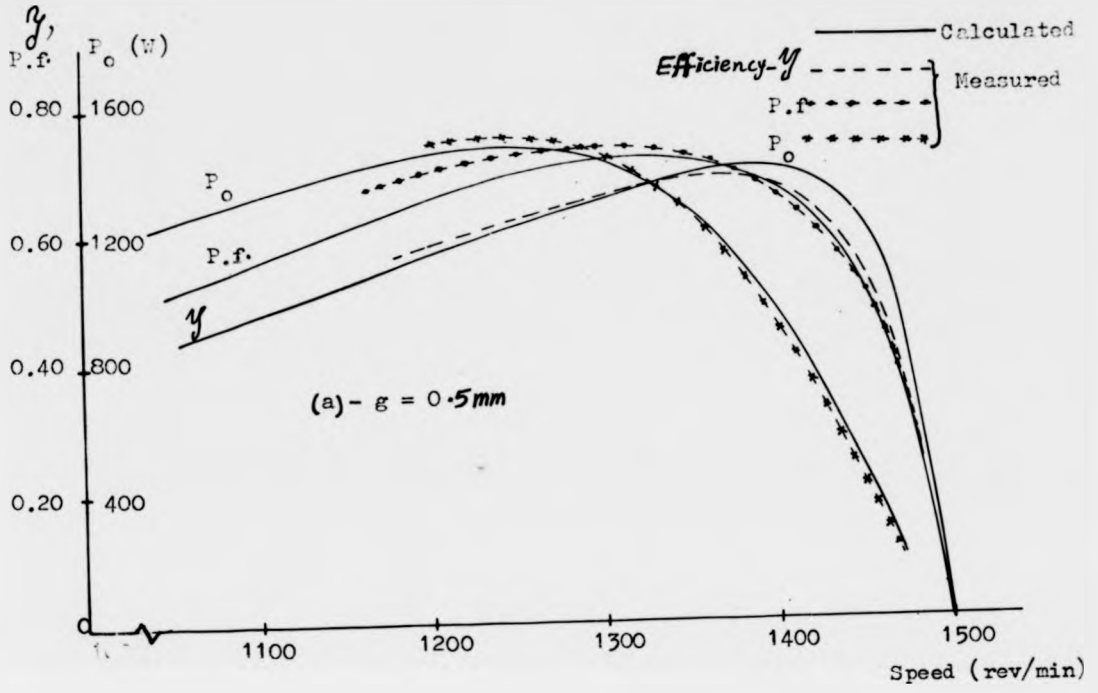

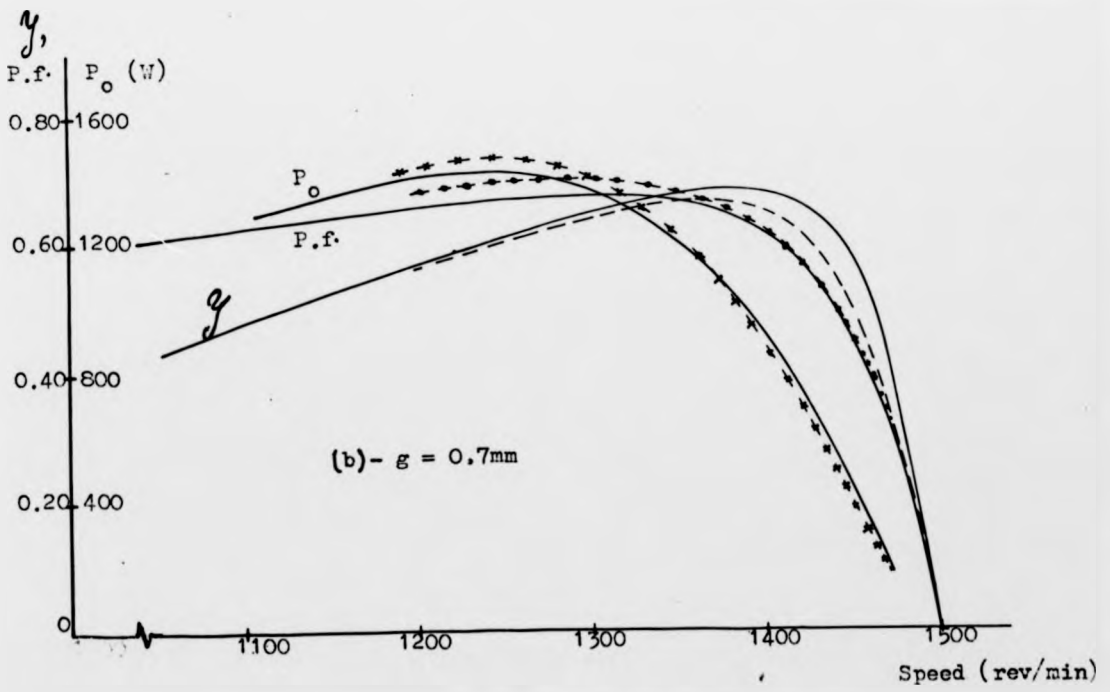

Fig.(6.6) - Performance characteristics of the experimental motor operated with rotor D at different air gap lengths.

a specified rotor. The theoretical results are obtained by calculations based on the equivalent circuit of chapter 4, using the machine parameters given in table 4.2. The effect of the temperature rise on stator and rotor windings, iron loss and F & W loss in each case, stator copper loss and rotor loss are included in these calculations. Results of fig.(6.6) are typical for induction motors, having a maximum efficiency of 69% at a slip of 0.08 and 0.5mm air gap length. It offers a rated output of 1.11kw and consequently a power/weight ratio of 60 watt/kg.

Fig.(6.7) shows the torque/speed and the phase current/speed curves. These curves fit very well with the theoretical results in the experimental range. To complete the torque curve, the starting torque is measured at voltages below the rated voltage and the curve is then extrapolated to give the starting torque at rated voltage as shown in fig.(6.8). By knowing the turning point of the curve and the starting torque it is possible to complete the torque curve as shown. In most of the load tests, values of the torque were obtained as near the turning point as possible indicating the range of maximum torque. Following a similar procedure and assuming that the starting torque is proportional to the square of the current, the complete phase current/speed curve is obtained. Fig.(6.9) shows the torque/speed curves at three air gaps showing that the starting torque and the maximum torque are falling with increasing air gap lengths.

Fig.(6.10) shows the performance results of the motor with rotor C with skewed bars at 0.5mm air gap length and three cage resistances. The change in the cage resistance is achieved by machining parts of the two end rings. By doing so, parts of the radial bars in the axial direction are machined also giving rise to an effective method of resistance change. Fig.(6.10a) shows the results before any machining (r_2=2.41Ωat 75°C) giving a maximum efficiency of 69% at a slip of 0.093 and rated power of about 0.9kw. Fig.(6.10b) shows the results when 4mm is machined from each end ring (r_2=2.72Ω) giving a maximum efficiency of 68% at a slip of 0.093 and an output power of 0.85kw.

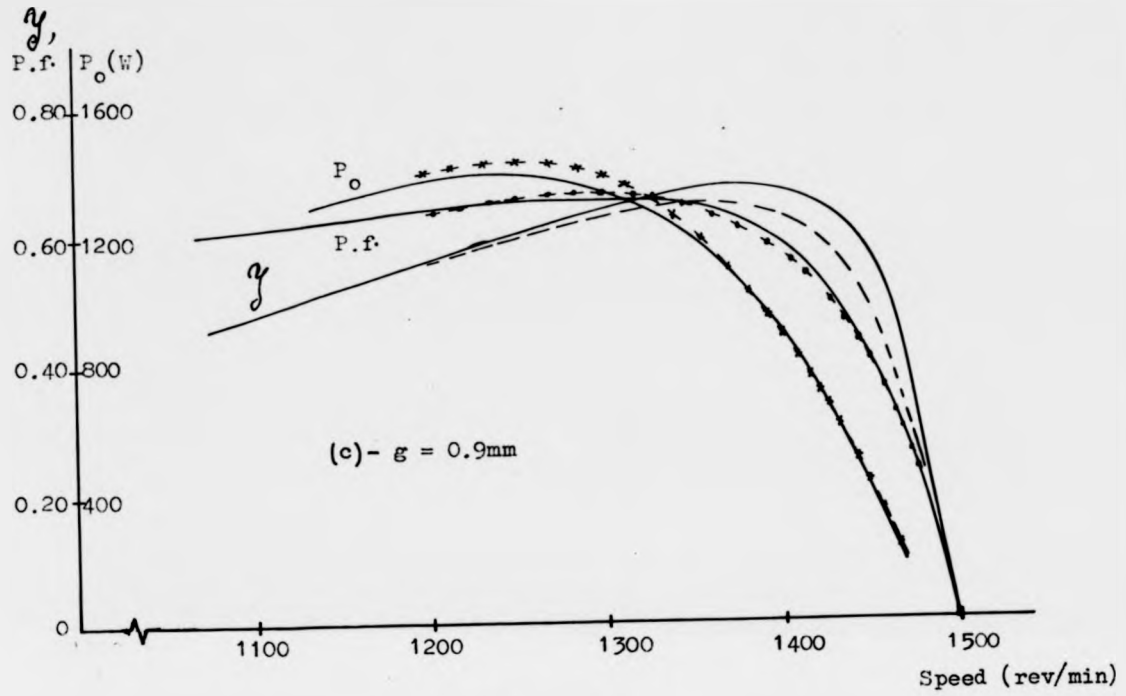

Fig.(6.6) - continued

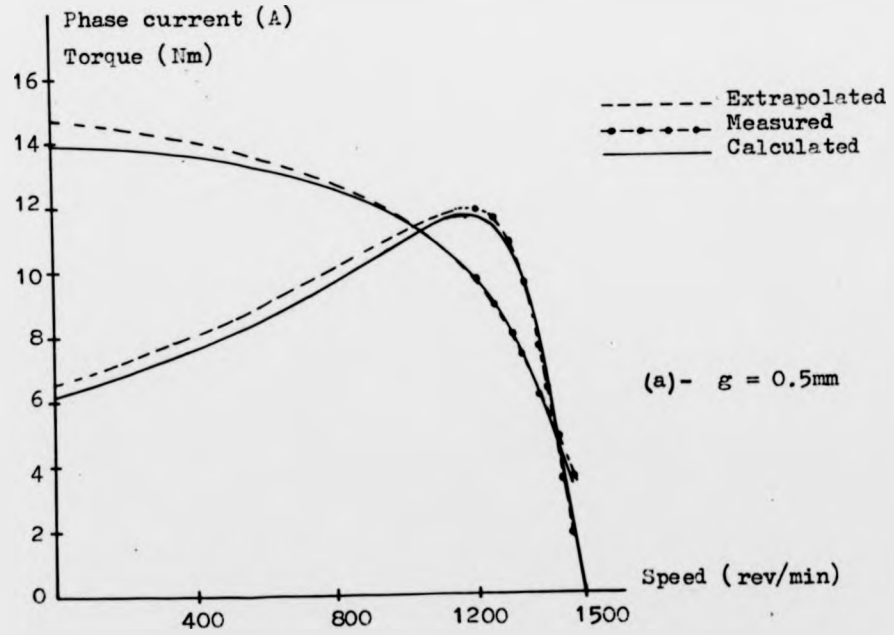

Fig.(6.7) - Torque/speed and phase current/speed curves of the experimental motor operated with rotor D at three different air gap lengths.

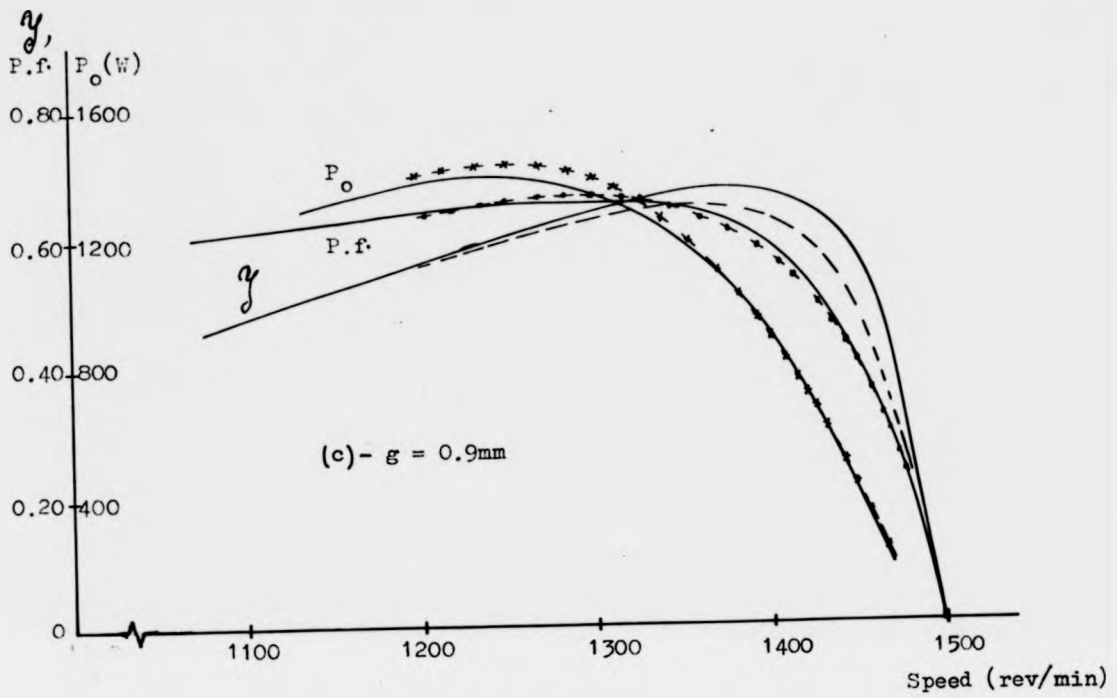

Fig.(6.6) - continued

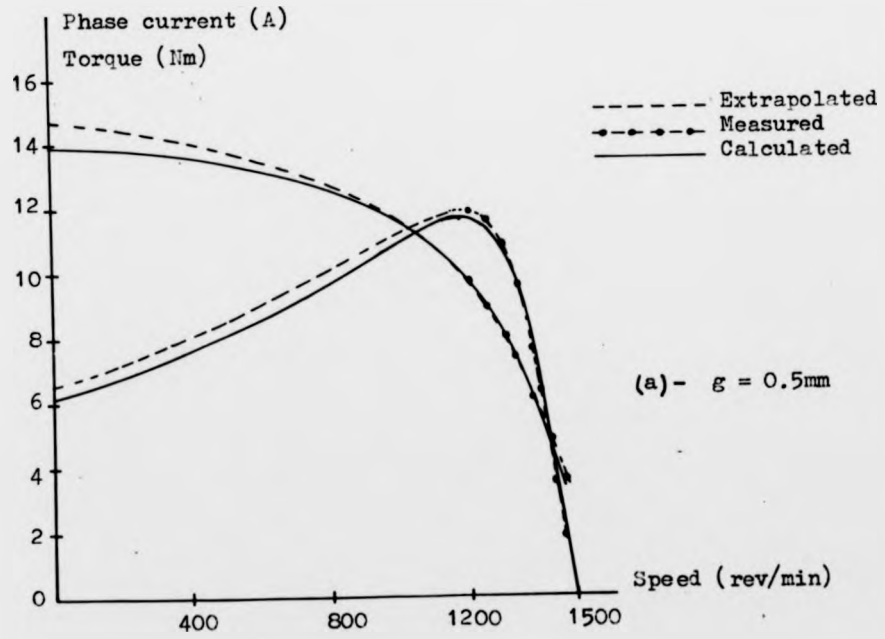

Fig.(6.7) - Torque/speed and phase current/speed curves of the experimental motor operated with rotor D at three different air gap lengths.

Fig.(6.7) - continued

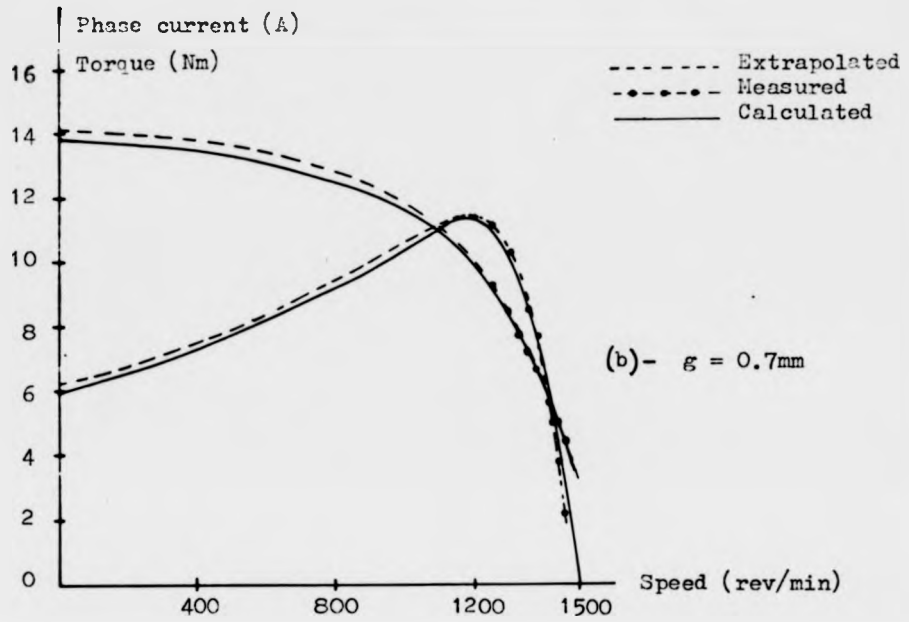

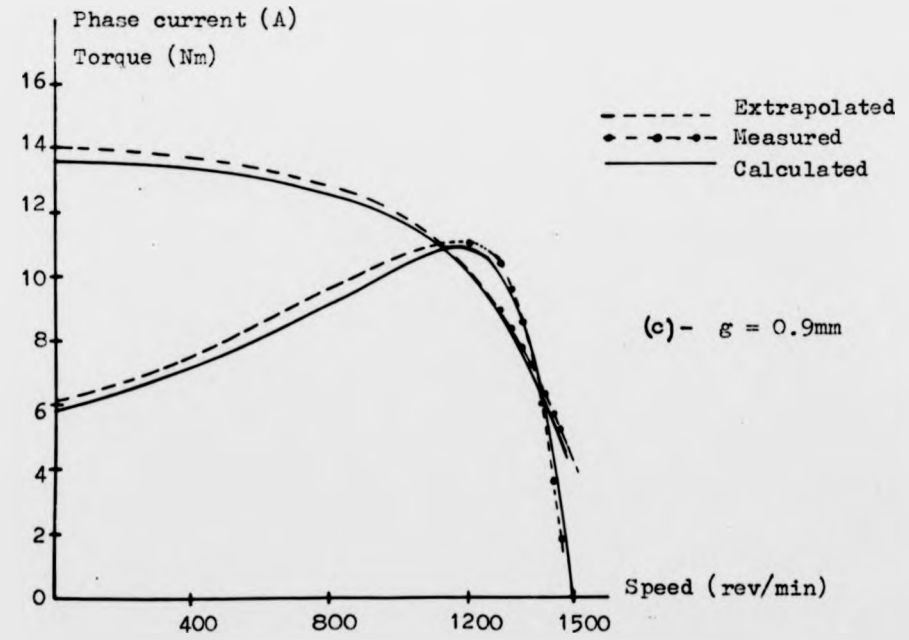

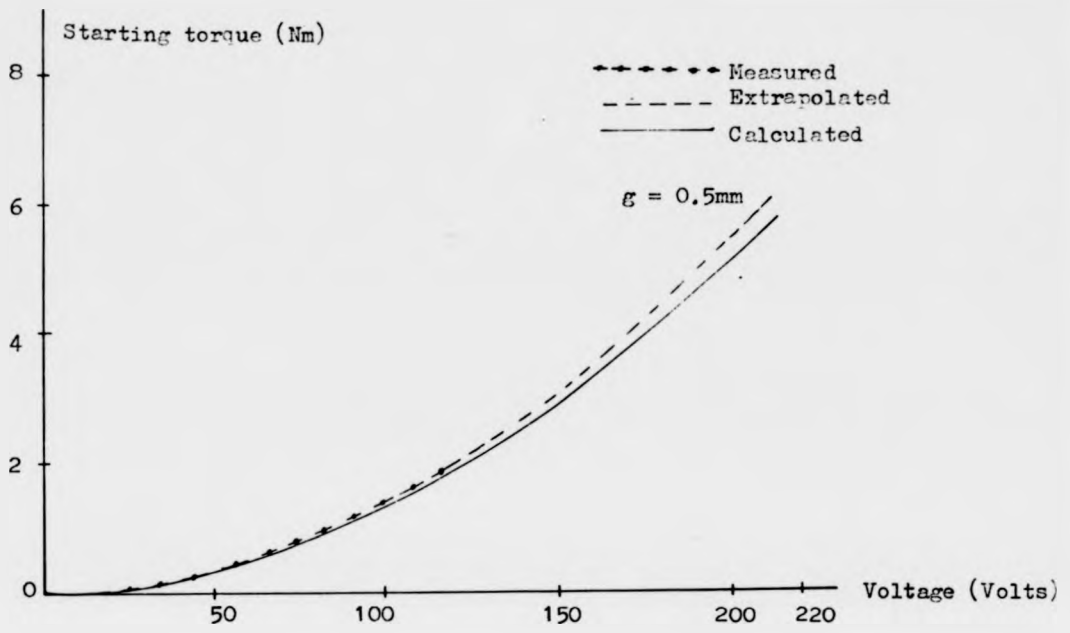

Fig.(6.8) - Starting torque as a function of the applied voltage for the experimental motor operated with rotor D.

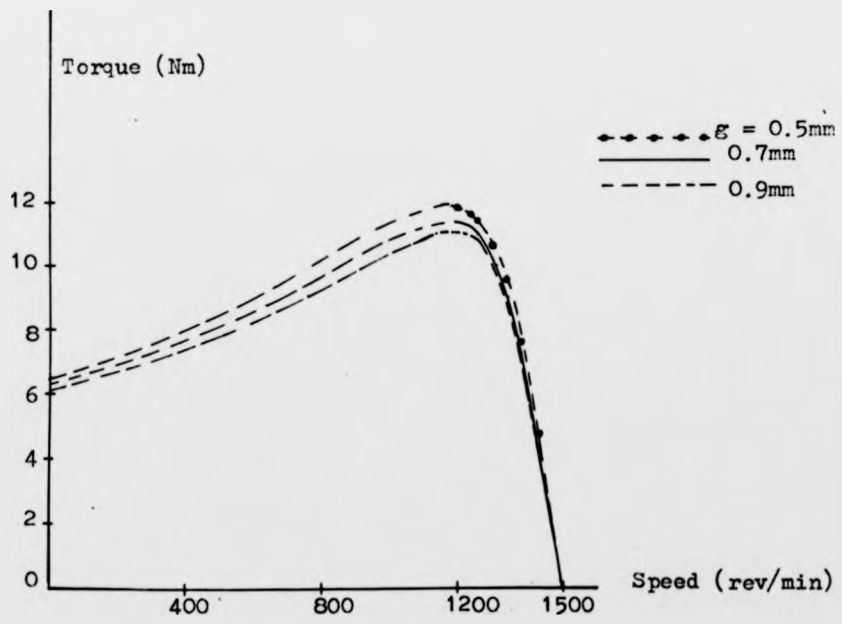

Fig.(6.9) - Torque/speed curves of the experimental motor operated with rotor D measured at three air gap lengths.

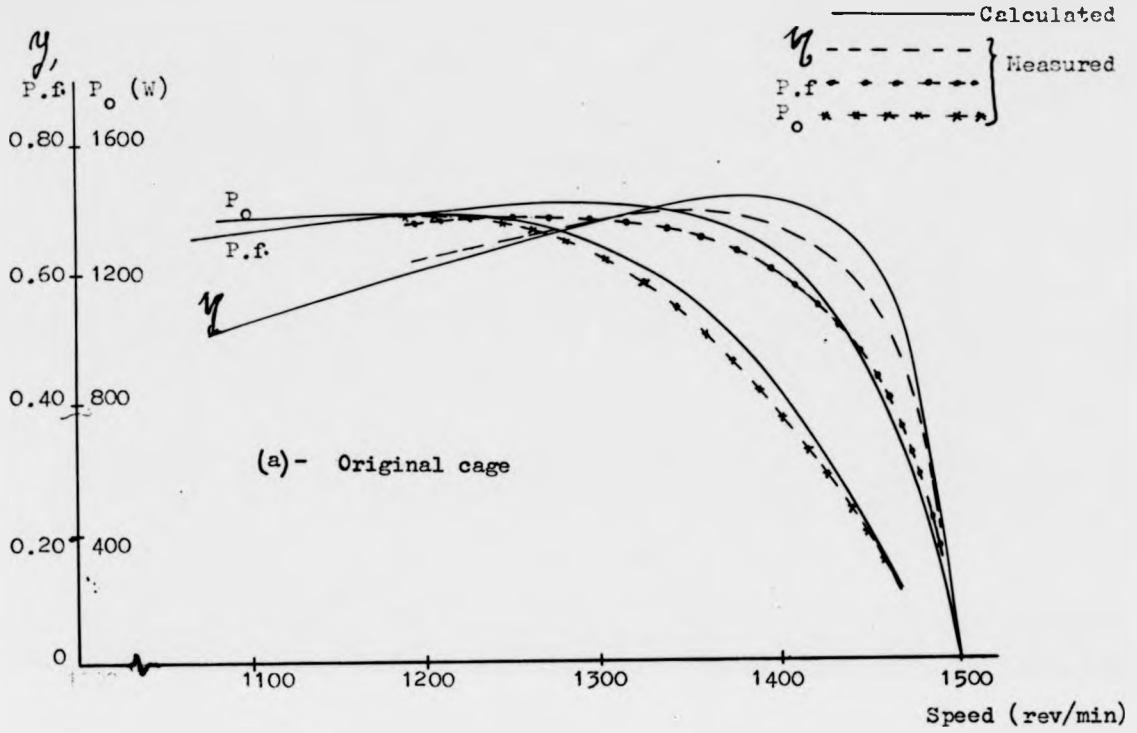

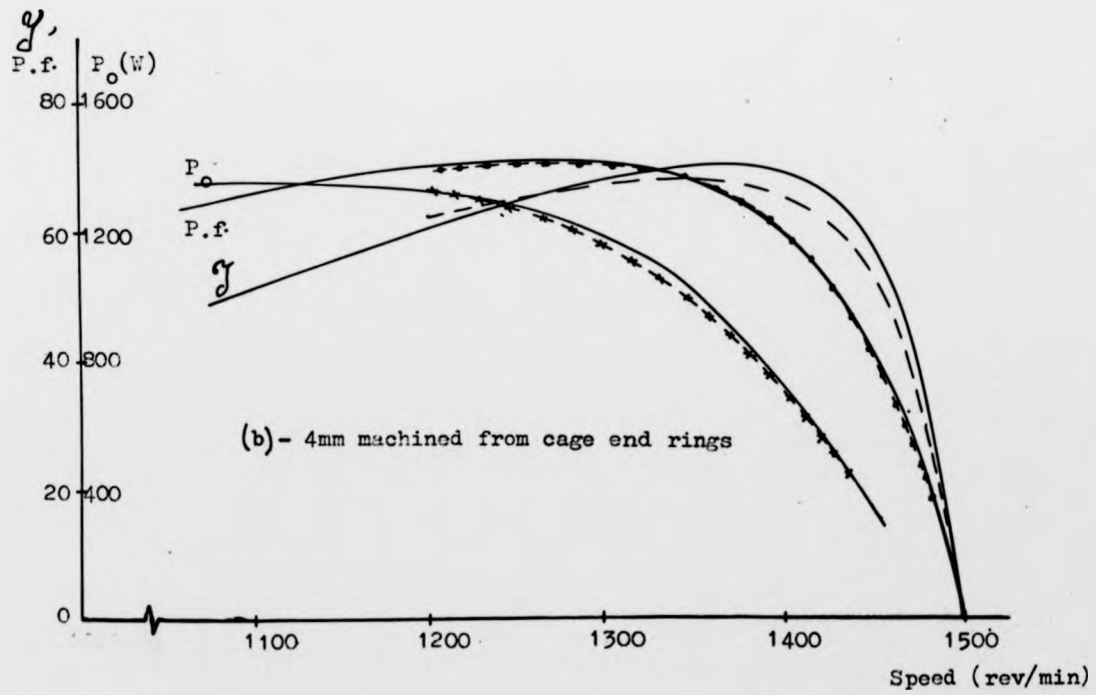

Fig.(6.10) - Performance characteristics of the experimental motor operated with rotor C for a fixed air gap length (0.5mm) and three values of cage resistance.

Fig.(6.10c) shows similar results after 7mm is machined (r_2= 3.2Ω) giving a maximum efficiency of 65.5% at a slip of 0.12 and an output power of 0.68 kw. All the three output powers given above are taken at a slip of 0.08. It is considered that the power output is reduced compared to that with rotor D due to the lower number of bars employed in this rotor. But the most significant is that the motor operated with rotor C runs smoothly and quietly compared to that when it is operating with rotor D due to the skewed bar effect, causing a reduction of about 9 dBA in the sound level (Sound level is the weighted rms combination of sound intensities of different frequencies actually existing,measured by using sound-level meter at a distance of about one meter from the motor). Following the same technique the complete torque/speed and phase current/speed curves are shown in figs. (6.11, 6.12). These figures show that the torque and phase current are falling as r_2 increases, but the starting torque increases and starting current decreases. Fig.(6.11) shows also that the maximum torque decreases as r_2 increases and it occurs at a larger slip. Test results on the motor fitted with rotor A are shown in figs.(6.13, 6.14). Maximum efficiency obtained at 0.5mm gap length is 56% at a slip of 0.12 and an output power of 0.8 kw is obtained at a slip of 0.08.

Fig.(6.13) shows the torque/speed and phase current/speed curves of the motor, showing that it has high starting torque and high starting current. It is found also that the motor has low rated current and consequently lower rated output power compared to the above rotors. The rest of the test is concerned with work on the motor operated with rotor B. This rotor consists of two single cages on a common core axially separated by a laminated bridge and electrically connected at common end rings produced in the casting process. Therefore when the two cages are connected together through these end rings, the rotor behaves as an effective single cage of relatively low resistance, but when the end rings are separated, the rotor behaves as two single cage rotors mechanically coupled back to back having higher effective cage resistance. The separation of the end rings by cutting through each common ring causes a reduction in the axial depth of the bars

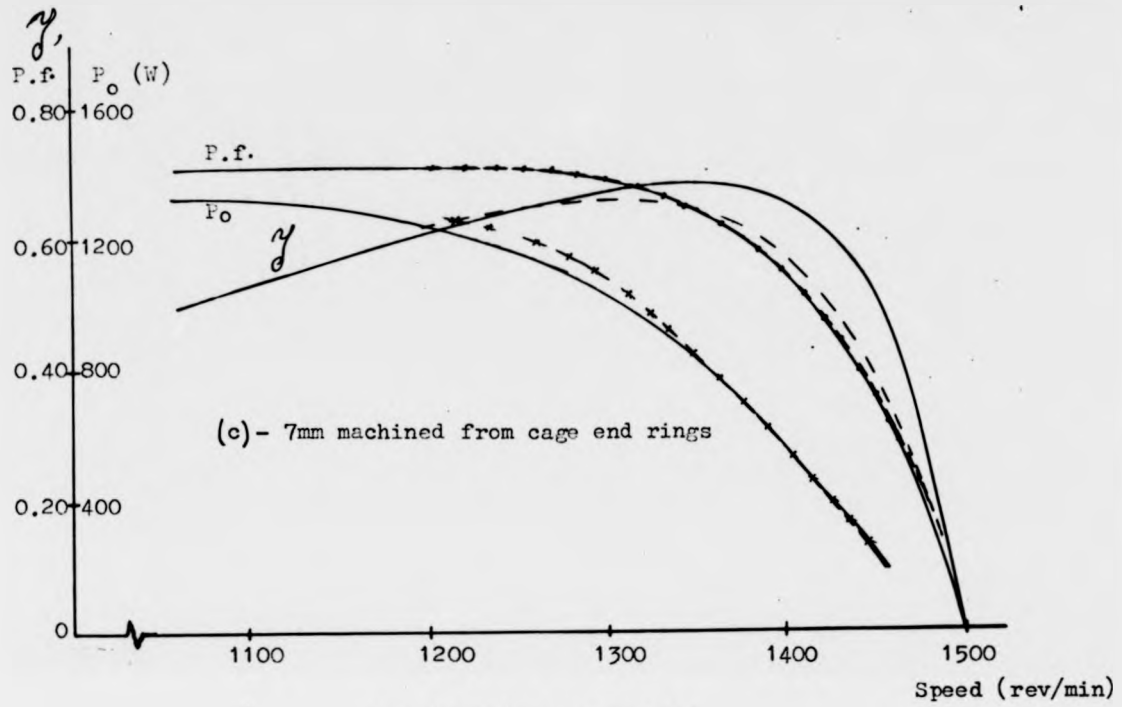

Fig.(6.10) - Continued

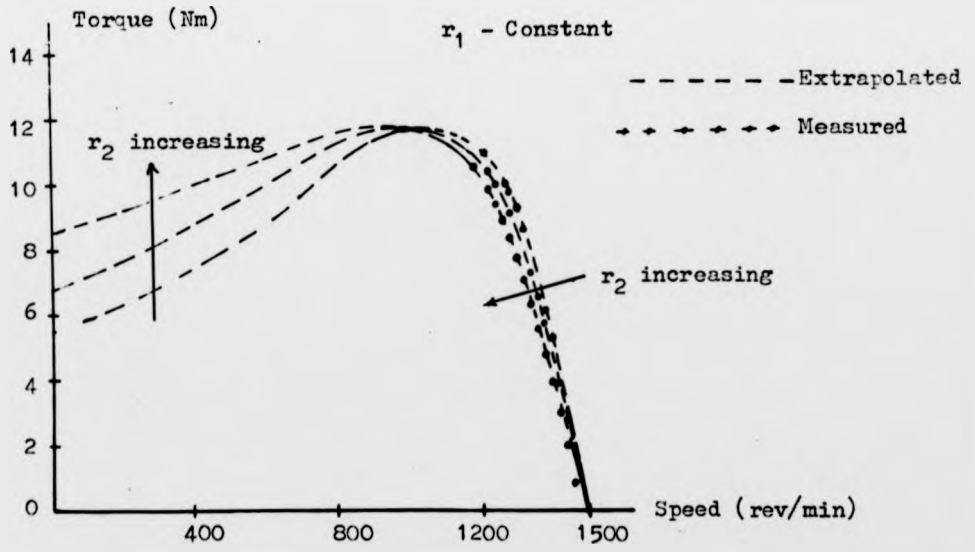

Fig.(6.11a) - Measured torque/speed curves of the experimental motor operated with rotor C for a fixed air gap length (g=0.5mm) and three values of cage resistance.

Fig.(6.11b) - Calculated torque/speed curves of fig.(6.11a)

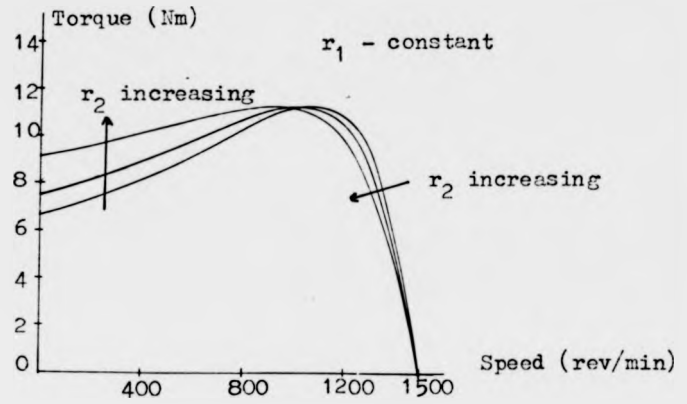

Fig.(6.12) - Phase current/speed curves of the experimental motor operated with rotor C for three values of cage resistance. (g = 0.5mm)

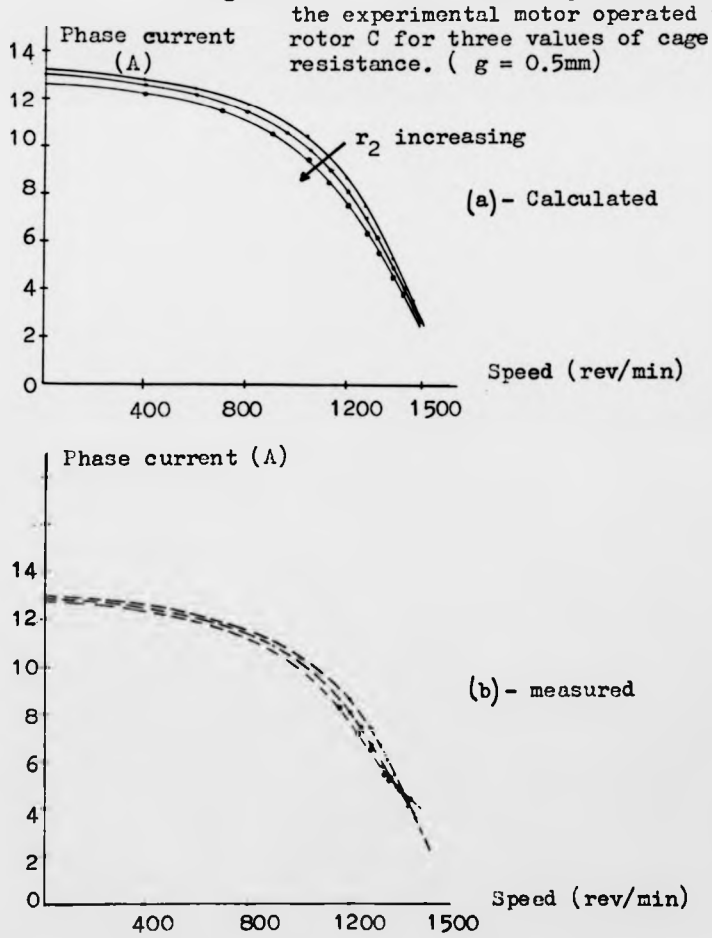

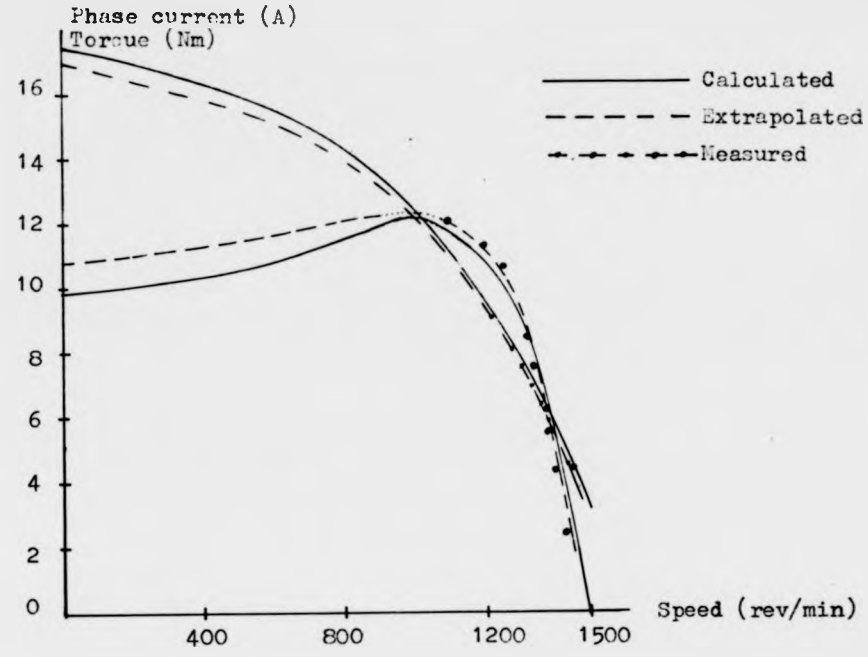

Fig.6.13) - Torque/speed and phase current/speed curves of the experimental motor operated with rotor A (g = 0.5mm)

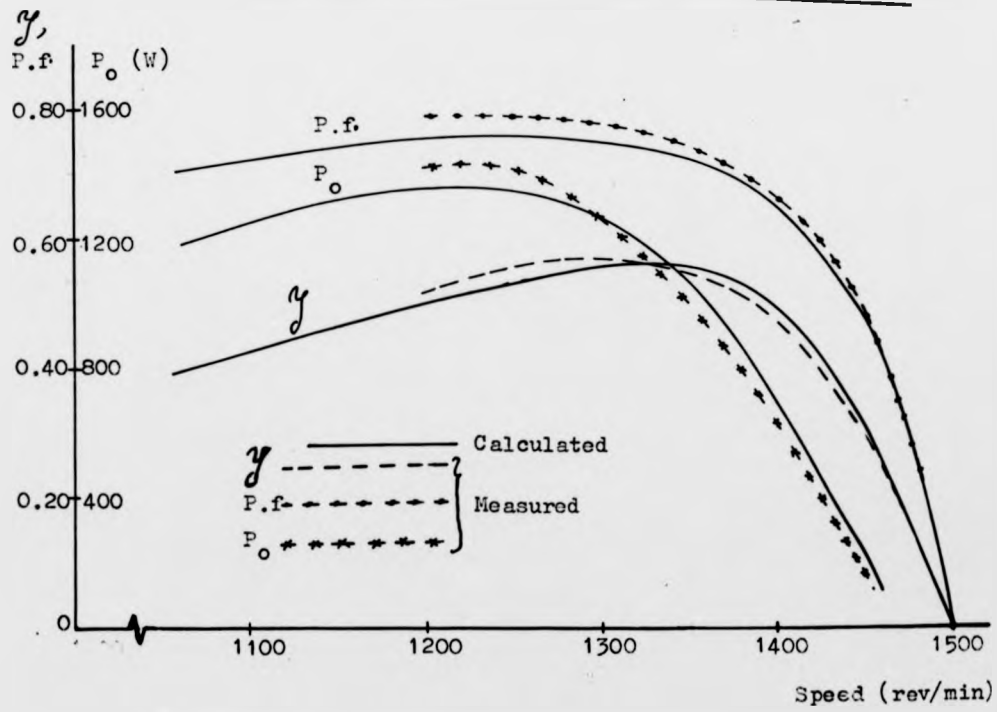

Fig.(6.14) - Performance characteristics of the experimental motor operated with rotor A (g = 0.5mm).

and in the width of the end rings giving rise to a larger effective cage resistance. Test results on the motor before separating the end rings (r_2 = 1.47Ω at 75°C) are shown in figs (6.15.6.16). The first set of figures gives a maximum efficiency of 71.5% at a slip of 0.07 and an output power of 1.5 kw at a slip of 0.8. The rated current is 7.7A and rated power is increased to 1.45 kw compared to that with rotor D giving rise to a power/weight ratio of 71 watt/kg. Fig.(6.16) shows that the starting torque is increased by about 10% and maximum torque by 27% at 0.5mm gap and the same slip. Figs.(6.17, 6.18) shows similar results when the end rings are separated causing the effective cage resistance to increase to 1.585 at 75°C. The first set of results show a maximum efficiency of 69.5% at a slip of 0.07 and an output power of about 1.385 kw at a slip of 0.08. The rated current is decreased to 6.95A and rated power to 1.25 kw making the power/weight ratio to be 62 watt/kg. Results of the second figure show an increase in the starting torque and a decrease in the maximum torque compared with the previous case. Generally it is possible to see that the two cases of rotor B offer very much improved performance characteristics compared with the first two rotors.

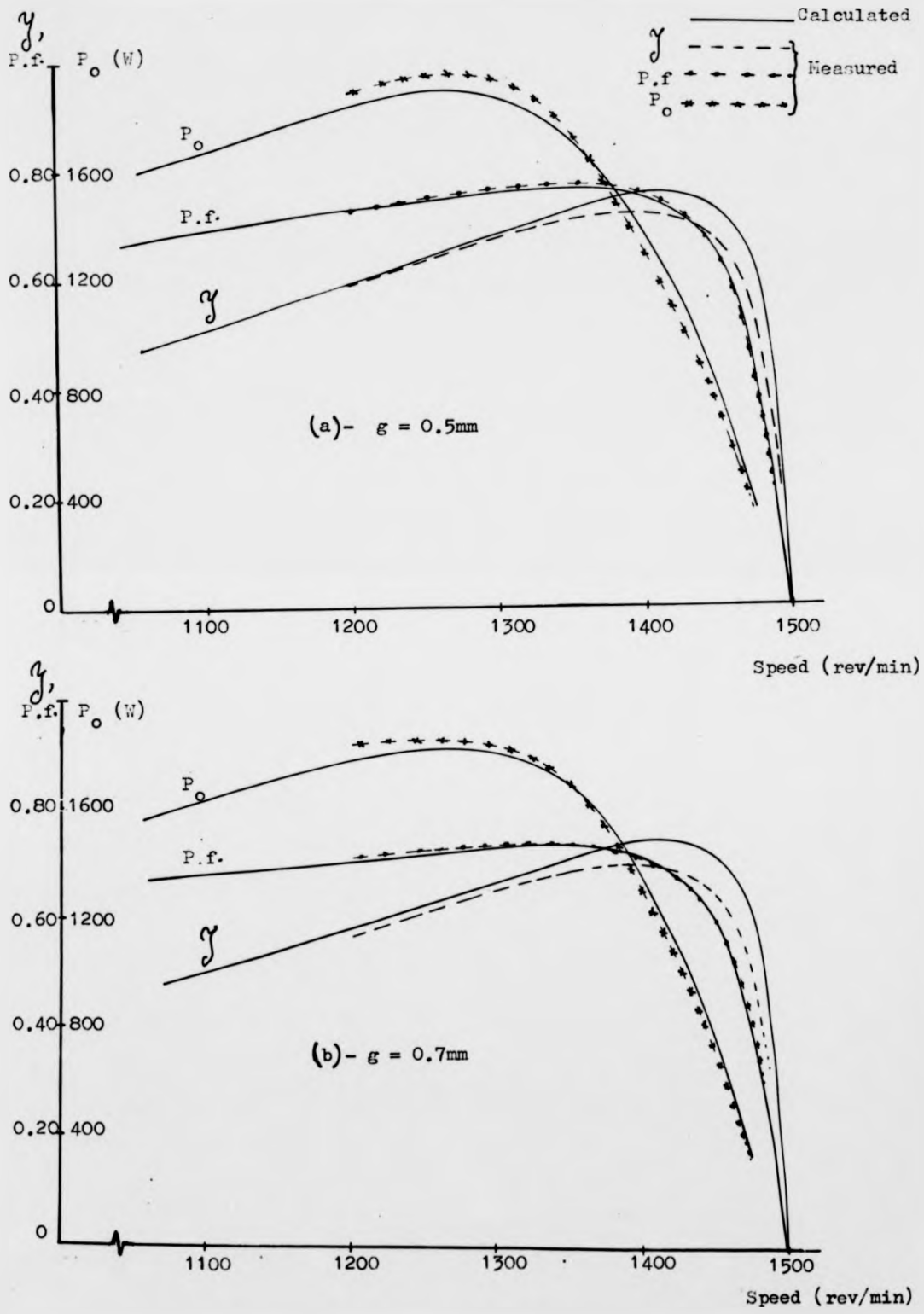

Fig.(6.15) - Performance characteristics of the experimental motor operated with rotor B at different air gap lengths.

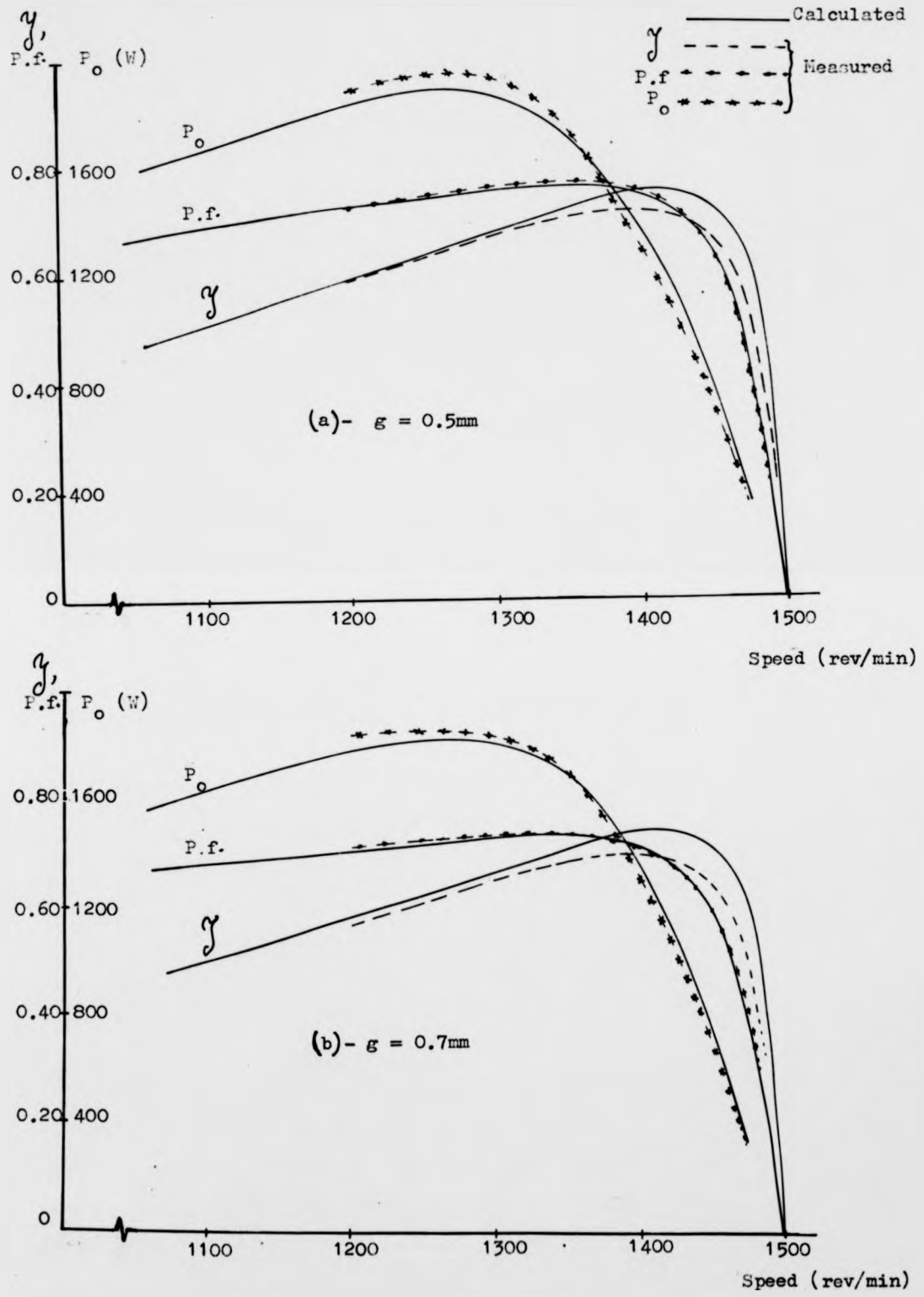

Fig.(6.15) - Performance characteristics of the experimental motor operated with rotor B at different air gap longths.

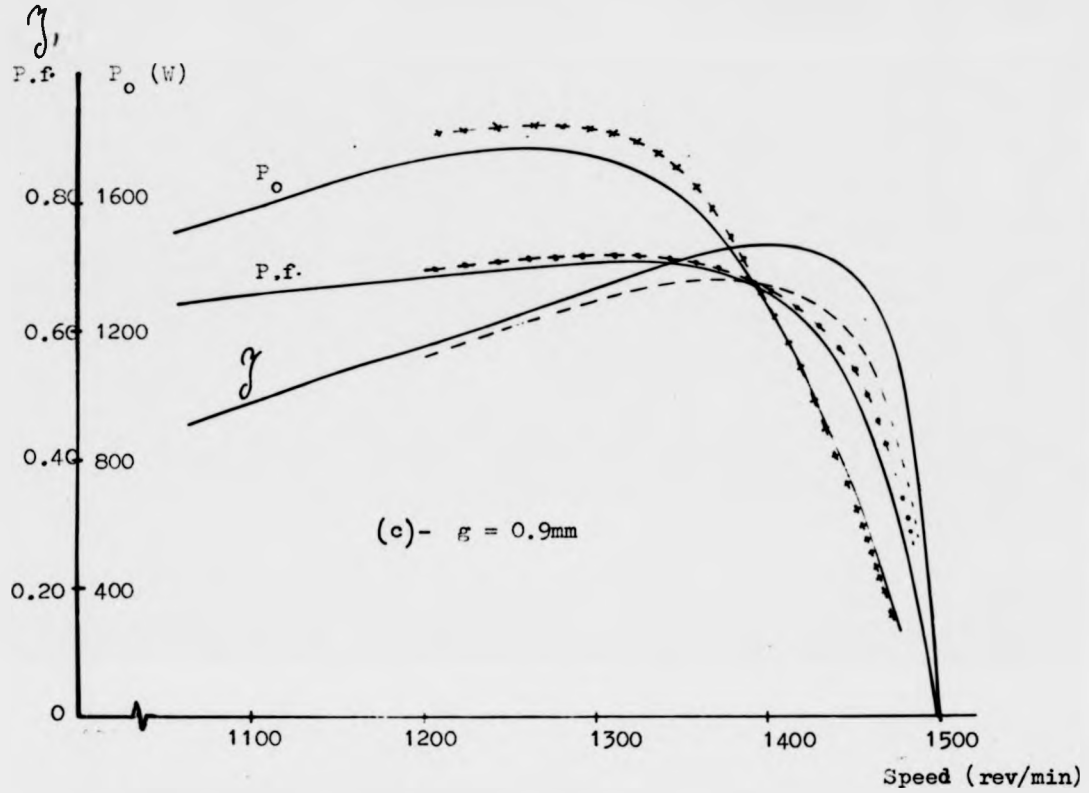

Fig.(6.15) - Continued

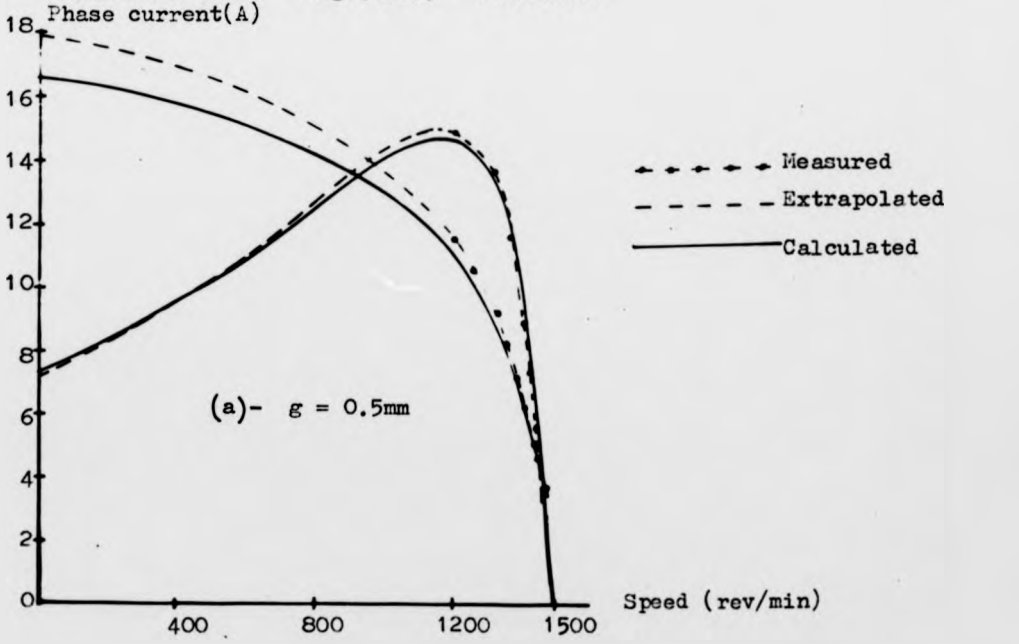

Fig.(6.16) - Torque/speed and Phase current/speed curves of the experimental motor operated with rotor B at three different air gap lengths.

Fig.(6.16) - Continued

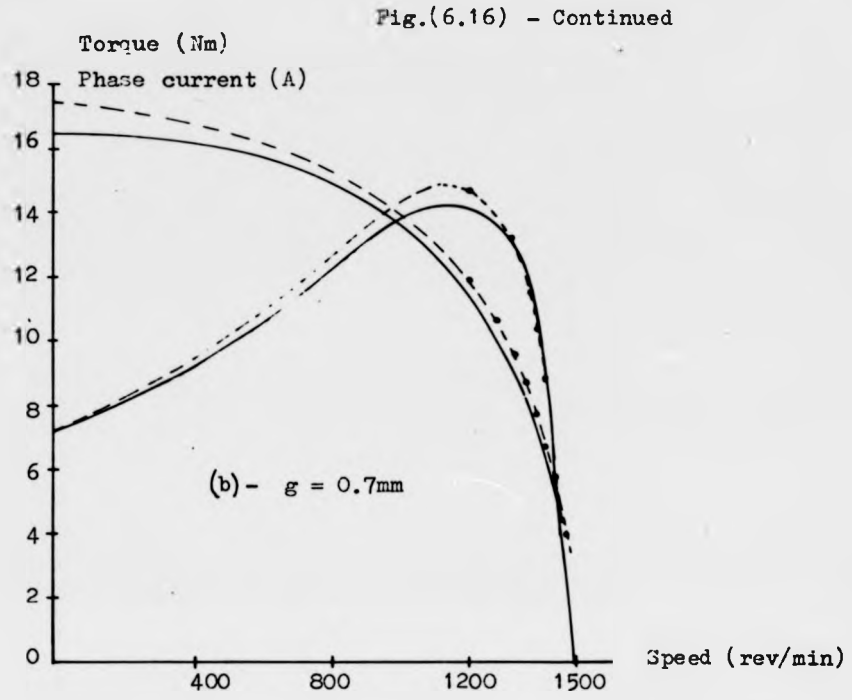

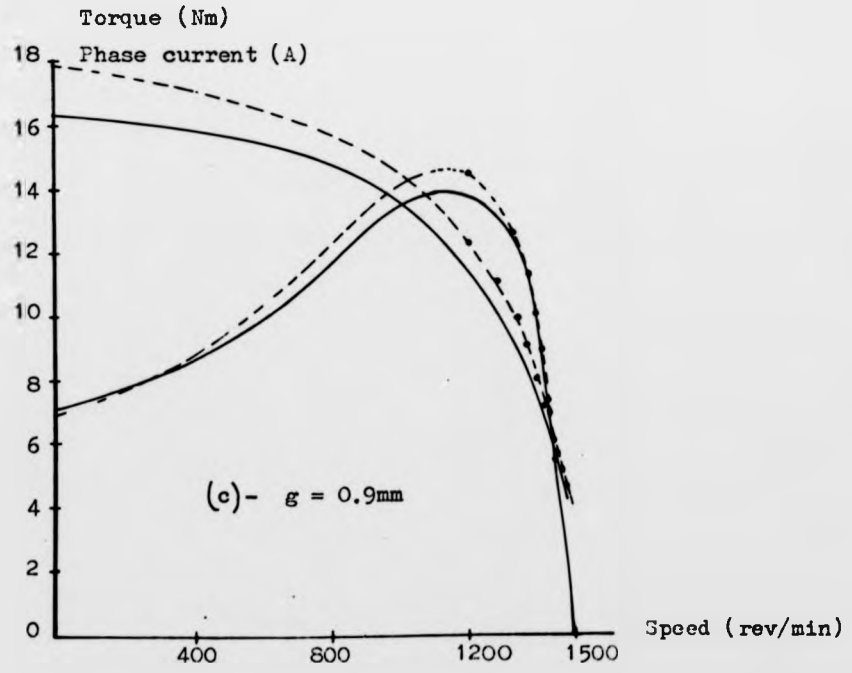

Fig.(6.17) - Performance characteristics of the experimental motor operated with rotor B after the two cages have been completely separated (g = 0.5mm)

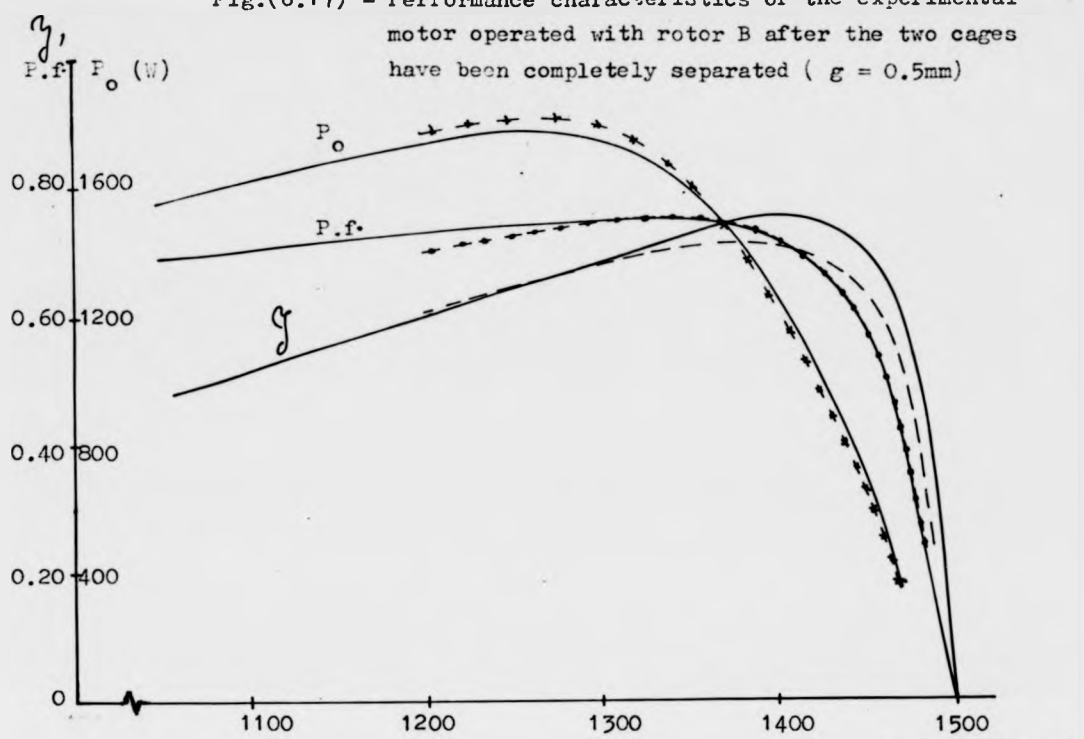

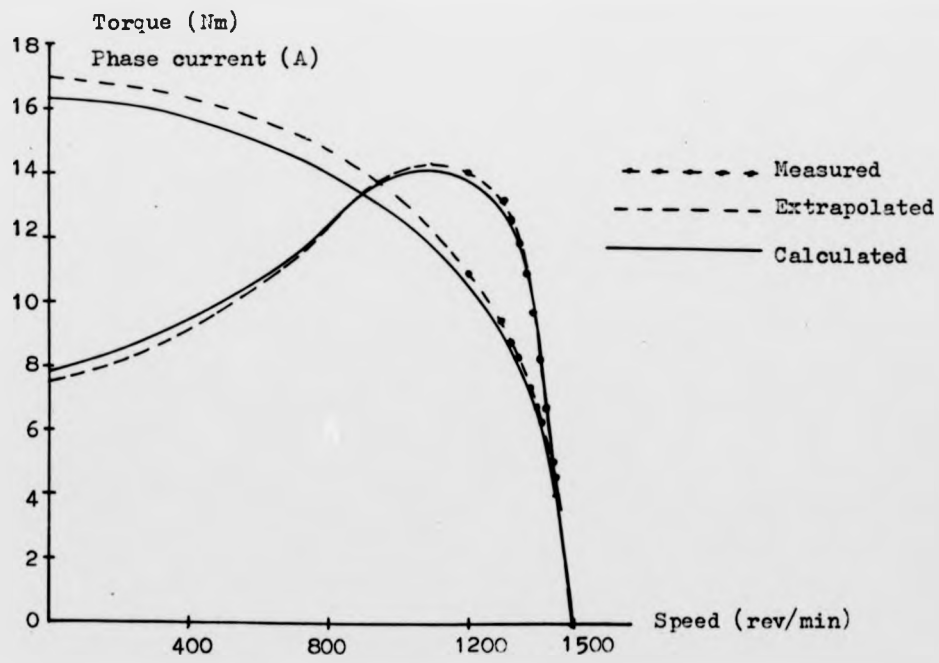

Fig.(6.18) - Torque/speed and phase current/speed curves of the experimental motor operated with rotor B after the two cages have been completely separated (g = 0.5mm)

6.4.2 Comparison of the machine performance

The relevant figures of the experimental machine tested with the four rotors (A,B,C and D of table 2.3) are compared with those introduced by Capaldi in ref.1.5. By doing so it is possible to observe directly the extent of improvements achieved in the experimental machine as a result of this research and development work. Two achievements may be born in mind, namely, that it is possible now to produce both single cage and double cage motors and that the motor has a low sound level such that it is difficult to notice it running in an ordinary laboratory. Table (6.1) shows a comparison of results of the experimental machine and Capaldi's machine operated as a double stator motor.

6.5 Performance of skewing and MSW's

The harmonic study technique outlined previously has been used in studying the harmonic content of the motor operated with different rotors and finally with the stator filled with MSW's. Fig.(6.19) shows the flux harmonics in the case of rotor D at three values of torque 0. 3.3, 6.6 Nm. The harmonics increase slowly with the load due to tooth tip saturation and the increase in slip. Experiments showed also that operating the motor with the non-skewed rotors A, B, D is always accompanied with a continuous whistling noise. It is shown in chapter 3 that skewing the rotor bars can reduce the slot harmonics and consequently reduce the noise considerably. This has been verified practically in rotor C of 18 bars each skewed by one stator slot pitch shown in fig. (6.20). The performance study and harmonic checking of figs. (6.19, 6.20,a,b) revealed the following important characteristics:

a. Skewing the rotor in this manner can help very much in reducing the harmonics. The slot harmonics 11 and 13 are found to be reduced considerably.

Table (6.1)

	Motor				
	1	2	3	4	5
Diameter mm	220	220	220	220	220
Length mm	98	98	87.75	110	110
Rotor inertia $Kg.m^2$	0.0161	0.0158	0.0154	0.0215	0.025
Power output (rated) Kw	1.11 $\acute{s}$ = 0.081	0.9 $\acute{s}$ = 0.093	0.8 $\acute{s}$ = 0.08	1.45 $\acute{s}$ = 0.08	0.6 $\acute{s}$ = 0.08
Efficiency (Max) %	69 $\acute{s}$ = 0.081	69 $\acute{s}$ = 0.093	56 $\acute{s}$ = 0.12	71.5 $\acute{s}$ = 0.08	65 $\acute{s}$ = 0.08
Power factor at rated output	0.69 $\acute{s}$ = 0.081	0.65 $\acute{s}$ = 0.093	0.78 $\acute{s}$ = 0.08	0.76 $\acute{s}$ = 0.08	0.5 $\acute{s}$ = 0.08
Weight Kg	19	18.93	18.85	20.4	22.5
Power/Weight Watt/Kg	60	47	42.4	71	55

1 - Experimental motor operated with the single cage rotor D.
2 - " " " " " " " " C.
3 - " " " " " " " " A.
4 - " " " " " double cage rotor B.
5 - Capaldi's axial induction motor (ref.1.5)

In all cases the motors are operated with double stators and with a total air-gap length of 0.5mm.

Fig.(6.19) - Performance characteristics of motors 1,2,3,4 and 5 of table 6.1, showing the efficiency, power output, power factor and power/weight ratio as a function of the shaft speed.

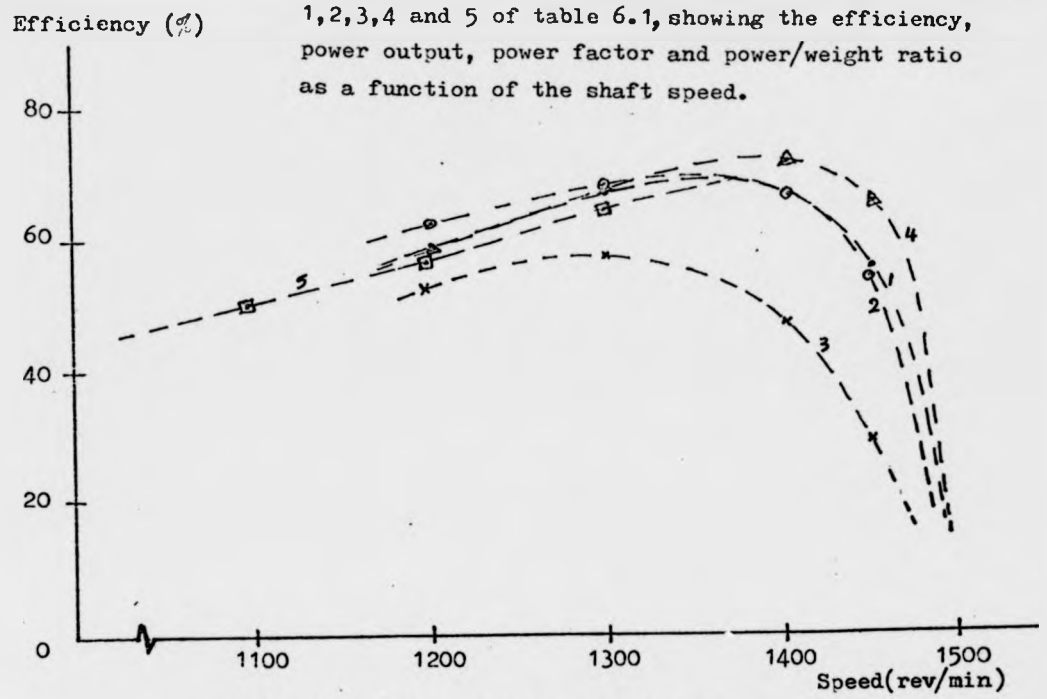

a - Efficiency/Speed experimental curves

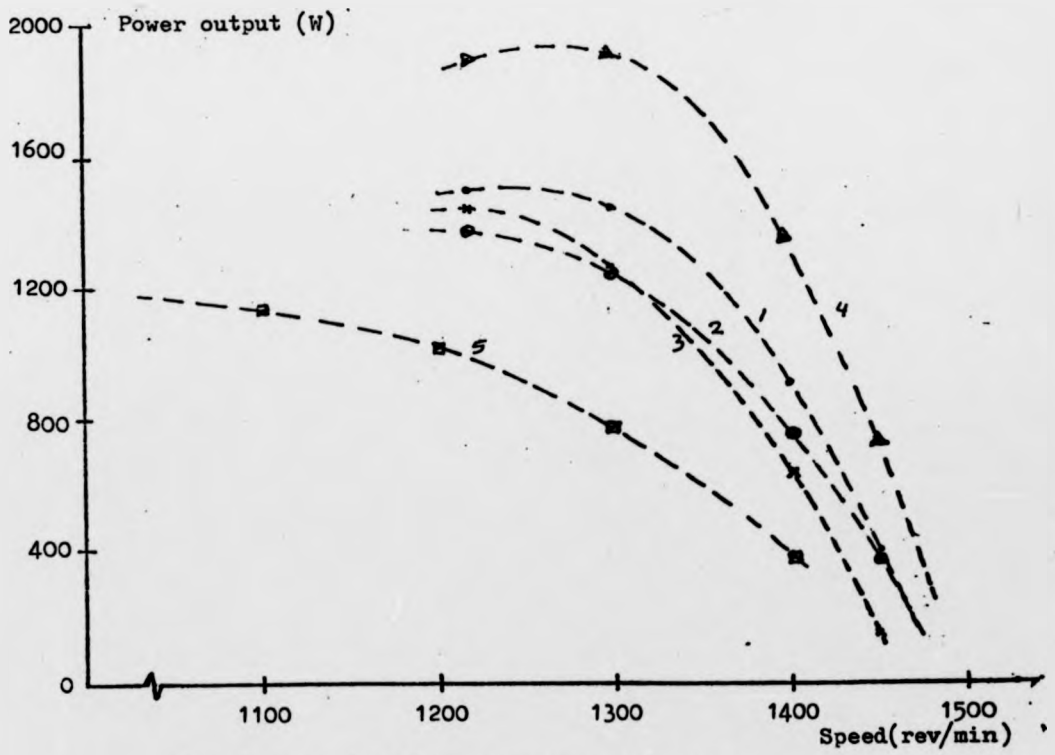

b - Power output/Speed experimental curves

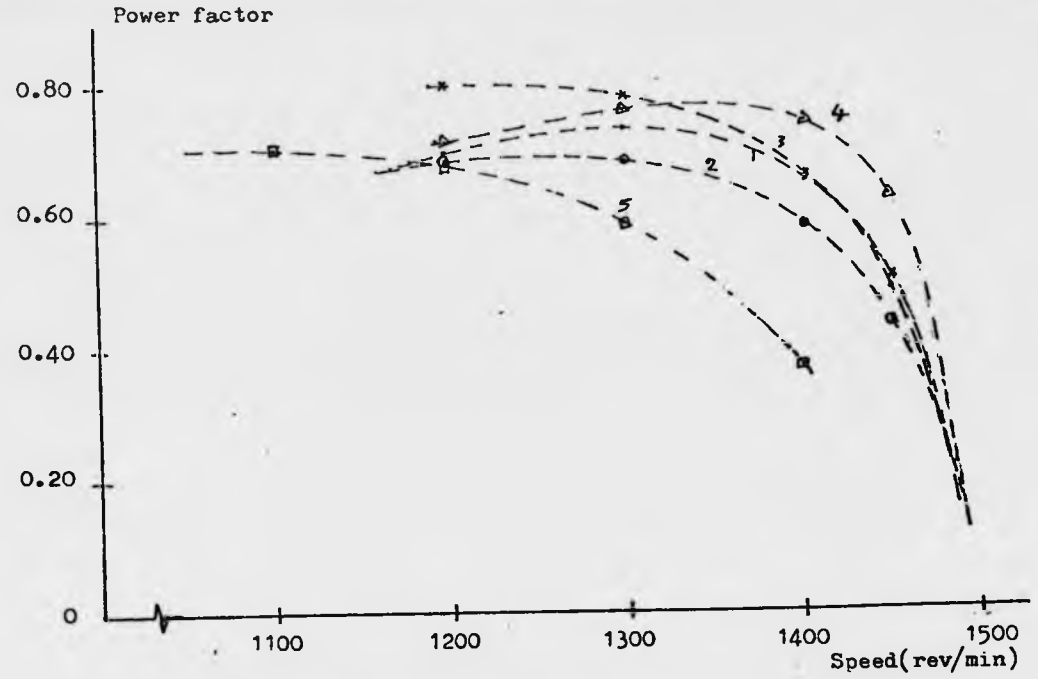

c – Power factor/Speed experimental curves

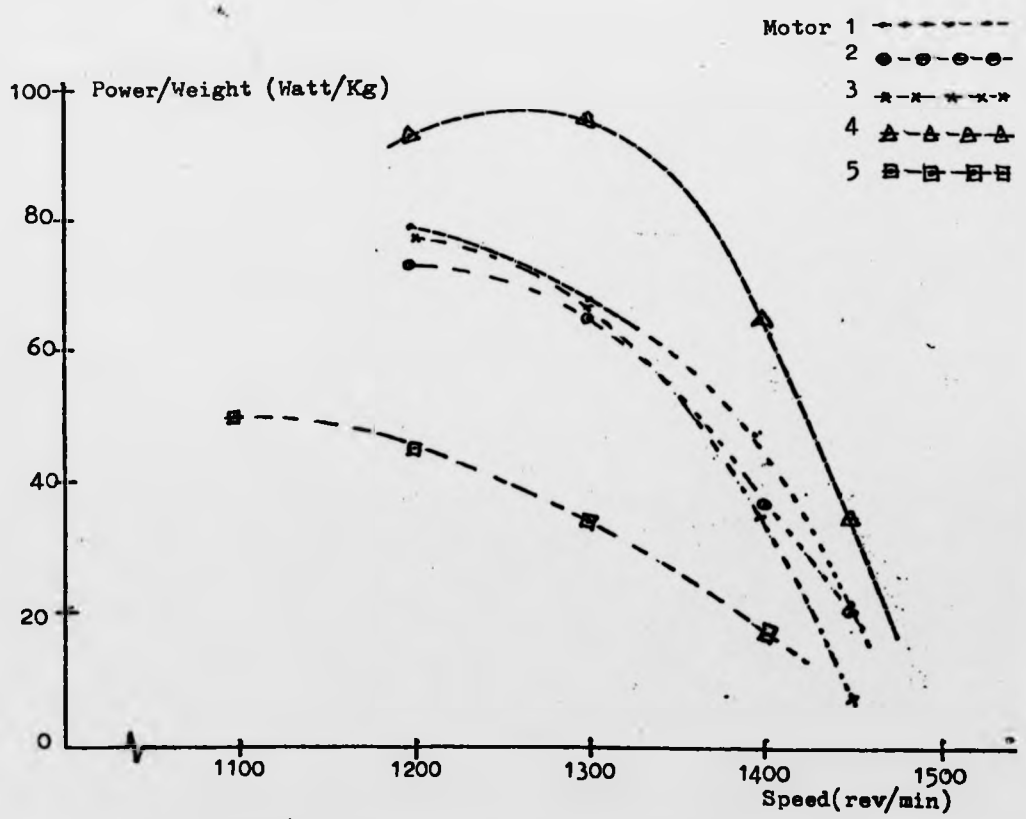

d – Power/Weight versus speed experimental curves

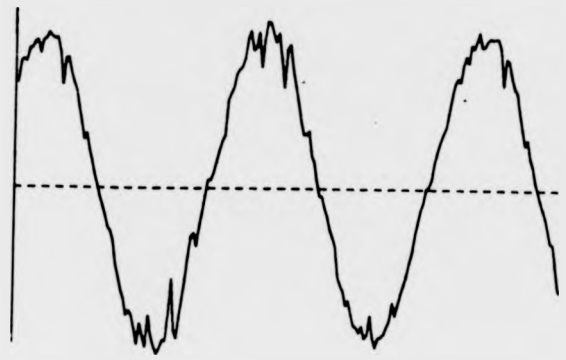

Flux per pole waveform

T = 0 N.m

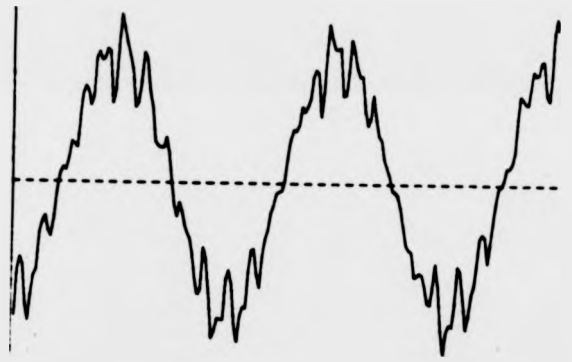

T = 3.3 Nm

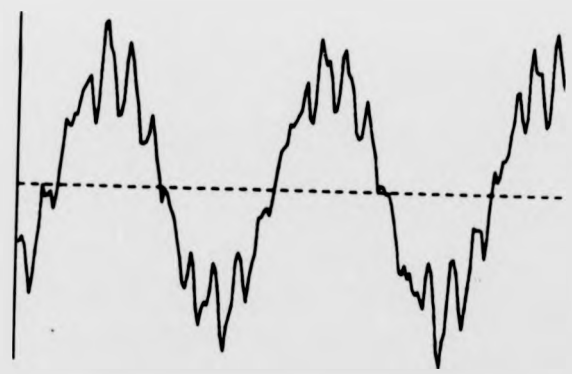

T = 6.6 Nm

Fig.(6.19a) - Air gap flux waveform in the case of non-skewed rotor D at three values of torque and g=0.5mm.

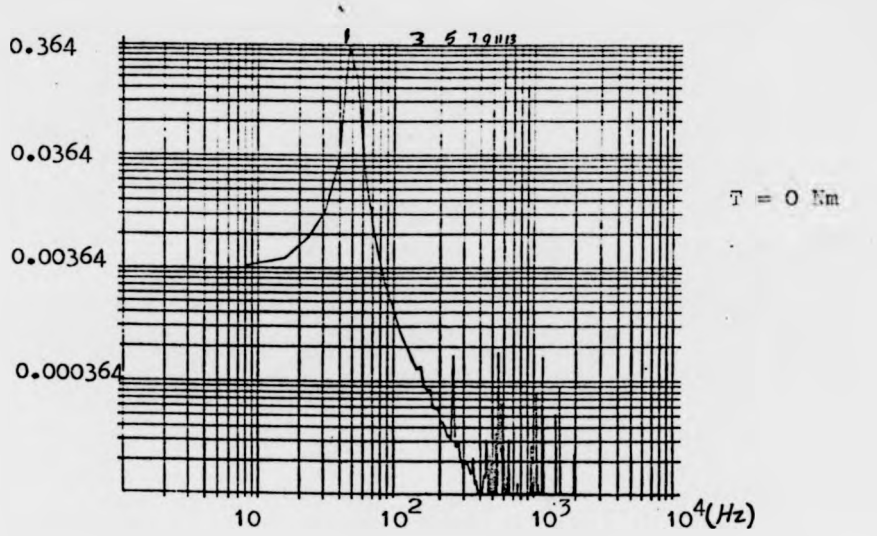

Fig.(6.19b) - Harmonic analysis of the flux waveform in the case of rotor D at three values of torque and g = 0.5mm.

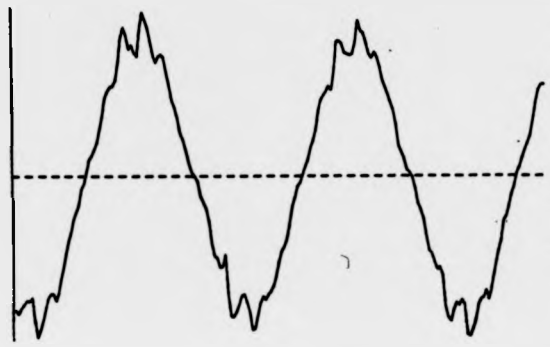

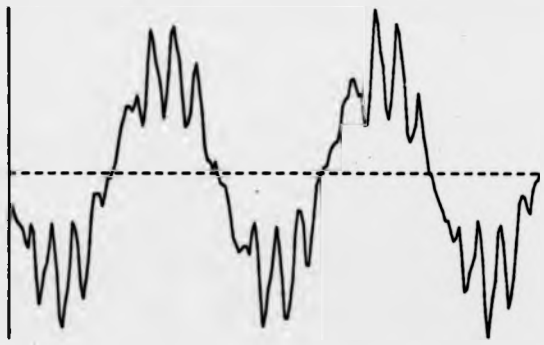

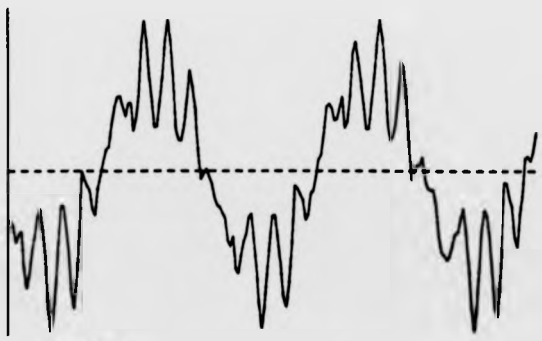

Fig.(6.19c) - Air gap flux waveform in the case of rotor D and stator slots filled with MSW at three values of torque and g = 0.5mm.

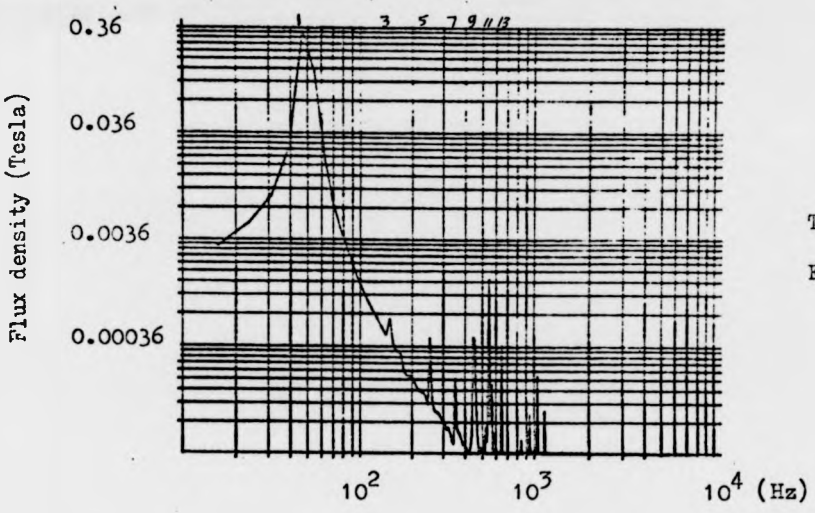

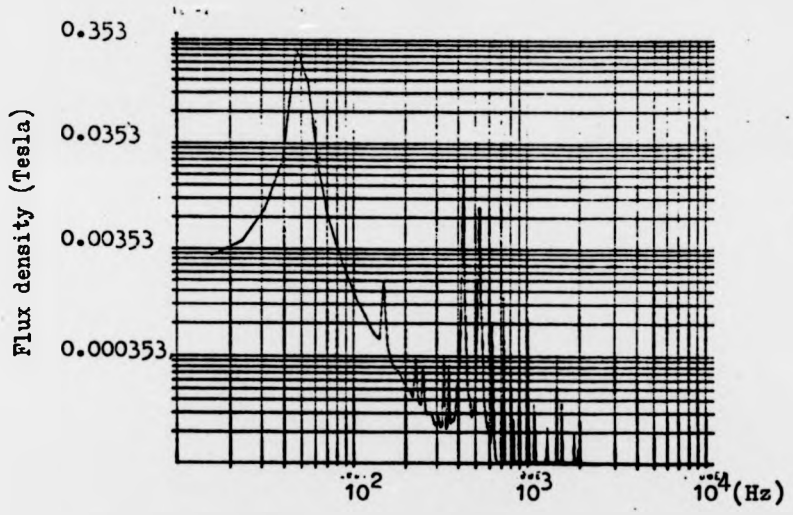

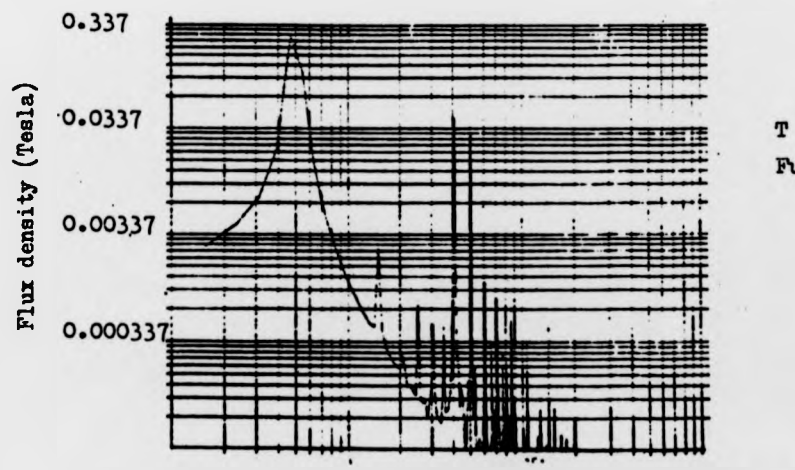

Fig.(6.19d) - Harmonic analysis of flux waveform in the case of rotor D and MSW at three values of torque and

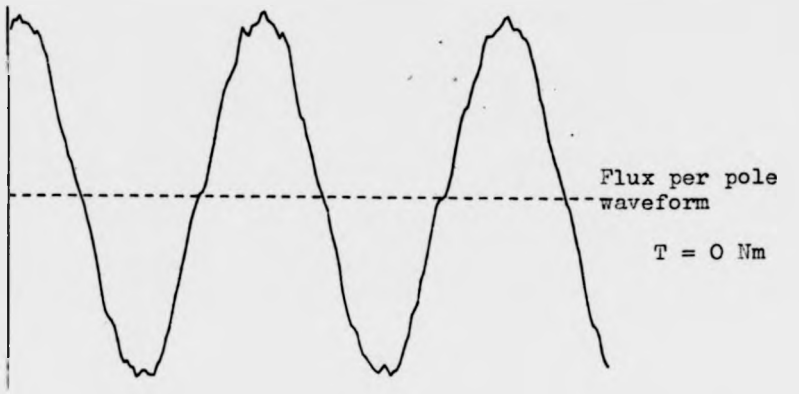

Fig.(6.20a) - Air gap flux waveform in the case of skewed rotor C at three values of torque and g=0.5mm.

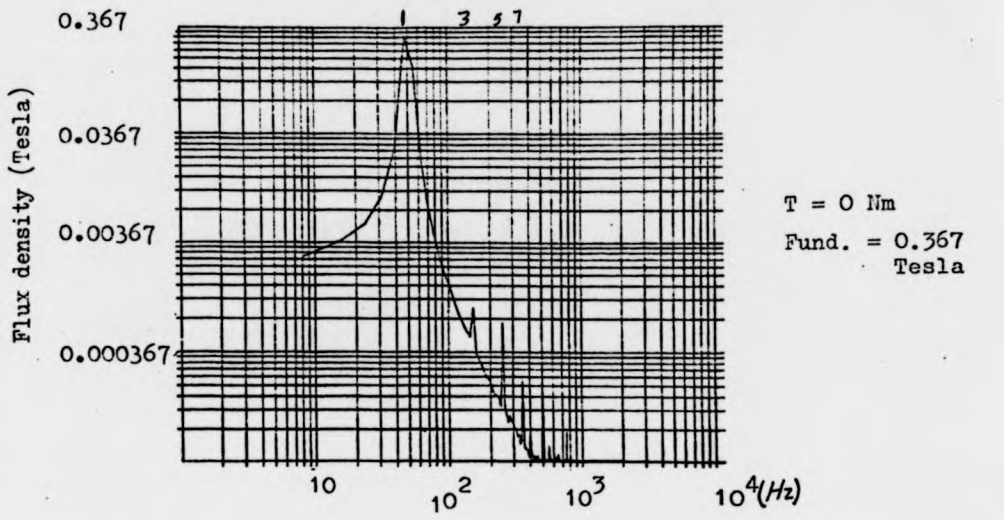

Fig.(6.20b) - Harmonic analysis of the flux waveform in the case of rotor C at three values of torque and g = 0.5mm.

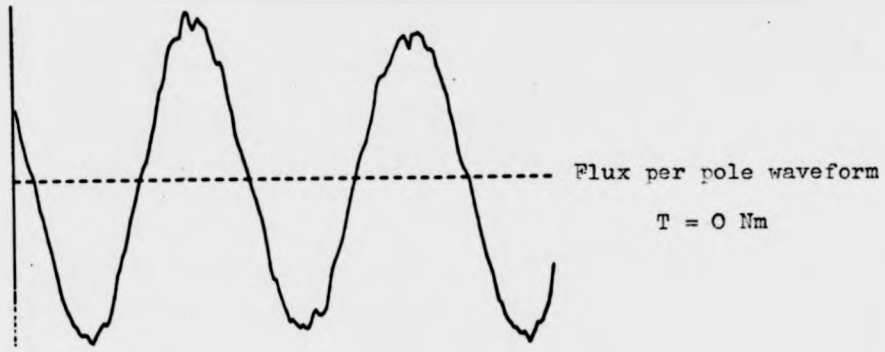

Fig.(6.20c) - Air gap flux waveform in the case of rotor C and stator slots filled with MSW at three values of torque and g = 0.5mm.

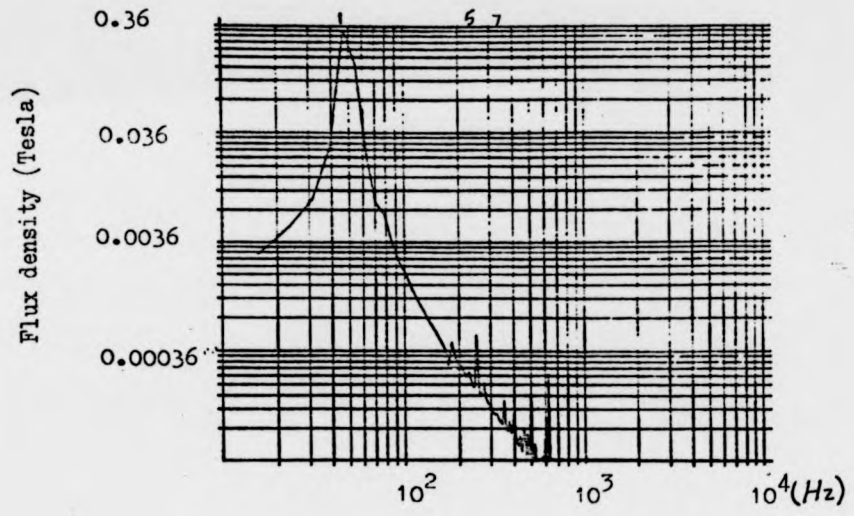

T = 0 Nm

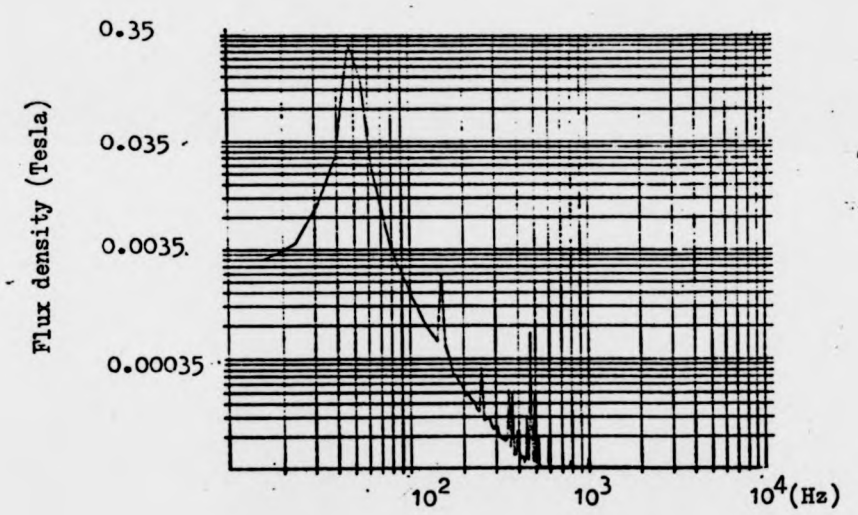

T = 0 Nm

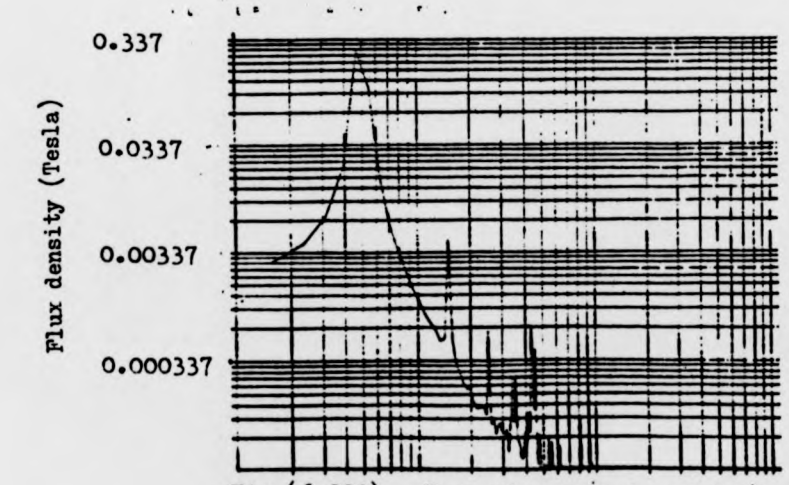

T = 6.6 Nm

Fig.(6.20d) - Harmonic analysis of flux waveform in the case of rotor C and MSM at three values of torque and g = 0.5mm.

b. There is a small improvement in the efficiency of the motor for the same air-gaps used with rotor D.

c. Skewing reduced the sound level by about 40%.

The advantages (a) and (c) provide the possibility of reducing the air-gap giving rise to further increases in the efficiency and power output. In virtue of chapter 3, magnetic wedges of 2 x 7.8 x 43 mm have been prepared and fitted into the stator slots. The harmonic study in the motor fitted with MSW and operated with rotors D and C is shown in figs.(6.19, 6.20,c,d). It is clear that there is an increase in the harmonics including the appearance of the third harmonic and its multiples. On the other hand it is found that the motor is running very quietly and smoothly when operated with any of the non-skewed rotors with the sound level reduced by about 60%. The new harmonics are due to the fact that the magnetic slot wedges are suffering saturation much greater than the rest of the magnetic circuit, starting at an earlier stage, and causing the flux waveform to approach a square shape having pronounced third harmonics. This saturation is load dependent causing the harmonics to increase with the applied load. The performance tests showed that reactances (x_1, x_2, x_m) of the new motor are increased for all the rotors with no considerable change in the resistances. Theoretically closing the slots reduces the effective air-gap and consequently increases the efficiency. But this does not happen due to the increase in the harmonic content of the machine which counterbalanced the increase in the efficiency giving the same order of efficiencies. It is therefore worthwhile to investigate different designs of the wedges introduced previously using different thicknesses and different materials and to study their effects on harmonic content and the motor's performance.

CHAPTER 7

Low inertia axial field d.c motor

7.1 Introduction

In the last decade certain demands in motor requirements initiated work in a new type of d.c motor known as the disc-armature or axial field motor. In 1967 a patent was registered in U.K by A.E. Corbett of the University of Warwick claiming the invention of a new type of electric motor(7.1), suitable for certain applications due to its special features and characteristics. The first application appeared at the University a few years later, when it was used in developing a d.c motor to operate an electric lawn-mower.

The present prototype of this motor has been built especially for an application which demands a high torque/inertia ratio. It is required to accelerate an inertia of 4×10^{-4} Kg.m^2 from rest to a speed of 6000 rev/min in less than 300 ms, and to stop it in less than 200ms. A solid steel disc having such an inertia coupled to the motor shaft has been used as a load.

The most unusual feature in this type of motor design is its construction which gives the special flat shape shown in fig.(7.1). The magnetic field is provided by eight magnetic poles on each side of the armature, fixed to mild steel end plates which act as flux return paths. The magnetic circuit is designed such that the highest air-gap flux can be obtained. To fulfil this purpose the air-gap is kept as small as possible and rectangular toroid shaped magnets are used to give an air-gap flux density more than 0.8 Tesla. The choice of the permanent magnet material is an important factor in connection with the motor size and weight. Since high flux density is essential in this application, a high remanence material, Columax has been chosen. This is a metal alloy with high flux density and relatively

CHAPTER 7

Low inertia axial field d.c motor

7.1 Introduction

In the last decade certain demands in motor requirements initiated work in a new type of d.c motor known as the disc-armature or axial field motor. In 1967 a patent was registered in U.K by A.E. Corbett of the University of Warwick claiming the invention of a new type of electric motor(7.1), suitable for certain applications due to its special features and characteristics. The first application appeared at the University a few years later, when it was used in developing a d.c motor to operate an electric lawn-mower.

The present prototype of this motor has been built especially for an application which demands a high torque/inertia ratio. It is required to accelerate an inertia of 4×10^{-4} Kg.m^2 from rest to a speed of 6000 rev/min in less than 300 ms, and to stop it in less than 200ms. A solid steel disc having such an inertia coupled to the motor shaft has been used as a load.

The most unusual feature in this type of motor design is its construction which gives the special flat shape shown in fig.(7.1). The magnetic field is provided by eight magnetic poles on each side of the armature, fixed to mild steel end plates which act as flux return paths. The magnetic circuit is designed such that the highest air-gap flux can be obtained. To fulfil this purpose the air-gap is kept as small as possible and rectangular toroid shaped magnets are used to give an air-gap flux density more than 0.8 Tesla. The choice of the permanent magnet material is an important factor in connection with the motor size and weight. Since high flux density is essential in this application, a high remanence material, Columax has been chosen. This is a metal alloy with high flux density and relatively

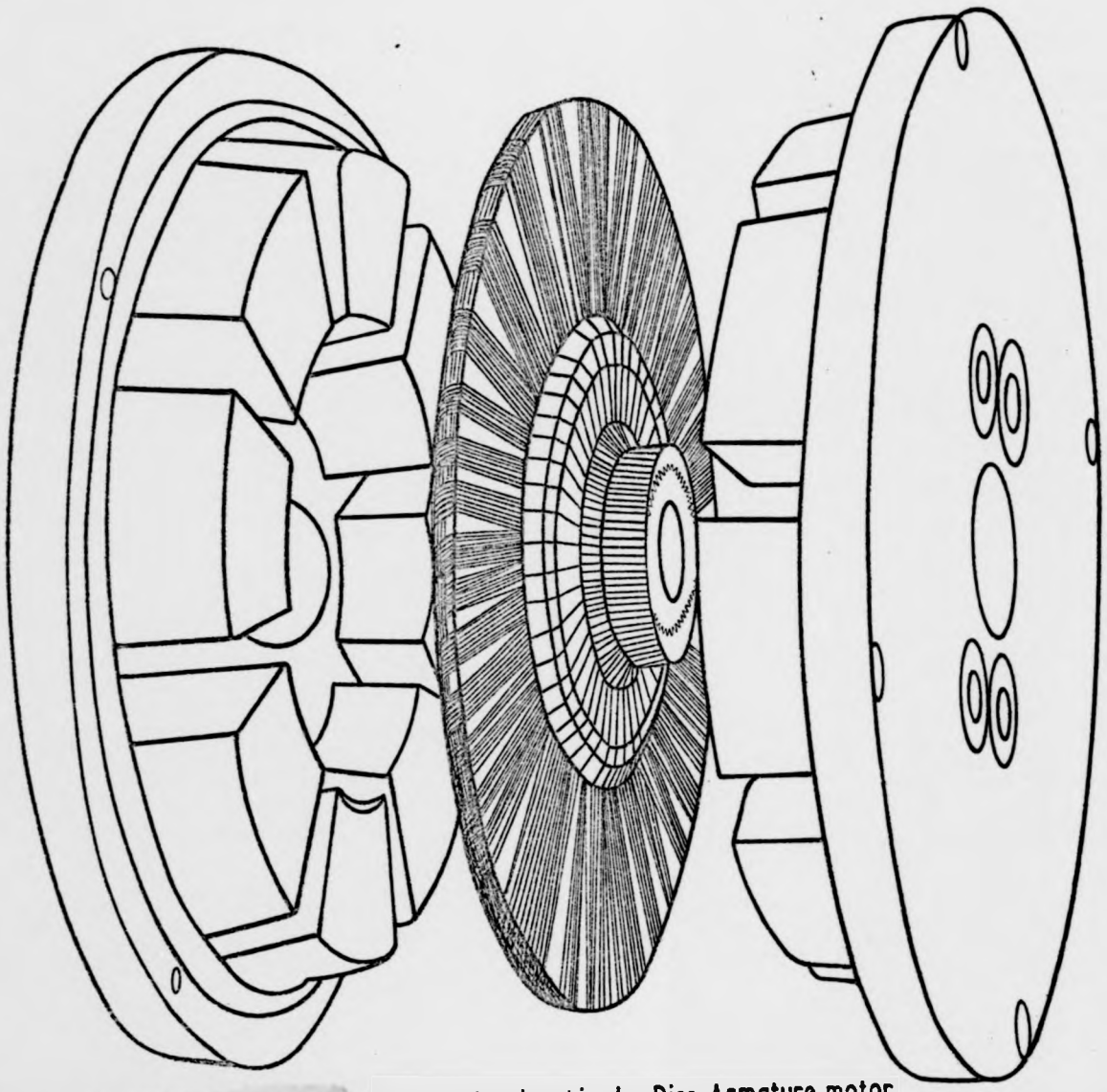

Fig.(7.1) Diagramatic view of a low inertia d.c. Disc-Armature motor.

low coercitivity. Because of these magnetic properties the axial length of the motor has to be extended to accommodate the full length of the poles and the poles have to be magnetized in situ every time the motor is disassembled. The choice of the magnetic material affects also the armature windings since the output torque depends on the air-gap flux and the winding's current. Consequently the choice of low flux density magnets for certain applications must be compensated by using higher armature current and therefore increasing the size of the wire and thickness of the armature. Where the cost or short axial length is important the ceramic ferrite (Feroba III) is to be preferred. Using this material will keep the cost and size down, but at the same time it will reduce the flux to half or less. Therefore it is disadvantageous to use this type of magnetic material for high torque/inertia motor.

The main important feature in the present motor is its low inertia armature which consists of a set of coils each as shown in fig.(7.2). The coils are arranged in a flat, disc shape such that their ends project into the centre and are connected to a face-type commutator. The required number of coils are prepared using a rectangular wooden former designed to give the coil shape required. The coils are rectangular in appearance and kept uniformly to one wire thickness by using strips of thin tape. The inner and outer edges of each coil are bent out of the plane of the active conductors to provide extra mechanical rigidity and to give a neat mechanical assembly. After connecting the wire ends to the commutator the whole assembly together with the commutator and the central aluminium bush are encapsulated in epoxy resin. The motor is expected to provide the following improved characteristics:

1. The elimination of magnetizing windings from the stator by employing permanent magnets; the elimination of the iron from the armature and consequently the elimination of any unbalanced

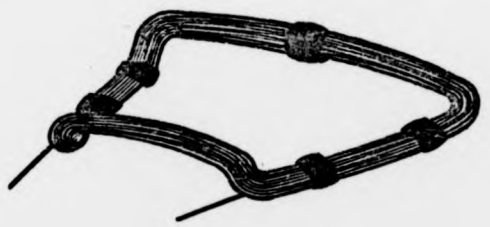

Fig (7.2) Perspective View of an Armature Coil

magnetic pull on the armature. and small air-gap. All these new features are expected to give rise to high motor efficiency.

2. The high power/weight ratio and the short axial length makes it suitable for applications such as electric vehicle, lawn mower and some domestic applications such as vacuum cleaners, coffee blenders and floor polishing machines.
3. The ironless thin armature has a low inertia which gives rise to a small mechanical time constant and consequently fast response to step inputs. This characteristic is useful for direct drive capstans for magnetic tape, paper tape and photographic film. The motor can also be a potentially serious competitor for clutch brake systems in fast response mechanisms and can cause the elimination of the clutch.
4. The elimination of the iron and the magnetic slots from the armature and the less amount of wire incorporated in armature windings are expected to lead to small armature inductance and therefore provide good commutation and extended brush and armature life.

The author was engaged for a long time in research works in d.c axial field motors. Some of these works appeared in a paper (7.2) published jointly with his supervisor. He introduced a number of modifications in design with the aim of improving the design of the low inertia motor. In this respect a commutator design method has been introduced to replace the old design method which did not give satisfactory results. The new method demonstrated very effective results in producing the first armature in a very satisfactory condition. This method makes it possible to produce the complete commutator before joining it into the armature and reduces the production cost by increasing the design reliability.

A method is developed for studying the dynamic performance of the

motor by measuring the time required for it to accelerate the load from rest to its top speed and the time required for it to stop. The times measured are found to be well within the expected range.

7.2 Design Details

Brief details of magnetic circuit and armature winding are given below:

7.2.1 Magnetic circuit

Permanent magnet material		Columax
Magnet length	m	19×10^{-3}
Magnet area	m^2	681×10^{-6}
Thickness of steel ring	m	9×10^{-3}
Total air gap length	m	2.55×10^{-3}
Pole arc/Pole pitch		0.75
Number of poles		8
B_m	tesla	1.25
H_m	AT/m	42500
Total flux/pole	wb	0.000735
Useful flux/pole	wb	0.000565

7.2.2 Armature winding

Number of parallel paths		4
Number of coils		46
Number of turns/coil		7
Wire gauge	m	0.4×10^{-3}
Method of winding		Duplex wave
Disc armature thickness	m	1.17×10^{-3}
coil pitch		1-7
Effective armature resistance (2-brushes)	ohm	0.78
Number of commutator segments		46
Commutator pitch		1-13

7.3 Dynamic Performance

7.3.1 Practical dynamic performance

In this section it is aimed to study the ability of the motor to accelerate and decelerate an inertia load in short periods of time. This has been done by using the speed of the shaft as the main element of study. The speed was measured by using a slotted disc with fifty slots attached to the shaft and held vertical between a small electric bulb and a sensitive photo-diode. As the shaft starts rotating, the photo-diode detects every slot by receiving a pulse of light. The waveform of the series of pulses is recorded in similar manner to the harmonic study of Chapter 3 and analysed by using a computer sampling method. A sample of such waveform is shown in fig.(7.3). This optical method is preferred in such work since it reduces the noise especially if it is compared to the magnetic pick-up methods. For the acceleration test the d.c voltage of 90 Volts from a set of batteries is suddenly applied across the motor terminals and the building of the slots speed waveform is recorded until the steady state is reached. For the deceleration test, the machine is running at maximum speed and its terminals are suddenly switched across a short circuited causing the machine to slow down under self braking effect.

The test has been carried out with two values of inertia supplied to the motor. Fig.(7.4a,b) shows the deceleration and acceleration curves of the experimental motor when it is running under its own inertia 0.7×10^{-4} $kg.m^2$ coupled to the slotted disc used in speed measuremont, giving rise to a total inertia of 1.85×10^{-4} $kg.m^2$. Curve-a gives the stopping time and the mechanical time constant of the motor as 56 and 10 ms respectively.

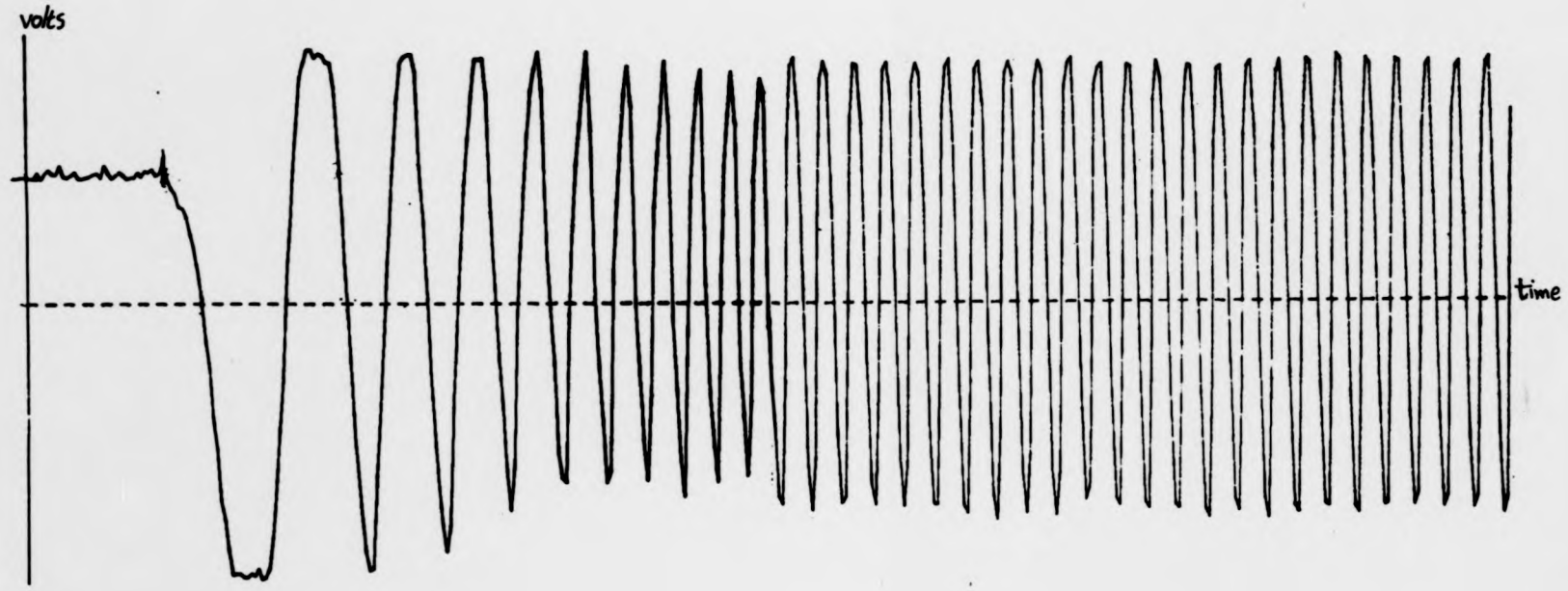

Fig.(7.3) - Waveform shows the acceleration of the printed circuit motor when a 90V d.c is suddenly applied to the motor

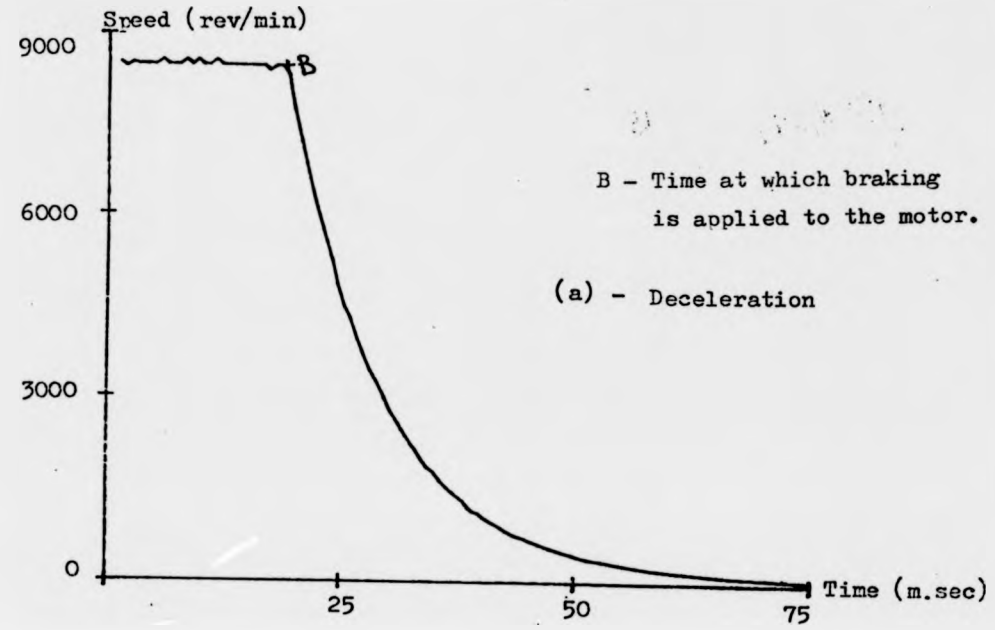

Fig.(7.4) - The dynamic performance of the experimental motor under total inertia $J = 1.85 \times 10^{-4} Kg.m^2$.

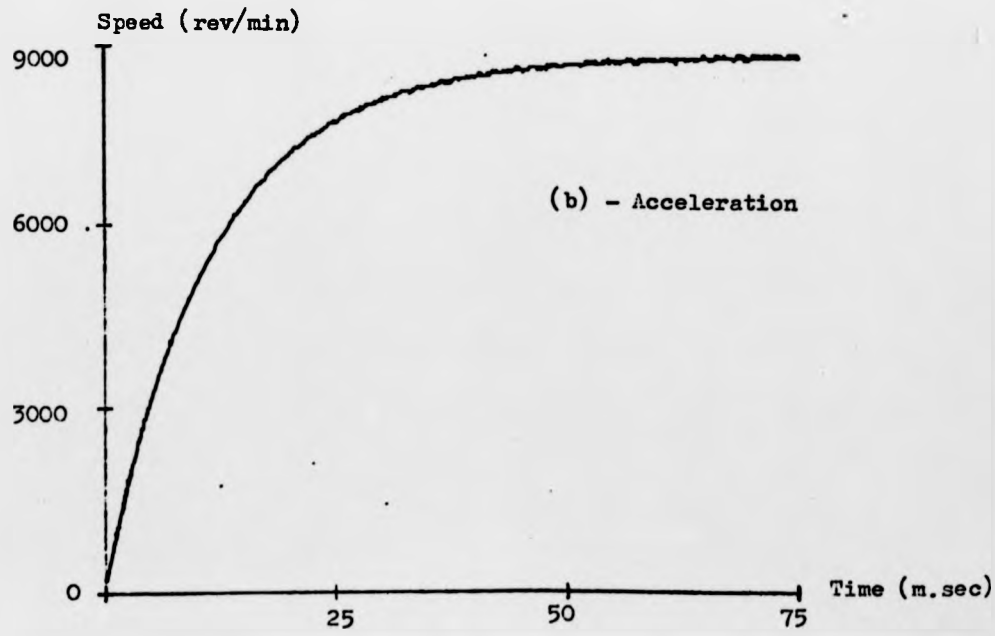

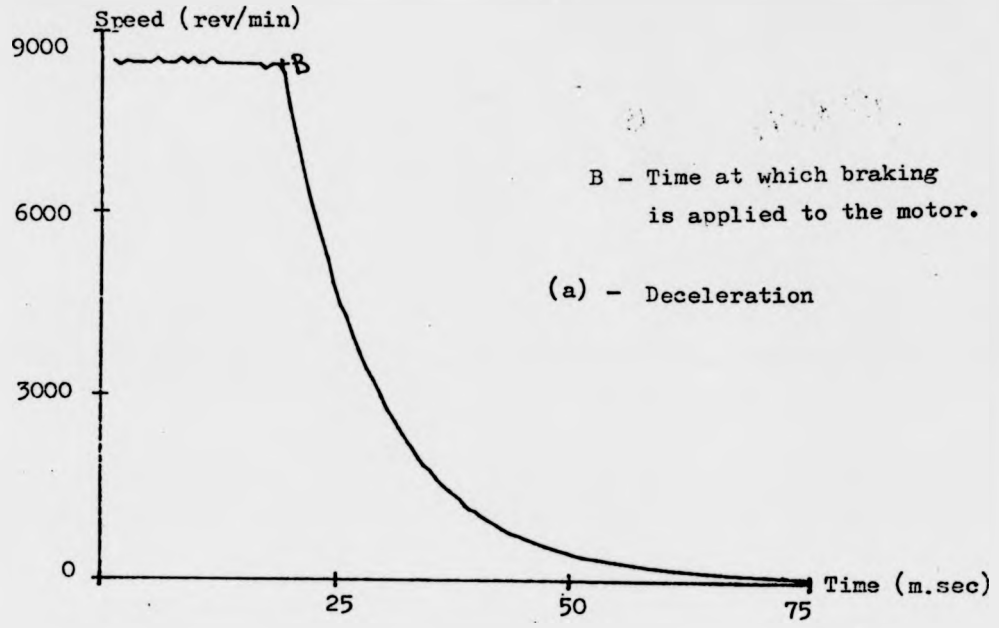

Fig.(7.4) - The dynamic performance of the experimental motor under total inertia $J = 1.85 \times 10^{-4} Kg.m^2$.

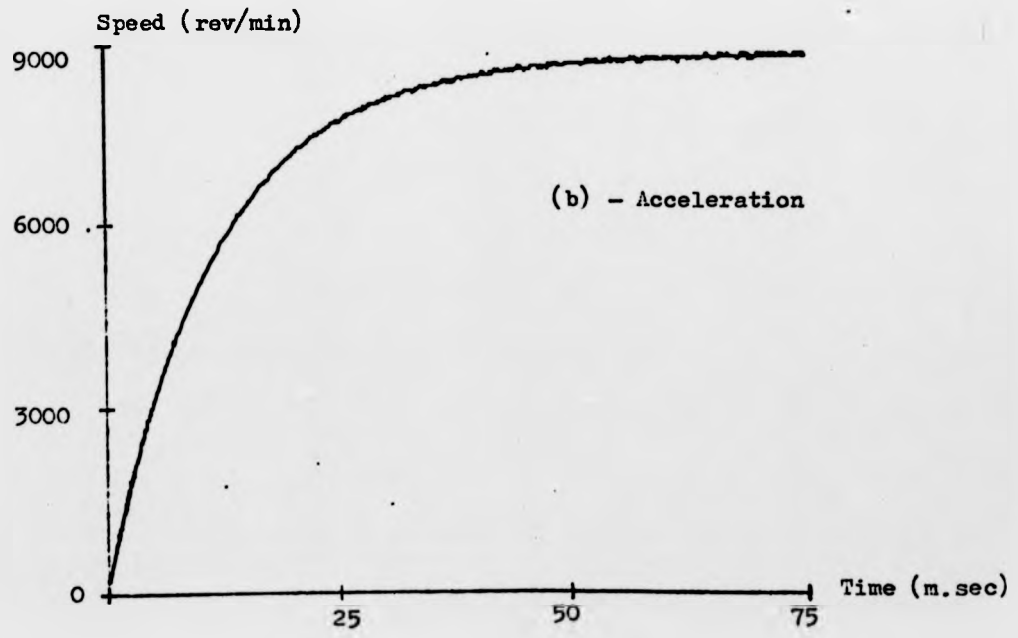

Curve-b shows that the time required by the motor to reach speed of 6000 rev/min and the mechanical time constant are 14 and 9.9 ms. Fig(7.4 c.d) - introduces similar curves when a solid steel disc of inertia 3.98 x 10^{-4}Kg.m^2 is coupled to the motor making the total inertia 5.83 x 10^{-4}Kg.m^2. Curve-c gives respective times of 274 and 46 ms and curve-d gives times of 43 and 34 ms.

A similar test is repeated on the printed circuit motor as shown in fig.(7.5). Fig.(7.5a,b) - shows the deceleration and acceleration curves of the motor running under its own inertia 1.63 x 10^{-4}Kg.m^2, coupled to the slotted disc giving rise to a total inertia of 2.78 x 10^{-4}Kg.m^2. Curve-a gives a stopping time and mechanical time constant of 96 and 25 ms and curve-b shows that the time required to reach a speed of 6000 rev/min and the mechanical time constant to be 36 and 37 ms.

Fig.(7.5c,d) shows similar curves when a solid steel disc of inertia 3.98 x 10^{-4}Kg.m^{2}is coupled to the motor making the total inertia 6.76 x 10^{-4} Kg.m^2. Curve-c gives respective times of 278 and 59 ms and curve-d gives respective times of 48 and 47 ms. The deceleration curves 7.4a,c and 7.5a,c start with an interval of time before the braking is applied to make sure that the complete deceleration curve is obtained. For any time measurements this interval of time is deducted from the total time.

7.3.2 Dynamic performance using the equivalent circuit

Since the motor incorporates permanent magnets, the field is therefore constant. Assuming the armature to have inductance L_a and effective resistance R_{eff}, the dynamic equation of the motor is given by:

$$V_t = e_a + i_a R_{eff} + L_a \frac{di_a}{dt} \quad \ldots\ldots\ldots\ldots\ldots 7.1$$

where the effect of the friction and damping is neglected, and

e_a and R_{eff} are the motor's induced e.m.f. and the motor's effective resistance

(0.78Ω)

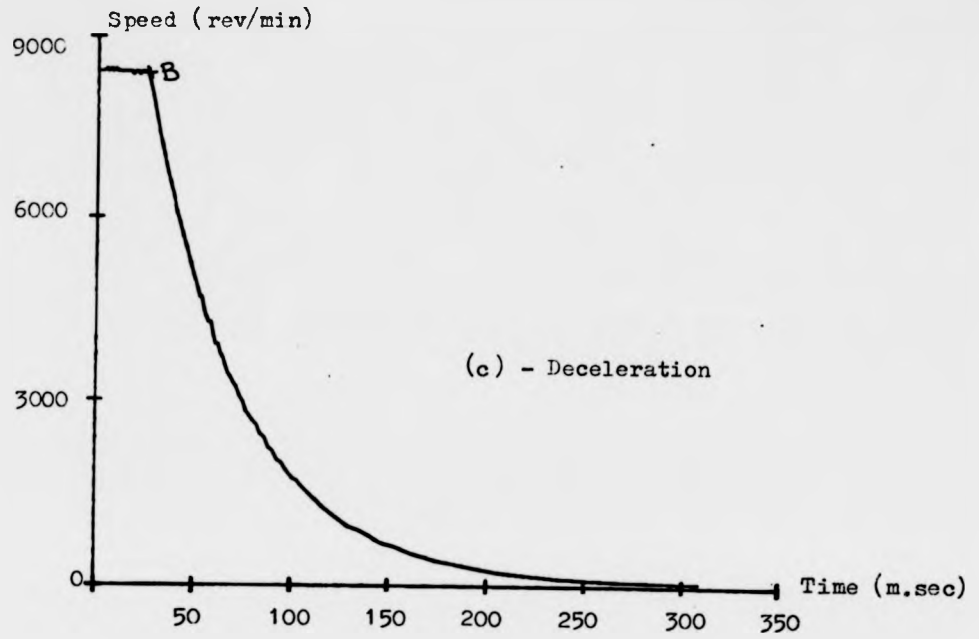

Fig.(7.4c,d) - The dynamic performance of the experimental motor under total inertia of $J = 5.83 \times 10^{-4}$ Kg.m^2

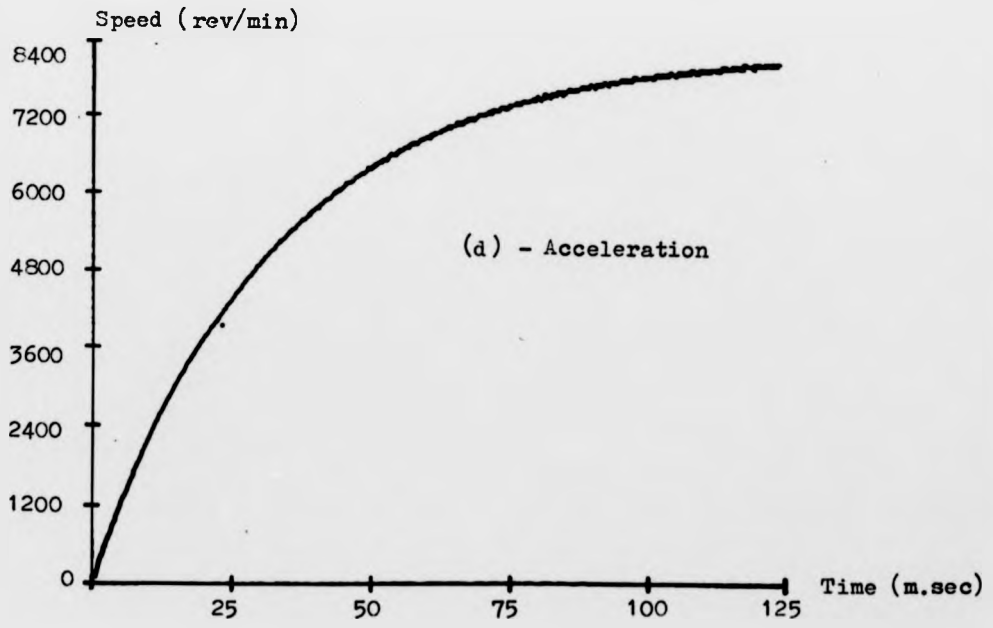

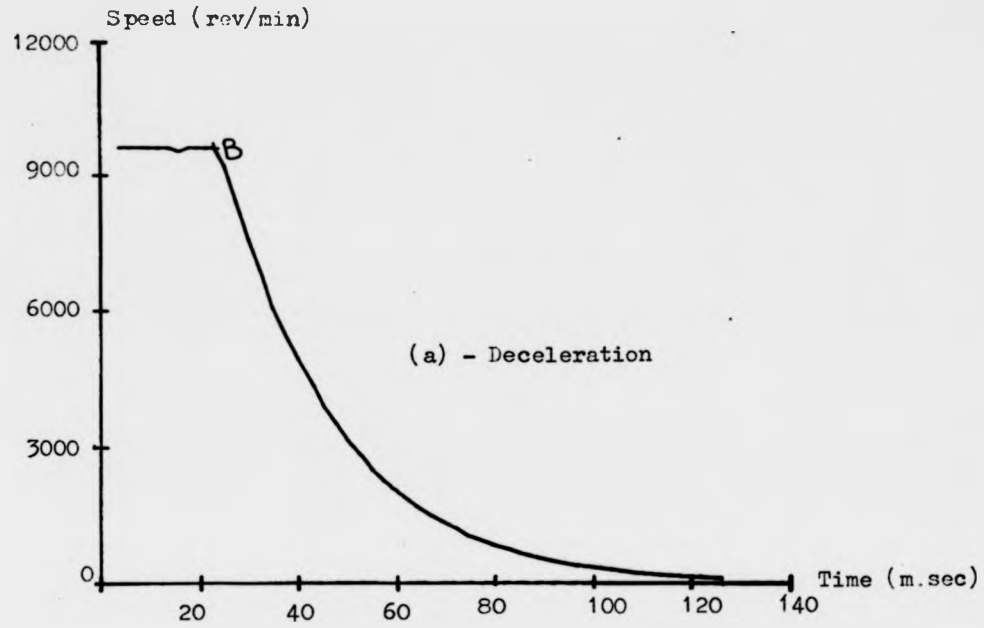

Fig.(7.5) - The dynamic performance of the printed circuit motor under total inertia of 2.78×10^{-4} Kg.m^2.

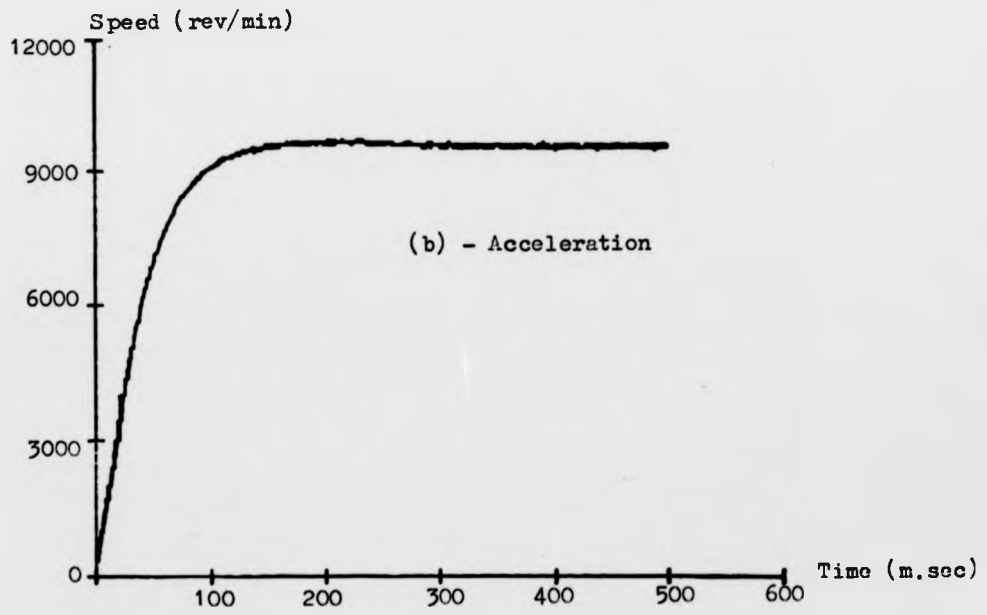

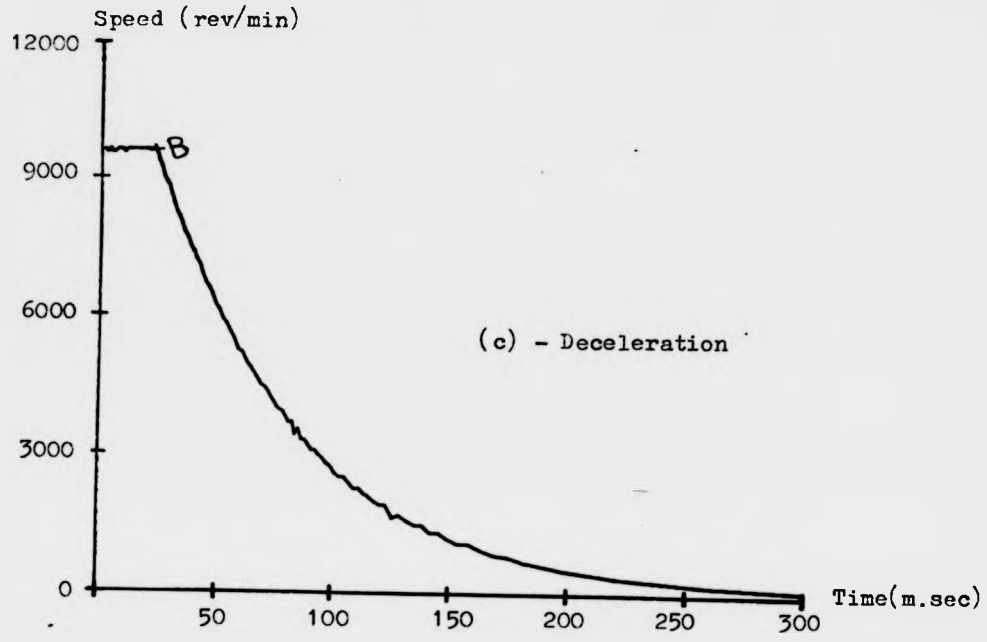

Fig.(7.5) - The dynamic performance of the printed circuit motor under total inertia of $6.76 \times 10^{-4} Kg.m^2$.

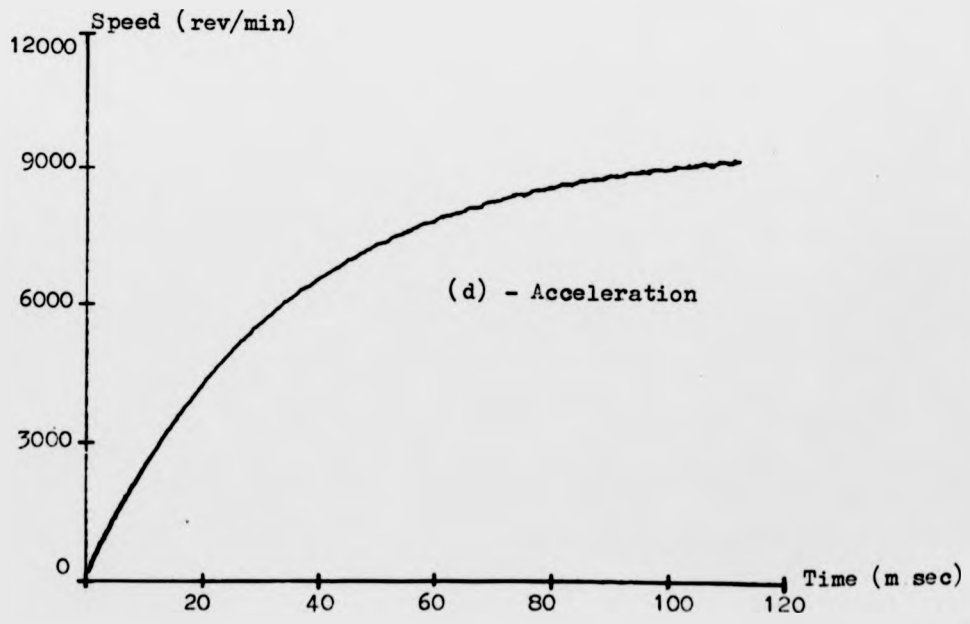

The torque:

$$T = Ki_a = J\frac{dw}{dt} \quad \text{.....7.2a}$$

and $$e_a = Kw \quad \text{.....7.2b}$$

where K is the motor's constant in (N.m/Amp), J is the total inertia and w is the instantaneous angular velocity of the motor shaft.

Putting equation 7.2 in equation 7.1 gives:

$$\frac{L_a J}{K^2}\frac{d^2w}{dt^2} + \frac{R_{eff}.J}{K^2}\frac{dw}{dt} + w = \frac{V_t}{K} \quad \text{.....7.3}$$

The armature inductance L_a was measured using an a.c bridge when the motor is complete and fully magnetised. L_a was found to be of the order of 40 μH which is ignored and the previous equation simplifies to:

$$\frac{J.R_{eff}}{K^2}\frac{dw}{dt} + w = \frac{V_t}{K} \quad \text{.....7.4}$$

which has the solution:

$$w = w_s(1 - e^{-t/T_m}) \quad \text{.....7.5}$$

where, $w_s = \frac{V_t}{K}$ Final steady state angular velocity

$T_m = \frac{J.R_{eff}}{K^2}$ Mechanical time constant 7.6

V_t = 90.0 Volts - Step input

The constant K for the experimental motor and the printed circuit motor calculated from the torque/current curves are found to be 0.127 and 0.094 Nm/Amp respectively. The mechanical time constant of each motor is found to be 3.4 and 13.84 ms respectively.

When the experimental motor is coupled to the slotted disc of inertia 1.15×10^{-4} Kg.m^2, T_m = 9.0 ms and when the solid disc of inertia 3.98×10^{-4} Kg.m^2 is added, T_m = 46.34 ms When the printed circuit is

coupled to the slotted disc T_m = 23.6 m$, and when the solid disc is added T_m = 57.4 m$

7.4 Commutation

7.4.1 Introduction

One of the important limiting factors on satisfactory operation of a d.c machine is the ability to transfer the necessary armature current through the brush contact at the commutator without excessive sparking and heating of the brushes and commutator. These could be due to some electrical characteristics like bar-to-bar voltage and reactance voltage, or due to mechanical difficulties in maintaining a homogenous commutator surface. Also some external effects such as ambient operating conditions can lead to unsatisfactory commutation. Commutation in general is the process in which successive coil sides pass from under the effect of one pole to that of another, suffering a reversal of current, which stays constant as long as each coil side is under the main pole. The flow of the current in coils embedded in slots creates a leakage field in which magnetic energy is stored. The reversal of the current there causes the field to suddenly collapse and rapidly rebuild again in the opposite direction. Such a rate of current change in a coil can give rise to a considerable reactance voltage in the coil undergoing commutation in the form "$L\frac{di}{dt}$". This voltage is usually calculated assuming a linear rate of current change. But in practice because of the coil self and mutual inductances the commutation is not linear. In the present prototype since the inductances are very small, the commutation is expected to be almost linear. One of the most important problems in commutation is sparking which is a result of high current densities accumulated at portions of the brush in non-linear commutation. Sparking causes destructive blacking, pitting and wear of both commutator and brushes, conditions which rapidly become worse and lead to burning the

copper and the carbon. Therefore any type of sparking can be considered as a sign of non-healthy commutation since it represents some form of energy dissipation.

Commutation study in the present work is base on the following: Visual check of the commutators of a number of old armatures already existing in the Department and used in tests for many years. The check concentrated on the surface finish and the insulation between segments, continuous watch for any sparking while the motor is under operation, and finally the amount of power loss due to commutation is found by separating the total loss calculated from input and output power into its different components within the motor.

7.42 The Commutator

The face type commutator is used to pass current to the rotating coils through brush contact and to occupy as small a space as possible in the axial direction. The segments are situated radially and their number in a motor can be altered without effecting the axial depth of the commutators. The brushes extend axially through one of the end-plates. The use of a cylindrical commutator is accompanied with a number of problems. Some of these include the limitation in space available in the axial direction and the need for brush gear radially disposed on the stator and consequently the need for a closed brush assembly.

7.4.3 Commutator design

Considerable work has been done to improve the making of the commutator, since the problems involved limited the production of the motors greatly at this University. The final shape of the existing commutator is arrived at as follows:

a. A suitable piece of high conductivity copper to B.S. 2874/C101,

is machined to the essentially hollow cylindrical shape of the commutator.

b. The cylinder is slotted at its wider face to produce the required number of segments.

c. The commutator is then joined to the windings through wire slots cut into each segment such that the wire is a tight push fit. The segments are made longer than the cylinder width by extending outside the cylinder at both diameters.

This method of commutator design has some disadvantages:

1. It is not possible to check the integrity of the windings before encapsulation due to the shorting of the segments at the solid conducting side.
2. Due to the open slots between the segments, it is possible that some molten solder will flow into the slots no matter how much care is taken.
3. During joining the wires to the individual segments, it has to pass over a number of segments and unless the wire is completely insulated, it will short out some of the segments.

The first disadvantage could be very serious since it means that the only possiblity of checking the armature is by machining the solid side of the commutator after encapsulation. Checking the winding at this stage is a useless process since nothing can be altered after encapsulation. Therefore due to this limitation a large number of armatures have been found to be faulty during the course of the study. It is essential therefore to introduce a new design procedure which can avoid such a limitation and provide a direct checking possibility before any encapsulation is done.

7.4.4 Modified Commutator design

The new construction procedure does not differ greatly from the above procedure. It follows the previous design up to the point "b" where the segments are produced at the wider side of the cylinder. The commutator is then encapsulated in epoxy resin by using the same steel mould employed in winding encapsulation. The commutator encapsulation gives the following important advantages:

1. It provides electrical insulation and mechanical rigidity between the segments by filling the slots, separating them electrically and moulding them together.
2. It produces an insulating layer over the segments at the wire side of the commutator which can be machined down to the required thickness. The conducting end of the commutator is now machined down until the segments are exposed to the surface and electrically separated. A hollow disc of tufnol having the same dimensions as the machined part and four tapped holes on its surface is fixed by araldite in place of part just machined to act as the part of the commutator which has to be fitted into the mould during encapsulation of the winding. The wire slots are now cut at each segment giving a complete commutator which can be checked fully before the winding is encapsulated.

7.5 Brush assembly

This in general consists of two main parts, the carbon brush and the holder. It is always necessary to know the size of the brush since this is related to the size of the machine and the commutation process. The size of any shaped brush is defined by the dimensions of the rectangular prism which will contain the whole brush. Fig.(7.6a)- shows the shape and dimensions of the brushes employed in the machine compared with cylindrical commutators.

Brush details in the experimental motor

T_1, T_2 = 5.5, 4.4 mm

w, L = 4, 10 mm

P(pressure/brush) = 300 gf/cm^2

μ(coefficient of friction) = 0.08

V_b(Brush voltage drop) = 1.45 Volts

T, T_1, T_2 - Brush thickness

w - Brush width

L - Brush length

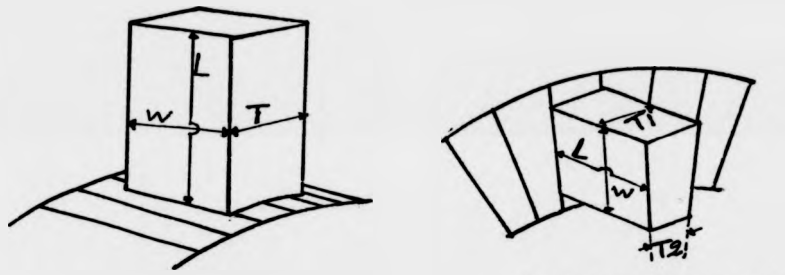

Cylindrical Commutation Face type Commutation

Fig.(7.6a) - Relative dimensions of the brush in cylindrical and face type commutators.

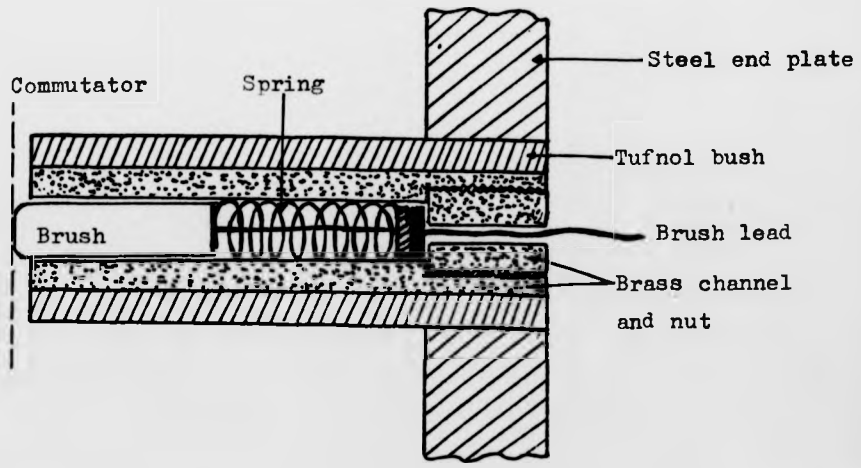

Fig.(7.6b) - Brush Assembly

Too small or too large brushes are not recommended since the first means good contact with the commutator but it is weak and fragile, and the second provides robust brushes but the contact with the commutator is ususally not so intimate as with smaller brushes. A size in between these two sizes and comparable with the machine size should be quite satisfactory. Sharp edges in the brush surface contact is not recommended and the brush can be chamferred with a standard chamferring angle of 45^{o}. In the experimental motor the current is reaching the face type commutator from the external d.c supply by the brush assembly shown in fig.(7.6b). The brush holder is of the slide type made of brass and consists of a channel at the centre having a shape and dimensions suitable to receive the brush and to allow it to slide freely.

Such an arrangement is expected to have a disadvantage in that at high speed, especially with small armatures, axial vibration or wobbling can be amplified at the brush contact causing it to rise at some places and consequently causing the current to fluctuate, giving non-stable performance characteristics. Therefore for high speed applications it is worthwhile to proceed with performance studies using a cylindrical type commutator even if some modifications are required. This type of commutator is more rigid due to the firm setting of the commutator on the shaft eliminating any axial or radial vibrations. Moreover this can simplify the commutator design also.

7.6 Performance Tests

The first set of tests on the motor are aimed to measure the different mechanical losses. The motor is run free to a maximum of 90 Volts, recording the applied voltage, input current and the speed. The input current of the motor operating with two and four brushes is shown in fig.(7.7). The effect of the brush friction on the mechanical loss is studied by running the printed circuit motor alone at first and then running it coupled to the experimental motor with no brushes, with two brushes and finally with four brushes. The mechanical loss is obtained by subtracting the I^2R loss at every current from the recorded power input. The curves obtained for currents and mechanical power loss versus voltage are shown in fig.(7.8-1,2). The friction losses due to bearings and the windage losses in experimental motor together with total mechanical loss in the braking dynamometer as a function of the speed is shown in fig.(7.8-3). The important test in this series is the load test since it gives the performance characteristics of the motor from which any unknown source of power loss in the motor can be detected using method of loss segregation into its known components. The load test was performed on the motor operating with 2 and 4 brushes and it was also performed on the printed circuit motor using the swinging frame dynamometer as an external load. The load test results are shown in fig (7.9) for the three cases.

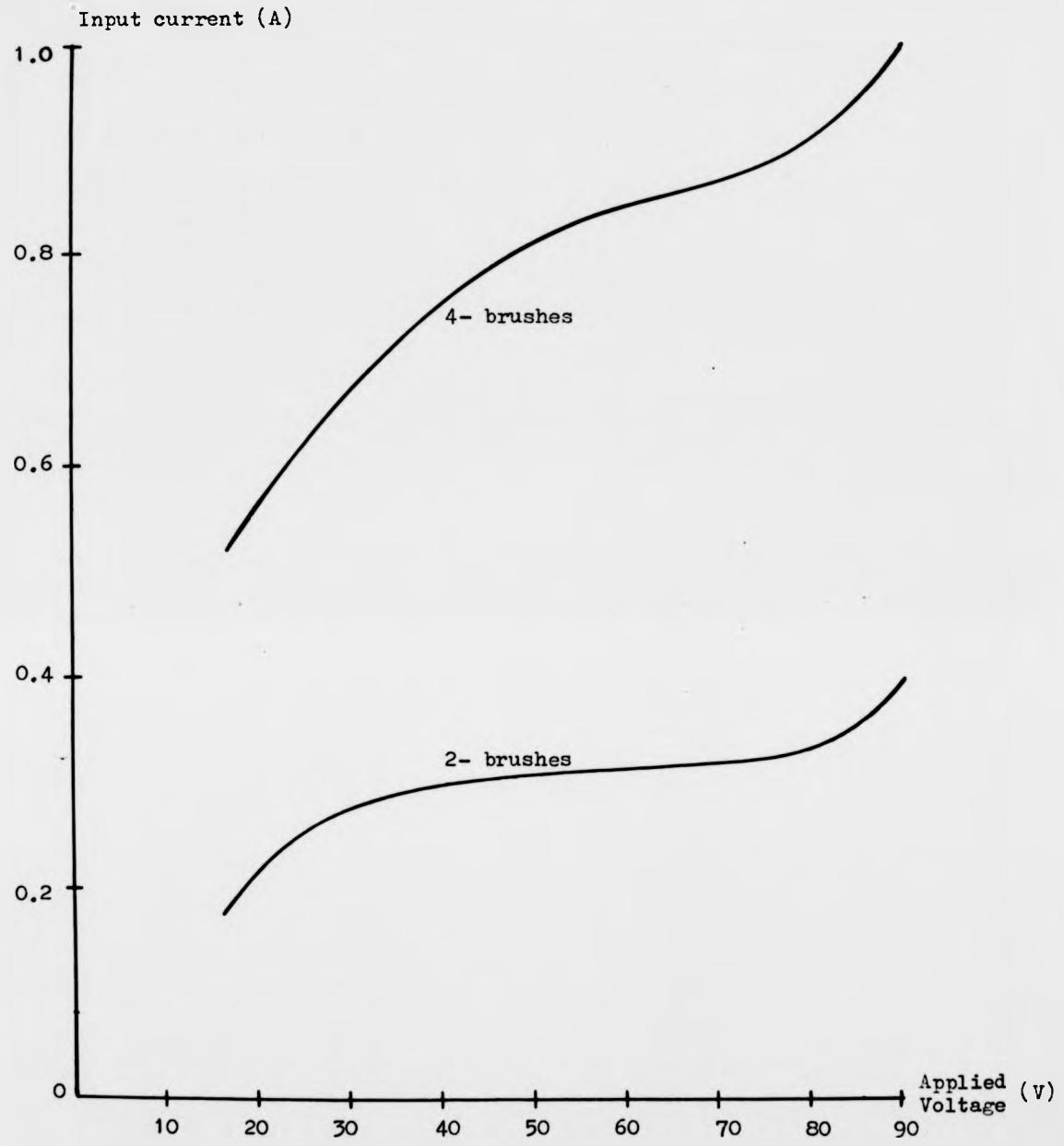

Fig.(7.7) - Running light test in experimental motor

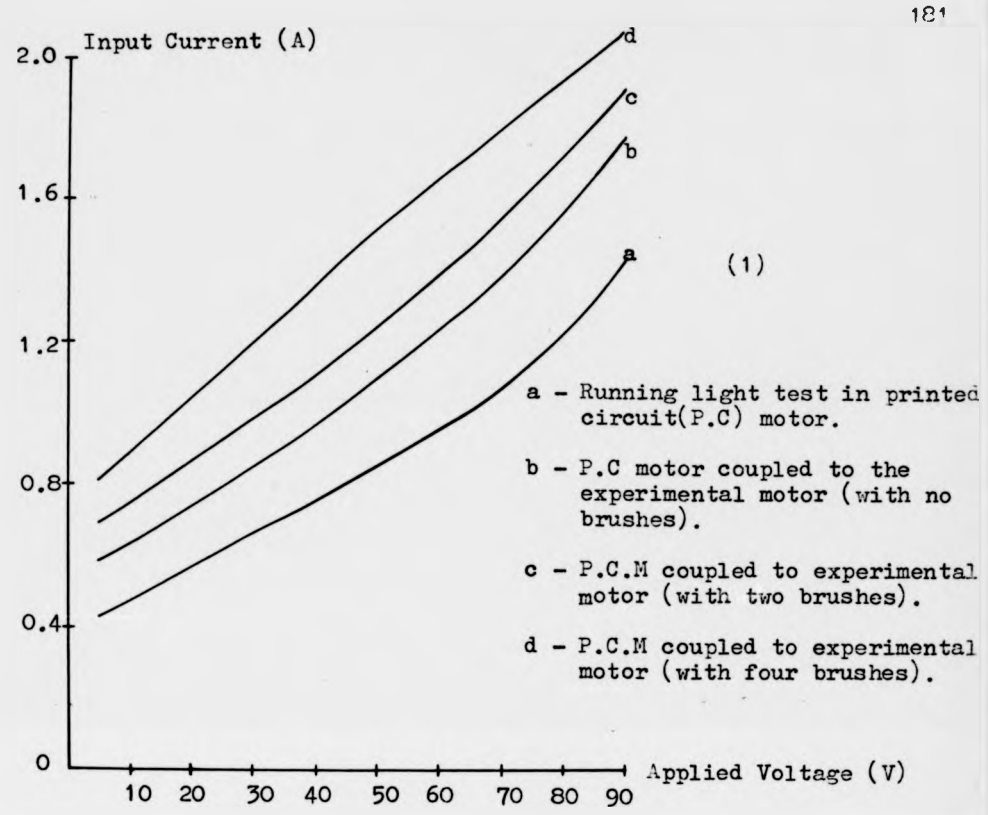

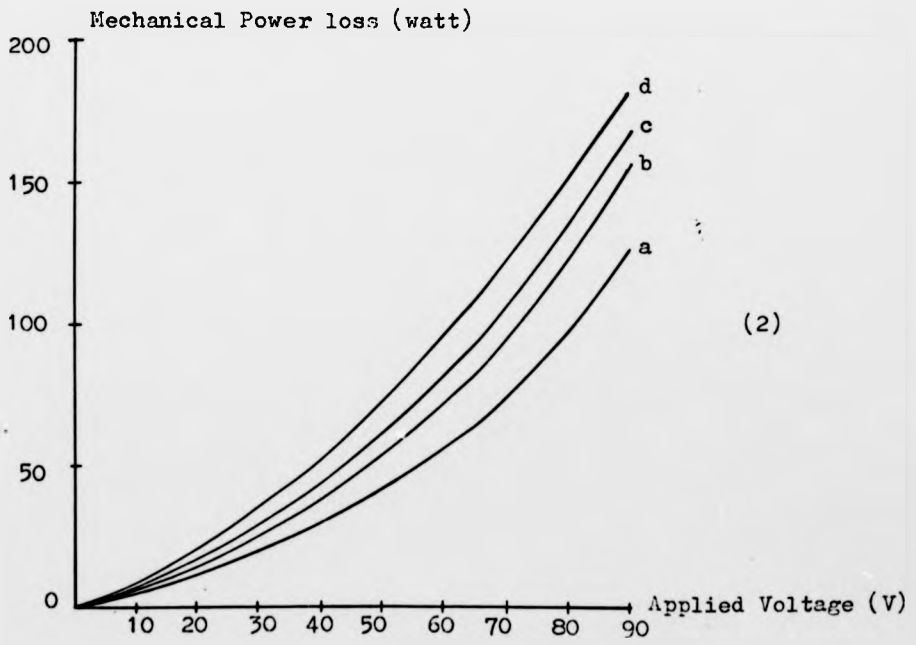

Fig.(7.8) - Driving test

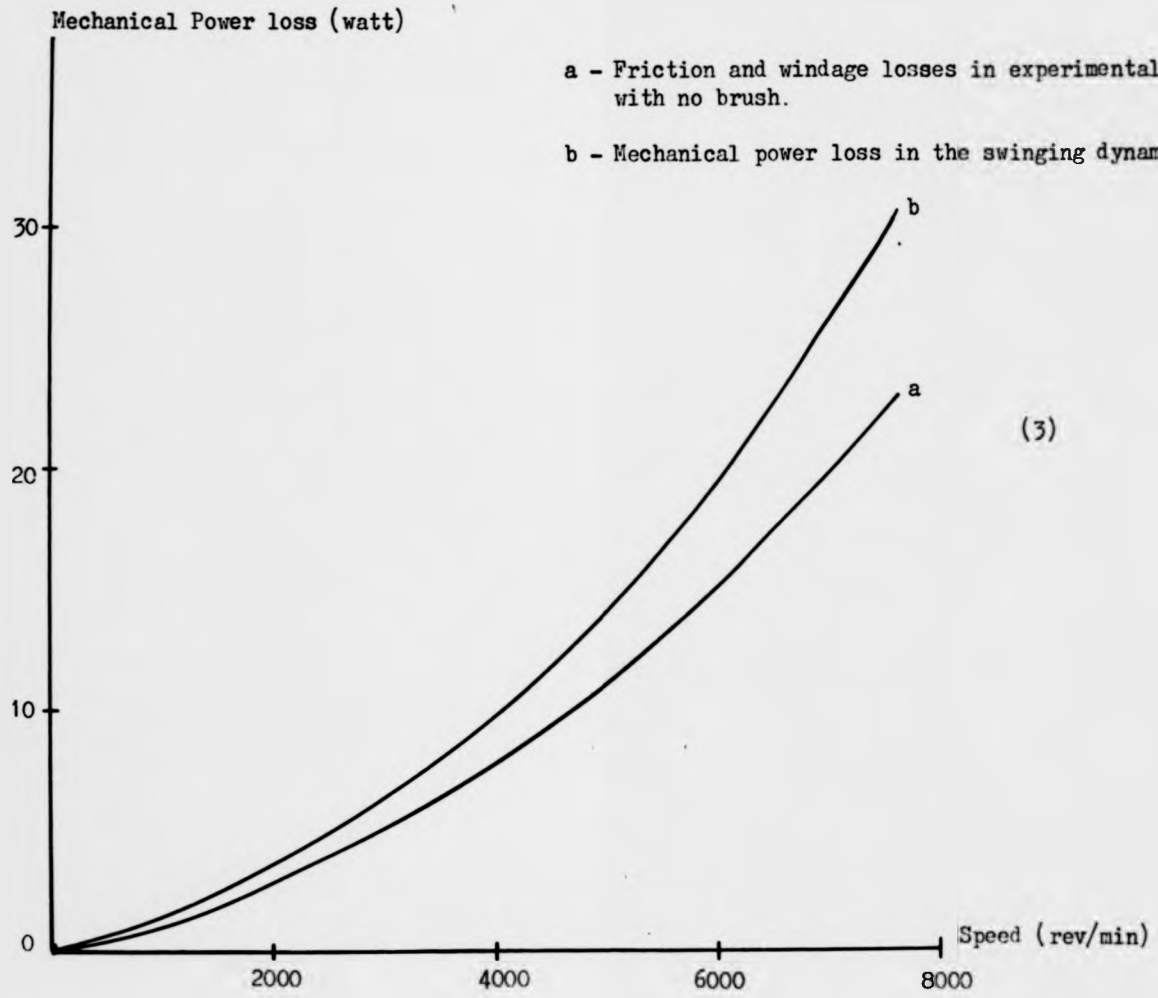

Fig.(7.8) - Driving test

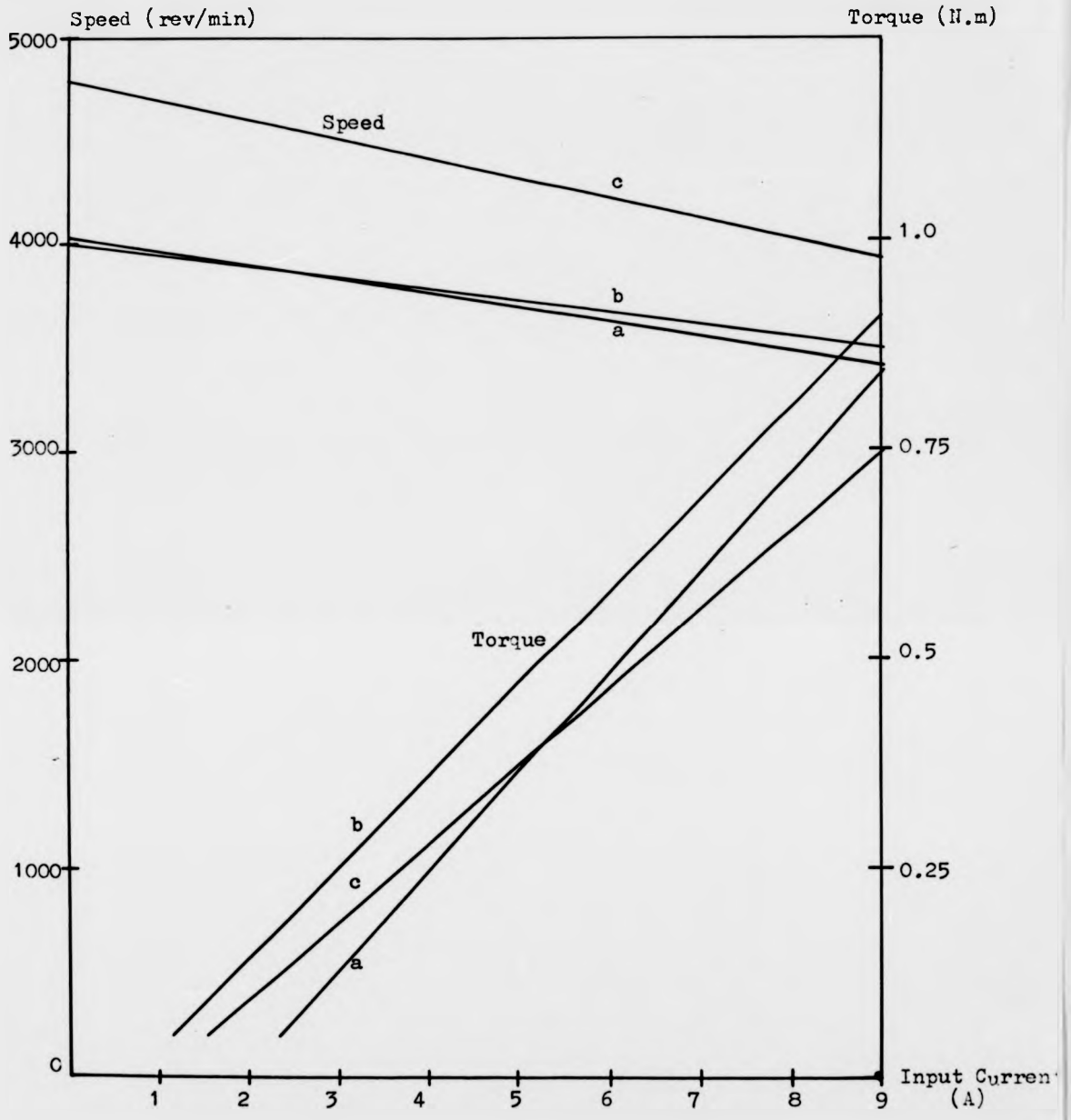

Fig.(7.9a) - Torque and speed as function of input current for constant voltage of 45.0V

a,b - Experimental motor with 4 and 2 brushes

c - Printed circuit motor

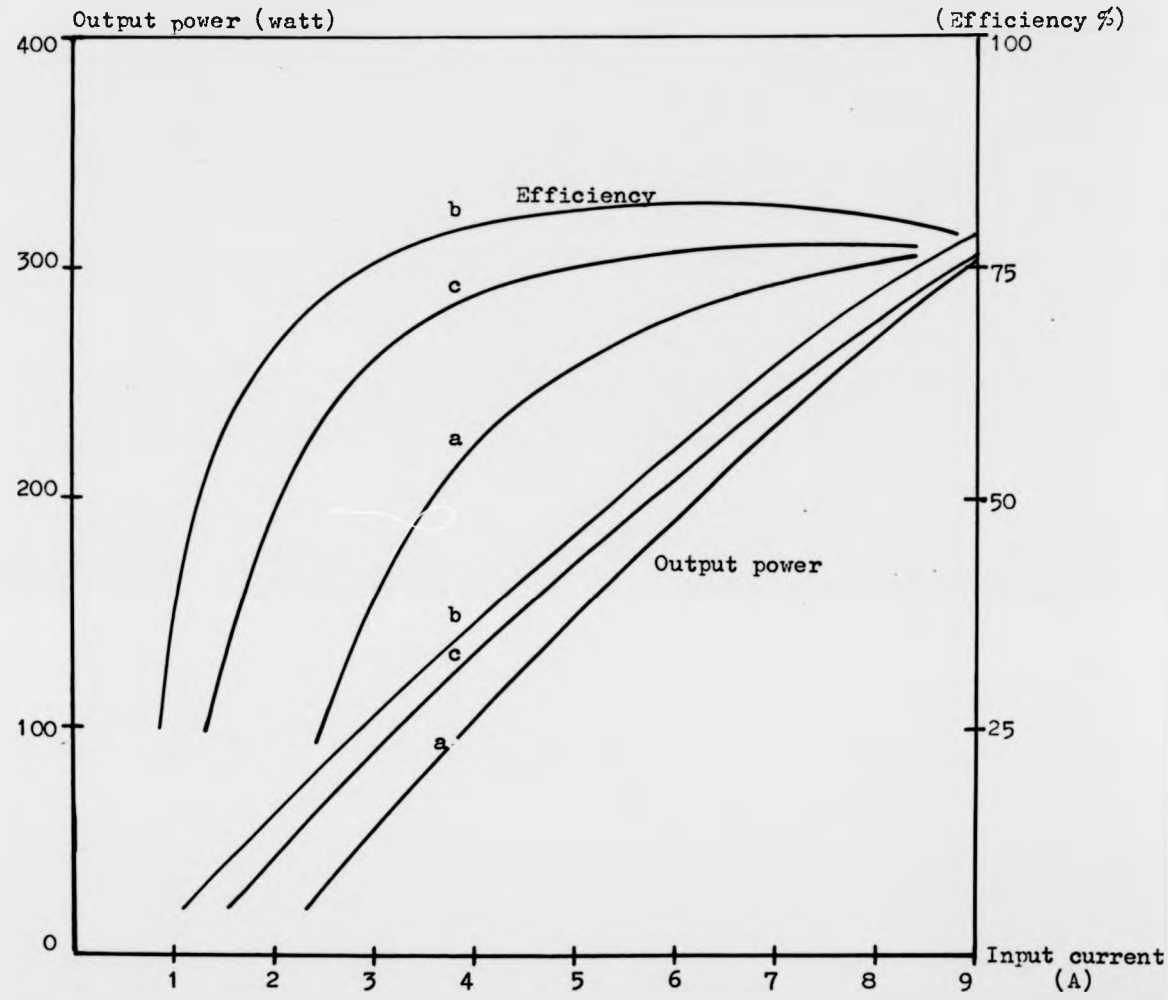

Fig.(7.9b) - Efficiency and output power as function of input current for constant voltage of 45.0V

a,b - Experimental motor with 4 and 2 brushes

c - Printed circuit motor

7.7 Results and Conclusions

7.7.1 Dynamic performance

The total motor inertia in equation 7.6 can be expressed as the sum of two parts as follows:

$$J = J_M + J_L$$

where J_M - Motor inertia only

J_L - Any other inertia applied to the shaft.

Therefore it is more convenient to write the equation as:

$$T_m = \frac{(J_M + J_L)\, R_{eff}}{K^2}$$

When $J_L = 0$, this gives the mechanical time constant of the motor under its own inertia, and is found to be 3.4 and 13.8 m.s for experimental and printed circuit motor respectively.

The time required by the experimental motor to reach speed of 6000 rev/min at extra inertia 1.15×10^{-4} $Kg.m^2$ and 5.13×10^{-4} $Kg.m^2$ are 14 and 43 ms respectively. Comparing these two values shows that the time is increasing linearly with inertia such that the time required to accelerate inertia of 4×10^{-4} $Kg.m^2$ is expected to be 30 ms. The stopping times under similar conditions are 56 and 274 ms. This increases more than linearly with inertia and the stopping time for inertia 4×10^{-4} $Kg.m^2$ is expected to be about 160 ms. The times required by the printed circuit to accelerate extra inertias 1.15×10^{-4} and 5.13×10^{-4} $Kg.m^2$ to a speed of 6000 rev/min are 36 and 48 ms, and the corresponding stopping times are 96 and 288 ms.

It was shown earlier that the mechanical time constant of the experimental motor is less than a quarter of that in printed circuit motor, giving rise to much faster response to step inputs. This could be explained

7.7 Results and Conclusions

7.7.1 Dynamic performance

The total motor inertia in equation 7.6 can be expressed as the sum of two parts as follows:

$$J = J_M + J_L$$

where J_M - Motor inertia only

J_L - Any other inertia applied to the shaft.

Therefore it is more convenient to write the equation as:

$$T_m = \frac{(J_M + J_L)\, R_{eff}}{K^2}$$

When $J_L = 0$, this gives the mechanical time constant of the motor under its own inertia, and is found to be 3.4 and 13.8 m.s for experimental and printed circuit motor respectively.

The time required by the experimental motor to reach speed of 6000 rev/min at extra inertia 1.15×10^{-4} Kg.m^2 and 5.13×10^{-4} Kg.m^2 are 14 and 43 ms respectively. Comparing these two values shows that the time is increasing linearly with inertia such that the time required to accelerate inertia of 4×10^{-4} Kg.m^2 is expected to be 30 ms. The stopping times under similar conditions are 56 and 274 ms. This increases more than linearly with inertia and the stopping time for inertia 4×10^{-4} Kg.m^2 is expected to be about 160 ms. The times required by the printed circuit to accelerate extra inertias 1.15×10^{-4} and 5.13×10^{-4} Kg.m^2 to a speed of 6000 rev/min are 36 and 48 ms, and the corresponding stopping times are 96 and 288 ms.

It was shown earlier that the mechanical time constant of the experimental motor is less than a quarter of that in printed circuit motor, giving rise to much faster response to step inputs. This could be explained

by the low inertia of the motor compared to the printed circuit motor (less than half) and larger torque produced by the motor for the same input current giving rise to higher motor constant, bearing in mind that the two motors have the same order of effective armature resistance. Moreover the good correlation between the theoretical and practical results indicates the validity of neglecting the armature inductance.

The experimental motor does not suffer any hysteresis losses and saturation. This permits the use of high peak currents. Under 90V d.c the motor draws 50A and when it is braked it gives a peak current of 90A. These currents can cause considerable heating of the motor if they last for a long time. It is found by experiment that an average of 15 start/stops per minute can rise the case temperature by 80°C. Moreover high peak currents can cause demagnetisation of metal alloy magnets.

7.7.2 Performance characteristics

The running light test of fig.(7.7) showed rather unusual behaviour when the input current is plotted against voltage. It starts with the current increasing linearly with the voltage, but at a certain voltage it changes very little for a wide range of voltage. Eventually it increases linearly again. The driving test of fig.(7.8-1,2)shows considerable brush friction loss, which is higher than the theoretical value by a factor of six. The performance test on the motor operating with 2 brushes shows very desirable characteristics. The speed falls slowly as the load increases. The torque is directly proportional to the input current in the loading. The efficiency is very high giving a maximum of 81%.

The total loss at each loading can be segregated into its expected loss components as follows:

From fig.(7.9b) at $I = 1.5A$

Power output (P_o) = 38.5W

Power input (P_{in}) = 67.5W

Therefore the total measured power loss (PL_1) = 29W. This loss is theoretically expected to be divided as follows:

Mechanical power loss at the motor(ML) = bearing friction and windage loss + brush friction loss.

The bearing friction and windage losses has been taken from the experimental curve of fig.(7.8c). This is a reasonable way of accounting for these losses, since the bearings available were not in a condition which allows calculation of these losses theoretically. These losses are found to be 9.0 watts. The brush friction losses are calculated using the formula ($P_b = 26n \times 10^{-5}$watts), where 'n' is the speed of rotation in rev/min. The loss calculated from this formula is 1.017 watts. The mechanical loss ML = 10.017W. The swinging dynamometer mechanical loss (DML) = 9.5W, The motor total $I^2R = I^2R_a + 2IV_b$ where ($R_a = 0.57$) is the armature resistance with no brush effect included.

Therefore,

$$I^2R_a = 1.28W$$

$$2IV_b = 4.35W$$

making $$I^2R = 5.63W.$$

The sum of these losses gives rise to (PL_2) = 25.15 Watts.

This procedure of loss segregation is applied at each loading and the final results are shown in table (7.1a). Similar results are shown in table (7.1b) for the motor operating with 4 brushes. The first table shows a good correlation between the measured losses(PL_1) and the losses calculated (PL_2). This indicates that almost all the losses at the motor under these conditions are known and expected. But when the motor is operated with 4 brushes under similar test conditions the results are less satisfactory. The efficiency dropped by at least 15% at an input current of 6A. The results of table (7.1b) are most important, showing no correlation between the measured and calculated losses. This indicates that there is

Table(7.1) - Power loss segregation

a-2- brushes

Amp.	rev/min	Watt							
I	N	P_θ	P_I	PL_1	ML	DML	I^2R	PL_2	$\lvert PL_2-PL_1\rvert$
1.5	3925	38.5	67.5	29	10.017	9.5	5.63	25.15	3.85
2.0	3885	60	90	30	9.009	9.4	8.08	26.5	3.5
3.0	3818	103	135	32	8.0	9.2	13.81	31.02	0.99
4.0	3770	143	180	37	7.8	9.0	20.72	37.52	0.52
5.0	3680	183	225	42	7.56	8.5	28.75	44.8	2.8
6.0	3615	220	270	50	7.44	8.4	37.92	53.76	3.76
7.0	3545	256	315	59	7.42	8.2	48.23	63.85	4.82
8.0	3480	287	360	73	7.2	7.95	59.68	74.83	1.83

b-4- brushes

2.0	3880	40.0	90.0	50.0	9.42	9.4	7.8	26.62	23.4
3.0	3820	54.5	135	80.5	8.99	9.15	13.2	31.34	49.16
4.0	3770	99.0	180	81	8.96	9.0	17.45	35.41	45.6
5.0	3710	144.5	225	80.5	8.83	8.75	27	44.6	35.9
6.0	3660	187	270	83	8.8	8.55	35.4	52.75	30.25
7.0	3600	230	315	85	8.67	8.4	44.8	61.87	23.13
8.0	3545	269	360	91	8.54	8.2	55.2	71.94	19.06

a certain amount of unexpected power dissipated somewhere within the motor. This could be due to the shorting of coils by two similar polarity brushes which would allow circulating currents to flow if the e.m.f is not zero as it should be ideally. It is therefore very essential to consider this result in the motor design in progress at this University for an electric vehicle project using a similar armature construction with four brushes.

It was very difficult to do any performance tests on the motor at 90 Volts, due to the continuous fluctuations of the readings. This could be due to the lifting of the brushes at high speed. Therefore it is perhaps worthwhile to change to harder spring brushes or to employ the cylindrical commutator design as pointed out before. The performance test on the printed circuit motor at similar applied voltage of 45V, showed satisfactory results. The speed is higher and falls down faster than that of the experimental motor at any load, but the efficiency at input current of 6A is lower by 6% than the experimental motor operating with 2 brushes and it is higher by 10% when the experimental motor is operating with 4 brushes.

CHAPTER 8

General Conclusions

The evolved design procedure gave a reliable flat-shaped 3 phase a.c. motor with good performance and high power/weight ratio. The casting method in rotor production was found to be successful. It provided answers to many problems and gave rise to many other advantages, such as ease of ventilation, fixing of the rotor on the shaft and the possibility of making single cage and double cage rotors. The rotors produced have lower weight and inertia and are more rigid and compact than that of the previous prototype built at Warwick University. The smallest rotor weight and inertia were found to be 3.35 kg, 0.0154 $kg.m^2$ and the largest 4.71 kg, and 0.0215 $kg.m^2$ for single and double cage rotors respectively. The centrifugal casting employed was found to be the most suitable for cage production with the help of grain refiners. Due to the balanced structure of these rotors, it is possible to achieve a small balanced air gap on each side of the rotor, an essential requirement in reducing UMP. The respective phases in the two stators were connected in series and the final phases are star connected giving a three-phase, four-pole, double-stator, axial-field disc motor. The load tests were carried out with the machine started by a regulated supply through a three phase variac. It is found also that the machine can start satisfactorily by direct switching to the supply.

Four rotors have been tested with the same pair of stators and these included rotor D-single cage non-skewed laminated core, rotor C-single cage skewed laminated core, rotor A-single cage non-skewed solid core and rotor B-double cage non-skewed laminated core.

The rated power and rated current of the machine with each rotor was measured by running the machine under load and recording the steady-state temperature of the external overhang of the stator winding until a loading is reached which causes a temperature of 110°C at the external overhang. It

is found that the temperature at the internal overhang exceeds that of the external overhang by about 20°C. Therefore the above temperature measurement at the external overhang can indicate the safty limit of the stator winding.

The starting torque and starting current of the machine were measured by locking the motor shaft (p.132) and recording input current, torque and winding temperature as the applied voltage increased up to half the rated voltage (i.e. 110 volts) and the values at rated voltage were found by extrapolating the curves obtained.

Tests on rotor D at 0.5mm air gap, gave rated power of 1.11kw at a slip of 0.08 and consequently a power/weight ratio of 60 watt/kg, maximum efficiency of 69%, projected starting torque and starting current of 6.5 N.m. and 14.8A respectively giving rise to starting torque/rated torque and starting current/rated current ratios of 0.84 and 2.37. Tests on the double cage rotor showed an increase in the rated power of 30% at the same slip for an increase in weight of 7%, giving rise to a power/weight ratio of 71 watt/kg and the same order of efficiency. Tests on rotors A,B and D revealed a sharp noise which could not be reduced no matter how balanced the air gaps were, but could be reduced effectively by increasing the gap length.

Tests on the skewed bar rotor C showed small improvement in the efficiency compared to rotor D, and a rated power of 1.067 kw at a slip of 0.117 and phase current of 6.6A. The effect of increasing the rotor resistance on machine performance is demonstrated on this rotor by machining portions of the end rings in two steps. Machining the end rings by 4mm reduces the cross section area of the end ring by 28% and the radial bars at each end by about 12% and consequently increase the total resistance of the cage effectively. Increasing the cage resistance reduces the efficiency, output power and power factor. It also increases the starting torque, reduces the maximum torque and moves it towards larger slip. In all these tests a good correlation between the calculated and the measured results is obtained except in the case of efficiency. This can indicate the existence of certain power loss which is not accounted for and this could be due to non-perfectly aligned gaps on the rotor sides. Some tests has been done on the motor with only one

stator energised and the other used as a magnetic return path. The tests showed very promising results for using the motor in single side applications.

Harmonic study furnished results which were used successfully in noise reduction. Rotor skewing and magnetic wedges in the stator are the two techniques found to reduce the noise effectively giving the possibility of using smaller air gap and consequently improving the performance characteristics. The iron powder magnetic wedges are used for the first time having such dimensions in small motors and especially for noise reduction purposes. It was found that skewing the rotor bars can reduce the sound level by 40%, while using magnetic wedges in the stator slots gives rise to more than 60% reduction, but the first gives rise to lower harmonic content. The harmonic results can be summarised as follows: The largest mmf harmonic is the fifth having amplitude 2% of the fundamental at a total gap of 0.45mm. This can be reduced to 0.67% by expanding the gap to 0.75mm, demonstrating the filtering effect of the gap reluctance. The alignment of the two stators has considerable effect on the harmonic content, magnetic balance and consequently iron loss. By increasing the misalignment at stages of 15, 30 and 45° at zero air gap it is found that the fifth harmonic increased by 2%, 3% and 6%. The harmonics in the core flux are found to be negligible. Insertion of the rotor D between the stators increased the gap flux and at the same time increased the harmonic content. These harmonics are found to be load dependent. Insertion of the skewed bar rotor C showed the same order of gap flux and a considerable drop in harmonic content compared with that in rotor D. These harmonics are also less load dependent. Most important is the considerable reduction in the noise. Similar tests on the two rotors after inserting the magnetic wedges showed considerable reduction in the existing harmonics and the creation of new harmonics due to early saturation of the wedge material. This was accompanied by a noise reduction of about 60% in the case of rotor D but no significant improvement has been noticed on the other performance characteristics.

Tests on a new low-inertia d.c motor operated with two brushes revealed that the motor due to its permanent magnet stator and ironless thin armature,

has very low power losses and consequently high efficiency. From the results at 45 volts and input current of 8A, the speed is 3480 rev/mins, output power 288 watt and efficiency 81% in a frame size of 150mm diameter and 60mm length. It is found also that the motor can reserve a respectable place in fast response applications as its time constant is 3.4 ms.

8.1 Expected applications in the market

The flat shape of the a.c. motor, the high power/weight ratio obtained and the satisfactory performance characteristics together with the improvements in manufacturing technique introduced could make the motor attractive for a number of industrial applications. The first practical application is expected to be in using the motor to drive directly the brush of a floor polishing machine. It is required for these polishing machines to be slim enough to enter freely under desks and tables. Applying the radial motors showed that the machine failed to demonstrate such a requirement satisfactorily. The author is expected to engage in further work in applying the new design to these machines after some modifications. The expected motor is a single-phase motor operating by one stator, while the removal of the stator from the other has to be used to lock the brush assembly to the rotor face.

The same design principles can be used to improve the pump-drive motors produced by SMC for small single phase and large three phase pump drives. The rotor can be produced by aluminium casting on a laminated core. The impeller can be produced by epoxy encapsulation on one side of the rotor.

8.2 Suggestions for future work

The following are some of the suggestions to be considered in any further improvement of the motor:

a. Laminated layer separation:

Using the same manufacturing technique it is worthwhile to think of a method which can help effectively in separating the strips after the radial holes and slots are made as follows; The core after being annealed is dropped at its centre on a steel cylinder filled with liquid nitrogen and allow to cool down. The layers nearest to the centre start to freeze early and shrink causing each individual layers to separate from others.

b. Unbalance magnetic pull:

The study on UMP should be continued and investigated practically in the experimental machine using the transducer of fig.(5.8). This transducer is designed to be used in the first prototype machine. Therefore to use it in the present motor some modifications are required. Special attention must be given to the single side motor and the techniques of magnetic pull reduction already suggested must be investigated fully.

c. Core design:

There is always a fundamental difference between the rotor and stator in that the stator is stationary while the rotor is rotating. Therefore the stator manufacturing method does not necessarily have to be suitable for rotor manufacturing also. Therefore it is logical to think of different design methods for rotor and stator core manufacture. A new stator core manufacturing method worth investigating involves the making of a steel mould of the exact shape and

dimensions of the stator core. The core is then produced by encapsulating iron powder and resin under high pressure. The iron powder must be of very high concentration (more than 97% by volume) and the resin has to be thinned to allow mixing, Ref. 81. Investigations and tests are required to examine the suitability of the method for stator core production and then could be extended to considerations on rotor core production.

d. The work must proceed with more tests on the motor with only one stator, covering performance studies and UHP investigations. It is required to proceed with a feasibility study on producing a single phase, single side motor using the same manufacturing tech nique.

APPENDICES

A1 - Stress Analysis in aluminium cage

It is useful to obtain a rough idea about the mechanical rigidity of the aluminium cage produced by the casting method of Chapter 2. This can be achieved by carrying out a stress analysis by considering the cage as a solid disc having the same radii R_1 and R_2 as the cage. It is assumed that the principal stresses on this disc are the radial stress P_r and the circumferential stress P_c, ρ is the specific gravity of aluminium and w the uniform angular velocity of rotation. For the calculation of the stresses on the disc, the total stress on a small element of the disc is calculated and then equated to the centrifugal stress. Considering an element dR of the disc in the radial direction at radius R having thickness t and subtending an angle $d\theta$ at the centre and using the method of stress analysis in ref. 8.2, it is possible to show that the relation between the two main stresses is:

$$P_c = \rho w^2 R^2 + \frac{d}{dR}(P_r R) \quad \ldots\ldots\ldots\ldots\ldots\ldots A1.1$$

Using the strain/stress principles in the same reference, it is possible to show that:

$$P_c = \frac{mE}{m^2-1}\left(m\frac{u}{R} + \frac{du}{dR}\right) \quad \ldots\ldots\ldots\ldots\ldots\ldots A1.2a$$

$$P_r = \frac{mE}{m^2-1}\left(\frac{u}{R} + m\frac{du}{dR}\right) \quad \ldots\ldots\ldots\ldots\ldots\ldots A1.2b$$

It is assumed that the aluminium is mechanically isotropic, and

u - the radial movement due to radial stress

u/R - the circumferential strain

du/dR - the radial stress

1/m - is the poisson's ratio ν E - Young's modulus.

Putting equations A1.2a and A1.2b in equation A1.1 and solving the second order equations using the complementary function method, it is possible to show that;

$$P_c = \frac{\rho_w^2}{8m}\left((3m+1)\left(R_1^2 + R_2^2 + \frac{R_1^2 R_2^2}{R^2}\right) - (m+3)R^2\right) \quad \text{.....A1.3a}$$

$$P_r = \frac{\rho_w^2}{8m}\left((3m+1)\left(R_1^2 + R_2^2 - \frac{R_1^2 R_2^2}{R^2} - R^2\right)\right) \quad \text{.....A1.3b}$$

Substituting $R_2 = 2R_1$ in these equations;

$$P_c = \frac{\rho_w^2}{8}\left((3+\nu)\left(5R_1^2 + \frac{4R_1^4}{R^2}\right) - (1+3\nu)R^2\right) \quad \text{.....A1.4a}$$

$$P_r = \frac{\rho_w^2}{8}\left((3+\nu)\left(5R_1^2 - \frac{4R_1^4}{R^2} - R^2\right)\right) \quad \text{.....A1.4b}$$

Fig.(8.1) shows the curves of the two stresses as a function of the radius R. P_c has the largest value at $R = R_1$ and P_r has its maximum value at $R = \sqrt{2}R_1$. These values of stresses are calculated using:

$$R_1 = 42.5\text{mm}, \quad n = 1500 \text{ rpm}, \quad \nu = 0.33, \quad \rho = 2700 \text{ kg/m}^3$$

and are found to be:

$$P_c(\text{max}) = 0.42 \text{ N/mm}^2$$

$$P_r(\text{max}) = 0.05 \text{ N/mm}^2$$

The proof stress - PS (the stress beyond which the metal deforms plastically) and the ultimate tensile strength - UTS (the maximum stress necessary to rupture the metal) of the two aluminium samples of fig.(2.6) found to be:

Putting equations A1.2a and A1.2b in equation A1.1 and solving the second order equations using the complementary function method, it is possible to show that;

$$P_c = \frac{\rho_w^2}{8m}\left((3m+1)\left(R_1^2 + R_2^2 + \frac{R_1^2 R_2^2}{R^2}\right) - (m+3)R^2\right) \quad .....A1.3a$$

$$P_r = \frac{\rho_w^2}{8m}\left((3m+1)\left(R_1^2 + R_2^2 - \frac{R_1^2 R_2^2}{R^2} - R^2\right)\right) \quad .....A1.3b$$

Substituting $R_2 = 2R_1$ in these equations;

$$P_c = \frac{\rho_w^2}{8}\left((3+\nu)\left(5R_1^2 + \frac{4R_1^4}{R^2}\right) - (1+3\nu)R^2\right) .....A1.4a$$

$$P_r = \frac{\rho_w^2}{8}\left((3+\nu)\left(5R_1^2 - \frac{4R_1^4}{R^2} - R^2\right)\right) .....A1.4b$$

Fig.(8.1) shows the curves of the two stresses as a function of the radius R. P_c has the largest value at $R = R_1$ and P_r has its maximum value at $R = \sqrt{2}R_1$. These values of stresses are calculated using:

$$R_1 = 42.5\text{mm}, \quad n = 1500 \text{ rpm}, \quad \nu = 0.33, \quad \rho = 2700 \text{ kg/m}^3$$

and are found to be:

$$P_c(\text{max}) = 0.42 \text{ N/mm}^2$$

$$P_r(\text{max}) = 0.05 \text{ N/mm}^2$$

The proof stress - PS (the stress beyond which the metal deforms plastically) and the ultimate tensile strength - UTS (the maximum stress necessary to rupture the metal) of the two aluminium samples of fig.(2.6) found to be:

Putting equations A1.2a and A1.2b in equation A1.1 and solving the second order equations using the complementary function method, it is possible to show that;

$$P_c = \frac{\rho_w^2}{8m}\left((3m+1)\left(R_1^2 + R_2^2 + \frac{R_1^2 R_2^2}{R^2}\right) - (m+3)R^2\right) \quad \text{.....A1.3a}$$

$$P_r = \frac{\rho_w^2}{8m}\left((3m+1)\left(R_1^2 + R_2^2 - \frac{R_1^2 R_2^2}{R^2} - R^2\right)\right) \quad \text{.....A1.3b}$$

Substituting $R_2 = 2R_1$ in these equations;

$$P_c = \frac{\rho_w^2}{8}\left((3+\nu)\left(5R_1^2 + \frac{4R_1^4}{R^2}\right) - (1+3\nu)R^2\right) \quad \text{.....A1.4a}$$

$$P_r = \frac{\rho_w^2}{8}\left((3+\nu)\left(5R_1^2 - \frac{4R_1^4}{R^2} - R^2\right)\right) \quad \text{.....A1.4b}$$

Fig.(8.1) shows the curves of the two stresses as a function of the radius R. P_c has the largest value at $R = R_1$ and P_r has its maximum value at $R = \sqrt{2}R_1$. These values of stresses are calculated using:

$$R_1 = 42.5\text{mm}, \quad n = 1500 \text{ rpm}, \quad \nu = 0.33, \quad \rho = 2700 \text{ kg/m}^3$$

and are found to be:

$$P_c(\text{max}) = 0.42 \text{ N/mm}^2$$

$$P_r(\text{max}) = 0.05 \text{ N/mm}^2$$

The proof stress - PS (the stress beyond which the metal deforms plastically) and the ultimate tensile strength - UTS (the maximum stress necessary to rupture the metal) of the two aluminium samples of fig.(2.6) found to be:

Putting equations A1.2a and A1.2b in equation A1.1 and solving the second order equations using the complementary function method, it is possible to show that;

$$P_c = \frac{\rho_w^2}{8m}\left((3m+1)\left(R_1^2 + R_2^2 + \frac{R_1^2 R_2^2}{R^2}\right) - (m+3)R^2\right) \quad \text{.....A1.3a}$$

$$P_r = \frac{\rho_w^2}{8m}\left((3m+1)\left(R_1^2 + R_2^2 - \frac{R_1^2 R_2^2}{R^2} - R^2\right)\right) \quad \text{.....A1.3b}$$

Substituting $R_2 = 2R_1$ in these equations;

$$P_c = \frac{\rho_w^2}{8}\left((3+\nu)\left(5R_1^2 + \frac{4R_1^4}{R^2}\right) - (1+3\nu)R^2\right) \quad \text{.....A1.4a}$$

$$P_r = \frac{\rho_w^2}{8}\left((3+\nu)\left(5R_1^2 - \frac{4R_1^4}{R^2} - R^2\right)\right) \quad \text{.....A1.4b}$$

Fig.(8.1) shows the curves of the two stresses as a function of the radius R. P_c has the largest value at $R = R_1$ and P_r has its maximum value at $R = \sqrt{2}R_1$. These values of stresses are calculated using:

$$R_1 = 42.5\text{mm}, \quad n = 1500 \text{ rpm}, \quad \nu = 0.33, \quad \rho = 2700 \text{ kg/m}^3$$

and are found to be:

$$P_c(\text{max}) = 0.42 \text{ N/mm}^2$$

$$P_r(\text{max}) = 0.05 \text{ N/mm}^2$$

The proof stress - PS (the stress beyond which the metal deforms plastically) and the ultimate tensile strength - UTS (the maximum stress necessary to rupture the metal) of the two aluminium samples of fig.(2.6) found to be:

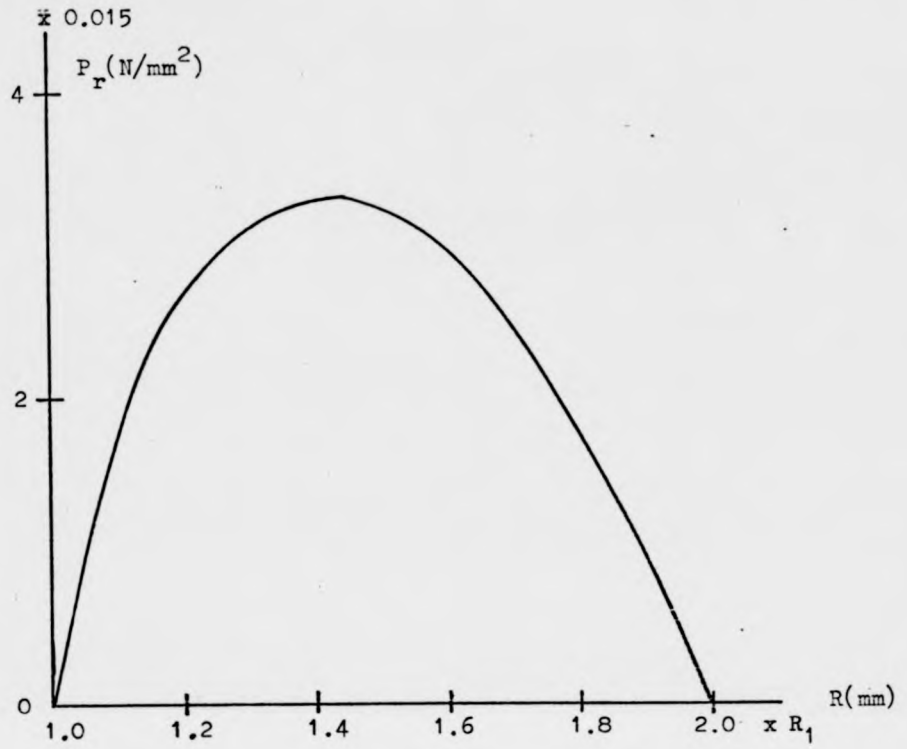

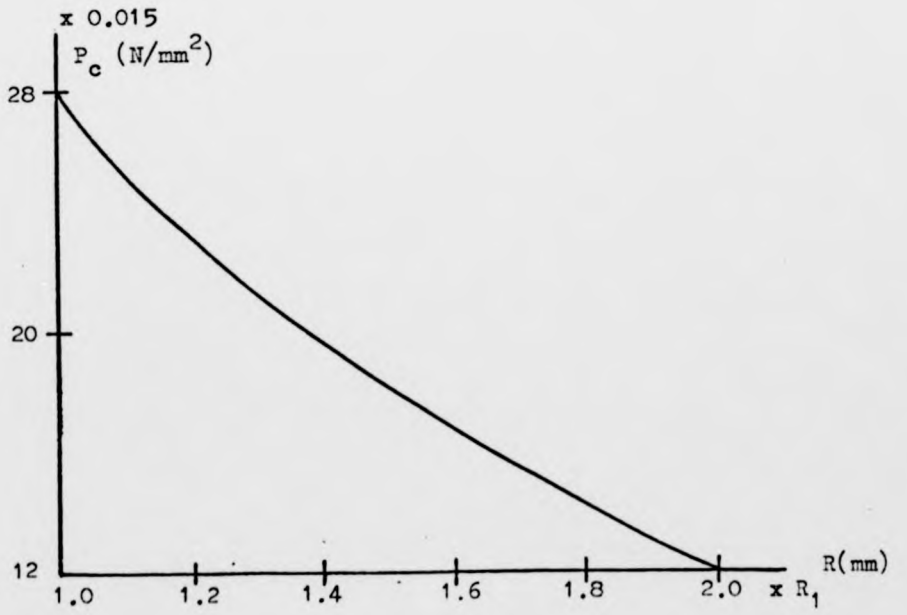

Fig.(8.1) - Radial and circumferential stresses as a function of the radius.

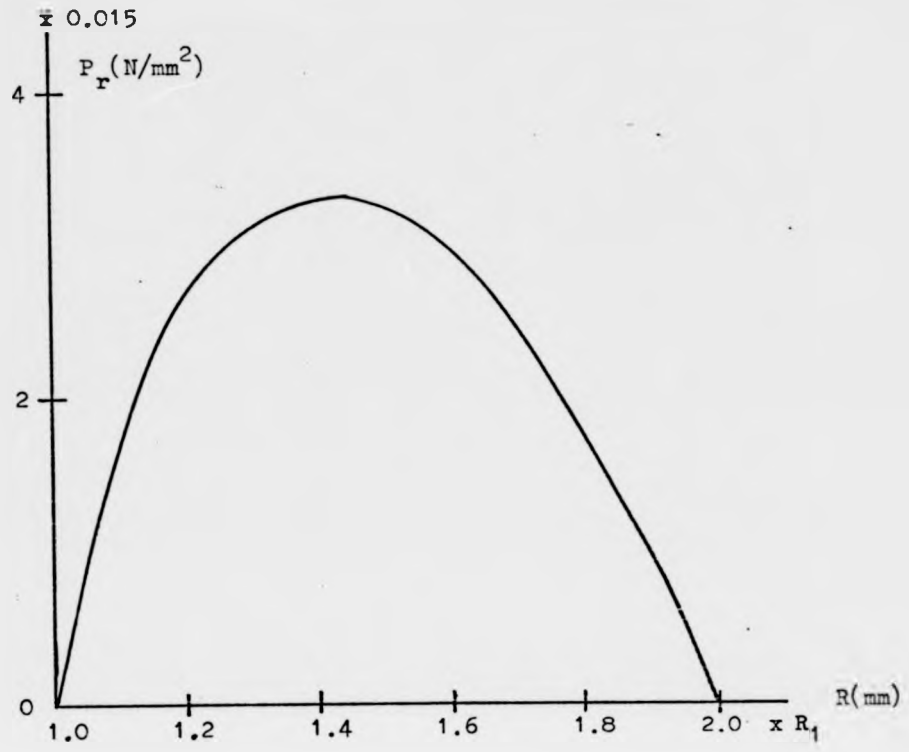

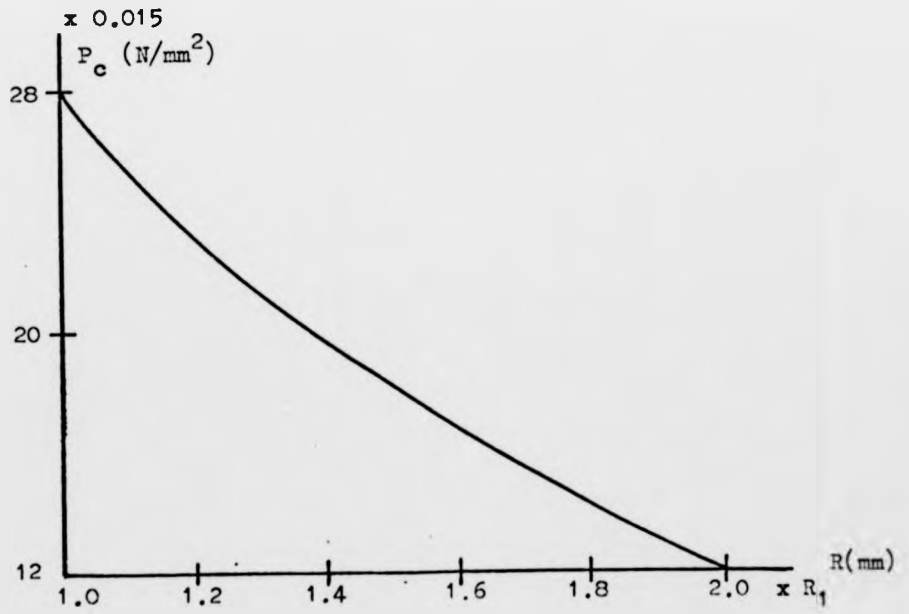

Fig.(8.1) - Radial and circumferential stresses as a function of the radius.

99.7% pure Al - 0.2% PS = 10.47 N/mm^2

UTS = 32.72 N/mm^2

Grain refined Al - 0.2% PS = 23.00 N/mm^2

UTS = 69.27 N/mm^2

The speed n_c of the cage at which the aluminium begins to loose its elasticity is found by equating the value of the PS to the $P_r(max)$ from equation A1.4b giving that;

$$n_c = 32000 \text{ rpm}$$

The bursting speed n_b can be found in similar way by equating the UTS to $P_r(max)$ giving that;

$$n_b = 96000 \text{ rpm}$$

This theory is an approximate approach to the practical situation and it can give a rough idea about the cage rigidity. The true values of the speeds are expected to be lower than the calculated value.

A2 - Slot combination

The slots in the motor can cause harmonics having a number of poles $2(P/2 \pm m)$, where m can represent the number of stator or rotor slots or the difference. The number of poles of the slot harmonics in the experimental machine of 4-poles are expected to be:

24 slots/stator produce 52,-44 poles

18 slots/rotor produce 40,-32 poles

20 slots/rotor produce 44,-36 poles

4 slots difference(24/20) produce 12,-4 poles

6 slots difference(24/18) produce 16,-8 poles

n	Number of poles
1	4
3	12
5	20
7	28
9	36
11	44
13	52
17	68
19	76
21	84

The above table shows the stator winding's number of poles.
By comparing the number of poles due to slot harmonics produced by each rotor or their differences by the nearest number of poles in stator winding, it is possible to check the differences in number of poles as follows;

18 slots rotor gives always differences of 4-poles.

20 slots rotor gives no pole differences.

4-slots difference - gives no pole differences.

6-slots difference - gives differences of 4 poles.

This brief study shows that all the pole combinations produced by the harmonic fields do not show any 2-poles differences. Therefore the motor is expected not to suffer from unbalanced magnetic pull due to 2-pole differences in the air-gap fields.

A3 - Effective reactance and resistance of the cage

Effective reactance and resistance of the bar

By changing the rotor resistance and reactance it is possible to secure a wide range of performance characteristics. The first is achieved by changing the bar cross sectional area or its material while the second is achieved by changing the shape of the bar. The size and shape of the slots can therefore affect the performance through changing the reactance, the air gap reluctance and magnetizing current. The thickness of the rotor in the experimental machine is affected by the shape of the slots. In the low resistance cage, an elongated shape bar in axial direction is used, while in the high resistance cage the axial depth of the bar is reduced and its shape approaches a circular slot reducing the thickness of the rotor. But the rotors cannot be designed too thin due to mechanical rigidity requirements and saturation effects arising in a limit on the smallest bar size which can be produced. There is also a limit on the width of the bar imposed by the central circumference of the rotor. The variation of the effective impedance of a deep bar has been studied by many investigators (Field (8.3), Bruges (8.4), and Swan (8.5)) employing different methods of analysis. The present analysis moves closely with that introduced by Swan using Poisson's equation for expressing the current distribution in the bar. The shape of the bars and slots in the experimental machine can be approximated to the rectangular shape shown in fig.(8.2) having semiclosed opening 1 and width and height of a and b respectively. It is assumed also that:

1. All the flux goes straight across the slot and the bar is in a uniform field.
2. The iron has infinite permeability.
3. The flux lines are tangential to the conductor surface at slot opening.

Fig.(8.2)

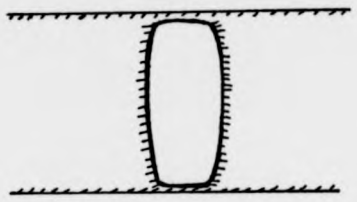

a - Actual shape of the bar and
the slot in experimental motor

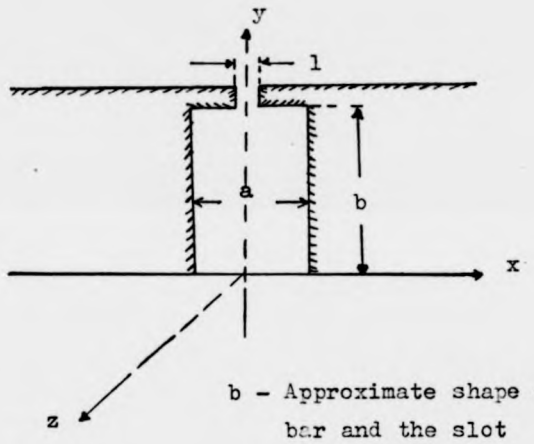

b - Approximate shape of the
bar and the slot

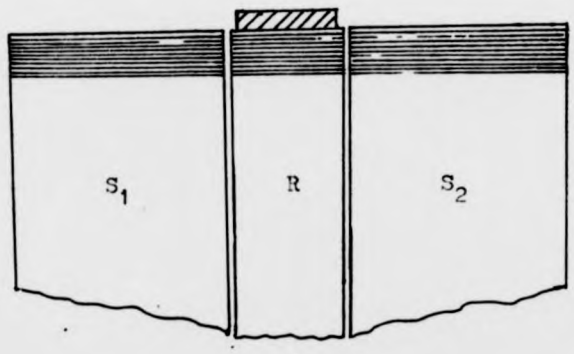

Fig.(8.5) - The cage end ring with one
iron boundary

4. Eddy currents in the laminations are neglected and the bar fills the slot completely.
5. No proximity effect.

To express the current density in the bar, the following formulae are used:

induction law $\quad \mathrm{Curl}\bar{E} = -\dot{\bar{B}}$ A3.1a

Ampere law $\quad \mathrm{Curl}\bar{H} = \bar{J}$ A3.1b

Ohm's law $\quad \bar{J} = \sigma\bar{E}$ A3.1c

Using these equations it is possible to show that:

$$\mathrm{Curl}\bar{J} = -j\bar{\alpha}^2\bar{H} \quad \text{..... A3.1d}$$

$$\nabla^2 \bar{J} = j\bar{\alpha}^2\bar{J} \quad \text{..... A3.1e}$$

where,

$$\bar{\alpha} = \sqrt{\frac{\mu_o w}{\rho}}$$

ρ - is the material resistivity

w - Angular frequency

But the bar in fig.(8.2b) is a two dimensional problem, for which equation A3.1e becomes:

$$\frac{\partial_2 J}{\partial x^2} + \frac{\partial_2 J}{\partial y^2} = j\bar{\alpha}^2\bar{J} \quad \text{..... A3.1f}$$

The current in this model flows in the Z-direction and varies with both x and y, and can be represented as:

$$J = X_{(x)} \cdot Y_{(y)} \quad \text{.....A3.2}$$

Putting equation A3.2 in eq. A3.1f gives:

$$\frac{\bar{\bar{X}}_{(x)}}{X_{(x)}} + \frac{\bar{\bar{Y}}_{(y)}}{Y_{(y)}} = j\bar{\alpha}^2 \quad \text{.....A3.3a}$$

This equation can be separated into two equations as:

$$\ddot{X}_{(x)} = K_1^2 X_{(x)} \quad \text{.....A3.3b}$$

$$\ddot{Y}_{(y)} = K_2^2 Y_{(y)} \quad \text{.....A3.3c}$$

where K_1 and K_2 are constants and,

$$K_2^2 = (j\bar{\alpha}^2 - K_1^2) \quad \text{.....A3.3d}$$

These two equations can have similar solutions as;

$$X_{(x)} = A\sinh K_1 x + B\cos K_1 x \quad \text{.....A3.4a}$$

$$Y_{(y)} = C\sinh K_2 y + D\cosh K_2 y \quad \text{.....A3.4b}$$

Boundary Conditions

As shown in fig.(8.2b), due to the symmetry of the bar about the y-axis ($J(-x,y) = J(x,y)$, $A = 0$). Due to the infinte iron permeability assumption, the magnetic intensity is diminished everywhere inside it. The tangential component is continuous at the copper/iron boundary and is zero at the surface of the conductor at all points on this boundary giving the following boundary conditions;

$$H_x = 0 \qquad y = 0 \quad \text{.....A3.5a}$$

$$H_y = 0 \qquad x = \pm a/2 \quad \text{.....A3.5b}$$

$$H_x = 0 \qquad y = b \quad \text{.....A3.5c}$$

$$-a/2 \leq x \leq -1/2$$
$$1/2 \leq x \leq a/2$$

$$H_x = \frac{-I}{l} \qquad -1/2 \leq x \leq 1/2 \quad \text{.....A3.5d}$$
$$y = b$$

The last two equations give the variation in H_x over the upper surface of the bar as a periodic function and this can be written using Fourier series as;

$$H_x = -\frac{I}{a}\left(1 + 2\sum_{n=1}^{\infty} G_n \cos n\frac{2\pi x}{a}\right) \quad \text{.....A3.6a}$$

where, $$G_n = \frac{\sin n\pi l/a}{n\pi l/a} \quad \text{.....A3.6b}$$

Equations A3.1d can be written as two equations as:

$$\frac{dJ}{dy} = -j\bar{\alpha}^2 H_x \quad \text{.....A3.7a}$$

$$\frac{dJ}{dx} = j\bar{\alpha}^2 H_y \quad \text{.....A3.7b}$$

From equations A3.7a and A3.3c and the boundary condition A3.5a, C = 0 and

$$J = B.D.\cosh K_1 x \cdot \cos K_2 y \quad \text{.....A3.8a}$$

From this equation, boundary condition A3.5b and equation A3.7b, $K_1 \sinh K_1 a/2 = 0$ giving that

$$K_1 = j\frac{2n\pi}{a} \quad \text{.....(n=0,1,2....) ...A3.8b}$$

and $$K_2^2 = j\bar{\alpha}^2 + \left(\frac{2n\pi}{a}\right)^2 \quad \text{.....A3.8c}$$

Using $K_2 = U_n + jV_n$, completing the square and separating real and imaginary parts:

$$U_n^2 - V_n^2 = \left(\frac{2n\pi}{a}\right)^2$$

$$2U_n V_n = \bar{\alpha}^2$$

Solving these two equations for real V_n and U_n gives;

$$U_n = \pm\frac{\sqrt{2n\pi}}{a}\left(\sqrt{1 + \left(\frac{\bar{\alpha}a}{2n}\right)^4} + 1\right)^{\frac{1}{2}} \quad \text{.....A3.9a}$$

$$V_n = \pm\frac{\sqrt{2n\pi}}{a}\left(\sqrt{1 + \left(\frac{\bar{\alpha}a}{2n}\right)^2} - 1\right)^{\frac{1}{2}} \quad \text{.....A3.9b}$$

From equations A3.9 and A3.8 it is possible to show that;

$$J = E_n \cos n\frac{2\pi x}{a} \cosh(U_n + jV_n)y \quad \text{.....A3.10a}$$

The sum of all the solutions for J gives the final solution as;

$$J = \sum_{n=0}^{\infty} E_n \cos n\frac{2\pi x}{a} \cosh(U_n + jV_n)y \quad \text{.....A3.10b}$$

From this equation and the boundary condition A3.5d and equation A3.7a:

$$\sum_{n=0}^{\infty} E_n(U_n + jV_n) \cos\frac{2n\pi x}{a}.\sinh(U_n+jV_n)b = j\bar{\alpha}^2\frac{I}{a}\left(1 + 2\sum_{n=1}^{\infty} G_n\cos\frac{2n\pi x}{a}\right)$$

and putting n = 0 in this equation gives;

$$E_o = j\bar{\alpha}^2\frac{I}{a}\ \frac{1}{(U_o+jV_o).\sinh(U_o+jV_o)b} \quad \text{.....A3.11a}$$

and putting n = 0 gives;

$$E_n = j\bar{\alpha}^2\frac{I}{a}\ \frac{2G_n}{(U_n+jV_n).\sinh(U_n+jV_n)b} \quad \text{.....A3.11b}$$

Substituting these two equations in equation A3.10b gives;

$$J = j\bar{\alpha}^2\frac{I}{a}\left(\frac{\cosh(U_o+jV_o)y}{(U_o+jV_o).\sinh(U_o+jV_o)b} + 2\sum_{n=1}^{\infty} G_n\frac{\cos(\frac{2n\pi x}{a}).\cosh(U_n+jV_n)y}{(U_n+jV_n).\sinh(U_n+jV_n)b}\right)$$

The potential difference per unit length of the bar at any point along the slot opening is given by:

$$I(R_e + jX_e) = \frac{1}{\sigma}J$$

and the d.c resistance per unit length of the bar is $R_{d.c} = \frac{1}{\sigma.a.b}$

Joining the last three equations together gives;

$$\frac{R_e + jX_e}{R_{d.c}} = j\bar{\alpha}^2 b \left(\frac{\coth(U_o+jV_o)}{(U_o + jV_o)} + 2 \sum_{n=1}^{\infty} G_n \frac{\coth(U_n+jV_n)b}{(U_n + jV_n)} \right)$$

Separating the real and imaginary parts gives;

$$\frac{R_e}{R_{d.c}} = \frac{\bar{\alpha} b}{\sqrt{2}} \left(\frac{\sinh\sqrt{2}b\bar{\alpha}+\sin\sqrt{2}b\bar{\alpha}}{\cosh\sqrt{2}b\bar{\alpha}-\cos\sqrt{2}b\bar{\alpha}} + 2\sqrt{2}\bar{\alpha} \sum_{n=1}^{\infty} G_n \frac{(U_n \sin 2V_n b + V_n \sinh 2U_n b)}{(U_n^2+V_n^2)\ (\cosh 2U_n b - \cos 2V_n b)} \right) \ldots \text{A3.12a}$$

and,

$$\frac{X_e}{R_{d.c}} = \frac{\bar{\alpha} b}{\sqrt{2}} \left(\frac{\sinh\sqrt{2}b\bar{\alpha}-\sin\sqrt{2}b\bar{\alpha}}{\cosh\sqrt{2}b\bar{\alpha}-\cos\sqrt{2}b\bar{\alpha}} + 2\sqrt{2}\bar{\alpha} \sum_{n=1}^{\infty} G_n \frac{U_n \sinh 2U_n b - V_n \sin 2V_n b)}{(U_n^2+V_n^2)\ (\cosh 2U_n b - \cos 2V_n b)} \right) \ldots \text{A3.12b}$$

where,

$$U_o + jV_o = j^{\frac{1}{2}}\bar{\alpha} = \frac{(1 + j)}{\sqrt{2}} \bar{\alpha}$$

and, $j = \sqrt{-1}$

Fig.(8.3) shows the variation of X_e and R_e with frequency for semi-closed and completely open slots rotor. It can be seen clearly that X_e is increasing with slot opening having a minimum value for completely open slot ($1/a = 1$, $G_n = 0$) and maximum value for completely closed slots ($1/a=0$, $G_n = 1$). This explains the reason for the increase of x_1, x_2 when SRW are inserted in the stator. The change of the resistance with slot opening is negligible. The change of the resistance with frequency is small also, especially at frequencies not more than 50Hz. On the other hand the change in X_e as a function of frequency is pronounced and is almost linear.

Fig.(8.4) shows the variation of X_e as a function of slot opening for constant frequency and values of b/a as parameters. The change in the ratio b/a is achieved by using b = 16mm and changing a. As a is changing the shape

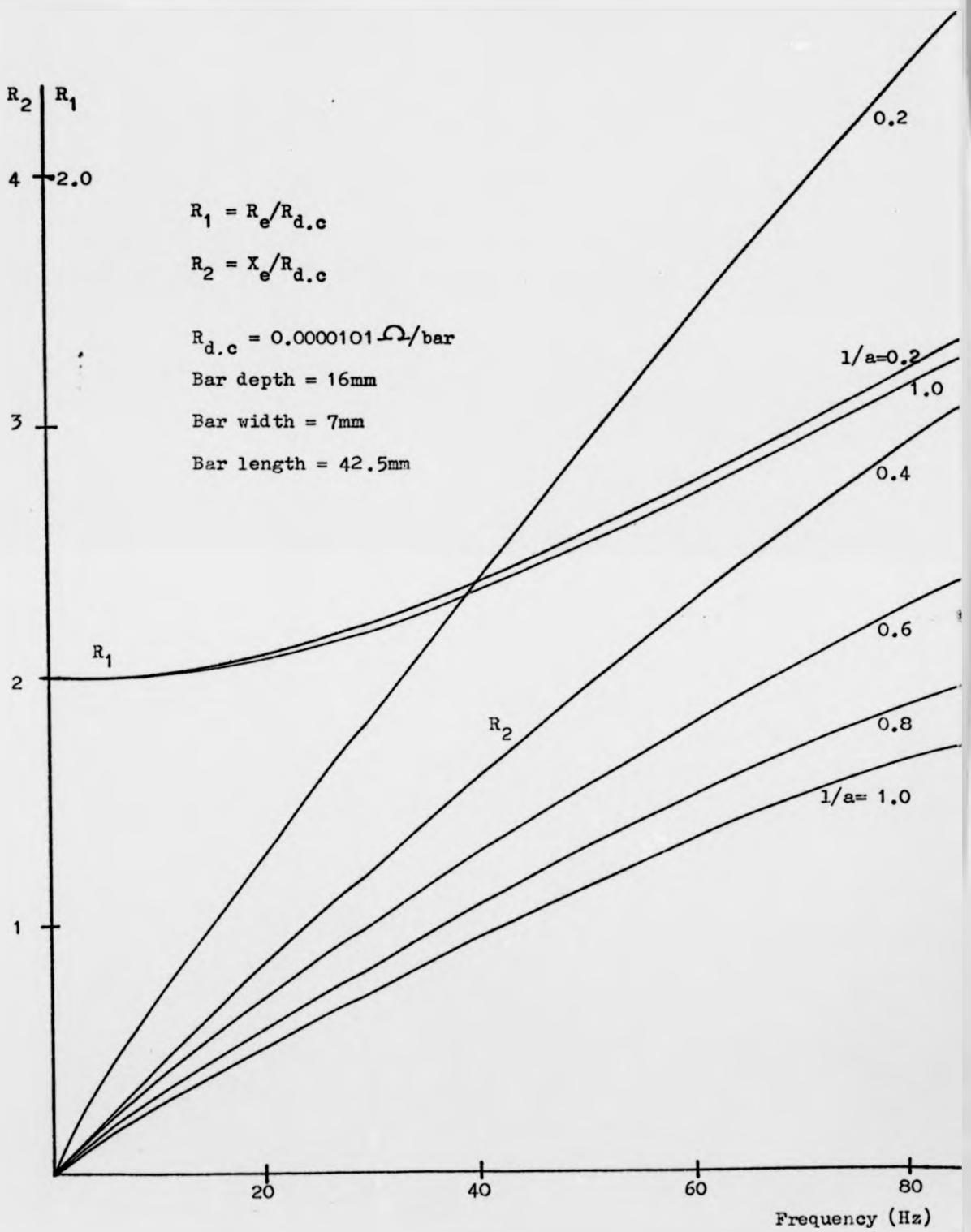

$R_1 = R_e/R_{d.c}$

$R_2 = X_e/R_{d.c}$

$R_{d.c} = 0.0000101\ \Omega$/bar

Bar depth = 16mm

Bar width = 7mm

Bar length = 42.5mm

Fig.(8.3) - R_1 & R_2 as a function of frequency for slot opening as parameter.

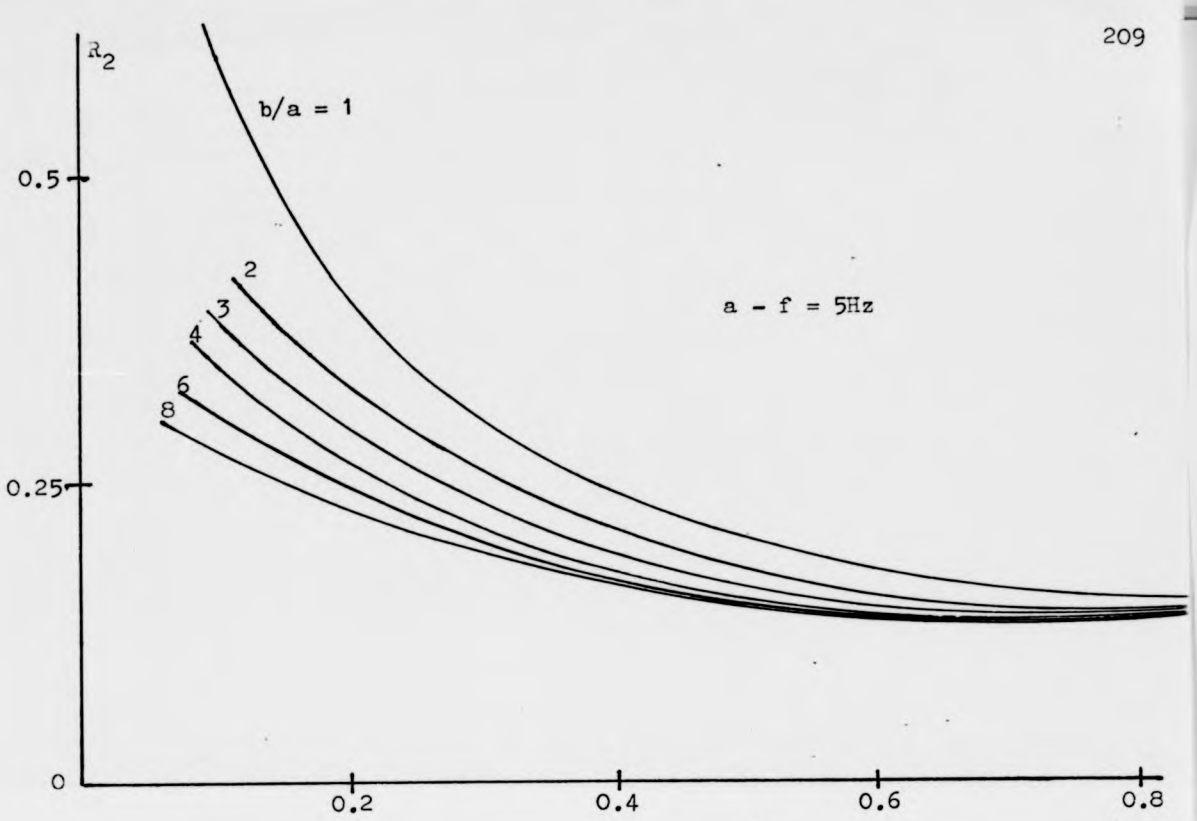

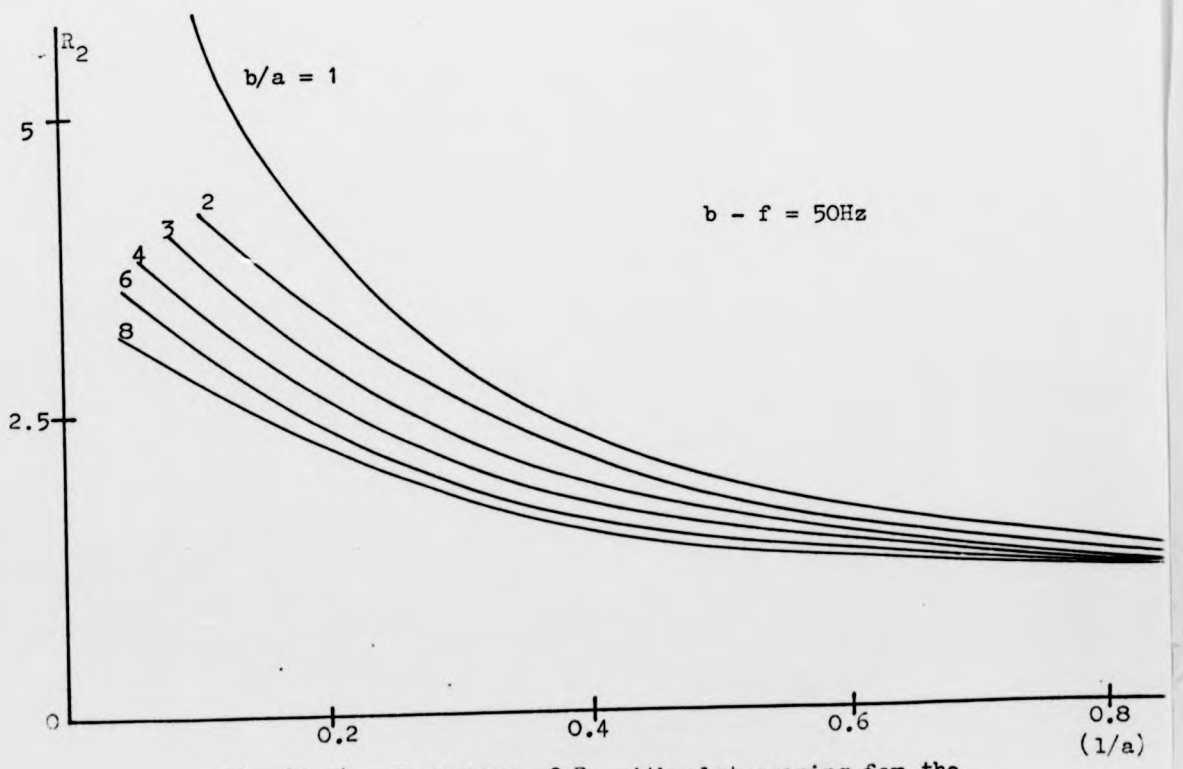

Fig.(8.4) - Variation of R_2 with slot opening for the slot height/slot depth (b/a) ratio as parameter

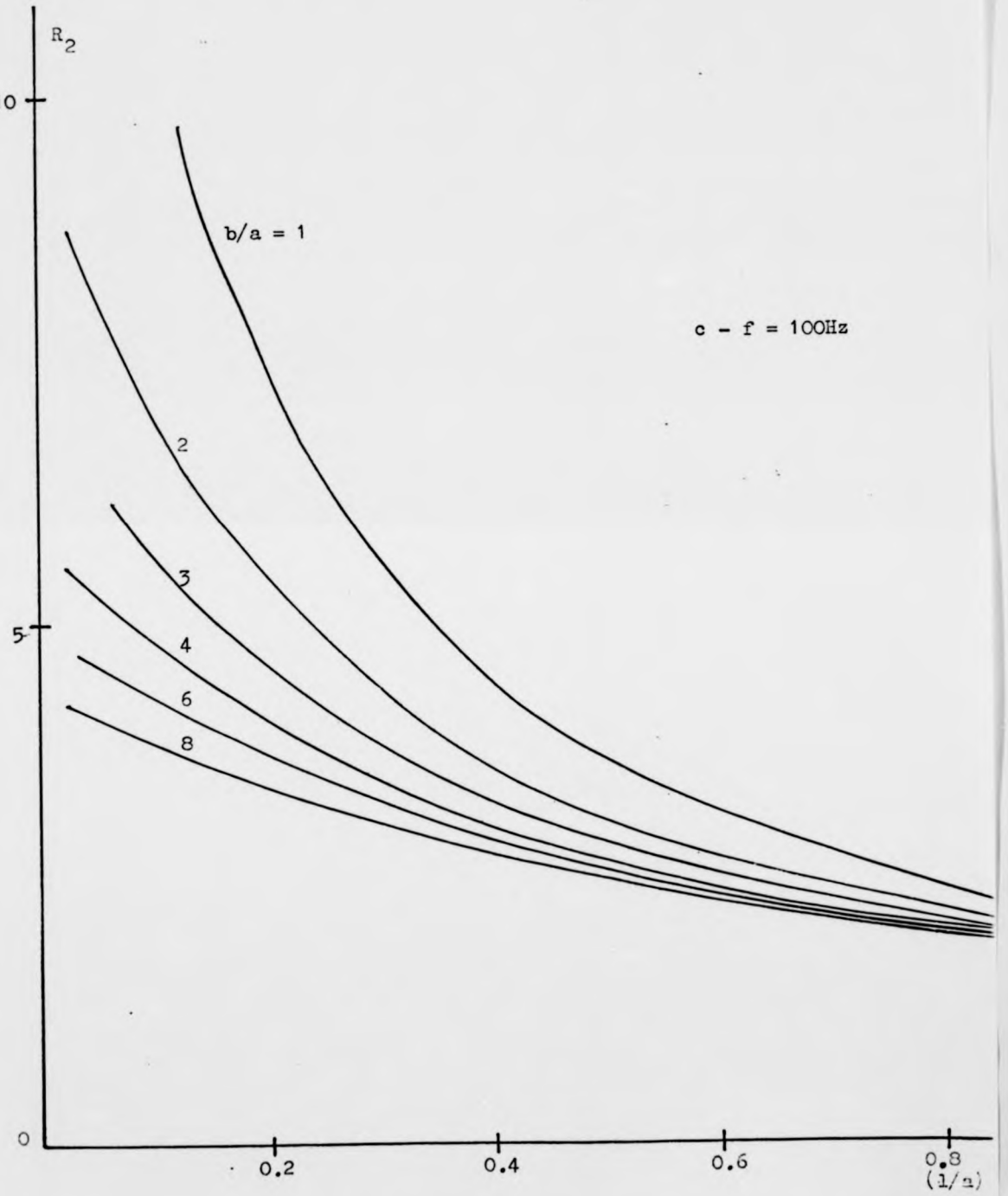
R_2
10
5
0
b/a = 1
2
3
4
6
8
c - f = 100Hz
0.2
0.4
0.6
0.8
(1/a)

of the bar is changing continuously. The change of X_e with slot opening is most marked for a square conductor with b/a = 1. It is possible to see that the curves approach the same value of X_e for the completely open slot and that this value is increasing with the frequency as 0.13, 1.2 and 2.0 for values of frequency equal to 5, 50 and 100 Hz. The same approach can be used in the case of the stator slot filled with wire by assuming uniform current distribution taking 1/a = 1 and consequently $G_n = 0$.

The variation in the reactance and resistance of the end rings with frequency can be obtained by adopting the arrangement shown in fig.(8.5) having aluminium ring and one iron boundary, employing the same approach used in ref.(1.5)

A4 - Magnetic pull

The operation of electromagnetic apparatus depends on the mechanical force which is exerted on the iron part when the magnetic field is in operation. The calculation of such mechanical force is often difficult. There are a number of methods for calculating the total force at the boundaries, such as equivalent pole or current distribution or a combined method of both, virtual work method and Maxwell's stress method. These methods give different surface force distributions but most give the same total force. The last two mentioned methods are considered here briefly and the virtual work method is used in force calculations.

a - Maxwell's stress method

The total force due to field sources can be calculated by drawing closed surfaces around them and integrating the Maxwell field stresses in vacuo over the surfaces, Ref. 86, 87. These stresses consist of a tension along the direction of force of magnitude $\frac{1}{2}\mu_o H_n^2$ and an equal pressure at right angles. The component of the stress directed away from the surface can be resolved into the normal and tangential components as:

$$F_n = \tfrac{1}{2}\mu_o (H_n^2 - H_t^2) \quad \text{.....A4.1}$$

$$F_t = \mu_o H_n H_t \quad \text{.....A4.2}$$

Assuming that the flux lines cross the air-gap normally (i.e to say that the tangential flux(radial) is very small compared with the normal component ($H_t = 0$) and integrating equation A4.1 for a pole pitch the total normal force can be found.

b - Concept of virtual work

This method of force calculation depends upon the change in the total stored magnetic energy due to a virtual displacement, and it gives simple results when applied to equipotential boundaries. Considering a magnetic field H with flux density B existing in an air-gap of length g and cross-sectional area A, the total magnetic energy stored in this gap volume is given by:

$$dw = \tfrac{1}{2}\mu(A.g)H^2 \quad \text{Joules}$$

Using the virtual work concept, assuming that due to some mechanical force F the air-gap is increased to $(g + \Delta g)$, keeping the gap flux constant, the new total magnetic energy becomes:

$$\bar{dw} = \tfrac{1}{2}\mu A(g + \Delta g)H^2 \quad \text{J}$$

giving rise to a change in the magnetic energy by the amount

$$\Delta w = \tfrac{1}{2}\mu(A.\Delta g)H^2 \quad \text{J}$$

This extra energy is supplied by the work done in expanding the air-gap against the resistance of the attractive force:

$$F = \tfrac{1}{2}\mu H^2 \quad \text{Newton/m}^2$$

Therefore when there is no magnetic material in the air-gap,

$$F_a = \frac{B^2}{2\mu_o} \quad \text{.....A4.3}$$

But when there is steel core in the gap, the force on the steel is a result of the air-gap flux modification due to the existence of the steel compared with the air. Therefore the attraction force becomes:

$$F_s = \frac{1}{2\mu_o}\frac{B^2}{\mu_r} \quad \text{.....A4.4}$$

where μ_r is the steel relative permeability.

The force applied on the steel due to the external field is.

$$F = \frac{B^2}{2\mu_o}(1 - 1/\mu_r) \qquad N/m^2 \quad \text{.....A4.5}$$

A50/ Fig.(8.6) - The experimental axial field a.c motor

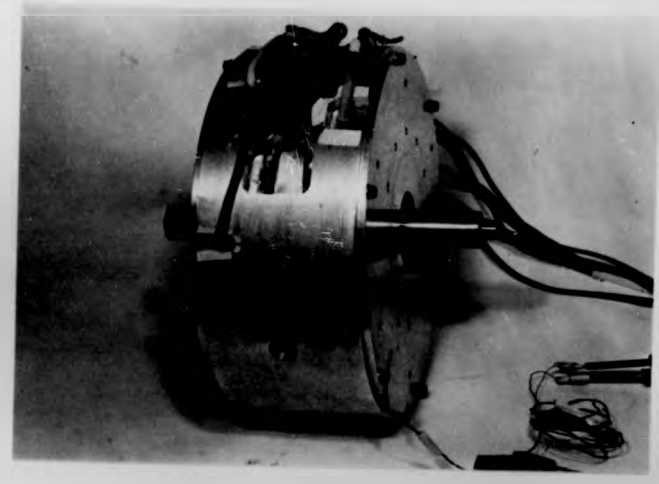

a - Single cage motor assembled

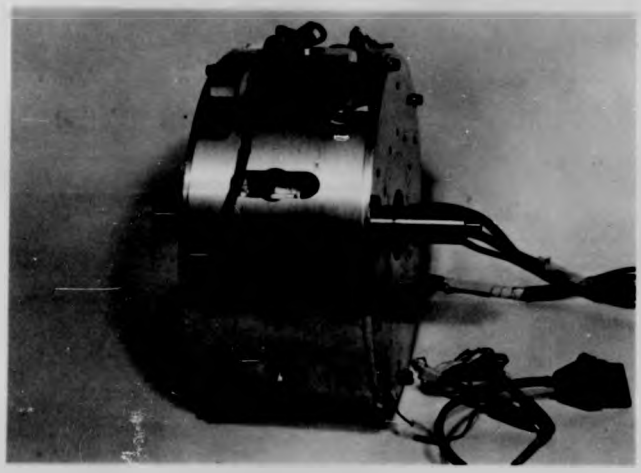

b - Double cage motor assembled

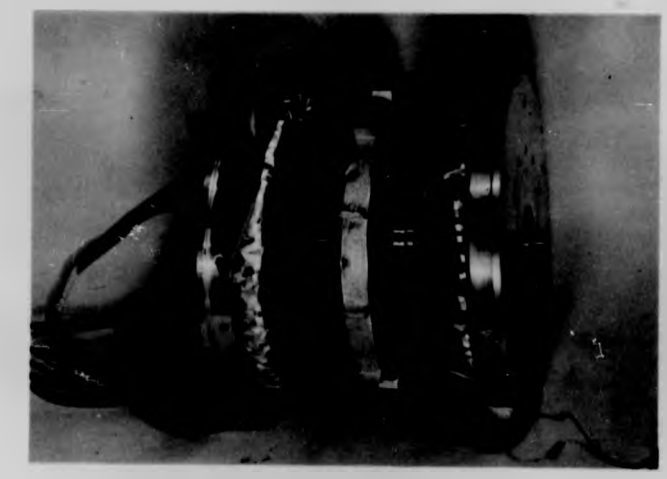

c - The motor opened

A50/ Fig.(8.6) - The experimental axial field a.c motor

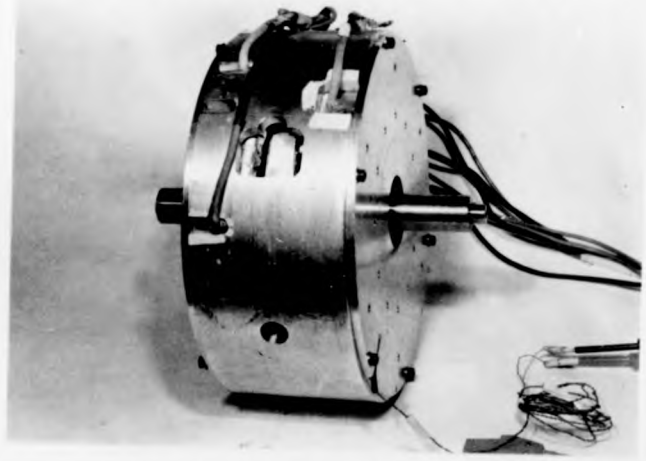

a - Single cage motor assembled

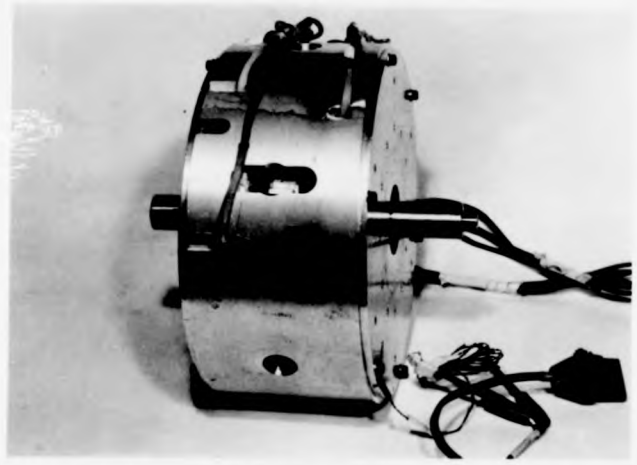

b - Double cage motor assembled

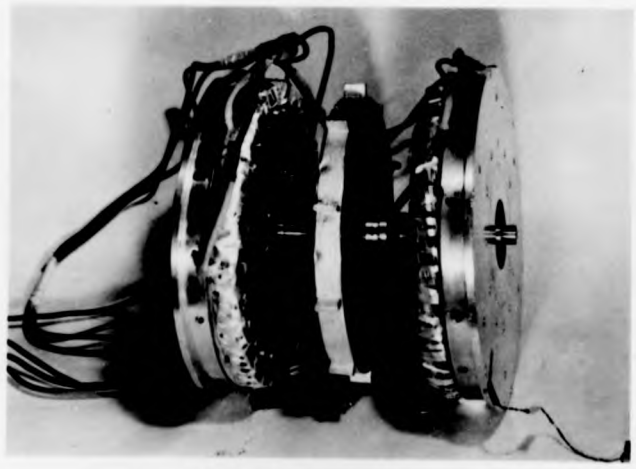

c - The motor opened

REFERENCES

1.1 Dunsheath, P. "The history of Electrical Engineer" Faber, London, 1962. (Book).

1.2 Pensabene, P. "Electric motor driven pumps" United States patent office 3171356, March 2nd. 1965.

1.3 Pensabene, N. "Improvements in or relating to Electric induction motors"
a - British patent 705937, March 24, 1954.
b - British patent 790566, Feb. 12, 1958.

1.4 Rustecki, R.Z. "Improvements in or relating to induction drive anemblies" British patent 1450033, 22 Sept. 1976.

1.5 Capaldi, B. "The theory and performance of A.C. axial flux machines" Ph.D. Thesis, University of Warwick, 1973/1974.

1.6 Say, M.G. "Performance and design of A.C. machines" Pitman and Sons Ltd., London, 1970. (Book).

1.7 Nasar, S.A. "An axial air gap, Variable speed, eddy current motor" I.E.E. Trans. on power apparatus and systems, vol.PAS-87, No.7 July, 1968.

1.8 Bramanti, A., et. al. "Experimental research on a prototype of a three phase induction motor with axial air-gap" International Conf. on electrical machines, Sept.1978.

1.9 Lawrenson, P.J. and Agu, L.A. "Theory and performance of polyphase reluctance machines" proc.I.E.E. 1964, 111(8).

1.10 Eastham, J.F. and Evans, P.D. "An axial flux reluctance motor" I.E.E. Trans. No.136, Conf. on small electric machines, 1976.

1.11 Evan, P.D. and Eastham, J.F. "Segmental rotor disc motor" Electrical power applications, vol.1, No.1, Feb. 1978.

2.1 Alcan (U.K.) Ltd., private communications.

3.1 Alger, P.L. "The nature of induction machines" Jhon Wiley and Sons Inc., New York, 1951. (Book).

3.2 Appleman, M.R. "The Cause and elimination of noise in small motors" A.I.E.E. Nov. 1937.

3.3 Kron, G. "Induction motor slot combinations" A.I.E.E. Trans. vol.50, June, 1931.

3.4 Fitzgerald, A.E. and Kingsley, C. "Electric Machinery" McGraw-Hill Inc. 1952. (Book).

3.5 a - Chalmers, B.J. "Performance of some magnetic slot wedges in an open-slot induction motor" proc. I.E.E. vol.114, Feb. 1967.
b - Ramey, B.B. "Use of metal slot wedges in induction motors" Elect. (cl.)J 1916, vol.13, P.407.

4.1 Gibbs, W.J. "Conformal transformation in Electrical Engineering" Chapman and Hall, London, 1958. (Book).

4.2 Coe, M.A. and Taylor, H.W. "Some problems in Electrical machine design involving Eliptic functions" The Phil.Mag. 7th. series, vol.6, 1928, P.100.

4.3 Dwight, H.B. "Tables of integrals and other mathematical functions" MacMillan, New York, 1964. (Book).

4.4 Heller, B. and Hamata, V. "Harmonic field effects in induction machines" Elsevier/North - Holland Inc., 1977. (Book).

4.5 Gupta, S.K. "Theory and performance of segmental rotor reluctance machines (including a new numerical conformal transformation method)" Ph.d. Thesis, University of Leeds, 1966/67.

5.1 Armitage, E. "Sixth form practical physics", J. Murray Ltd., London, 1960. (Book).

5.2 Von Kaehne, P. "Unbalanced magnetic pull in rotating electric machines" Electric Research Association, Z/T142, March, 1963.

5.3 Upankar, L. and Miericke, J. "Forces on null-flux magnetic levitation systems" J.Appl.phys. vol.44, No.4, April 1973.

5.4 Richards, P.L. and Tinkham, M. "Magnetic suspension and propulsion systems" J.Appl.phys. vol.43, No.6, June 1972.

5.5 Laithwaite, E.R. and Barwell, F.T. "Application of linear induction motors to high speed transport systems" proc.I.E.E. 1969, 116 (5).

7.1 Carter, A.H. and Corbett, A.E. "Electrical motor" British patent 1231782, 12 May, 1971.

7.2 Corbett, A.E. and Mohammad, M.T. "The disc-armature d.c. motor and its applications" I.E.E. Trans. No.136, Conf. on Small Electric Machines, 1976.

8.1 Stott, G. "Iron powder compacts for electromagnetic applications" M.Sc. Thesis, University of Warwick. 1971/1972½

8.2 Morley, A. "Strength of Materials" (Book) Longmans, Geen and Co., 1954.

8.3 Field, A.B. "Eddy currents in large slot-wound conductors" Trans. A.I.E.E., 1905, 24, P.83.

8.4 Bruges, W.E. "The evaluation of certain ladder-type networks" Proc. Roy. Soc., Edinburgh, A, 1943-62, page 175.

8.5 Swann, S.A. and Salmon, J.W. "Effective resistance and reactance of a rectangular conductor placed in a semi-closed slot" Proc. I.E.E. Vol.110, No.9, Sept.1963, page 1656.

8.6 Carpenter, C.J. "Surface-integral method of calculating forces on magnetized iron paths" Proc. I.E.E., Monograph 342, August 1959, 107C, page 19.

8.7 Binns, K.J. and Lawrenson, P.J. "Analysis and Computation of Electric and Magnetic field problems". Pergamon Press (1963), (Book).

THE DISC-ARMATURE D.C. MOTOR AND ITS APPLICATIONS *

A.E. Corbett and M.T. Mohammad

Engineering Department, University of Warwick, UK.

INTRODUCTION

The disc-armature d.c. motor is an axial airgap machine with a multipolar, permanent-magnet field system, and a disc-shaped, wire-wound armature which is encapsulated in a plastic material such as epoxy resin. An example of the machine is shown in Figure 1. It differs from conventional machines in that the airgap flux is predominantly axial, and the active armature conductors are radially disposed with respect to the shaft. Most commonly the armature is iron-free, but if required, iron can be introduced by mixing iron powder with the encapsulating material (1).

Research and development on this type of machine began at Warwick University in 1967, and since that time several prototype motors for various applications have been built and evaluated. The work was initiated by the desire to build wheel motors for a battery car, and the patent specification (2) makes reference to this application. But the first prototype to be built was a lawnmower motor (3) rated at 12 V, 900 W, 2500 rev/min which was successfully tested in a 24-inch cut, ride-on lawnmower.

Later a motorised wheel unit (4) was developed using a disc motor with a design rating of 36 V, 1.86 kW, 10500 rev/min and incorporating a two-stage epicyclic gearbox of ratio 16 : 1. Two prototypes were built for testing in an electric vehicle, but unfortunately faults developed on both machines during bench testing and the work was discontinued.

During the same period a fan motor (5) was developed for car radiator cooling. This unit is rated at 14 V, 90 W, 2730 rev/min and has an axial length of only 30 mm.

The latest prototype to be completed is a low inertia motor which is described below.

LOW INERTIA DRIVE

Description

A low inertia disc-armature motor has been built to satisfy a requirement for rapid acceleration and deceleration in an industrial application. A high torque/inertia ratio is required and the design philosophy adopted is to make the rotor as light as possible and to use the highest airgap flux density attainable with commercially available permanent magnets.

Figure 1 illustrates the construction of the prototype motor. The field system comprises sixteen segments of permanent magnet material (Columax) which are fixed to the mild steel end plates by epoxy resin adhesive. The segments are magnetised with alternate polarity to produce an 8-pole axial magnetic field in the airgap. To obtain maximum field energy with this type of magnet material it is essential to magnetise after assembly of the motor, and for this purpose a few turns of copper are wound around each magnet segment. These are left in place so that the motor can be readily remagnetised should the motor be dismantled for any reason.

The armature consists of a double layer duplex wave winding with 46 coils having 7 turns per coil and wound with polyester enamelled wire (class F) of 0.4 mm diameter. The coil ends are connected to a 46-segment face-type commutator and the whole is encapsulated in a high temperature grade of epoxy resin using a moulding technique. The objects in moulding are to provide adequate mechanical strength and to keep the disc thickness as near as is practicably possible to the thickness of the winding itself. In the low inertia motor the disc thickness in the active region is only 1.2 mm. It is also important to ensure that the armature disc runs truly perpendicular to the shaft so that minimum clearance can be allowed between the disc and magnet faces. The airgap between magnet faces in the prototype is 2.5 mm, giving a nominal clearance on each side of the disc of 0.6 mm. Since the armature contains no iron, it is the airgap between magnet faces which determines (almost completely) the axial length of the magnets necessary to establish the required flux density in the gap. To use a material like Columax most effectively requires that the magnet length should be approximately 20 times the length of the airgap, which emphasises the importance of keeping the airgap down to the absolute minimum.

The mechanical design is largely influenced by the need to maintain small axial clearances between the disc and the magnets, and special attention is paid to the bearing arrangement. The brushgear is quite conventional. Provision is made for 4 brushes in the prototype but much testing has in fact been carried out using only 2 brushes. The application demands that the motor frame should be totally enclosed.

Test Results

Steady-state performance. Figure 2 shows the performance characteristics of the motor on test with a supply voltage of 45 V. The characteristics are typical of disc-armature motors in that the torque is directly proportional to armature current; the speed falls only slightly with increasing load; and the efficiency is fairly constant at a high value over the normal operating range.

Transient performance. A flywheel was coupled to the motor shaft to represent the load inertia. A voltage of 90 V was applied to the motor terminals and the time taken to reach 6000 rev/min from standstill was recorded. Ignoring the effects of friction and of armature inductance (which is extremely small), the motor speed, ω at time, t after application of the supply to the motor at rest is given by

$$\omega = \omega_m (1 - \exp(-t/T_m)) \quad \ldots\ldots(1)$$

where ω_m is the final or maximum speed and T_m is the motor time constant. But

$$T_m = JR_a/k_m^2 \quad \ldots\ldots(2)$$

where J is the moment of inertia of the motor-plus-load, R_a is the armature resistance, and k_m is the motor constant given by the slope of the torque/current characteristic.

The actual time recorded was higher than the

* Presented at the I.E.E. conference No.136 on "Small Electrical Machines", London, March, 1976.

theoretical figure calculated from the above simple theory, and this is accounted for by several factors, one of which is the voltage dip caused by the source impedance. However, the measured time was found to be well within the specified limit.

OTHER APPLICATIONS

In addition to the motors already described, designs have also been produced for several other applications.

Domestic Appliances

One important field of application is domestic appliances, A rectifier must, of course, be employed to provide a d.c. supply from a.c. mains, but this is hardly a significant factor considering the reliability and low cost of diodes nowadays.

The disc-armature motor is very suitable for those appliances, such as vacuum cleaners, which traditionally employ the 'universal' series commutator motor as a means of obtaining speeds higher than that obtainable from an induction motor operated at mains frequency. Using the disc-armature motor, high speeds can be obtained with good commutation. High power/weight ratios can therefore be achieved which, together with the 'pancake' shape, can lead to benefits in the overall design of the appliance.

The ease with which the speed can be controlled also makes the motor suitable for those applications which require either continuously-variable or step-change speed control.

Figure 3 shows a sectional view of a motor designed for an output of 300 W at 17500 rev/min when operated from 240 V a.c. mains with a full-wave rectifier. Barium ferrite (Feroba III) permanent magnets are used instead of the metal alloy magnets used in the low inertia motor. Ferrite magnets provide a much lower airgap flux density than the alloy types, but this disadvantage is offset by their higher coercivity which is extremely important in disc-armature motors since it permits efficient design of machines with large airgaps. Ferrite magnets also offer the advantage of not requiring to be magnetised after assembly of the motor, thus obviating the need for built-in magnetising coils. Not least in importance, ferrite magnets are cheaper than alloy magnets for a given energy and, unless there are good reasons for specifying alloy magnets (e.g. as in the low inertia motor), ferrite magnets are to be preferred in general.

Automotive Accessories

Another important field of application is automotive electrical equipment and accessories. The requirements of particular applications differ but, in general, low cost, compactness, reliability, and high efficiency are all important.

A fan motor (5) for radiator cooling has already been mentioned. The design offers the same benefits as any electrically driven, thermostatically controlled fan, and in addition occupies very little space in the engine compartment.

A fan motor has also been designed for driving a car heater blower. Figure 4 shows the motor coupled to twin impellers. In this application the size of the whole installation is considerably reduced owing to the space saved by the short axial length of the motor. The motor uses barium ferrite magnets and is designed to develop 66 W at 4200 rev/min on a 12 V supply.

Other obvious applications in the automotive field are window winders and rear window wipers for estate-type vehicles which can accommodate the motor neatly within the space between the rear door panel and its trim.

Battery Electric Drives

Reference has already been made to a lawnmower motor (3) and a motorised wheel for battery electric cars (4). For battery propelled vehicles and equipment to be successful, the motor must provide high efficiency on account of the low energy densities obtainable from existing batteries, and high efficiency will remain important even when improved batteries become available.

Design studies show that very high efficiencies can be achieved by disc-armature motors using alloy magnets (e.g. Hycomax III) of the type with B - H characteristics intermediate between those of Columax and Feroba III.

Of all the applications considered, the traction motor is the most difficult owing to the heavy currents drawn by the motor on accelerating and ascending gradients. When a series motor is used, the problem is to some extent alleviated by an increase in the field strength under these conditions, but with the permanent-magnet disc-armature motor, the torque is strictly proportional to armature current. The problem is aggravated by the low thermal capacity of the armature, and these factors dictate that the motor must be carefully rated in relation to the application. For many duties it is advisable to incorporate a current limit facility in the control circuit and forced cooling should also be considered.

A 72 V, 4.5 kW, 2500 rev/min motor has been designed to drive a small electric car and it is planned to build a prototype in the near future. Further development of the motorised wheel is also planned.

COMMERCIAL PROSPECTS

The work described in this paper is a brief account of the development of disc-armature motors undertaken in a university engineering department over a period of eight years. Much of the work has been done with industrial support and there has been no lack of potential users of the motors, but it has proved difficult to persuade manufacturers to take up commercial production. The main obstacle has been the unorthodox production techniques required to wind and encapsulate disc-type armatures. However, this obstacle has been surmounted and a limited range of motors is now being produced commercially (6). It seems likely that in the next few years the use of disc-armature motors will become quite significant in those applications where its special characteristics offer distinct advantages.

Perhaps a parallel should be drawn with the two types of axial airgap motors which have already been in production for a number of years, namely the printed circuit motor (7) and the disc-type induction motor (8). Production of both machines requires unorthodox techniques, but manufacturing facilities have been developed, and today both machines hold a significant market.

ACKNOWLEDGMENTS

The authors wish to express their gratitude to the staff of the University of Warwick Workshops for the manufacture of the prototype motors, and in particular to Mr. D.G. Wood who is responsible for the mechanical design. Grateful acknowledgement is also made to the many companies and individuals who have sponsored work and given advice, assistance and encouragement.

REFERENCES

1. Stott, G., 1971, "Iron powder compacts for electromagnetic applications", M.Sc. thesis, University of Warwick.

2. Carter, A.H. and Corbett, A.E., 1971, "Electric Motor", British Patent 1231782.

3. Corbett, A.E., 1970, "A disc-armature d.c. motor", EM 70 Conference Publication, University of Dundee, 42.

4. Campbell, P., 1972, "A new wheel motor for electric commuter cars", Elect. Rev. 190, 10, 323 - 333.

5. Campbell, P. and Corbett, A.E., 1974, "The pancake motor", Automotive Des. Engng. 13, July/August 1974, 34 - 35.

6. Kitamori, T. and Takeda, N., 1973, "Wound coreless flat commutator motor - contributing to production of compact, lightweight devices", J.E.E. 78, 39-42.

7. Knights, D.E., 1975, "Prospects for the printed motor", Engineering 215 No. 3, 199 - 202.

8. Capaldi, B., 1973, "The theory and performance of a.c. axial flux machines", Ph.D. thesis, University of Warwick.

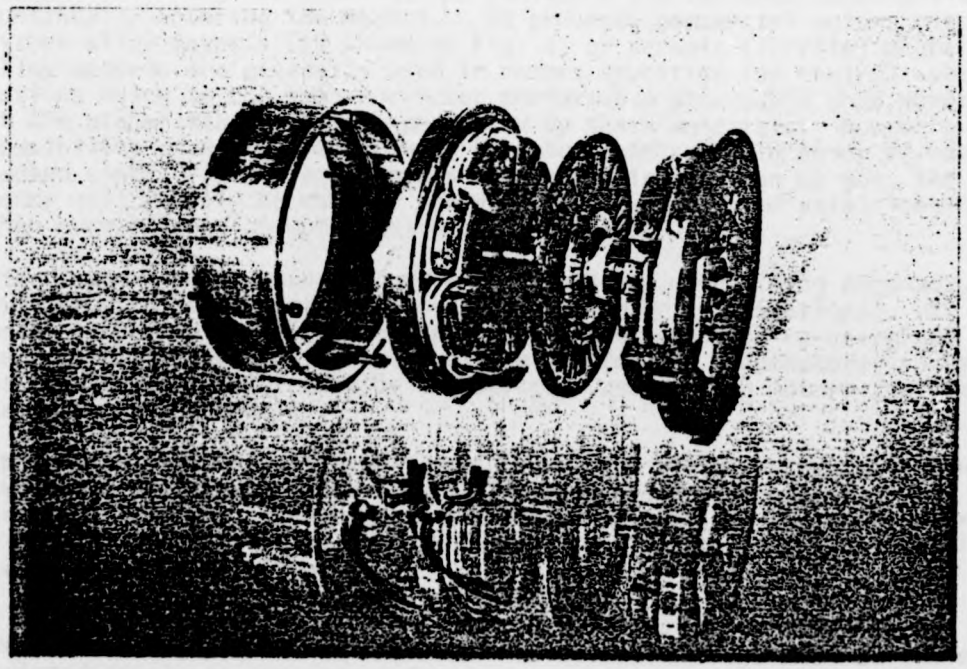

Figure 1 Low inertia disc-armature motor

3. Corbett, A.E., 1970, "A disc-armature d.c. motor", EM 70 Conference Publication, University of Dundee, 42.

4. Campbell, P., 1972, "A new wheel motor for electric commuter cars", Elect. Rev. 190, 10, 323 - 333.

5. Campbell, P. and Corbett, A.E., 1974, "The pancake motor", Automotive Des. Engng. 13, July/August 1974, 34 - 35.

6. Kitamori, T. and Takeda, N., 1973, "Wound coreless flat commutator motor - contributing to production of compact, lightweight devices", J.E.E. 78, 39-42.

7. Knights, D.E., 1975, "Prospects for the printed motor", Engineering 215 No. 3, 199 - 202.

8. Capaldi, B., 1973, "The theory and performance of a.c. axial flux machines", Ph.D. thesis, University of Warwick.

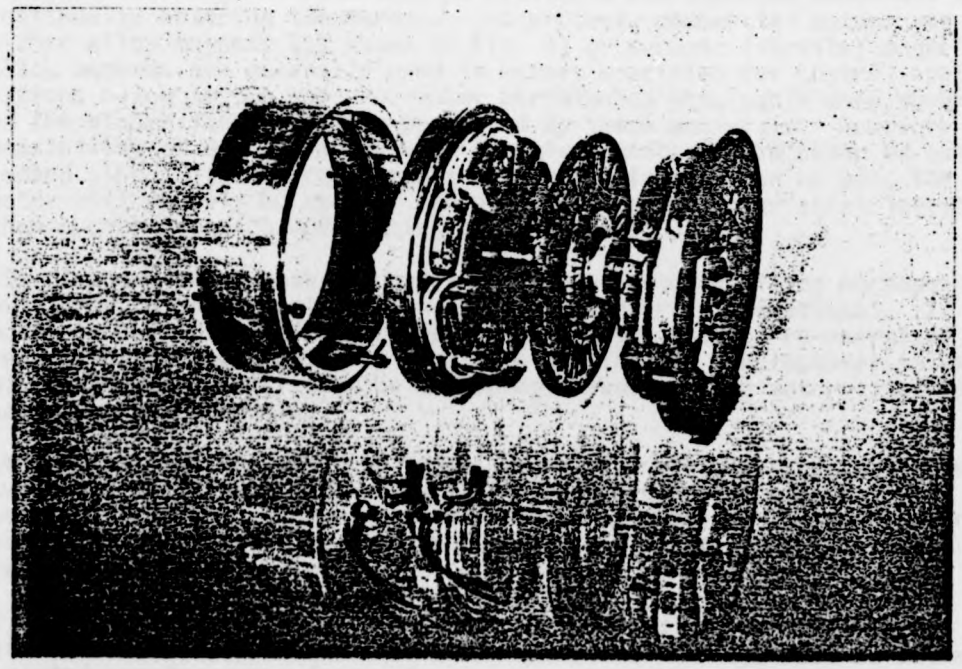

Figure 1 Low inertia disc-armature motor

THE DISC MOTOR AS A CONTROL SYSTEM ELEMENT *

A.E. Corbett and M.T. Mohammad

(University of Warwick)

1 INTRODUCTION Direct-current disc motors are available in two distinct constructional forms, namely printed armature and wire-wound armature. Fig. 1 shows examples of the two forms in exploded view. The two motors share a common basic geometry and operate according to the same principle: torque is produced by radial currents interacting with axial magnetic flux.

2 CONSTRUCTION

2.1 Magnetic circuit Both motors use permanent magnets to establish a stationary multipolar field system, the main components of which are parallel to the axis of rotation. For this reason the machine is sometimes called an axial field (or axial airgap) motor, in contrast to conventional machines in which the main components of flux are radial. In Fig. 1 the printed motor employs circular section magnets while the wire-wound machine is fitted with segmentally-shaped magnets. This is in no way connected with the armature type but is a question of economics; segments provide a higher flux per pole, but circular magnets are cheaper. The selection of magnet material is not straightforward since a wide range of materials is available and improved materials are continually entering the market.[1] At present, commercial motors use either alloy magnets (as shown in Fig. 1) or ceramic (ferrite) magnets. Alloy magnets are generally used in motors specified for control applications owing to the superior motor performance attainable when working at the higher flux densities permitted by these materials. However, the possibility of using a motor with ceramic magnets should never be overlooked since, if the requirements of the application can be met, the motor will usually be cheaper and will have even shorter axial length than a corresponding motor using alloy magnets.

Fig. 1 shows coils wound around the magnets for magnetising purposes, but these coils are not energised when the motor is operational. If the motor is ever dismantled for repair the magnets must be re-energised on re-assembly. Magnetising is usually a job for the manufacturer so users of this type of motor must be discouraged from opening motors just to satisfy their curiosity.

The magnets are energised to form a heteropolar field system, with the two rings of magnets aligned so that opposite poles face each other across the airgap. The magnets are bonded by adhesive to steel motor endplates which serve to close the magnetic circuit. The cylindrical case is usually of aluminium.

2.2 Armature construction In early printed motors the armature was made using printed circuit techniques, but nowadays most so-called printed armatures are formed from copper sheet by a punching process. In a typical motor, four sets of conductors produced in this way are

* To be presented at the ERA seminar on "Selecting small motors for control application", London, Jan.1979.

sandwiched together with thin layers of insulation between them, and connected electrically to form a continuous winding. The commutator 'segments' are formed in the same process since they are merely extensions of the armature conductors. The motor thus has a face-type commutator with a number of segments equal to the number of conductors per layer.

Wire-wound armatures are made by winding coils of enammelled copper on a special former. The coils are assembled in a jig and connected to a conventional commutator which may be of the drum or face type. The whole armature is then encapsulated in epoxy resin to give it rigidity and mechanical strength.

2.3 Mechanical considerations The mechanical design of disc motors is largely influenced by the need to maintain small axial clearances between the rotating disc and the stationary magnets, and special attention is paid to the bearing arrangement to ensure that axial movement is strictly limited. The brushgear is quite conventional. Motor frames are commonly totally enclosed and forced cooling is sometimes specified. Motors are frequently supplied with integral gearboxes and tachogenerators.

3 DISC MOTOR CHARACTERISTICS

3.1 Attributes arising from the construction The salient features of the disc motor which arise from its construction may be summarised as follows:

(a) The magnetic field established by the permanent magnets is constant and is not modified by currents flowing in the armature. Thus there are no magnetic saturation and armature reaction effects.

(b) Since there is no iron in the armature there are no associated power losses owing to eddy currents and hysteresis. Also the armature inductance is extremely low and the inertia is small.

(c) The absence of iron losses and field winding losses leads to high efficiency.

(d) The absence of a slotted iron structure on the rotor eliminates cogging. This property coupled with a high number of commutator segments enables the motor to operate smoothly with low torque ripple over a wide speed range down to standstill. (The same property makes the machine eminently suitable for use as a tachogenerator).

(e) Low armature inductance leads to a small (often negligible) electrical time constant and also ensures very good commutation and long brush life.

(f) Low inertia means that the mechanical time constant is small.

(g) The absence of saturation and armature reaction effects means that the torque developed is proportional to the

armature current. Thus the torque is limited only by the thermal capabilities of the armature and brushes and by any limitations of the drive circuit. Very high torques can be developed for short periods.

(h) Small electrical and mechanical time constants combined with the ability of the motor to develop torques many times greater than the continuously rated value make the motor ideally suited for control applications where fast response is required.

(i) Good commutation and robust mechanical construction enable disc motors to operate at high speeds.

(j) High speed capability combined with low power losses lead to high power-to-weight and power-to-volume ratios. Often the short axial length is an added advantage.

(k) The absence of rotating iron leads to silent operation.

3.2 Theory of operation The simplicity of disc motor construction continues to provide benefits when considering its theory of operation. To aid understanding of the basic principles it is justifiable to ignore

(a) armature inductance,

(b) mechanical friction and windage,

and (c) eddy currents induced in the armature conductors.

Under these assumptions the equations governing the steady-state and dynamic performance of the motor are extremely simple. As in all constant-field d.c. machines the induced electromotive force, e is given by

$$e = k\omega \text{ volts} \qquad \ldots\ldots(1)$$

where k is a constant depending on the number of poles and armature winding details which are a concern of the designer only, and ω is the rotational speed measured in radians per second. If the armature carries a current i amperes, the gross torque T developed is given by

$$T = ki \text{ Nm} \qquad \ldots\ldots(2)$$

Since in this simplified approach, friction, windage and eddy currents are ignored, the torque T represents also the output torque.

When the motor is supplied from a constant voltage source V,

$$V = e + iR \text{ volts} \qquad \ldots\ldots(3)$$

where R is the terminal resistance of the motor, comprising armature resistance and a resistance representing brush voltage drop. It should be noted that k in equation (2) is equal to k in equation (1) only if SI units are used. Unfortunately, manufacturers' literature does not use SI units universally, and two constants, k_e and k_t must then be

introduced.

3.3 Steady state performance From equations (1), (2) and (3) it can be shown that

$$\omega = \frac{V}{k} - \frac{RT}{k^2} \text{ rad/s} \qquad \ldots\ldots(4)$$

i.e. the torque/speed characteristic is linear with a negative slope R/k^2. Thus there will be such a characteristic for each value of voltage as shown in Fig. 2.

3.4 Dynamic performance The dynamic behaviour of the disc motor can be readily appreciated by considering its performance when coupled to a pure inertia load. In this case the torque T is required only to accelerate or decelerate the combined inertia of motor-plus-load, J. The equation governing the system is

$$T = J \frac{d\omega}{dt} \qquad \ldots\ldots(5)$$

where J is measured in kg m^2.

But, from equation (4)

$$T = \frac{k}{R}(V - k\omega) \qquad \ldots\ldots(6)$$

therefore $$\frac{k}{R}(V - k\omega) = J\frac{d\omega}{dt} \qquad \ldots\ldots(7)$$

or $$\frac{JR}{k^2}\frac{d\omega}{dt} + \omega = \frac{V}{k} \qquad \ldots\ldots(8)$$

This is the differential equation relating the motor speed with time. It can be solved if the initial conditions are known. For example, if the motor is initially at rest and then a voltage V is suddenly applied to its terminals, the motor speed is given by

$$\omega = \omega_s[1 - \exp(-t/\tau)] \qquad \ldots\ldots(9)$$

where ω_s is the final or maximum speed attained and τ is called the mechanical time constant. It can be seen from equation (9) that τ is the time taken for the motor to reach 63.2% of its final speed.

Alternatively, if the motor is initially running at its maximum speed with an applied voltage V when suddenly the supply to the motor terminals is replaced by a short circuit, then the motor speed is given by

$$\omega = \omega_s \exp(-t/\tau) \qquad \ldots\ldots(10)$$

Fig. 3 shows graphically the variation of motor speed with time as described by equations (9) and (10).

4 WARWICK DISC MOTOR The wire-wound disc motor shown in Fig. 1 is a prototype which has been developed at Warwick University for an industrial sewing machine drive. An important requirement of the drive is to accelerate and decelerate an inertia load in the way described in section 3.4. Design details of the motor are given elsewhere,[2] but it is worthwhile including here experimental results obtained from the motor since they are typical of disc motors of this class (wire-wound and printed). The results are interesting also because they agree very closely with theoretical predictions based on the simplified theory of Section 3.

Fig. 4 shows steady state performance characteristics of the motor when operated with a constant supply voltage of 45 V. The linear relationship between torque and current is clearly demonstrated and the presence of mechanical losses accounts for the line not passing through the origin. The linearity of the torque/speed relationship is also clearly shown. It can be noted that speed falls only slightly with increasing load and the efficiency curve shows that the motor has a high efficiency over a wide range of loading.

Figs. 5 and 6 illustrate the dynamic behaviour of the motor when coupled to an inertia load of 1.15×10^{-4} kg m^2. Fig. 5 shows the response of the motor when a step of 90V is applied to the motor at rest while Fig. 6 shows how the speed falls when the motor terminals are short circuited at full speed. Both responses correspond closely with the results predicted from the simplified theory of Section 3.

5 CONTROL OF DISC MOTORS The essential requirement for control of the disc motor is a variable voltage d.c. supply. This may be derived from single-phase or polyphase a.c. supplies or from a d.c. supply. A number of suitable controllers is available, using thyristor or transistor based circuits, but the subject is too extensive to be covered adequately here. Disc motor suppliers can advise on control aspects and can often supply suitable controllers to meet customers' requirements.

6 APPLICATIONS AND SELECTION OF DISC MOTORS Applications where the disc motor is being used include magnetic and paper tape transports, tape spoolers (magnetic, paper and cine), chart recorders, computer input-output equipment, business machines, and machine tools. It seems likely that the motor's use will become even more widespread in the future as demand grows for more sophisticated control systems and as more engineers become aware of this still little-known machine and its special capabilities.

Manufacturers generally have a catalogue of 'standard' motors which are listed in terms of their rated power, voltage, speed, etc., but requirements falling outside these specifications can usually be considered. Rated powers vary from 14 W to 20 kW and rated voltages from 12 V to 240 V. Some motors have maximum permissible speeds up to 10,000 rev/min. In addition to information on the continuous rating of their motors, manufacturers supply important data on dynamic characteristics such as mechanical time constant and maximum torque.

Important information is also provided on motor cooling, how to model the motor thermally, and how the continuous rating can be increased by forced ventilation.

7 REFERENCES

1 Corbett, A.E. and Roerig C.S.: 'Selecting permanent magnet materials for disc-armature d.c. motors', Proceedings International Conference on Electrical Machines, Brussels, September 1978.

2 Corbett, A.E. and Mohammed, M.T.: 'The disc-armature d.c. motor and its applications', IEE Conference publication 136, Small Electrical Machines, March 1976.

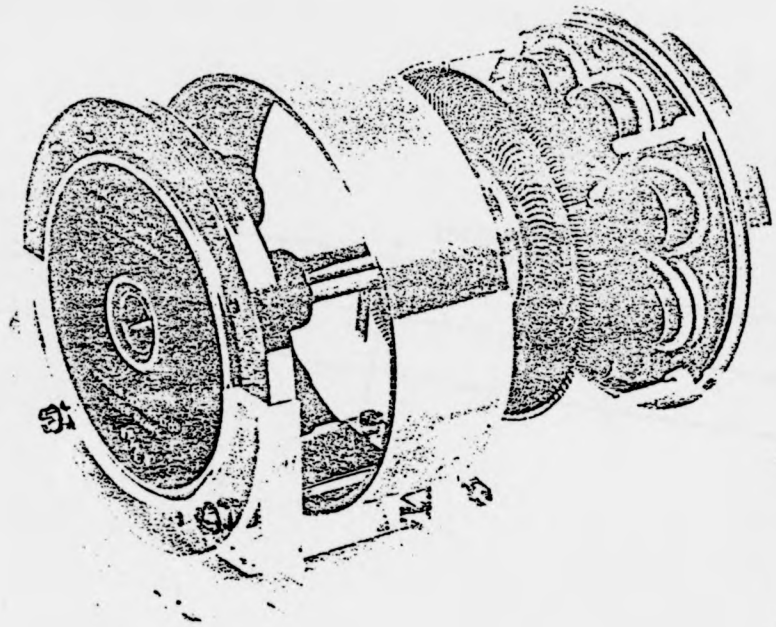

(a) printed type

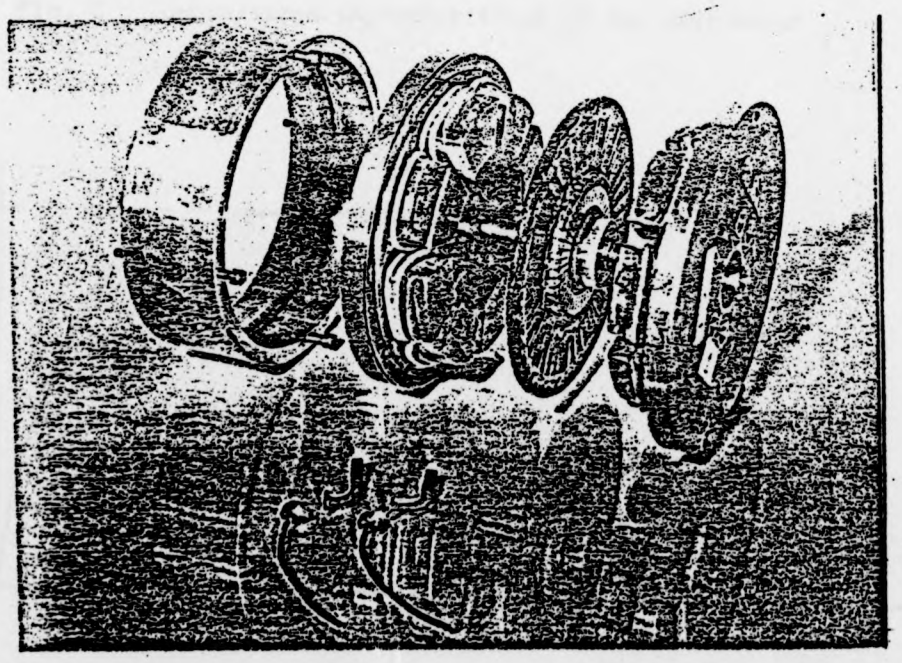

(b) wire-wound type

Fig. 1 Exploded views of two forms of disc motor

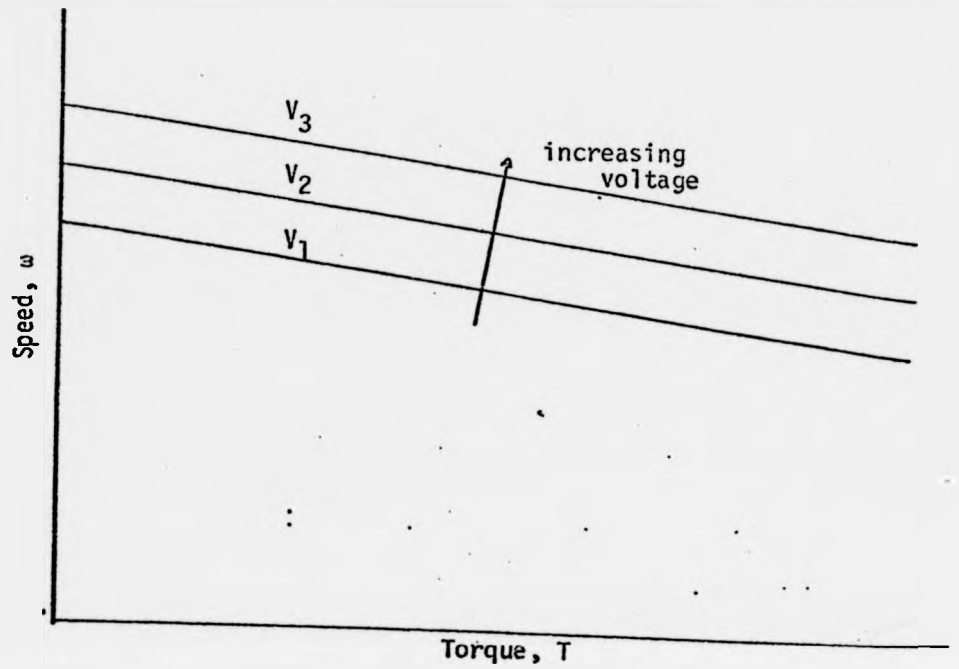

Fig. 2 Torque/speed characteristics of the disc motor

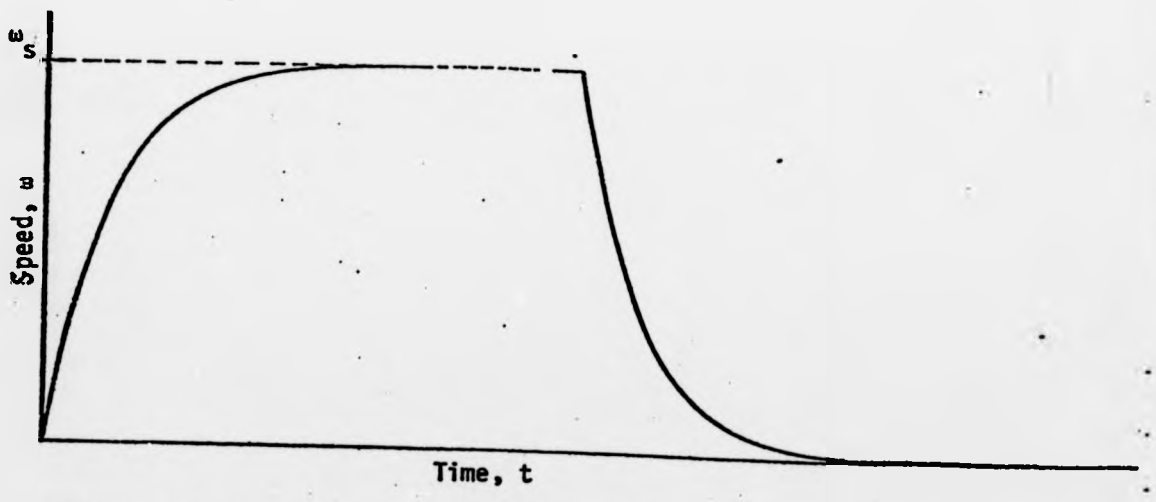

Fig. 3 Dynamic response of the disc motor

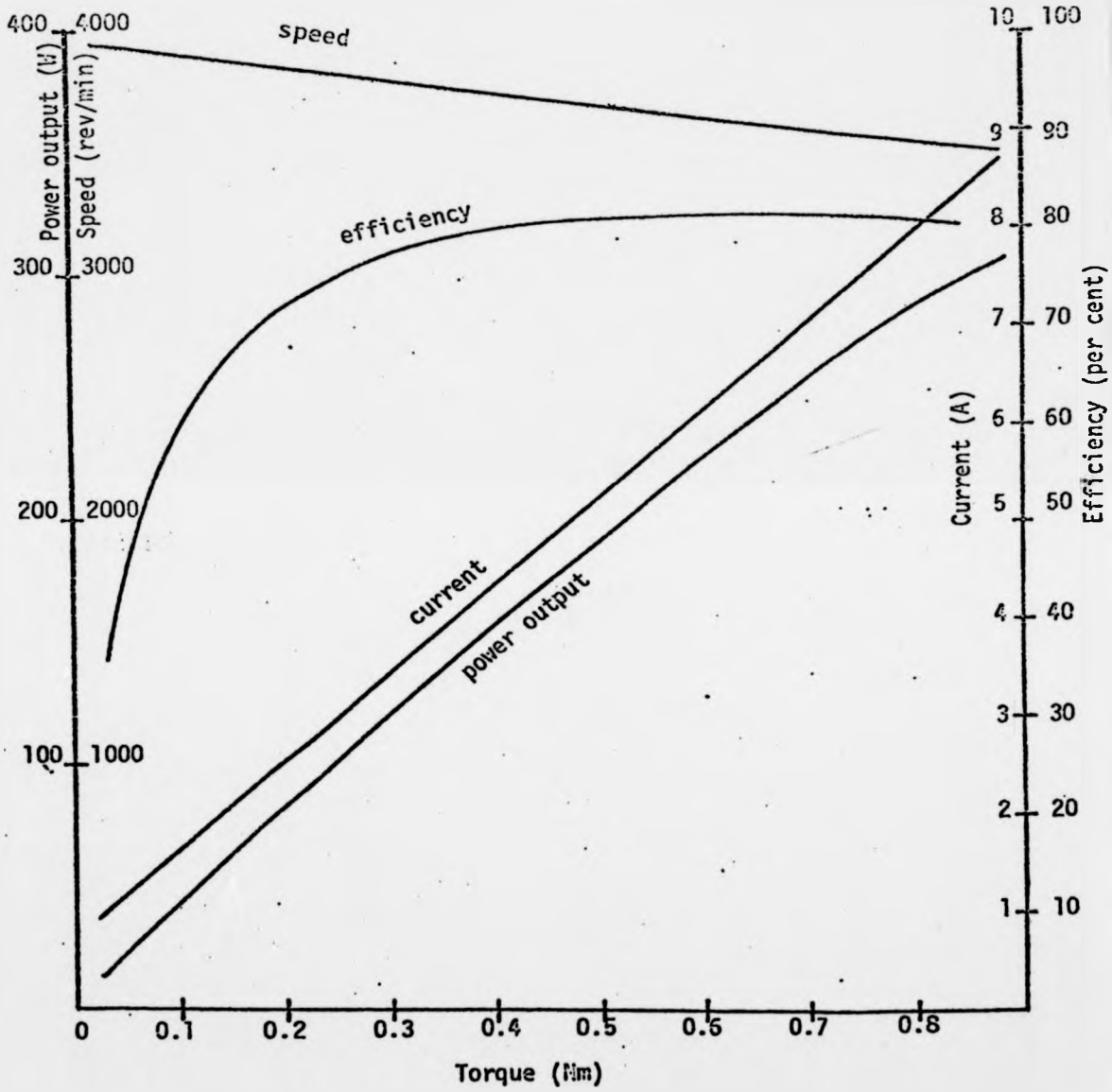

Fig. 4 Performance characteristics of Warwick disc motor at 45 V

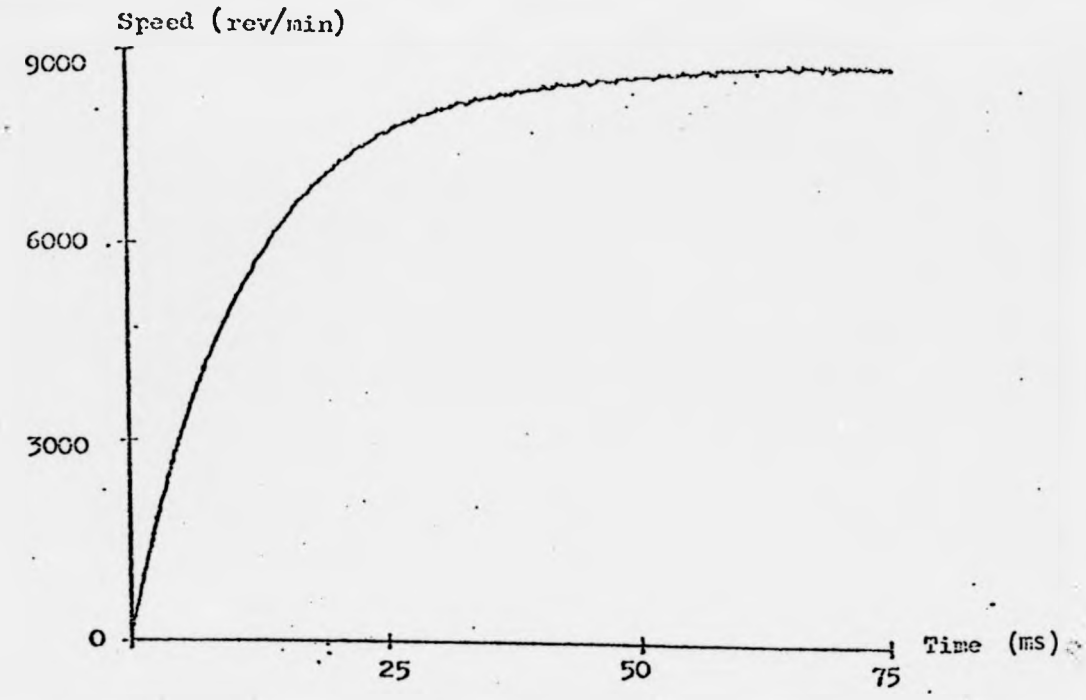

Fig. 5 Response of Warwick disc motor to step input of 90 V (total inertia = 1.85×10^{-4} Kg m^2)

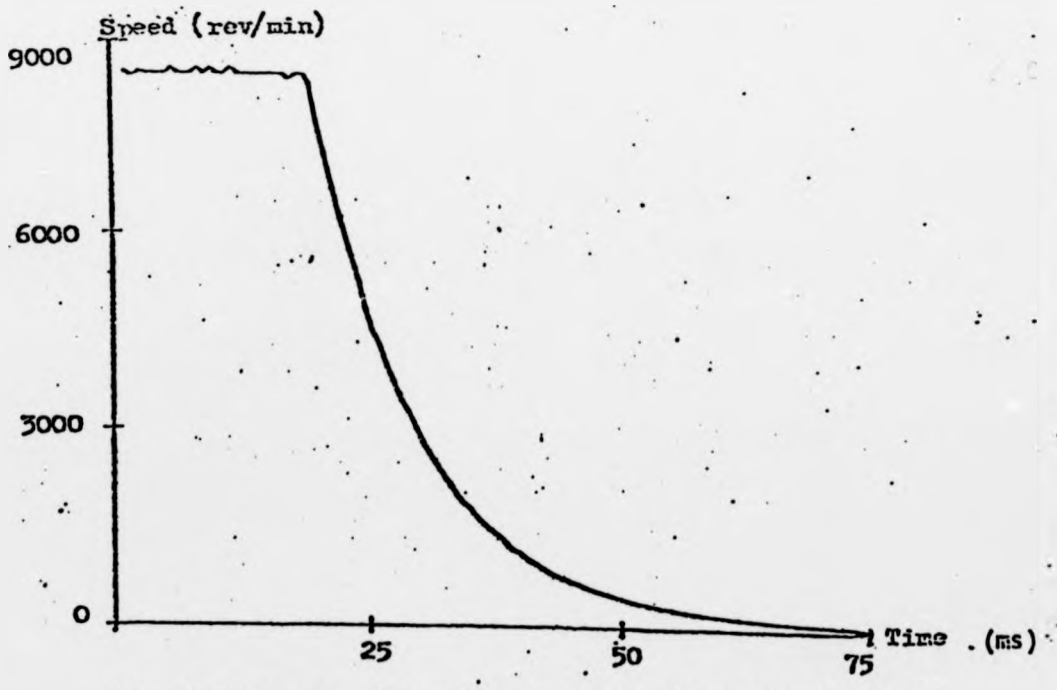

Fig. 6 Response of Warwick disc motor to short circuit of armature at full speed (total inertia = 1.85×10^{-4} Kg m^2)